Magnetic Ionic Liquids: Design, Properties and Application

A Thesis presented to the School of Chemistry and Chemical Engineering

The Queen's University of Belfast

In Fulfilment of the Requirements

for the Degree of

Doctor of Philosophy

By

Éadaoin McCourt MSc

The Queen's University of Belfast

September 2018

DECLARATION

I declare that this Thesis, except where otherwise stated, is based on my research, carried out in the School of Chemistry and Chemical Engineering, The Queen's University of Belfast, between October 2014 and June 2018.

Signed ……

Date ……..

Publications

1. Éadaoin McCourt, Zaneta Wojnarowska, Johan Jacquemin, Peter Nockemann, Haresh G. Manyar, Lukasz Hawelek and Marian Paluch, *Temperature and pressure induced structural changes of cobalt (II) in a phosphonium based ionic liquid*, The Journal of Physical Chemistry C, 2016, 120 (19), 10156 – 10161.

2. Éadaoin McCourt, Kane Esien Li Zhenyu, Solveig Felton, and Peter Nockemann, *Designing Dimeric Lanthanide(III)-Containing Ionic Liquids*, **Submitted.**

3. Mark Gilmore, Éadaoin McCourt, Francis Connolly, Peter Nockemann, Malgorzata Swadźba-Kwaśny and John D. Holbrey, Liquefied TOPO for metal separations: Transferring ionic liquid and deep eutectic solvent strategies into advanced liquid materials, **Submitted.**

Acknowledgements

There are many people whose encouragement and guidance made the completion of this thesis possible. My first and foremost gratitude goes to my supervisors; Dr. Peter Nockemann, Dr. Johan Jacquemin, and Dr. Haresh Manyar. I thank you for introducing me to this interesting field, for always making time to discuss my work and for your encouragement, and guidance throughout. I am particularly grateful for the wonderful collaborations which have enriched this PhD and would not have been possible without you. Johan thanks for the many visits to Marian's lab which really helped progress this work. It is much appreciated.

Of course, this research would not have been possible without the financial support of EPSRC, and for this, I am extremely thankful.

Throughout, I was lucky to have the opportunity to collaborate with Professor Marian Paluch and his research group in the Institute of Physics, Chorów, Poland. I am so thankful to Marian, Zaneta Wojnarowska, Justyna Knapik and Marzena Rams-Baron for welcoming me into their group, for their time, genuine interest in my work, enthusiasm and importantly, for showing me the sights of their beautiful country.

Sometimes to fully explore theories and hypothesis we need to combine expertise. In this respect, it has been a great collaborating with Dr Solveig Felton and Kane Esien from the School of Maths and Physics, QUB. Gaining a different perspective and their knowledge of the field of magnetism has enriched our understanding of various aspects of this research. I thank you both for taking the time to run our samples and for the helpful discussions regarding analysis.

My sincere thanks to Angela and Suzi in QUILL, and Trevor, Donal, Daren and Katherine in ASEP, for analysis and instrument training over the course of this work.

Thanks to Ken in the school office for always sending out-reach work my way! To Karen and Julie in the research office for always being on hand to answer any of my research related queries and to Kieran and Clive in the stores for always helping me out.

I am very grateful to Seren Technologies for giving me the opportunity to complete a 3-month work placement within QUB. This gave me a great insight into lab scale-up processes and has given me essential experience for post PhD life!

Massive thanks to the guys in the Nockemann group for making the past 4 years so enjoyable. To Rachel, Robert, Ena, Ciaran, Donnacha and Ritesh. I thank you all for providing such a wonderful and stress-free working environment, and most importantly for your advice and friendship over the years.

A special mention to my closest friends Maeve, Sarah, Shauneen, and Rebekah, I am so lucky to have such great friends and housemates. I cannot thank you enough for your patience, guidance and advice over the years, and, most importantly, for making my university years so enjoyable! To Ena and Sophie, thanks for all the advice and for keeping me sane with breaks in the sun during the writing of this thesis. It is much appreciated!

Last, but certainly not least, to my wonderful family. To Maighréad, Róisín, Peter and Aoife and new additions Richie and Éabha. I am so blessed to have such a wonderful and supportive family. You guys have provided the most welcomed distractions over the course of this work and your encouragement and belief in me over the years I am so grateful for. Maighréad, Richie, and Aoife thanks for coming to visit me in Poland. They were the best holidays!! To mam and dad, your constant support, financially and emotionally, genuine interest in the progression of my work and for instilling a belief in us that we should never stop learning has encouraged me to complete this research and is something I will be forever grateful for.

To Mam and Dad...

Abstract

Magnetic ionic liquids are a class of ionic liquids which are intrinsically paramagnetic due to the incorporation of transition metals, lanthanides, or actinides in either the anionic or cationic structure. Such incorporation leads to interesting magnetic, optical, and catalytic properties, depending on the metal incorporated. Owing to their intrinsic paramagnetic behaviour, manipulation of the transport properties of magnetic ionic liquids can be achieved by means of external stimuli.

This research aimed to design and synthesise novel magnetic ionic liquids and to gain an in-depth understanding of their physical properties, to explore the stimuli-responsive nature of magnetic ionic liquids and to look into the possibility of designing magnetic ionic liquids for particular applications. This took the form of three main chapters.

In Chapter 2, our interest lies in developing magnetic ionic liquids containing transition metals. The ability of cobalt salt in ionic liquid reservoir to change coordination upon cooling was taken as a case study to explore the stimuli-responsive nature of transition-metal based ionic liquids. Through the use of dielectric measurements we were able to investigate the effects of temperature and, importantly, pressure on the coordination behaviour of a cobalt thiocyanate based system over very wide frequency, temperature and pressure ranges, meaning the dynamic behaviour could be monitored over the liquid, supercooled and glassy region.

In Chapter 3, we looked at the design of a series of lanthanide(III)-containing ionic complexes which were dimeric in nature. Starting from the design of dimeric solids,

we demonstrate that by tuning of anion and cation structures we can lower the melting points below room temperature, while maintaining the dimeric structure. Magnetic measurements were able to establish the spin-spin interactions of the neighbouring lanthanide(III) ions in the liquid state at low temperatures and matched the interactions of the analogous crystalline solid compounds.

Finally, in Chapter 4, we combine the ability of a functionalised ionic liquid to selectively coordinate to a metal cation in solution and the magnetic properties of an ionic liquid, which is expected to lead to easier separation of the organic phase from an aqueous phase. In this context, we explore the development of a task-specific magnetic ionic liquid for the extraction of uranyl nitrate. We show that by incorporating specific features into the cation and anion structures, we can impart properties such as, hydrophobicity, extracting ability and magnetic functionality to the ionic liquid.

Table of Contents

List of Figures

List of Tables

List of Equations

Chapter 1. Introduction

1.1 Ionic liquids

Within the domain of chemistry, ionic liquids (ILs) are defined as low-melting salts which consist solely of ions having melting points below 100 °C. Originating from the pioneering work of Paul Walden *et al.*, in 1914 with the synthesis of ethylammonium nitrate $[EtH_3N][NO_3]$ (m.p. 12 – 14 °C)[1], the course of the next 100 years would see research transform this field with developments diverging into various sub-fields, for example; 1st generation chloroaluminate ionic liquids (1980s),[2,3] 2nd generation air and moisture stable ILs (1990s)[4] and 3rd generation functionalised ionic liquids (2000s).

1.1.1 Typical structures and properties

ILs are generally composed of organic quaternary cations (e.g. imidazolium, ammonium, and phosphonium) and small inorganic anions (Figure 1). The highly desirable physiochemical properties of ILs are often cited as being; non-volatile, non-flammable, having wide electrochemical windows, high chemical, and thermal stability, outstanding solubility characteristics and tuneable anion and cation structures.[5] Such remarkable features have attracted considerable attention as greener alternatives to traditional molecular solvents,[6] in catalysis,[7,8] electrochemistry and in separations.[9,10]

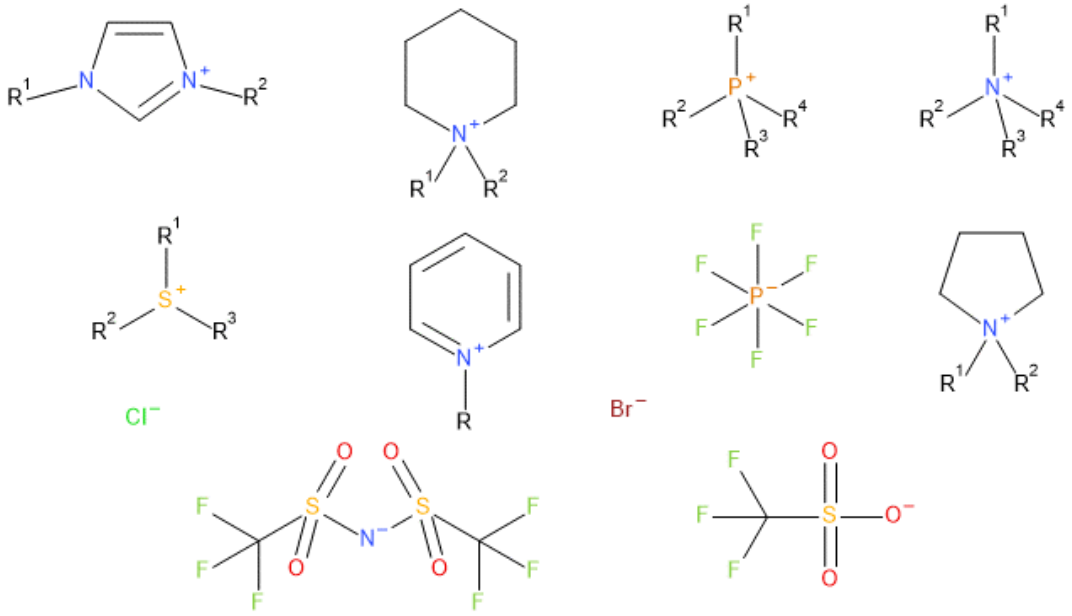

Figure 1. Common cations and anions used in ionic liquid synthesis.

1.1.2 Functionalised Ionic Liquids

Stemming from the awareness that the cation and anion of ionic liquids can be fine-tuned, the concept of functionalising ionic liquids was introduced by Davis *et al*.[11] A functional group can be covalently tethered to either the anionic or cationic structure of the IL[11–13], providing not only a suitable reaction medium but also the means of imparting reagent or catalyst functionality to the IL structure. Functionalised ionic liquids (FILs) or so-called task-specific ionic liquids (TSILs) have further expanded the field of ILs with developments spanning to areas such as catalysis[14,15], novel extractants[16–19], CO_2 capture[20], and stabilisation of metal nanoparticles.[21] Here, the anion or cation has specific functionality incorporated to meet the requirements of the end application. Examples of some TSILs in which

functionality is incorporated into the cation structure, and their potential applications are presented in Figure 2.

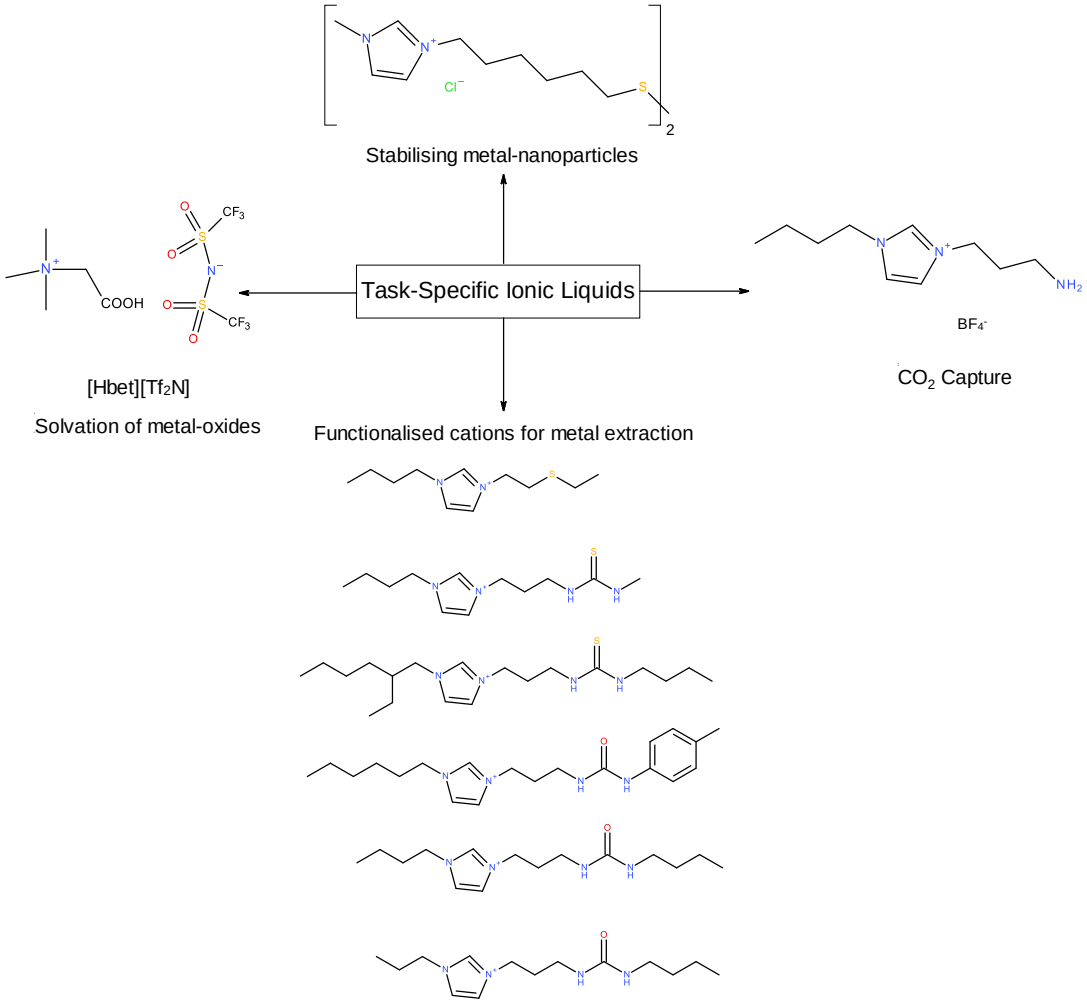

Figure 2. Examples of task-specific ionic liquid applications.

1.1.3 Melting points, viscosity and solubility properties of ionic liquids

The properties of ionic liquids are generally governed by the type of cation and anion and their interactions. Melting points, for example, can be decreased by reducing the anion and cation symmetry and charge accessibility. The imidazolium cation has a relatively acidic proton on the 2-position of the ring which ultimately leads to it being a strong hydrogen donor and interactions with the anion can aid crystallisation. Bulky trialkylphosphonium cations, on the other hand, have localised charge and low symmetry, leading to low melting points and a low tendency towards crystallisation.[22] Instead, the bulky phosphonium based ionic liquids tend to vitrify upon cooling.

Viscosity is one such property that is often important when looking at potential applications of ionic liquids. In contrast to water or widely utilised molecular solvents, the viscosity of ILs is often several orders of magnitude higher.[23] Such properties can directly affect properties such as conductivity, with the conductivity of ionic liquids inversely proportional to its viscosity. Viscosity is generally seen to increase with increasing cation and anion size and is strongly dependent on temperature.[12]

Solubility and solvation in ionic liquids are important characteristics and, again, are very much dependent on the cation and anion and their end purpose. In applications whereby the IL is used as a catalyst, for example, the solubility of the reagents and catalyst in the IL is important. The reagents, catalyst, and products must also, however, have differing solubilities in order to be easily separated.[12] In reactions, it can also be desired to have hydrophobic ILs, e.g. in aqueous/IL biphasic systems. By tuning of the anion and cation components, this can be easily achieved.

The solubility characteristics of Ionic liquids have found application in the dissolution of cellulose,[24] functionalised ionic liquids have also been used to dissolve large quantities of metal-oxides successfully, as demonstrated by Nockemann *et al*.[19], whereby, protonated betaine bis(trifluoromethylsulfonyl)imide, [Hbet][Tf_2N], had selective metal-solubilising power. This is an important parameter in the development of new extractants.

1.2 Metals in ionic liquids

Metal-containing ionic liquids are those in which a metal complex or ion is incorporated into the anionic or cationic structure and can be dated back to first generation ILs. The integration of metals into ILs can be in the form of metal complexes containing; transition metals, and lanthanides and actinides, a field which has become known as magnetic ionic liquids, chloroaluminates[25] or nanoparticles in ionic liquids.[26] Many review articles outlining the progression of the field of magnetic ionic liquids in areas of synthesis and application have been reported.[27–31] A review of the work done in this field, with a particular focus on the field of MILs and their applications is presented herein.

1.2.1 Magnetic ionic liquids

An important sub-field of ILs is the field of magnetic ionic liquids (MILs). MILs are single-component materials which have inherent paramagnetic properties due to the incorporation of transition or f-block (lanthanide and actinide) elements in either their anion or cation structure. As a result, in addition to the fundamental properties

of ILs, MILs can have intrinsic, magnetic responsiveness, colour, photophysical and luminescent properties, depending on the metal incorporated.

1.2.2 Transition metal-containing ionic liquids

Although metal-containing ionic liquids were amongst the earliest ILs to be extensively developed with that of the chloroaluminate ILs,[32–34] and moreover, investigations into transition metal-based systems were ongoing,[35,27] the field of magnetic ionic liquids emanated from investigations by Hayashi and Hamaguchi[36] and Yoshida *et al.,*[37,38] whereby the magnetic properties of 1-butyl-3-methylimidazolium tetrachloroferrate, $[C_4Mim][FeCl_4]$ (Figure 3), and 1-ethyl-3-methylimidazolium tetrachloroferrate, $[C_2Mim][FeCl_4]$, respectively, were extensively explored.

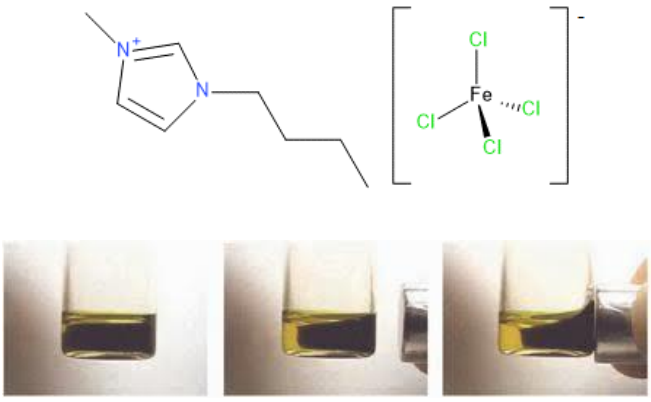

Figure 3. Structure of $[C_4Mim][FeCl_4]$ and response to an external neodymium magnet.[37]

These initial studies and the established unique properties, *i.e.* long-range magnetic ordering and magnetic manipulation, arouse much interest and provided a solid foundation for further development with many mono- and divalent magneto-active systems proceeding. The halometallates with anion structure, $[MX_4]^{z-}$ have been investigated with M = transition metals; Co, Ni, Mn and Fe in combination with

various cations; *N*-alkyl-*N*-methylimidazolium, *N,N*-dialkylpyrrolidinium, *N*-alkylpyridinium and tetraalkylphosphonium.[22,39,40] The anion structures of these halometallate based systems have in general; isolated tetrahedral anions and have large distances between the nearest neighbouring metal centers.[41] Notable is the ease of synthesis of the described MILs. For example, $[C_4Mim][FeCl_4]$ can be prepared by simply mixing $[C_4Mim]Cl$ with either anhydrous $FeCl_3$ or $FeCl_3{\cdot}6H_2O$ in equimolar amounts.[42] Similarly, the $[P_{666\ 14}][MCl_4]$ series, M = Fe, Co and Mn, can be prepared by addition of metal chloride salt to trihexyl(tetradecyl)phosphonium chloride, $[P_{666\ 14}]Cl$, in an organic solvent. With drying, viscous oils are obtained in high yields.[43]

To realise RTILs with divalent anions, the cation and anion structure can be further tuned. Bulky tetraalkylphosphonium cations, for example, $[P_{666\ 14}]^+$, have the ability to minimise Coulomb interactions and additionally the anion structures can be further tuned by investigating different ligands. MILs based on the tetraisothiocyanatocobaltate anion, $[Co(NCS)_4]^{2-}$, were introduced by Peppel *et al.*[44] in the form, $[C_nMim]_2[Co(NCS)_4]$ (n= 2, 4), and the physical properties thoroughly investigated.[45] Low viscosities were found (145 MPa s for $[C_2Mim]_2[Co(NCS)_4]$) despite the divalancy of the anion. The soft pseudo-halide anion, isothiocyanate, has weaker directed interactions with the hard hydrogen atoms of the imidazolium cations compared to that of the halogen groups thus contribute to the low-melting of these salts. A dicationic MIL, $[C_4Mim_2][FeCl_3Br]_2$ with a melting point of 52 °C has also been realised by Brown *et al.*[46] By ensuring a sufficient alkyl length linker between the two imidazolium rings and by incorporating a large asymmetric $[FeCl_3Br]^-$ anion, a low-melting product could be achieved. These investigations highlight the advantageous tuneable properties of ILs.

1.2.3 Lanthanide-containing ionic liquids

Ionic liquids are well-known to provide a unique coordination environment for a range of metal ions. Recent reviews by Binnemans *et al*.[47] and Prodius *et al.*[48] highlight the research surrounding lanthanide and actinide containing ionic liquids. Nockemann *et al.* were the first to incorporate highly-charged species of the type, $[Ln(NCS)_6]^{3-}$ Ln = Y, La, Pr, Nd, Sm, Eu, Gd, Tb, Ho, Er, Yb and La, into an ionic liquid forming a series of low-melting lanthanide-containing ILs (Figure 4).[49] The large coordination sphere of the lanthanide species can be attributed to their relatively large ionic radii when compared with first-row d-block elements.

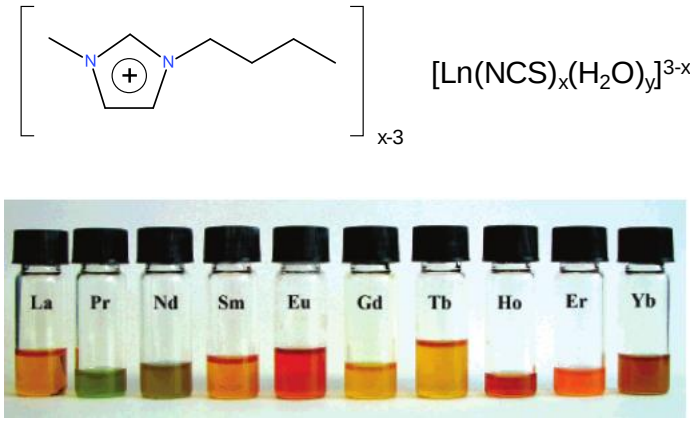

Figure 4. The first low-melting, lanthanide(III)-containing ionic liquids.[49]

The magnetic and luminescent properties of $[C_6Mim]_{5-X}[Dy(SCN)_{8-X}(H_2O)_X]$ where subsequently explored by Mallick *et al.*[50] displaying an effective magnetic moment (μ_{eff}) equal to 10.4 μ_B. A downfall of these lanthanide-containing ILs is, however, that they are completely hydrolysed in aqueous solutions.[47]

To eliminate the coordination of water molecules in lanthanide-containing ILs, Ji *et al.*[51] synthesised a series of MILs based on nitrate ligands, $[C_nMim]_3[Ln(NO_3)_6]$

(n = 1, 2, 4, 6, 8, 12, 14, 16, 18). In addition, the creation of hydrophobic MILs could also be achieved by incorporating the bulky tetraalkylphosphonium cation, $[P_{666\,14}^{+}]$. The physical and magnetic properties of the series $[P_{666\,14}][LnCl_6]$ were reported by Alvarez Vincente *et al*.[52] Further low-temperature magnetic measurements on $[P_{666\,14}][LnCl_6]$ ILs were subsequently carried out by Monson *et al.,*[53] reporting unusual behaviour at temperatures below 50 K, attributed to the trapping of intermediate structures, anisotropic bridged lanthanide clusters, during glass formation.

Lanthanide-containing ILs based on the bis(trifluoromethylsulfonyl)imide ion, $[NTf_2]^-$, have also been of interest for their spectroscopic properties. Depending on the environment, *i.e.* whether water is present, the $[NTf_2]^-$ ion can be non-coordinating or weakly coordinating as reported by Babai *et al.*[54] $[C_4C_1pyr]_4[PrI_6][Tf_2N]$, was obtained by reacting anhydrous praseodymium(III) iodide with 1-butyl-1-methylpyrrolidinium, $[C_4C_1pyr][Tf_2N]$. Additionally, $[C_4C_1pyr]_2[Pr(Tf_2N)_5]$ was synthesised from reaction of $Pr(Tf_2N)_3$ with $[C_4C_1pyr][Tf_2N]$. Crystal structures of both ILs were obtained and it was shown how the ILs are promising media to study the luminescent properties of rare-earth cations in the liquid state.[54]

Further lanthanide-containing ILs have been explored with interesting magnetic and photophysical properties which will be discussed when looking at the properties of MILs.

1.2.4 Magnetic nanoparticles in ionic liquids

Traditional magnetic fluids are those where metal nanoparticles are suspended in a carrier fluid and are generally separated into magnetorheological fluids (MRF) and ferrofluids. These fluids find application as lubricants, as semi-active shock absorbers in the automotive industry, as dampers for seismic damage control and in aerospace and mechanical engineering.[55] RTILs have been seen as ideal candidates for the stabilisation of metal nanoparticles producing fluids with a magnetic response. Oliveira *et al.*[56] report on stable dispersions of maghemite (γ-Fe_2O_3) and $CoFe_2O_4$ in $[C_4Mim][BF_4]$. However, the hydrophilic nature of the $[C_4Mim][BF_4]$ IL meant that these were unstable in water. Further advancing this work, surface-modified stable dispersions of γ-Fe_2O_3, $CoFe_2O_4$ and Fe_3O_4 were prepared in the hydrophobic IL, 1-butyl-3-methylimidazolium bis(trifluoromethanesulfonyl)imide, $[C_4Mim][NTf_2]$.[57] Guerrero *et al.*[58] looked at a series of magnetorheological fluids based on ILs. The dispersion of magnetic particles in $[C_4Mim][PF_6]$, yielded MRFs with low rates of sedimentation and diminished the need for additional stabilizing agents. Additionally, Rodríguez-Arco *et al.*[59] report on the stabilisation of magnetite using 1-ethyl-3-methylimidazolium ethylsulphate, $[C_2Mim][EtSO_4]$. Citric acid was further seen to stabilise the magnetic particles, albeit, only short-term stability was achieved.

A major advantage of using ionic liquids in nanoparticle synthesis is increased stability due to the (i) electrostatic and (ii) steric properties of ILs reducing the need for additional stabilisers (Figure 5). Chemical reduction or decomposition are methods by which M-NPs in ionic liquids are commonly synthesised. In the former,

M-NPs have been synthesised for a range of metals; Rh, Ir, Pt, Ag and Au using an array of reducing reagents *e.g.* H_2, $NaBH_4$ or citrate, imidazolium cation of IL. Zero-valent metal atoms, metal carbonyls ($M_x(CO)_y$) can also be decomposed to metal nanoparticles in ILs by conventional heating, UV photolysis or microwave irradiation.[26]

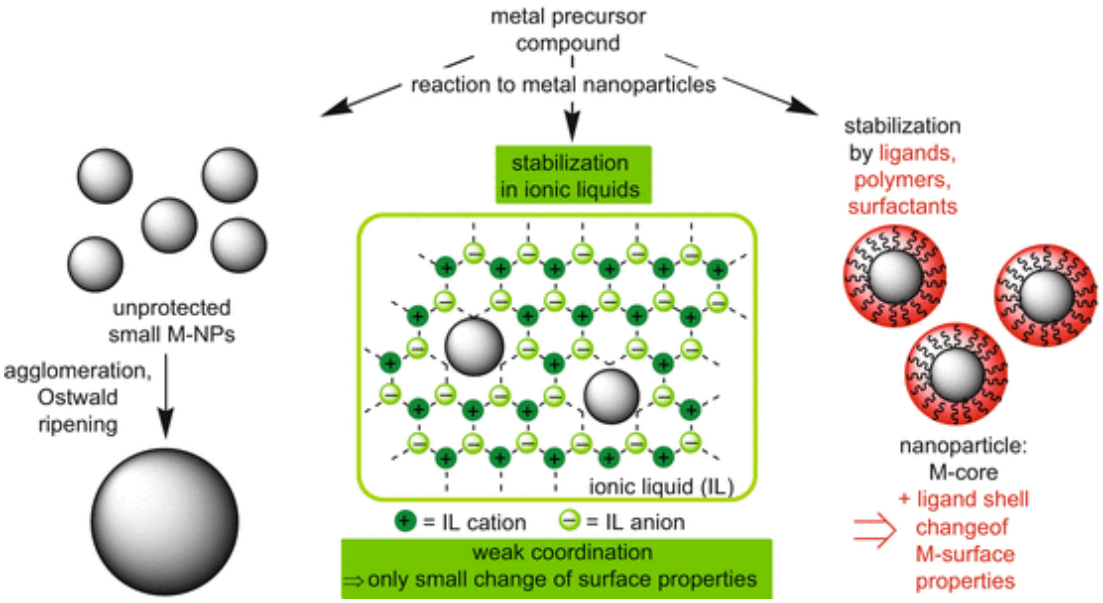

Figure 5. Ionic liquids for stabilising nanoparticles.[26]

1.3 Properties of magnetic ionic liquids

Traditional magnetorheological and ferrofluids, and now magnetic ionic liquids alike, have distinctive stimuli-responsive properties. Stimuli may be in the form of temperature, pressure, light, solvents or magnetic field application. This results in a class of materials which have tuneable physical and chemical properties.

In addition, photophysical/optical and catalytic properties are characteristic of magnetic ionic liquids. Incorporating metals, e.g., transition metals, lanthanides or actinides into the structures of ionic liquids impart an array of characteristics specific to that of the metal. The magnetic and luminescence properties and the stimuli-responsive nature of MILs will be discussed in the sub-sections that follow.

1.3.1 Magnetic properties

Magnetic ionic liquids are paramagnetic in nature. Under application of an external magnetic field, the spins become aligned parallel to the applied field resulting in changes in the physical properties of the system. In the absence of the applied field, the thermal motion causes the spins to become randomly orientated as demonstrated in Figure 6.[60]

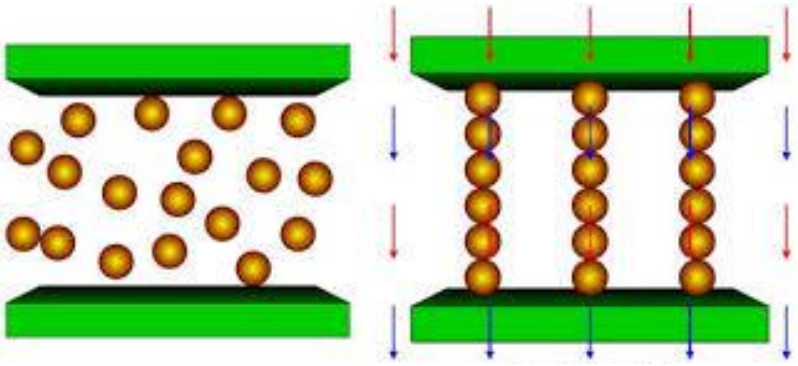

Figure 6. Magnetorheological fluid with (Right) and without (Left) applied magnetic field.[60]

As a consequence of investigations into the magnetic properties of $[C_4Mim][FeCl_4]$ and $[C_2Mim][FeCl_4]$, interest in the field of MILs soared. Long-range magnetic ordering was observed for the first time in $[C_2Mim][FeCl_4]$, displaying antiferromagnetic ordering below the Néel temperature ($T_N \approx 3.8$ K).[61,62]

$[C_4Mim][FeCl_4]$ displayed paramagnetic temperature dependence on the magnetic susceptibility and has an effective magnetic moment (μ_{eff}) equal to 5.8 Bohr magnetons (μ_B), in accordance with a high-spin *S* = 5/2 state for Fe(III). Under applied pressure, however, the low-temperature long-range antiferromagnetic ordering observed in $[C_2Mim][FeCl_4]$ was seen to change to ferromagnetic ordering. Looking for ways to further increase the effective magnetic moments in MILs, Brown *et al.*[63] looked at dicationic imidazolium-based MILs which had two paramagnetic $[FeCl_3Br]^-$ anions and led to an effective magnetic moment of 8.75 μ_B. Furthermore, Nacham *et al*.[64] looked at tricationic imidazolium MILs with three $[FeCl_3Br]^-$ anions which increased the magnetic moment to 11.56 μ_B.

In the quest to find novel paramagnetic materials Yoshida *et al*. reported a purely organic paramagnetic ionic liquid based on the radical (TEMPO-OSO_3) in combination with $[C_nMim]^+$ (n = 2, 4 , 6, 8).[65] Magnetic susceptibility measurements provided evidence of paramagnetic behaviour at room temperature with μ_{eff} in the range of 1.61 – 1.73 μ_B, resembling that of the expected paramagnetic S = ½ state. In the low-temperature region, antiferromagnetic behaviour is evident. Further exploring the tuneable properties of the anion and cation structure has led to the synthesis of a bimagnetic IL named, [Imin-TEMPO][$FeCl_4$], with paramagnetism incorporated into the cation structure by tethering a TEMPO radical to the imidazolium structure and from the $[FeCl_4]^-$ anion (Figure 7). In doing this, a magnetic moment of 6.66 μ_B could be achieved and was attributed to a cooperative contribution from both the S = 5/2 high-spin state of iron(III) (μ_{eff} = 5.92 μ_B), and the S = ½ radical spin of TEMPO, (μ_{eff} = 1.73 μ_B).[66]

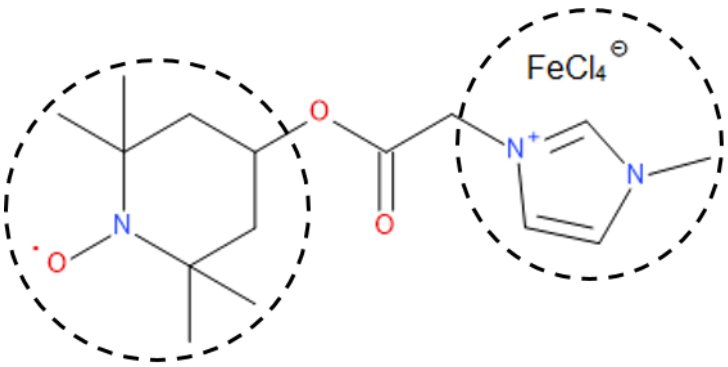

Figure 7. Dual functionalised Fe/TEMPO based MIL.[66]

The magnetic susceptibilities can be greatly increased by the incorporation of lanthanide ions which possess considerably higher magnetic moments, typically 8 – 11 μ_B.[48] The highest recorded effective magnetic moment has been recorded for the quindecim charged pentanuclear rare earth based ionic liquid, $[RE_5(C_2H_5\text{-}C_3H_3N_2\text{-}CH_2COO)_{16}(H_2O)_8][(Tf_2N)_{15}]$ (RE = Ho ; $C_3H_3N_2$ = imidazolium moiety) equal to 23.3 μ_B.[67]

1.3.2 Stimuli-responsive nature of MILs

1.3.2.1 Thermochromic ionic liquids

Thermochromism is the ability of a substance to change colour upon heating. A number of thermochromic MILs have been reported.[68–74] Osborne *et al.*[69] investigated the thermochromic behaviour of a cobalt-based ionic liquid, 1-butyl-3-methylimidazolium tetrathiocyanatocobaltate(II) complex in excess of 1-butyl-3-methylimidazolium thiocyanate ionic liquid, $[C_4Mim][SCN]$. Ultraviolet−visible spectroscopy and superconducting quantum interference device measurements were used to demonstrate the reversible switching of cobalt coordination from

tetrahedral, $[Co(NCS)_4]^{2-}$, to octahedral, $[Co(NCS)_6]^{4-}$, with neat imidazolium-based cation, resulting in a change in the magnetic susceptibility and colour from blue to pink upon cooling (Figure 8). The reason for this coordination change can be attributed to an entropic effect.

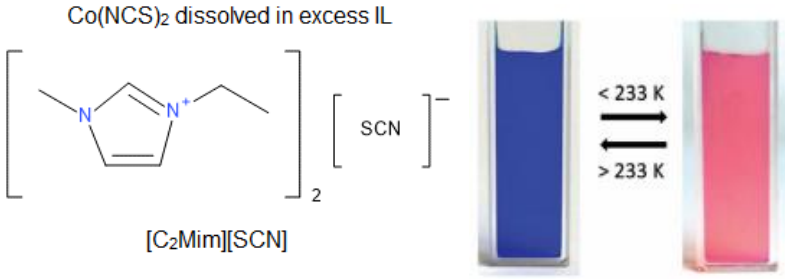

Figure 8. Thermochromic nature of Co(II) in excess ionic liquid.[69]

Kohno *et al.*[68] prepared the MIL, $[P_{4444}]_2[Co(sal)_2]$ (sal = bis(salicylate)), whereby additional coordination of two water molecules was observed upon cooling, forming $[P_{4444}]_2[Co(sal)_2(H_2O)_2]$ and resulting in a colour change from blue to pink. This behaviour was reversible whereby upon heating the metal-bound water molecules are released, and the $[P_{4444}]_2[Co(sal)_2]$ is reformed.

Temperature-dependent yellow-to-red colour changes were observed in the uranyl-containing ionic liquid, $[C_4Mim]_3[UO_2(NCS)_5]$, which could be speculated to be a result of an equilibrium shift at high temperatures due to entropy as seen in (scheme 1).

$$[UO_2(NCS)_4(NCS)]^- \leftrightarrows [UO_2(NCS)_4]^{3-} + [SCN]^- \qquad (1)$$

Okuhata *et al.*[72] prepared a cationic spin-crossover (SCO) complex, [Fe(acacen)(1-butylimidazole)$_2$][Tf$_2$N] based on the Schiff base ligand, acacen (acacen = *N,N'*-bis(acetylacetone)-ethylenediamine) (Figure 9). SCO in the liquid state was observed resulting in a rapid decrease in the magnetic susceptibility reported when cooled from room temperature to 203 K. In addition, a reversible colour change from blue-green (248 K) to violet-blue (313 K) was seen. A downfall of this system is, however, long-term stability issues. This system nevertheless paved the way for further investigation into SCO complexes in the liquid state.

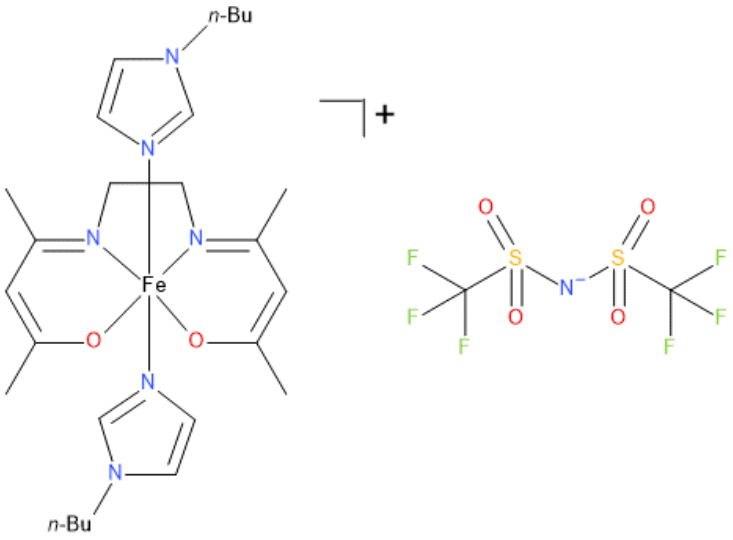

Figure 9. Cationic iron(III) Schiff-base complex, [Fe(acaen)(1-butylimidazole)$_2$][Tf$_2$N].[72]

Fitzpatrick *et al.*[73] developed an Fe^{III} SCO RTIL based on the Schiff-base ligand H$_2$R-Sal$_2$222 structure presented below in Figure 10, in this case, R = 1-butyl-3-methylimidazole. This SCO RTIL was air and moisture stable.

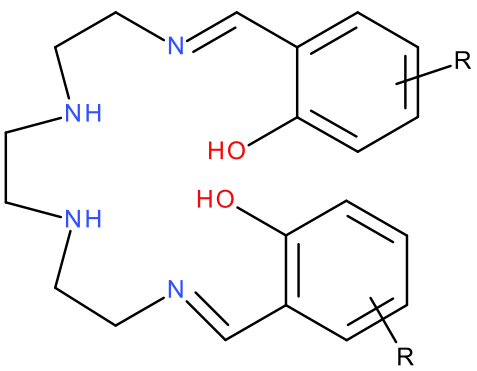

Figure 10. Schiff-base ligand $H_2R\text{-}Sal_2222$.[73]

Other thermochromic MILs exhibiting thermochromic behaviour are a cationic nickel(II) complex, $[Ni(acac)(R\text{-diamine})]^+$ (acac = acetylacetone and R = ether side-chain), which showed intramolecular coordination equilibrium, changing from diamagnetic (red) to paramagnetic (blue) at low temperatures.[71] Those incorporating lanthanide metals have also been reported.[75]

1.3.2.2 Other stimulants

MILs which respond to applied potential, solvents, vapours or light have also been investigated. Materials which change colour upon application of applied potential *i.e.* electrochromic materials are of high importance in the fabrication of smart materials, *e.g.* information displays, automobiles and smart windows.[76] Branco *et al*. published a series of ILs capable of reversible oxidation/reduction processes which result in a change in the magnetic properties (diamagnetic to paramagnetic) and colour of the systems. These MILs contained cobalt(III), chromium(III) and iron(III) ethylenediaminetetraacetic (EDTA) complexes as anions and a range of cations; 1-ethyl-3-metyhylimidazolium, $[C_2Mim]^+$, 1-butyl-3-methylimidazolium, $[C_4Mim]^+$, 1-octyl-3-methylimidazolium $[C_8Mim]^+$, tri-octylmethylammonium

[ALIQUAT] and trihexyltetra(decyl)phosphonium, $[P_{666\ 14}]^+$. Of particular interest was the results of cyclic voltammetry showing [Co(EDTA)] ILs reversibly switching from diamagnetic to paramagnetic upon oxidation/reduction.[76]

MILs which respond to solvents or vapours have been investigated by Funasako *et al*.[77] Of the series developed, [Ni(acac)(C_4Me_3en)][Tf_2N], ($BuMe_3$en = *N*-butyl-*N,N',N'*-trimethylethylenediamine) showed significant colour changes upon absorption of organic vapours with high donor numbers, *e.g.* DFM, DMSO and pyridine. The colour change from dark red to green observed upon absorption was indicative of a change in the coordination number and ultimately a change from a diamagnetic to paramagnetic complex.

Lanthanides possess unique optical properties, so their incorporation into ILs imparts such properties making them potential candidates in the engineering of new optical devices. Tang *et al*.[78] have prepared a series of low-melting europium-containing ionic liquids, [C_3Mim][Eu(Tf_2N)$_4$], [C_4Mim][Eu(Tf_2N)$_4$] and [C_4mpyr][Eu(Tf_2N)$_4$]. High colour purity, small linewidth, and long life-times at high Eu(III) concentration were reported for these ILs. Lunstroot *et al*.[79] further incorporated europium(III) into an ionogel observing vivid red luminescence upon irradiation (Figure 11). A particular advantage of the ionogel synthesis is the ability to mould and therefore control the shape and size of the produced material.

Figure 11. Luminescent properties of europium(III)-doped ionogel.[79]

Lunstroot *et al.*[80] prepared lanthanide tetrakis β-diketonate complexes, $[C_6Mim][Ln(tta)_4]$ (tta is 2-thenoyltrifluoroacetonate), which were further confined in the pores of a nano-porous silica network. The main finding here was that the lanthanide(III) coordination sphere remained unaffected by the confinement of the ionic liquid within the silica matrix. In addition, the ionic liquid, 1-hexyl-3-methylimidazolium bis(trifluoronethanesulfonyl)imide, $[C_6Mim][Tf_2N]$, is seen to have a beneficial effect on the photostability of 1-hexyl-3-methylimidazolium tetrakis(2-thenoyltrifluoroacetonato)europate(III) complex, attributing the hydrogen bonding between the cation and ligands to this enhanced stability.[81]

Along with the magnetic properties, the luminescent properties of $[C_6Mim]_3[Dy(SCN)_6(H_2O)_2]$ were investigated by Mallick *et al*.[50] Long luminescence decay and high colour purity was reported for this MIL.

Pitula *et al.*[40] explored the luminescent properties of transition metal-based ionic liquids, $[C_3Mim]_2[MnCl_4]$, $[C_3Mim]_2[MnBr_4]$ and $[C_3Mim][Mn(Tf_2N)_3]$. It was observed that when tetrahedrally coordinated, Mn^{2+} displayed green luminescence emission whilst red luminescent emission was observed in the octahedral state, $[C_3Mim][Mn(Tf_2N)_3]$. Getsis *et al*. have explored the luminescent properties of $[C_{12}Mim]_3[DyBr_6]$[82] showing bright white or orange-yellow emission upon irradiation with UV light and $[C_{12}Mim]_3[EuBr_6]Br$[83] displaying strong red emission. Liquid crystalline behaviour was also observed in these samples over the temperature range studied (115 °C down to -20 °C) for $[C_{12}Mim]_3[DyBr_6]$ displaying a lamellar structure and $[C_{12}Mim]_3[EuBr_6]Br$ adopts a smectic liquid crystal phase in the temperature range -3 – 98 °C.[82,83]

Water can, however, have a dramatic effect on the luminescent properties of MILs. Arenz *et al.*[84] investigated the luminescent behaviour of NdI_3 and ErI_3 dissolved in 1-dodecyl-3-methylimidazolium bis(trifluoromethylsulfonyl)imide, $[C_{12}Mim][Tf_2N]$, observing intense near-infrared luminescence under anhydrous conditions. In the presence of moisture, the luminescent intensity was, however, quenched and fell back to zero. Making use of this property, lanthanide-containing ILs have demonstrated the ability to function as sensors or fluorescent probes. The quenching of fluorescence by external species has been validated with Fe(III) ions in the ionic liquids; $[C_4Mim][Ln(NO_3)_4]$ (Ln = Dy and Sm).[85]

The wide range of interest in the stimuli-responsive nature of MILs reflects their potential applications. The ability to have stimuli-responsive materials in the liquid state and in particular, as ionic liquid-based materials, is seen as a huge advantage due to their advantageous physical properties.

1.4 Applications of magnetic ionic liquids

As the field of magnetic ionic liquids has progressed, many groups have looked at their prospective applications.[86–91] Such has been the influx of interest; there are now multiple review articles to highlight these.[28,30,92,93] The ease of design and ability to incorporate specific features into the structure of ILs has enabled progression of their application in areas such as catalysis, separations, extraction and in biomedical applications. This next section explores how the intrinsic properties of MILs have been used in specific applications.

1.4.1 Catalysis

Lewis acidic MILs, for example, those based on the chloroferrate anion, [C_4Mim][$FeCl_4$], have been widely investigated and identified as novel sustainable and environmentally benign catalysts for a myriad of reactions.[94] Friedel-Crafts acylation and alkylation, cross-coupling, oxidations, cycloadditions, polymerization and depolymerisation reactions have all benefitted from the use of MILs with examples given below.

Some of the earliest cases of such reactions is in the Friedel-Crafts acylation. Hölderich and co-workers[95] explored the Friedel-Crafts acylation of aromatics; mesitylene, anisole, *m*-xylene, toluene and benzene using acetyl chloride or acetic anhydride as acylation reagent. The chloroferrate IL proved superior, in terms of conversion and selectivity, over the chloroaluminate and chlorostannate ILs studied. They also looked at the immobilisation of such MILs on silica or charcoal supports or gas phase reactions which proved unfavourable. Similarly, Li *et al*. explored the Friedel-Crafts acylation of benzene with benzoyl chloride or phenol acetyl chloride showing again highest conversions in chloroferrate ILs.[96] An additional benefit is the reusability of such catalysts.

The alkylation of α-methylnaphthalene with long-chain mixed alkenes is a key intermediate in the synthesis of long-chain alkylmethylnaphthalene sulfonate (AMNS) surfactants which have potential for enhanced oil recovery. The preparation of such is carried out by Friedel-Crafts alkylation. Zhao *et al.*[97] have investigated numerous Lewis-acid ILs catalysts for these reactions. Different ionic liquids; 1-ethyl-3-methylimidazolium bromide ([C_2Mim][Br]), butylpyridinium bromide (C_4PyBr) and

methylenedipyridinium dichloride (MeDiPyCl), in combination with chlorometalate anions; chloroaluminate, chloroferrate and chlorocuprate were synthesised. In this case, the best catalytic performance was achieved using the butylpyridinium bromochloroaluminate ($C_4PyBr–AlCl_3$) ionic liquid.

Bica *et al.*[89] were the first group to report on the use of $[C_4Mim][FeCl_4]$ for Grignard cross coupling reactions. The coupling of dodecyl bromide and 4-fluorophenylmagnesium was examined, see Figure 12. Fast reaction times (10 mins), high yields, a reduction in by-products produced and catalyst recyclability favour this reaction.

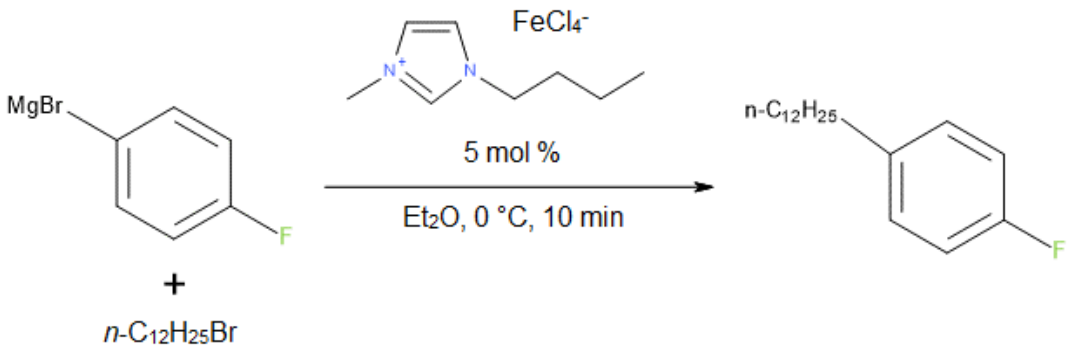

Figure 12. $[C_4Mim][FeCl_4]$ catalysed aryl Grignard cross-coupling of alkyl halides.[89]

Along with the outstanding magnetic properties of the quindecim charged MIL, $[RE_5(C_2H_5\text{-}C_3H_3N_2\text{-}CH_2COO)_{16}(H_2O)_8][(Tf_2N)_{15}]$, discussed above, it's catalytic properties have also been investigated for the synthesis of 2-pyrrolo-3'-yloxindole with extremely low catalyst loading (<0.035 mol %). Multicomponent reactions catalysed by MILs has also been presented by Panya *et al.*[98] for the one-pot synthesis of quinazolines (Figure 13).

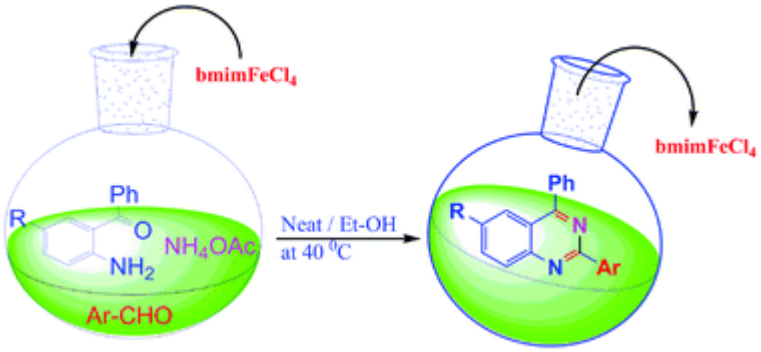

Figure 13. [C_4Mim][$FeCl_4$]-catalysed multi-component synthesis of quinazolines.[98]

In contrast to traditional methods, which can often be hindered by the use of volatile solvents, as well as toxic and expensive metal catalysts and high temperatures, [C_4Mim][$FeCl_4$] offers an alternative eco-friendly route to the synthesis of quinazolines.

In organic synthetic chemistry, MILs have been seen as efficient catalysts for the cycloadditions,[99] esterification[100] and depolymerization of PET (poly(ethylene terephthalate).[86,101] In the depolymerisation of PET highest conversion and selectivity to bis-(hydroxyethyl) terephthalate (BHET) was achieved with [C_4Mim]$_2$[$CoCl_4$] as reported by Wang *et al.*[101] Milder reaction conditions and the ability to reuse the catalyst, up to six times, is a major advantage over traditional metal acetates which require high temperatures and pressures.

Reports of the first liquid fixed-bed reactor using MILs was by Misuk *et al.*[100] By bubbling the reactants cyclohexanol and acetic anhydride (Ac_2O) over the magnetically fixed catalyst, [C_4Mim][Fe_2Cl_7], a yield of 78.5 % could be achieved in 1.3 seconds (Figure 14).

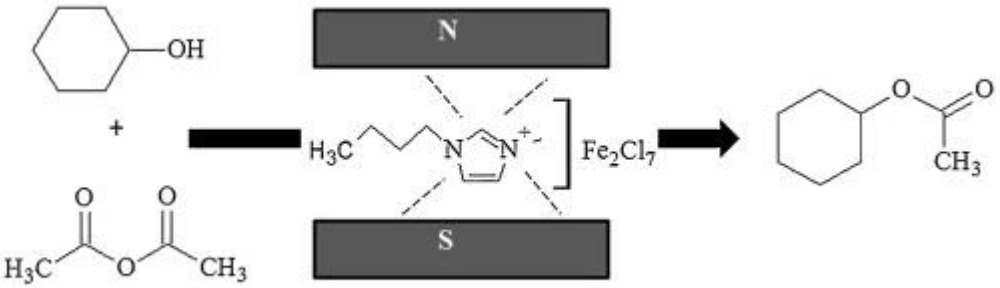

Figure 14. Liquid fixed-bed catalyst for the esterification of Ac_2O with cyclohexanol.[100]

The removal of sulfur compounds from fuels is a particular challenge for the petroleum industry owing to rigorous regulations on sulfur content in transport fuels.[102] Oxidative desulfurization (ODS) methods have been looked at as an alternative to traditional catalytic hydrodesulfurization. Zhu *et al.*[102] and Jiang *et al*.[103] have explored the use of MILs as dual catalysts and extractants in a process referred to as ECODS (extractive and catalytic oxidation desulfurization system). A temperature-responsive MIL, *N*-butylpyridinium tetrachloroferrate ($[C_4Py][FeCl_4]$), reported by Zhu *et al.*[102], was seen as an effective catalyst for the oxidative desulfurization of model oils with benzothiophene (BT), dibenzothiophene (DBT) and 4,6-dimethyldibenzothiophene (4,6-DMDBT) using H_2O_2 as oxidant. The reversible melting and solidifying nature of $[C_4Py][FeCl_4]$ aids the separation of the MIL post reaction (Figure 15). In addition, Jiang *et al.*[103] showed that Brönsted and Lewis acidity was an important parameter in the effective oxidative desulfurization of

benzothiophene. The molar fraction of $FeCl_3$ had to be above 1 to achieve this. [C_3H_6-COOHmim]Cl/2$FeCl_3$ was seen most efficient catalyst which could be easily separated due to its magnetic responsiveness.

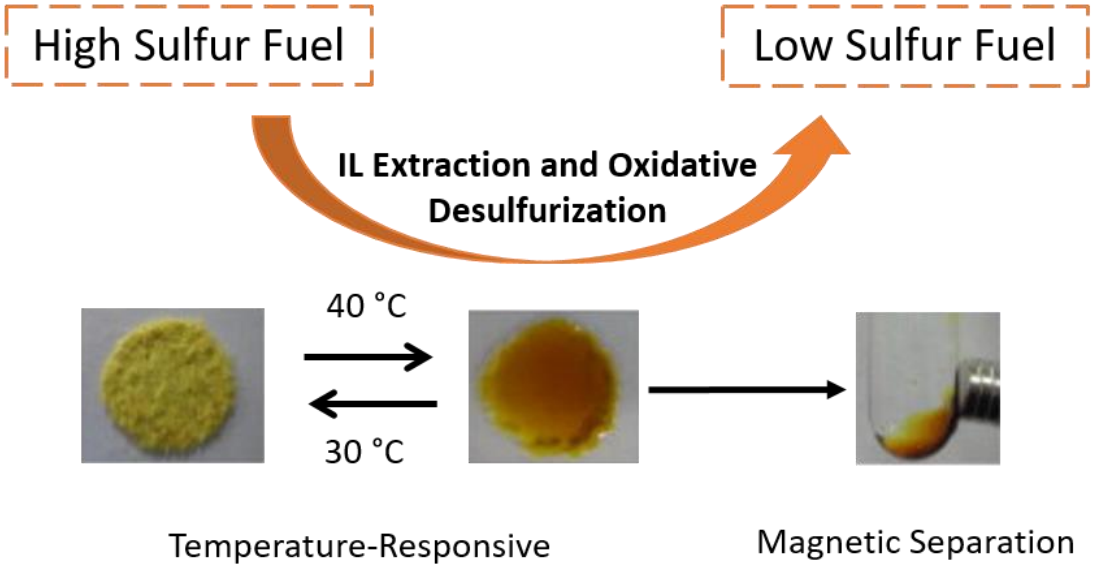

Figure 15. Temperature-responsive nature of [C_4Py][$FeCl_4$] as an effective catalyst for the oxidative desulfurization of model fuels whilst displaying effective separation capability.[102]

1.4.2 Separation and Extraction

The inherent magnetic properties of MILs have led to wide-spread attention in the fields of separation and extraction. Lee *et al.*[104] looked at the separation of the MIL, [C_4Mim][$FeCl_4$], from its mixture with water. It must be noted that at concentrations greater than 20 % (v/v) MIL in aqueous solution, the MIL was completely miscible, and separation could not be achieved by applying a magnetic field, highlighting the requirement for more hydrophobic systems.

Okuno *et al.*[105] have explored the movement of a non-magnetic material (nitrogen gas bubbles) through [C_4Mim][$FeCl_4$]. In the presence of an applied

magnetic field the nitrogen was repelled from the magnet. The path of the bubbles was dependent on both the magnetic field gradient and the density of the bubbles and it has been suggested that this may be a method for the separation of non-magnetic materials in a MIL, based on density.[106]

Santos *et al*.[107] looked at the IL series based on the trihexyl(tetradecyl)phosphonium cation and various magnetic anions; $[P_{666\ 14}]_2[CoCl_4]$, $[P_{666\ 14}][FeCl_4]$, $[P_{666\ 14}]_2[MnCl_4]$ and $[P_{666\ 14}]_3[GdCl_6]$ and investigated the solubility of CO_2 for CO_2 capture. The solubility of CO_2 in this series was, however, low in comparison to what has been achieved in other ILs systems.

In biological processes, MILs have been seen as rapid and efficient for the extraction and separation of DNA. Clark *et al.*[90,91,108] explored various MILs for such processes, monocationic (benzyl-trioctylammonium bromotrichloroferrate, $[(C_8)_3BnN][FeCl_3Br]$, trihexyl(tetradecyl)phosphonium tetrachloroferrate $[P_{666\ 14}][FeCl_4]$), and dicationic (1,12-di(3-hexyldecylbenzimidazolium)dodecane bis[(trifluoromethyl)sulfonyl]imide bromotrichlorferrate (III), $([(C_{16}BnIm)_2C_{12}][NTf_2,FeCl_3Br])$ (Figure 16). For smaller single-stranded and double-stranded DNA molecules, high extraction efficiencies were achieved when using monocationic MILs whilst for larger DNA molecules the dicationic MIL was better suited. In this paper, the use of the recovered DNA polymerase chain reaction amplification was touched upon. This was further developed in a follow-up paper. Buffers capable of relieving inhibition caused by $FeCl_3$ or hydrophobic cations in polymerase chain reaction amplification were explored.[90]

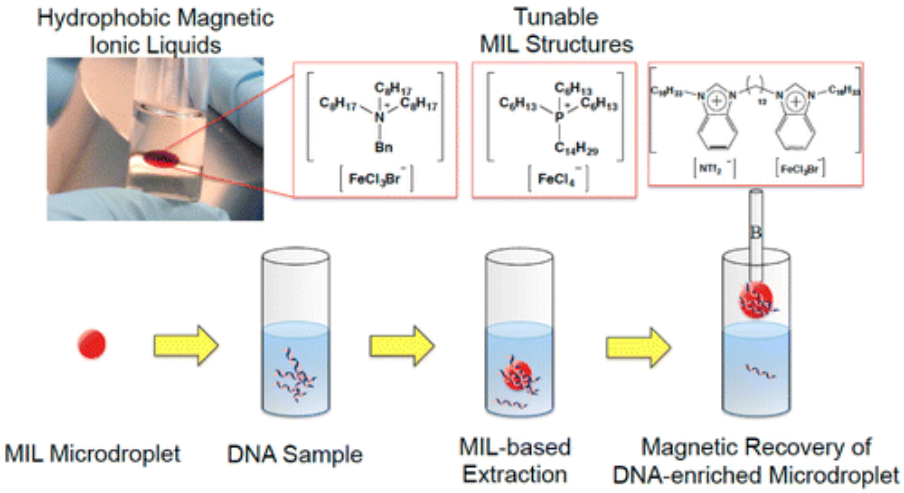

Figure 16. Extraction and separation of DNA using magnetic ionic liquids.[90]

MILs based on the tetrachloroferrate anion and various imidazole, pyridine, and pyrollidine-based cations have been used in investigating the separation and extraction of asphaltene fractions from coal direct liquefaction residues (CDLR).[109] Out of the three, the pyridine-based MIL proved most effective at extracting asphaltene fractions which are important for producing high-value-added carbon materials. Deng and co-workers[110] showed the effective extraction of phenolic compounds which are known pollutants with high toxicity, from acidic aqueous solutions using a hydrophobic MIL, $[P_{666\ 14}][FeCl_4]$. In terms of separation techniques, liquid-liquid extraction is seen as a highly effective technique. Shirvani *et al.*[111] proposed an environmentally friendly method for the extraction of uranium from wastewater using an applied magnetic field. Extraction in the region of 86 % was achieved. The process was based on the use of $[C_4Mim][FeCl_4]$ as an extracting solvent in a dispersive liquid-liquid extraction process (dispersive solvent =

acetonitrile). After extraction the MIL could be removed from the water stream by magnetic filtration.

MILs, and in particular, MILs with tetrachloroferrate anions $[FeCl_4]^-$, have been widely investigated for separation and extraction proposes. Hydrophobicity is a key property when designing a MIL for extraction from aqueous solutions. The hydrophobic character can generally be tuned by selection of appropriate bulky cations. However, the anion is also important. The tetracholoroferrate anion is prone to hydrolysis in water which will hinder its separation and impede the magnetic properties. Pierson *et al.,*[112] and Mehdi *et al*.[113] explored the synthesis of more hydrophobic MILs based on transition metals, Co(II), Mn(II), Ni(II), and lanthanide, Gd(III), Dy(III) and Nd(III), hexafluoroacetylacetonate chelated anions paired with trihexyl(tetradecyl)phosphonium ($[P_{666\,14}]^+$) cation. Extremely hydrophobic, low viscous liquids were prepared and in addition, the incorporation of lanthanides meant that high magnetic moments could also be obtained.

1.5 Conclusion

The incorporation of transition of f-block elements into ionic liquids endows an array of additional properties to the widely explored ILs. Much work is still needed to fully explore the potential magnetic and stimuli-responsive nature of this class of liquids. In applications there is no doubt MILs based on the $[FeCl_4]^-$ anion have been the most extensively studied, however, further functionalising the anion and cation properties will pave the way for a wide range of applications. The efficient recycling and reuse of catalysts is key to developing and prolonging cost-efficient reactions. In this sense, MILs offer the potential properties to obtain this.

1.6 Experimental techniques

To probe the physical and chemical properties of the ionic liquids synthesised in this thesis, various techniques such as Fourier Transform Infrared (FTIR), UV/Vis, elemental analysis, thermogravimetric analysis, and differential scanning calorimetry, commonly used in the characterisation of ILs, were employed. The aim of this section is not to go into details of the more common techniques but to give an overview of two specific techniques, broadband dielectric spectroscopy (BDS) and superconducting quantum interference device (SQUID) magnetometry, which have been invaluable in obtaining and further probing the properties of the MILs throughout the course of this research. BDS was one of the primary techniques employed in Chapter 2, so this section begins with a description of the background to this technique and the equipment used. The second technique considered important to look at in detail is SQUID magnetometry which was used in Chapter 3 enabling investigation of the magnetic properties of the therein studied systems.

1.6.1 Electromagnetic spectrum

The electromagnetic spectrum (Figure 17) forms the basis of many of the characterisation techniques employed. Electromagnetic radiation can be described in terms of a stream of photons, each travelling in a wave-like pattern at the speed of light. The energy of light travels because of local fluctuating changes in electrical and magnetic fields. The different types of radiation are defined by the amount of energy found in the photons and can be expressed in terms of energy, wavelength or frequency as seen in Figure 17.

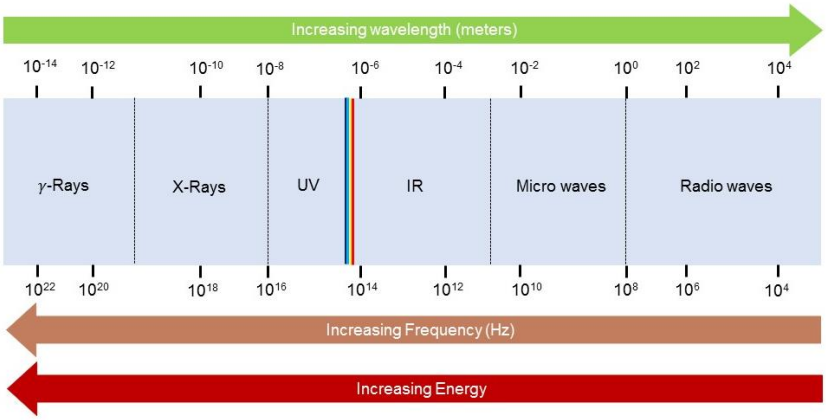

Figure 17. Spectrum of electromagnetic waves.

1.6.2 Relevance to broadband dielectric spectroscopy?

The interaction of electromagnetic radiation with molecules gives important insight into the transitions between rotational, vibrational, and translational molecular energy states.[114] The most frequently used techniques to analyse these transitions include UV/Vis and infrared spectroscopy, which provide information on the movement of molecules above a frequency of 10^{12} Hz. To gain a more complete picture of ion movements, frequencies below 10^{12} Hz are also important. At frequencies below 10^{12} Hz dielectric dispersion and absorbance phenomena due to dipole relaxation and electrical conduction, arising from the translational motions of ions or electrons are observed. This is the domain of broadband dielectric spectroscopy as eloquently described by Kremer *et al.*[114] BDS has enabled insight into the motions of ions in the region of 10^{-2} and 10^{12} Hz, ultimately giving insight into structural properties of complex systems as discussed further in Chapter 2.

1.6.3 Broadband Dielectric Spectroscopy (BDS)

Broadband dielectric spectroscopy allows for the complete characterisation of relaxation behaviours over wide frequency, temperature and pressure ranges. Especially sensitive to intermolecular interactions, it is able to monitor cooperative processes at a molecular level.[115] As the name suggests, broadband dielectric spectroscopy measures the dielectric properties of a material as a function of frequency. It looks at how a material responds to a weak alternating electric field, often expressed in terms of the permittivity, ε.

Important is the consideration of the time-dependent nature of different relaxations, *i.e.* a frequency range of 10^{-2} to 10^{6} Hz corresponds to a testing time of 100 to 10^{-6} seconds. Dipoles which cannot track the applied electric field experience some degree of energetic loss termed dielectric loss. Thus, permittivity responses are complex ε^* as they have a storage component (ε') and a loss component (ε'') as will be seen in the equations that follow.

1.6.4 Basic workings

Using a generator, a sinusoidal voltage U_1^* with frequency *(f)* is applied to the sample covering a frequency range of 10^{-6} – 10^7 Hz. A resistor is used to convert sample current, $I_S^*(f)$, into voltage, $U_S^*(f)$ using a second phase sensitive analyser (Figure 18).[116]

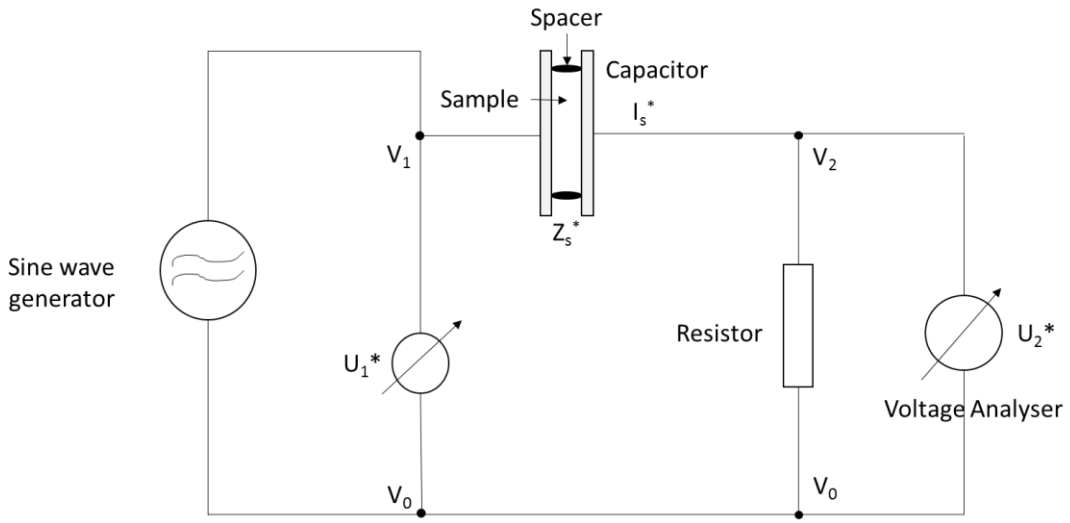

Figure 18. Circuit representation of the workings of an alpha analyser.[115]

Combining the results of sample current $I_S^*(f)$, and voltage $U_S^*(f)$ the sample impedance, $Z_S^*(f)$, can be calculated.

$$Z_S^* = \frac{U_S^*(f)}{I_S^*(f)}$$

Equation 1-1

Z_S^* = Sample impedance

$U_S^*(f)$ = Sample voltage

$I_S^*(f)$ = Sample current

From sample impedance, complex permittivity (ε^*), complex modulus (M^*) and complex conductivity (σ^*) formalisms can be readily obtained related by the following equation:

$$M^*(f) = \frac{1}{\varepsilon^*(f)} = \frac{i2\pi f \varepsilon_0}{\sigma^*}$$

Equation 1-2

M^* = Complex modulus

ε^* = Complex permittivity

σ^* = Complex conductivity

ε_0 = Dielectric permittivity of vacuum (ε_0 = 8.854 x 10^{-12} As V^{-1} m^{-1})

1.6.5 Measurement procedure/ Equipment used

All dielectric measurements were performed on a Novo-control Alpha Analyser (equipment set-up is shown in Figure 19) which has the ability to measure frequencies ranging from 10^{-6} to 10^{12} Hz. In practice, however, measurements were performed to frequencies of 10^{-2} Hz as measurements with frequencies below this require lengthy periods of time.

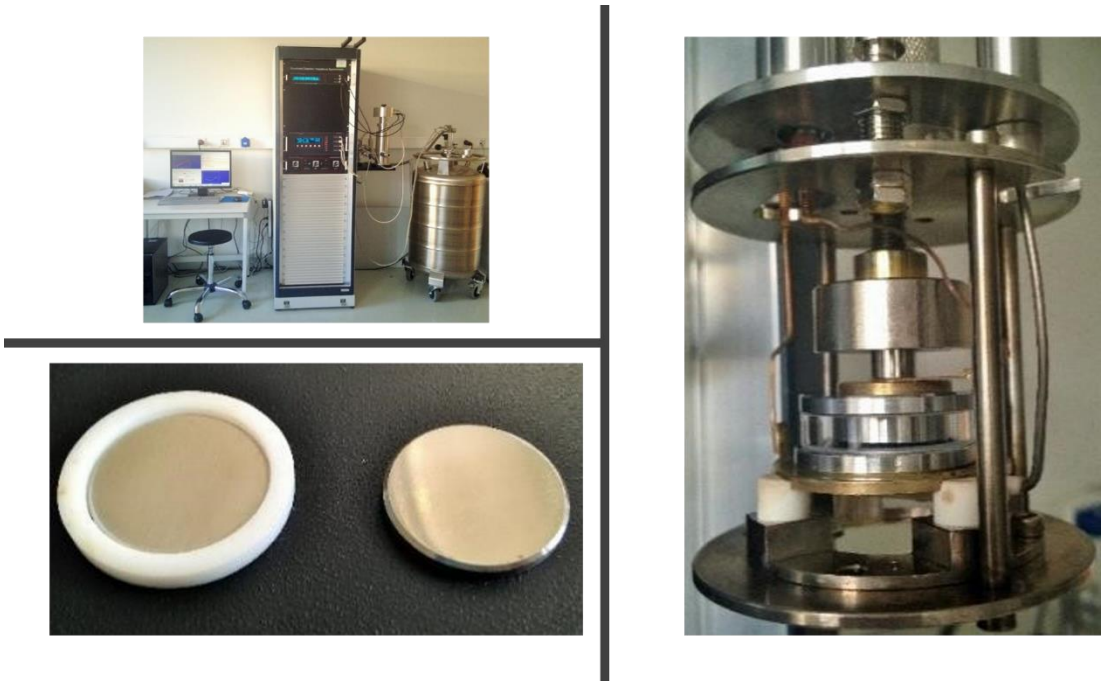

Figure 19. Novo-control Alpha Analyser equipped with liquid nitrogen cryostat (top left), Stainless steel electrodes with a spacer (bottom left) and sample stage (right).

1.6.6 Sample cell preparation ambient pressure

After a thorough cleaning of two stainless steel electrodes (diameter 20 mm) a drop of sample was placed in the centre of one electrode. A quartz glassy spacer was used to separate the plates forming a simple capacitor. The sample was measured over a wide temperature range from -100 °C to 120 °C in steps of either 5 or 2 °C, controlled by a Novocontrol Quattro system using a liquid nitrogen cryostat, as shown in Figure 19. Temperature stability is better than 0.1 K.

1.6.7 Broadband Dielectric Spectroscopy under high pressure

For high-pressure measurements, a Novo-control Alpha Analyser equipped with a fridge and pressure unit (chamber with oil) as seen in Figure 20 was used. Different isotherms or isobars could be measured, and results could be compared with those obtained from ambient pressure measurements.

1.6.8 High-pressure sample Preparation

In a similar method as described for ambient pressure measurements, the liquid sample was placed between two stainless steel electrodes separated this time by Teflon spacers, forming a capacitor. With wires connected the capacitor was wrapped in a roll of Teflon tape. The capsule was sealed tight and added to the chamber. The sample is compressed by compressing the oil inside the chamber.

Pressures ranging from 20 MPa to 600 MPa can be achieved.

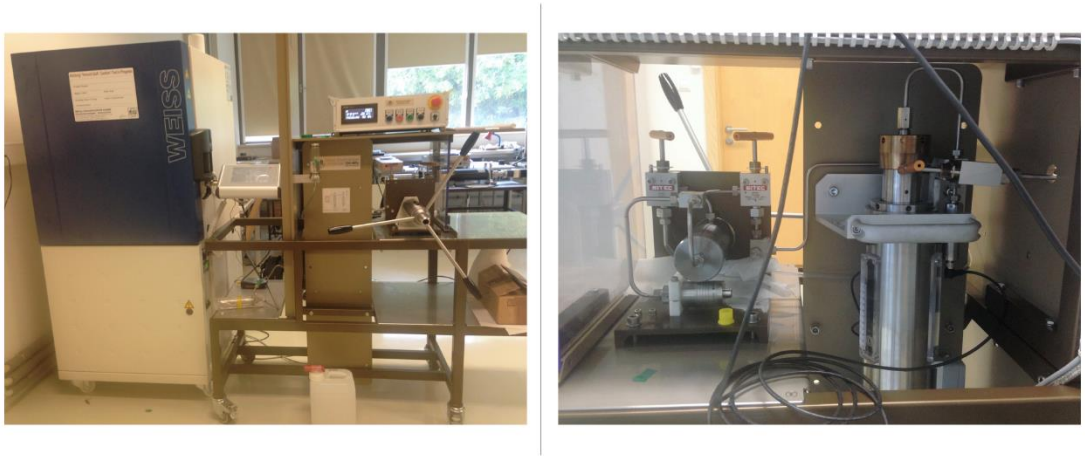

Figure 20. High pressure set-up composed of a Novo-control Alpha analyser equipped with fridge and pressure unit.

1.6.9 Superconducting quantum interference device (SQUID)

To measure the magnetic properties of a series of bis-lanthanoates (Chapter 3), we employed a DC- Superconducting quantum interference device (DC-SQUID) (Figure 21) which allows for the detection of very subtle magnetic fields enabling the magnetic susceptibility of the material to be analysed. The main workings of this technique described below.

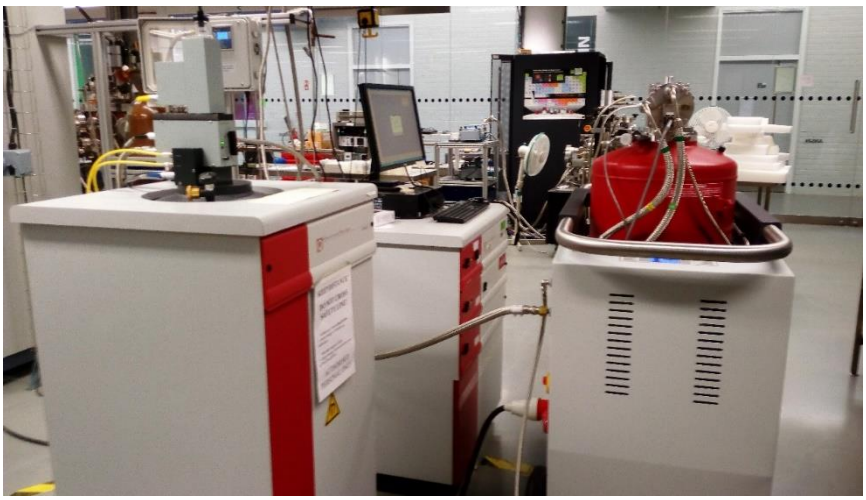

Figure 21. Superconducting quantum interference device.

1.6.10 Background of DC-SQUID

As its name suggests, SQUID makes use of superconducting materials in the generation of a magnetic field, however, as opposed to standard superconducting devices the SQUID is constructed to make use of the current flowing to carry out magnetic probing in the sample. The “quantum” part of the name comes from the fact the SQUID makes use a macroscopic quantum effect (called the Josephson Effect) for the analysis of the magnetic nature of the sample.

DC-SQUID is composed of two parallel Josephson junctions, that is, two superconductors separated by thin insulators from which Cooper pairs of electrons can tunnel through the junction (Figure 22).[117]

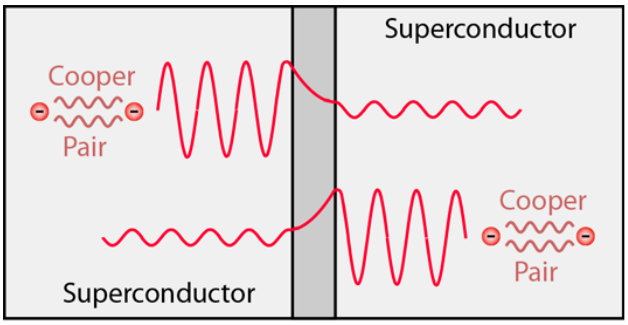

Figure 22. Josephson Junction.[116]

The cooper pair on each side of the junction can be represented by a wavefunction. Cooper pairs make up a supercurrent. The size of the supercurrent that flows through the gap depends on whether the superconductor at either edge of the gap has the same or a different phase.[118] If a magnetic flux is passed through the loop it changes the relation between the phase difference across the two junctions and hence the currents through them (Figure 23). SQUID uses this interaction between magnetic flux and the Josephson junction, with magnetic flux modulating the current through the junction.

Depending on the type of machine used, more than one of these junctions may be present within the system, with each type of machine employing a different method to detect small changes in a magnetic field. Either *via* the change in voltage of the external circuit across the junction or the resistance of the SQUID to the magnetic field of the sample, quantitative measurements can be made on the magnetic

character of the sample and the magnetic dipole moments can be detected, even for species as small as individual molecules.

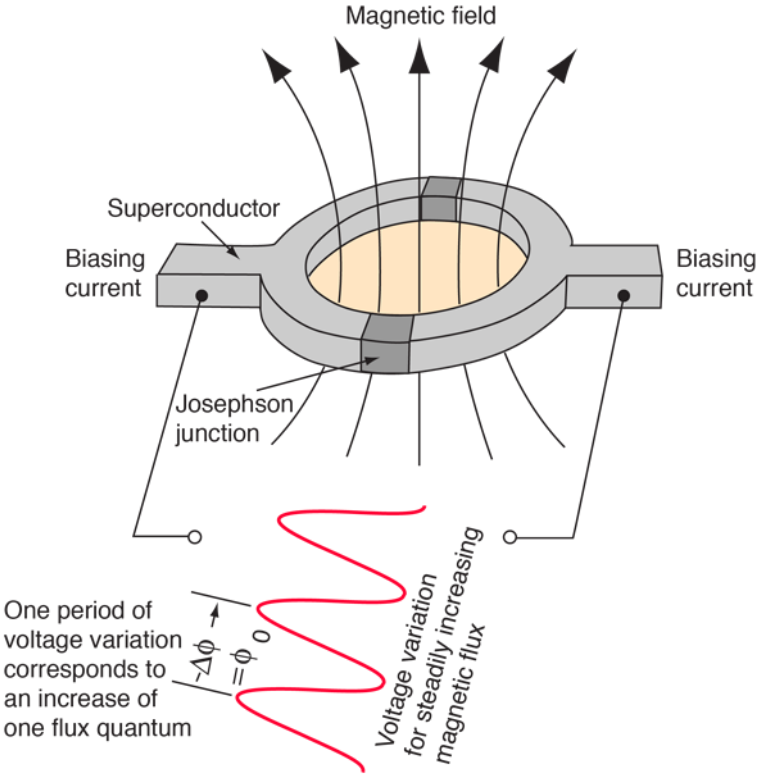

Figure 23. D.C. Superconducting quantum interference device.[117]

1.7 References

1. Walden, P. Molecular Weights and Electrical Conductivity of Several Fused Salts. *Bull. Russ. Acadamy Sci.* 405–422 (1914).

2. Chum, H. L., Koch, V. R., Miller, L. L. & Osteryoung, R. A. An Electrochemical Scrutiny of Organometallic Iron Complexes and Hexamethylbenzene in a Room Temperature Molten Salt Sir. *J. Am. Chem. Soc* **11,** 3264 - 3265 (1974).

3. Gale, R. J., Gilbert, B. & Osteryoung, R. A. Raman Spectra of Molten Aluminum Chloride: 1-Butylpyridinium Chloride Systems at Ambient Temperatures. *Inorg. Chem.* **17,** 2728 - 2729 (1978).

4. J S Wilkes, M. J. Z. Air and water stable 1-ethyl-3-methylimidazolium based ionic liquids. *J. Chem. Soc. Chem. Commun.* 965–967 (1992). doi:10.1039/c39920000965

5. Freemantle, M. *An Introduction to Ionic Liquids*. *The Royal Society of Chemistry* (RSC Pub, 2010). doi:10.1016/S1351-4180(10)70136-7

6. Seddon, K. R. Ionic Liquids for Clean Technology. *J. Chem. Technol. Biotechnol.* **68,** 351–356 (1997).

7. Welton, T. Room-Temperature Ionic Liquids. Solvents for Synthesis and Catalysis. *Chem. Rev.* **99,** 2071–2084 (1999).

8. Boon, J. A., Levisky, J. A., Pflug, J. L. & Wilkes, J. S. Friedel-Crafts Reactions in Ambient-Temperature Molten Salts. *J. Org. Chem* **51,** 480–483 (1986).

9. Visser, A. E., Holbrey, J. D. & Rogers, R. D. Hydrophobic ionic liquids incorporating N-alkylisoquinolinium cations and their utilization in liquid–liquid separations. *Chem. Commun.* 2484–2485 (2001). doi:10.1039/b109340c

10. Plechkova, N. V. & Seddon, K. R. Applications of ionic liquids in the chemical industry. *Chem. Soc. Rev.* **37,** 123–150 (2008).

11. Davis, J. H. & Forrester, K. J. *Thiazolium-ion based organic ionic liquids (OILs). Novel OILs which promote the benzoin condensation. Tetrahedron Letters* **40,** 1621 - 1622 (1999).

12. Wasserscheid, P. & Welton, T. *Ionic Liquids in Synthesis*. (Wiley-VCH, 2002). doi:10.1002/3527600701

13. H. Davis, Jr., J. Task-Specific Ionic Liquids. *Chem. Lett.* **33,** 1072–1077 (2004).

14. Brauer, D. J. *et al. Phosphines with 2-imidazolium and para-phenyl-2-imidazolium moieties-synthesis and application in two-phase catalysis*. *Journal of Organometallic Chemistry* **630,** 177 - 184 (2001).

15. Kottsieper, K. W., Stelzer, O. & Wasserscheid, P. *1-Vinylimidazole-a versatile building block for the synthesis of cationic phosphines useful in ionic liquid biphasic catalysis*. *Journal of Molecular Catalysis A: Chemical* **175,** 285 - 288 (2001).

16. Visser, A. E. *et al.* Task-specific ionic liquids for the extraction of metal ions from aqueous solutions. *Chem. Commun* 135–136 (2001). doi:10.1039/b008041l

17. Wu, D., Cai, P., Zhao, X., Kong, Y. & Pan, Y. Recent progress of task-specific ionic liquids in chiral resolution and extraction of biological samples and metal ions. *J. Sep. Sci.* **41,**

373 - 384 (2017).

18. Sun, X., Luo, H. & Dai, S. Ionic liquids-based extraction: A promising strategy for the advanced nuclear fuel cycle. *Chem. Rev.* **112,** 2100–2128 (2012).

19. Nockemann, P. *et al.* Task-specific ionic liquid for solubilizing metal oxides. *J. Phys. Chem. B* **110,** 20978–20992 (2006).

20. Bates, E. D., Mayton, R. D., Ntai, I. & Davis, J. H. CO $_2$ Capture by a Task-Specific Ionic Liquid. *J. Am. Chem. Soc.* **124,** 926–927 (2002).

21. Itoh, H., Naka, K. & Chujo, Y. Synthesis of Gold Nanoparticles Modified with Ionic Liquid Based on the Imidazolium Cation. *J. Am. Chem. Soc.* **126,** 3026–3027 (2004).

22. Sesto, R. E. Del *et al.* Structure and magnetic behavior of transition metal based ionic liquids. *Chem. Commun* **4,** 447–449 (2008).

23. Paduszyński, K. & Domańska, U. Viscosity of ionic liquids: An extensive database and a new group contribution model based on a feed-forward artificial neural network. *J. Chem. Inf. Model.* **54,** 1311–1324 (2014).

24. Swatloski, R. P., Spear, S. K., Holbrey, J. D. & Rogers, R. D. Dissolution of cellose with ionic liquids. *J. Am. Chem. Soc.* **124,** 4974–4975 (2002).

25. Estager, J., Holbrey, J. D. & Swadźba-Kwaśny, M. Halometallate ionic liquids – revisited. *Chem. Soc. Rev.* **43,** 847–886 (2014).

26. Janiak, C. Ionic Liquids for the Synthesis and Stabilization of Metal Nanoparticles. *Z. Naturforsch* **68,** 1059–1089 (2013).

27. Yoshida, Y. & Saito, G. Progress in Paramagnetic Ionic Liquids. *InTech* **3,** (2011).

28. Biao, C., Quan, L. & Baozhong, Z. Application of Magnetic Ionic Liquids. *Prog. Chem.* **24,** 225–234 (2012).

29. Clark, K. D., Nacham, O., Purslow, J. A., Pierson, S. A. & Anderson, J. L. Magnetic ionic liquids in analytical chemistry: A review. *Anal. Chim. Acta* **934,** 9–21 (2016).

30. Joseph, A. *et al.* Paramagnetic ionic liquids for advanced applications: A review. *J. Mol. Liq.* **218,** 319–331 (2016).

31. Santos, E., Albo, J. & Irabien, A. Magnetic ionic liquids: Synthesis, properties and applications. *RSC Adv.* **4,** 40008–40018 (2014).

32. Seiler, J., Wilkes, J. S., Levisky, J. A., Wilson, R. A. & Hussey, C. L. Dialkylimidazolium Chloroaluminate Melts: A New Class of Room-Temperature Ionic Liquids for Electrochemistry, Spectroscopy, and Synthesis. *Inorg. Chem* **21,** 1263–1264 (1982).

33. Wilkes, S., Levisky, J. A. & Seiler, F. J. Dialkylimidazolium Chloroaluminate Melts: A New Class of Room-Temperature Ionic Liquid for Electrochemistry, Spectroscopy, and Synthesis. *Inorg. Chem.* **21,** 1263 - 1264 (1982).

34. Estager, J., Holbrey, J. D. & Swad Ba-Kwa Ny, M. Chem Soc Rev Halometallate ionic liquids – revisited. *Chem. Soc. Rev. Chem. Soc. Rev* **43,** 737–962 (2014).

35. Sitze, M. S., Schreiter, E. R., Patterson, E. V & Griffith Freeman, R. Ionic Liquids Based on $FeCl_3$ and $FeCl_2$. Raman Scattering and ab Initio Calculations. *Inorg. Chem* **40,** 2298–2304 (2001).

36. Hayashi, S. & Hamaguchi, H. Discovery of a Magnetic Ionic Liquid [bmim]FeCl $_4$. *Chem. Lett.* **33,** 1590–1591 (2004).

37. Yoshida, Y. *et al.* Highly conducting ionic liquids based on l-ethyl-3-methylimidazolium cation. *Synth. Met.* **153,** 421–424 (2005).

38. Yoshida, Y. *et al.* Conducting and magnetic properties of 1-ethyl-3-methylimidazolium (EMI) salts containing paramagnetic irons: Liquids [EMI][MIIICl4] (M = Fe and Fe0.5Ga0.5) and solid $[EMI]_2[FeIICl_4]$. *Bull. Chem. Soc. Jpn.* **78,** 1921–1928 (2005).

39. Hitchcock, P. B., Seddon, K. R. & Welton, T. Hydrogen-bond acceptor abilities of tetrachlorometalate(II) complexes in ionic liquids. *J. Chem. Soc. Dalt. Trans.* 2639–2643 (1993). doi:10.1039/DT9930002639

40. Pitula, S. & Mudring, A. V. Synthesis, structure, and physico-optical properties of manganate(II)-based ionic liquids. *Chem. - A Eur. J.* **16,** 3355–3365 (2010).

41. Wussow, K., Haeuseler, H., Kuske, P., Schmidt, W. & Lutz, H. D. Lattice vibration spectra. *J. Solid State Chem.* **78,** 117–125 (1989).

42. Hayashi, S. & Hamaguchi, H.-O. Discovery of a Magnetic Ionic Liquid [bmim]$FeCl_4$. *Chem. Lett.* **33,** 1590–1591 (2004).

43. Albo, J. *et al.* Separation performance of CO_2 through Supported Magnetic Ionic Liquid Membranes (SMILMs). *Sep. Purif. Technol.* **97,** 26–33 (2012).

44. Peppel, T. *et al.* Low-Viscosity Paramagnetic Ionic Liquids with Doubly Charged [Co(NCS)4]2− Ions. *Angew. Chemie Int. Ed.* **49,** 7116–7119 (2010).

45. Geppert-Rybczy, M., Lehmann, J. K., Peppel, T., Köckerling, M. & Heintz, A. Studies of Physicochemical and Thermodynamic Properties of the Paramagnetic 1-Alkyl-3-methylimidazolium Ionic Liquids $(EMIm)_2[Co(NCS)_4]$ and $(BMIm)_2[Co(NCS)_4]$. *J. Chem. Eng. Data* **55,** 5534–5538 (2010).

46. Brown, P. *et al.* Dication magnetic ionic liquids with tuneable heteroanions. *Chem. Commun* **49,** 2765-2767 (2013).

47. Binnemans, K. Lanthanides and actinides in ionic liquids. *Chem. Rev.* **107,** 2592–2614 (2007).

48. Prodius, D. & Mudring, A.-V. Coordination Chemistry in Rare Earth Containing Ionic Liquids. *Handb. Phys. Chem. Rare Earths* **50,** 395-420 (2016).

49. Nockemann, P. *et al.* Anionic rare-earth thiocyanate complexes as building blocks for low-melting metal-containing ionic liquids. *J. Am. Chem. Soc.* **128,** 13658–13659 (2006).

50. Mallick, B., Balke, B., Felser, C. & Mudring, A.-V. Dysprosium Room-Temperature Ionic Liquids with Strong Luminescence and Response to Magnetic Fields. *Angew. Chemie Int. Ed.* **47,** 7635–7638 (2008).

51. Ji, S. P., Tang, M., He, L. & Tao, G. H. Water-free rare-earth-metal ionic liquids/ionic liquid crystals based on hexanitratolanthanate(III) anion. *Chem. - A Eur. J.* **19,** 4452–4461 (2013).

52. Alvarez-Vicente, J. *et al.* Easily Accessible Rare-Earth-Containing Phosphonium Room-Temperature Ionic Liquids: EXAFS, Luminescence, and Magnetic Properties. *J. Phys. Chem. B* **120,** 5301–5311 (2016).

53. Monson, T. C. *et al.* Unprecedented magnetic behaviour in lanthanide-based ionic liquids. *Chem. Commun.* **53,** 11682–11685 (2017).

54. Babai, A. & Mudring, A. V. Anhydrous praseodymium salts in the ionic liquid [bmpyr][Tf_2N]: Structural and optical properties of [bmpyr]$_4$[PrI_6] [Tf_2N] and [bmyr]$_2$[$Pr(Tf_2N)_5$]. *Chem. Mater.* **17,** 6230–6238 (2005).

55. Santos, E., Albo, J. & Irabien, A. Magnetic ionic liquids: Synthesis, properties and applications. *RSC Adv.* **4,** 40008–40018 (2014).

56. Oliveira, F. C. C., Rossi, L. M., Jardim, R. F. & Rubim, J. C. Magnetic Fluids Based on γ - Fe2O3 and CoFe2O4 Nanoparticles Dispersed in Ionic Liquids. *J. Phys. Chem. C* **113,** 8566–8572 (2009).

57. Medeiros, A. M. M. S. *et al.* Magnetic ionic liquids produced by the dispersion of magnetic nanoparticles in 1-n-butyl-3-methylimidazolium bis(trifluoromethanesulfonyl)imide (BMI.NTf_2). *ACS Appl. Mater. Interfaces* **4,** 5458–5465 (2012).

58. Guerrero-Sanchez, C., Lara-Ceniceros, T., Jimenez-Regalado, E., Raşa, M. & Schubert, U. S. Magnetorheological Fluids Based on Ionic Liquids. *Adv. Mater.* **19,** 1740–1747 (2007).

59. Rodríguez-Arco, L., López-López, M. T., González-Caballero, F. & Durán, J. D. G. Steric repulsion as a way to achieve the required stability for the preparation of ionic liquid-based ferrofluids. *J. Colloid Interface Sci.* **357,** 252–254 (2011).

60. Truong, D. Q. & Ahn, K. K. MR Fluid Damper and Its Application to Force Sensorless Damping Control System. *INTECH,* 384 - 423 (2012). doi:10.5772/51391

61. De Pedro, I. *et al.* Long-range magnetic ordering in magnetic ionic liquid: Emim[$FeCl_4$]. *J. Phys. Condens. Matter* **22,** 296006–4PP (2010).

62. De Pedro, I., Rojas, D. P., Blanco, J. A. & Fernández, J. R. Antiferromagnetic ordering in magnetic ionic liquid Emim[$FeCl_4$]. *J. Magn. Magn. Mater.* **323,** 1254–1257 (2011).

63. Brown, P. *et al.* Dication magnetic ionic liquids with tuneable heteroanions. *Chem. Commun* **49,** 2765 - 2767 (2013).

64. Nacham, O., Clark, K. D., Yu, H. & Anderson, J. L. Synthetic Strategies for Tailoring the Physicochemical and Magnetic Properties of Hydrophobic Magnetic Ionic Liquids. *Chem. Mater* **9,** 923 - 931 (2015).

65. Yoshida, Y., Tanaka, H. & Saito, G. Organic Paramagnetic Ionic Liquids Based on Anion Containing 2,2,6,6-Tetramethyl-1-piperidinyloxyl Radical Moiety. *Chem. Lett.* **36,** 1096–1097 (2007).

66. Miao, C.-X. *et al.* Synthesis of bimagnetic ionic liquid and application for selective aerobic oxidation of aromatic alcohols under mild conditions. *Chem. Commun* **47,** 2697–2699 (2011).

67. Prodius, D. *et al.* Breaking the paradigm: record quindecim charged magnetic ionic liquids. *Mater. Horiz.***4,** 217 - 221 (2017). doi:10.1039/C6MH00468G

68. Kohno, Y. *et al.* A cobalt(II) bis(salicylate)-based ionic liquid that shows thermoresponsive and selective water coordination. *Chem. Commun* **50,** 6633–6636 (2014).

69. Osborne, S. J. *et al.* Thermochromism and switchable paramagnetism of cobalt(ii) in thiocyanate ionic liquids. *Dalt. Trans.* **44,** 11286–11289 (2015).

70. Aoyagi, N. *et al.* Thermochromic properties of low-melting ionic uranyl isothiocyanate complexes. *Chem. Commun* **47,** 4490–4492 (2011).

71. Lan, X. *et al.* Thermochromic Magnetic Ionic Liquids from Cationic Nickel(II) Complexes Exhibiting Intramolecular Coordination Equilibrium. *Chem. - A Eur. J.* **23,** 823–831 (2017).

72. Okuhata, M., Funasako, Y., Takahashi, K. & Mochida, T. A spin-crossover ionic liquid from the cationic iron(III) Schiff base complex. *Chem. Commun* **49,** 7662–7664 (2013).

73. Fitzpatrick, A. J., O 'connor, H. M. & Morgan, G. G. A room temperature spin crossover ionic liquid. *Dalt. Trans.* **44,** 20839 - 20842 (2015).

74. Nockemann, P. *et al.* Cobalt(II) complexes of nitrile-functionalized ionic liquids. *Chem. - A Eur. J.* **16,** 1849–1858 (2010).

75. João Paulo Leal, S. *et al.* Showcasing research from the Photochemistry and As featured in: A thermochromic europium(III) room temperature ionic liquid with thermally activated anion–cation interactions. *Chem. Commun* **850,** 850–853 (2017).

76. Branco, A., Branco, L. C. & Pina, F. Electrochromic and magnetic ionic liquidsw. *Chem. Commun* **47,** 2300–2302 (2011).

77. Funasako, Y., Mochida, T., Takahashi, K., Sakurai, T. & Ohta, H. Vapochromic ionic liquids from metal-chelate complexes exhibiting reversible changes in color, thermal, and magnetic properties. *Chem. - A Eur. J.* **18,** 11929–11936 (2012).

78. Tang, S., Babai, A. & Mudring, A. V. Europium-based ionic liquids as luminescent soft materials. *Angew. Chemie - Int. Ed.* **47,** 7631–7634 (2008).

79. Lunstroot, K. *et al.* Luminescent ionogels based on europium-doped ionic liquids confined within silica-derived networks. *Chem. Mater.* **18,** 5711–5715 (2006).

80. Lunstroot, K. *et al.* Lanthanide-doped luminescent ionogels. *J. Chem. Soc. Dalt. Trans.* 298–306 (2009). doi:10.1039/b812292j.

81. Nockemann, P. *et al.* Photostability of a highly luminescent europium beta-diketonate complex in imidazolium ionic liquids. *Chem. Commun. (Camb).* 4354–4356 (2005). doi:10.1039/b506915g

82. Getsis, A., Balke, B., Felser, C. & Mudring, A. V. Dysprosium-based ionic liquid crystals: thermal, structural, photo- and magnetophysical properties. *Cryst. Growth Des.* **9,** 4429–4437 (2009).

83. Getsis, A., Tang, S. & Mudring, A. V. A luminescent ionic liquid crystal: $[C_{12}mim]_4[EuBr_6]Br$. *Eur. J. Inorg. Chem.* 2172–2177 (2010). doi:10.1002/ejic.200901220.

84. Arenz, S. *et al.* Intense near-infrared luminescence of anhydrous lanthanide(III) iodides in an imidazolium ionic liquid. *Chem. Phys. Lett.* **402,** 75–79 (2005).

85. Fan, B. *et al.* Synthesis of Lanthanide-Based Room Temperature Ionic Liquids with Strong Luminescence and Selective Sensing of Fe(III) over Mixed Metal Ions. *Ind. Eng. Chem. Res.* **55,** 2267–2271 (2016).

86. Yue, Q. F., Xiao, L. F., Zhang, M. L. & Bai, X. F. The glycolysis of poly(ethylene terephthalate) waste: Lewis acidic ionic liquids as high efficient catalysts. *Polymers*

(Basel). **5,** 1258–1271 (2013).

87. Wang, J. *et al.* Application of iron-containing magnetic ionic liquids in extraction process of coal direct liquefaction residues. *Ind. Eng. Chem. Res.* **51,** 3776–3782 (2012).

88. Albo, J. *et al.* Separation performance of CO_2 through Supported Magnetic Ionic Liquid Membranes (SMILMs). *Sep. Purif. Technol.* **97,** 26–33 (2012).

89. Bica, K. & Gaertner, P. An iron-containing ionic liquid as recyclable catalyst for aryl Grignard cross-coupling of alkyl halides. *Org. Lett.* **8,** 733–735 (2006).

90. Clark, K. D., Yamsek, M. M., Nacham, O. & Anderson, J. L. Magnetic ionic liquids as PCR-compatible solvents for DNA extraction from biological samples. *Chem. Commun* **51,** 16771–16773 (2015).

91. Clark, K. D. *et al.* Extraction of DNA by magnetic ionic liquids: Tunable solvents for rapid and selective DNA analysis. *Anal. Chem.* **87,** 1552–1559 (2015).

92. Zazybin, A. G. *et al.* Metal-containing ionic liquids: Current paradigm and applications. *Russ. Chem. Rev.* **86,** (2017).

93. Santos, E., Albo, J. & Irabien, A. Magnetic ionic liquids: synthesis, properties and applications. *RSC Adv.* **4,** 40008–40018 (2014).

94. Bica, K., Wien, T., Gaertner, P. & Leder, S. From Solvent to Sustainable Catalysis – Chloroferrate Ionic Liquids in Synthesis. *Curr. Org. Synth.* **8,** 1–15 (2011).

95. Valkenberg, M. H., Decastro, C. & Hölderich, W. F. Friedel-Crafts acylation of aromatics catalysed by supported ionic liquids. *Appl. Catal. A Gen.* **215,** 185–190 (2001).

96. Li, C., Liu, W. & Zhao, Z. (Kent). Efficient synthesis of benzophenone derivatives in Lewis acid ionic liquids. *Catal. Commun.* **8,** 1834–1837 (2007).

97. Zhao, Z., Qiao, W., Wang, G., Li, Z. & Cheng, L. Alkylation of-methylnaphthalene with long-chain alkenes catalyzed by butylpyridinium bromochloroaluminate ionic liquids. *J. Mol. Catal. A Chem.* **231,** 137–143 (2005).

98. Panja, S. K. & Saha, S. Recyclable, magnetic ionic liquid bmim[$FeCl_4$]-catalyzed, multicomponent, solvent-free, green synthesis of quinazolines. *RSC Adv.* **3**, 14495 - 14500 (2013). doi:10.1039/c3ra42039f.

99. Bica, K., Gmeiner, G., Reichel, C., Lendl, B. & Gaertner, P. Microwave-assisted synthesis of camphor-derived chiral imidazolium ionic liquids and their application in diastereoselective Diels-Alder reaction. *Synthesis (Stuttg).* 1333–1338 (2007). doi:10.1055/s-2007-966018

100. Misuk, V., Breuch, D. & Löwe, H. Paramagnetic ionic liquids as 'liquid fixed-bed' catalysts in flow application. *Chem. Eng. J.* **173,** 536–540 (2011).

101. Wang, Q., Geng, Y., Lu, X. & Zhang, S. First-Row Transition Metal-Containing Ionic Liquids as Highly Active Catalysts for the Glycolysis of Poly(ethylene terephthalate) (PET). *ASC Sustain. Chem. Eng.* **3,** 340–348 (2015).

102. Zhu, W. *et al.* Pyridinium-based temperature-responsive magnetic ionic liquid for oxidative desulfurization of fuels. *Chem. Eng. J.* **229,** 250–256 (2013).

103. Jiang, W. *et al.* Fast oxidative removal of refractory aromatic sulfur compounds by a

magnetic ionic liquid. *Chem. Eng. Technol.* **37,** 36–42 (2014).

104. Lee, S. H., Ha, S. H., You, C.-Y. & Koo, Y.-M. Recovery of magnetic ionic liquid [bmim]$FeCl_4$ using electromagnet. *Korean J. Chem. Eng.* **24,** 436–437 (2007).

105. Okuno, M., Hamaguchi, H.-O. & Hayashi, S. Magnetic manipulation of materials in a magnetic ionic liquid. *Cit. Appl. Phys. Lett* **89,** 132506-1 - 132506-2 (2006).

106. Clark, K. D., Nacham, O., Purslow, J. A., Pierson, S. A. & Anderson, J. L. Magnetic ionic liquids in analytical chemistry: A review. *Anal. Chim. Acta* **934,** 9–21 (2016).

107. Santos, E., Albo, J., Rosatella, A., Afonso, C. A. M. & Irabien, Á. Synthesis and characterization of Magnetic Ionic Liquids (MILs) for CO_2 separation. *J. Chem. Technol. Biotechnol.* **89,** 866–871 (2014).

108. Santra, K., Clark, K. D., Maity, N., Petrich, J. W. & Anderson, J. L. Exploiting Fluorescence Spectroscopy to Identify Magnetic Ionic Liquids Suitable for the Isolation of Oligonucleotides. *J. Phys. Chem. B* **122**, 7747-7756 (2018). doi:10.1021/acs.jpcb.8b05580.

109. Wang, J. *et al.* Application of iron-containing magnetic ionic liquids in extraction process of coal direct liquefaction residues. *Ind. Eng. Chem. Res.* **51,** 3776–3782 (2012).

110. Deng, N. *et al.* Highly efficient extraction of phenolic compounds by use of magnetic room temperature ionic liquids for environmental remediation. *J. Hazard. Mater.* **192,** 1350–1357 (2011).

111. Shirvani, S., Hassan Mallah, M., Ali Moosavian, M. & Safdari, J. Magnetic Ionic Liquid in Magmolecular Process for Uranium Removal. *Chem. Eng. Res. Des.* **109,** 108–115 (2016).

112. Pierson, S. A. *et al.* Synthesis and characterization of low viscosity hexafluoroacetylacetonate-based hydrophobic magnetic ionic liquids. *New J. Chem. New J. Chem* **5498,** 5498–5505 (2017).

113. Mehdi, H., Binnemans, K., Van Hecke, K., Van Meervelt, L. & Nockemann, P. Hydrophobic ionic liquids with strongly coordinating anions. *Chem. Commun.* **46,** 234–236 (2010).

114. Kremer, F. & Schonhals, A. *Broadband Dielectric Spectroscopy*. *Springer - Verlag Berlin Heidelberg* (2003). doi:10.1007/978-3-642-56120-7

115. Feldman, Y., Puzenko, a. & Ryabov, Y. Dielectric relaxation phenomena in complex materials. *Adv. Chem. Phys.* **133,** 125 (2006). https://doi.org/10.1002/0471790265.ch1.

116. Wojnarowska, Z. & Paluch, M. Recent progress on dielectric properties of protic ionic liquids. *J. Phys. Condens. Matter* **27,** 073202 (20 PP) (2015).

117. Rod Nave. SQUID Magnetometer and Josephson Junctions. 1–5 (2012). Available at: http://hyperphysics.phy-astr.gsu.edu/hbase/solids/squid.html. (Accessed: 3rd April 2018)

118. Simmonds, R. W. Quantum interference heats up. *Nature* **492,** 358–359 (2012).

Chapter 2. Effects of external stimuli on the properties of magnetic ionic liquids

2.1 Chapter Aims

A key property of magnetic ionic liquids is their ability to be influenced by external stimuli. In this chapter our interest lies in further investigating the effects of temperature and pressure on the physical properties of a number of transition metal-based ILs. To achieve this, broadband dielectric spectroscopy was used to probe the molecular properties across a wide temperature, pressure and frequency range.

The effects of temperature and pressure on the molecular dynamics of cobalt(II) thiocyanate in imidazolium and phosphonium ILs are analysed across the liquid, supercooled liquid and glassy regions and we ultimately investigate whether changes in the coordination of the cobalt(II) iso-thiocyanate complex in a neat ionic liquid system are visible in the conductivity behaviour of the sample. Most importantly, we investigate the effects of hydrostatic pressure in the range of 0.1−600 MPa in inducing this transition. The results of this work were published in the *Journal of Physical Sciences C*, in 2016.

2.2 Introduction

ILs are renowned for their remarkable transport properties, *i.e.* wide electrochemical windows, polarity, electrical conductivity.[1] An in-depth study of the thermodynamic and transport properties is fundamental to better understand these systems for use in potential applications.[2] Frequently used spectroscopic techniques such as; IR, UV/Vis, and Raman, cover high frequency dynamics normally at room temperature or higher. In order to obtain an accurate picture of the transport properties, low-temperature dynamic properties are vital. This is because upon cooling ILs have a tendency to be vitrified which ultimately impacts the transport properties.[3] The behaviour upon approaching the glass transition has been a point of interest for many years. As described by Leys *et al.*[4] ion mobility, which is related to viscosity and electric conductivity values, is strongly influenced in the vicinity of the glass transition (T_g). Approaching T_g, the viscosity and the relaxation times of the ions increase by many orders of magnitude in a narrow temperature range.[5] Questions arise as to "*what is the physical reason for this behaviour?*", "*are structural changes occurring?*", "*Do the ions move cooperatively or are single ions just starting to move more slowly?*.[5]

To shed light on this behaviour, wide-temperature ranges are therefore important to gain a complete understanding of the relation between glass formation and molecular structure.[4] Broadband dielectric spectroscopy (BDS) is sensitive to the orientational motions of permanent dipoles and translational contributions of ions. Furthermore, measurements can be carried out over wide temperature, frequency, and pressure ranges. Ultimately, by combining the traditional high-

frequency spectroscopic techniques with the low-frequency dielectric properties, a relationship between the molecular structure and physicochemical properties may be developed.

The dielectric response of a material can be analysed in different formalisms, electric conductivity (σ') and electric modulus (M'').[6] Each representation gives a different insight into aspects of the ion conductivity of the studied system. In modulus representation different processes may be visible, namely;

(i) alpha process (α)

(ii) beta process (β)

(iii) gamma process (γ)

The alpha process is referred to as a dynamic glass transition that corresponds to the collective molecular reorientations. The β and γ processes stem from both intra- and intermolecular motions arising from the dipole vector's localised rotational fluctuations. The β-relaxation is generally associated with short range motions.[7]

Different groups have explored the dielectric properties of ionic liquids. Leys *et al.*[4] looked at the electrical conductivities of imidazolium-based ILs with different alkyl chain lengths (n = 2, 4, 6, 8, 10) and various different anions (Br^-, Tf_2N^-, FAP^-). The T_g was seen to increase with an increase in alkyl chain length, whilst the conductivity and fragility (steepness of temperature dependence of structural relaxation time) decreased which could be attributed to the reduced mobility of charge carriers induced by stronger van der Waals interactions. In addition, the effect of anion size was further investigated.[8] Increasing the anion size resulted in an increase in the electrical conductivity and a decrease in the T_g, fragility and activation

energy. This could be reasoned by looking at the effect of increasing ion mass which reduced interionic interactions and, in this case, led to higher mobility.

The stimuli-responsive nature of MILs has led to interesting thermochromic, electrochromic, vapochromic and solvatochromic properties.[9–16] Stimuli can be in the form of temperature, pressure, magnetic field application, solvents, and light. Compared with the many investigations into the thermochromic behaviour of MILs, investigations into the effect of pressure on the properties of MILs are relatively scarce. García-Saiz and co-workers[12] explored the impact of hydrostatic pressure on the magnetic properties of $[C_2Mim][FeCl_4]$, observing interesting results under pressure. At ambient pressure this MIL displayed three-dimensional ordering below the Néel temperature $T_N \approx 3.8$ K.[17] However, upon applied pressure an induced transition from antiferromagnetic to ferromagnetic three-dimensional ordering was observed.

Interestingly, well before this, in 1973 Angell and Abkemeier,[18] investigated the effects of pressure on inducing coordination changes in Ni(II) chloride in the molten salt medium; α-picolinium (α-$CH_3C_5H_4NH^+$) chloride and ethanolaminium ($OHCH_2CH_2NH_3^+$) chloride, using a diamond anvil optical cell under hydrostatic pressure. At ambient pressure the prevailing structure is tetrahedral $[NiCl_4]^{2-}$ whilst upon application of pressure the octahedral $[NiCl_6]^{4-}$ dominates. Martinez *et al.*[19] used electronic spectra as a method of analysis to further look at the relaxation profiles; both chemical ordering time-scales and structural relaxation time-scales, of known Co(II) complexes that change coordination upon heating/cooling.

Important prior art to the work undertaken in this chapter is that of Osborne *et al*. who showed the temperature-dependent switching of paramagnetism of cobalt(II) in an ionic liquid system.[16] A switch from tetrahedral, $[C_4Mim]_2[Co(NCS)_4]$, at room temperature to octahedral, $[C_4Mim]_4[Co(NCS)_6]$ at temperatures <233 K was reflected in a colour change from blue (RT) to red (233 K) as observed by UV/Vis and importantly, a change in the magnetic properties (Figure 24) when an excess of mobile thiocyanate ions was present (Scheme 1). This can be attributed to an entropic effect whereby at low temperatures (<233 K), equilibrium shifts to the right-hand side and favours the octahedral formation.

Scheme 1. Equilibrium between tetrahedral and octahedral complex formation.

$$[C_4Mim]_2[Co(NCS)_4] + 2[C_4Mim][SCN] \leftrightarrows [C_4Mim]_4[Co(NCS)_6]$$

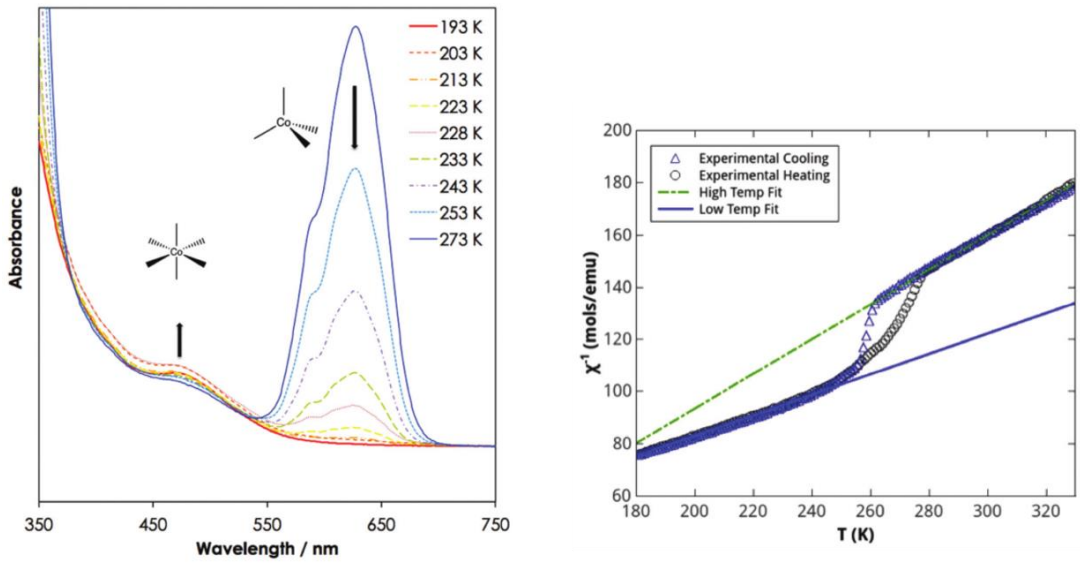

Figure 24. Temperature-dependent UV-Vis absorption spectra (left) and magnetic susceptibility measurements (right) of Co(II) in 1-butyl-3-methylimidazolium thiocyanate, $[C_4Mim][SCN]$ ionic liquid.

The relaxation dynamics of $[C_2Mim]_2[Co(NCS)_4]$ and $[C_4Mim]_2[Co(NCS)_4]$ were previously reported using broadband dielectric spectroscopy, by Hensel-Bielowka *et al*.[20] On approaching the glass transition (T_g), a common feature of the molecular dynamics of liquids is a characteristic crossover above T_g, manifested as a change in Vogel-Fulcher-Tammann (VFT) dependence. In the case reported for $[C_4Mim]_2[Co(NCS)_4]$ system (T_g = 208 K) a single VFT was able to adequately describe the temperature dependence of conductivity over the temperature range studied, suggesting that the dynamical heterogeneity and cooperativity play the same role in the molecular dynamics in the vicinity of T_g as it does in the normal liquid state.[20]

We believe that further investigations would be beneficial to investigate the influence of pressure on this system. Furthermore, reflecting on the work by Osborne *et al.*[16] it would be advantageous to investigate the temperature and pressure effects on different mole ratios of cobalt(II) salt to ionic liquid, given that evidence of a coordination change from tetrahedral to octahedral was observed upon cooling.

We first investigate the physicochemical properties of cobalt(II) thiocyanate salt, $Co(NCS)_2$, in different mole ratios of the ionic liquids, trihexyl(tetradecyl)phosphonium thiocyanate ($[P_{666\,14}][SCN]$) and 1-butyl-3-methlyimidazolium thiocyanate ($[C_4Mim][SCN]$), using techniques such as IR, TGA and DSC. Furthermore, the relaxation dynamics are then investigated under various temperature and pressure conditions using broadband dielectric spectroscopy and rheology.

The studies of conductivity behaviour of $[P_{666\,14}][SCN]$ + $Co(NCS)_2$ mixture, in particular, over a wide temperature (193−403 K) and pressure ranges (0.1−600 MPa) combined with calorimetric; differential scanning calorimetry (DSC) and structural X-

ray diffraction (XRD) investigations enable us to provide new insight into the field of stimuli-responsive magnetic ionic liquids. By investigating the reorientational structural dynamics and charge transport properties of these MILs under various temperature and pressure conditions we explore the effects of stimulants in inducing changes in the structure of the magnetic ionic liquid described above. The results presented go a long way in delivering the answers to two important questions, namely, (i) *Is it possible to recognise changes in the structural properties of Co(II) from its conductivity behaviour?* (ii) *Is it possible to induce changes in the coordination geometry of a cobalt complex through the use of high pressure?*

2.3 Results and discussion

2.3.1 Synthesis

Cobalt thiocyanate was added to trihexyl(tetradecyl)phosphonium thiocyante and 1-butyl-3-methylimidazolium thiocyanate in molar ratios (1:2, 1:4, 1:5, 1:6 and 1:10) (Scheme 2). Upon mixing of the salt with ionic liquid at room temperature, a royal blue solution formed instantaneously, indicative of the formation of a tetrahedral cobalt complex.

Scheme 2. Reaction scheme for the synthesis trihexyl(tetradecyl)phosphonium thiocyanate and 1-methyl-3-butylimidazolium with cobalt thiocyanate. (x = 2, 3, 4, 5, 6, 10).

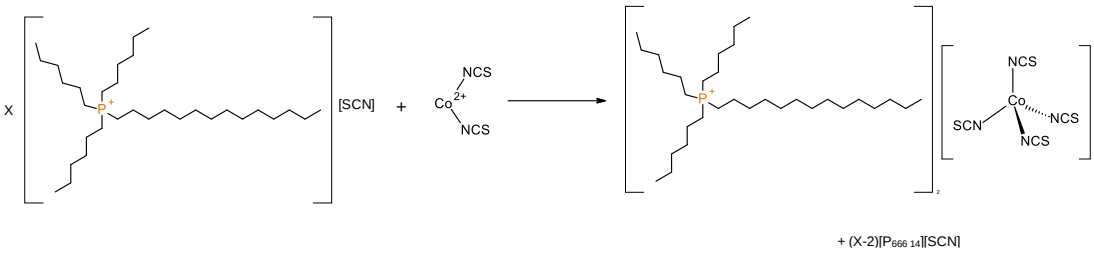

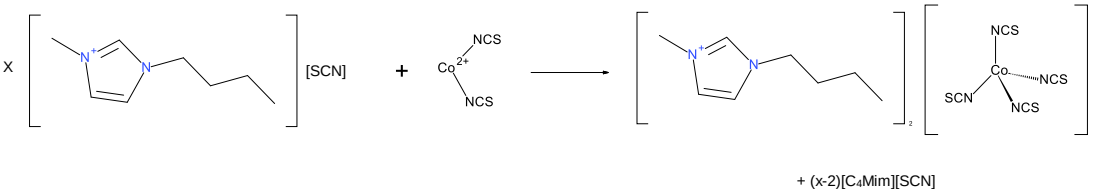

2.3.2 Spectroscopic properties

Infrared was used to give insight into the structure of the liquids prepared. As there are different bonding modes of the thiocyanate ligand, IR was used to identify the mode of metal-thiocyanate bonding. The thiocyanate ligand showed a strong absorption band at ~ 2051 cm^{-1}, characteristic of the M-NCS vibration. If cobalt was bonding through the M-SCN bonding mode, the spectra would have a characteristic band at ~2100 cm^{-1}. We can also assign the peak between 826 cm^{-1} to that of the M- CS vibration and at 2700 and 3300 cm^{-1} to that of the C-H stretching modes of the 1-butyl-3-methylimidazolium cation. As the ratio of ionic liquid to salt is increased the system becomes more dilute and the intensity of the Co-NCS is seen to decrease, seen more clearly when spectra are superimposed (Figure 25 (b)).

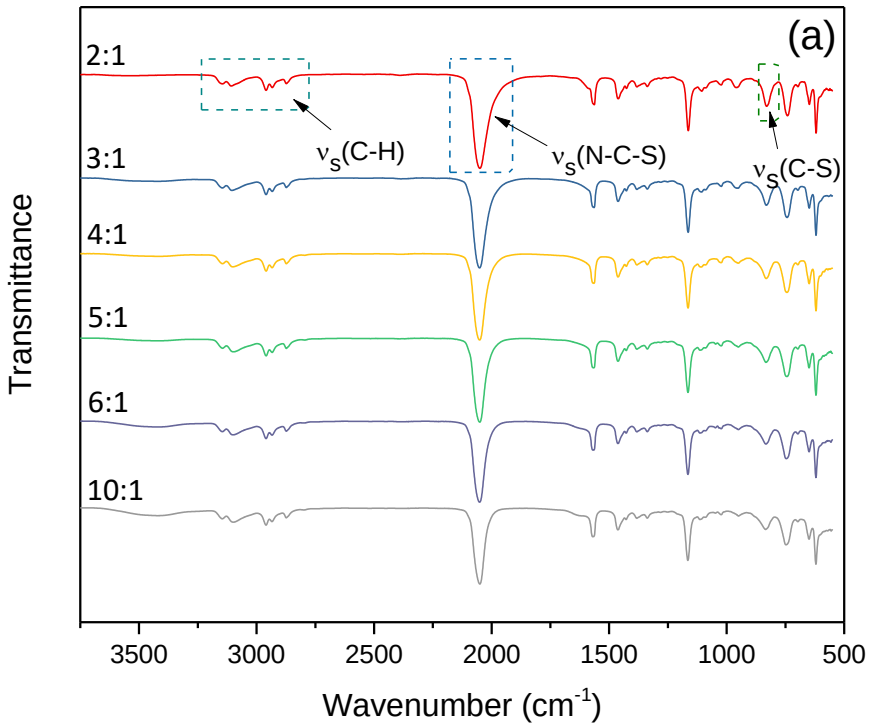

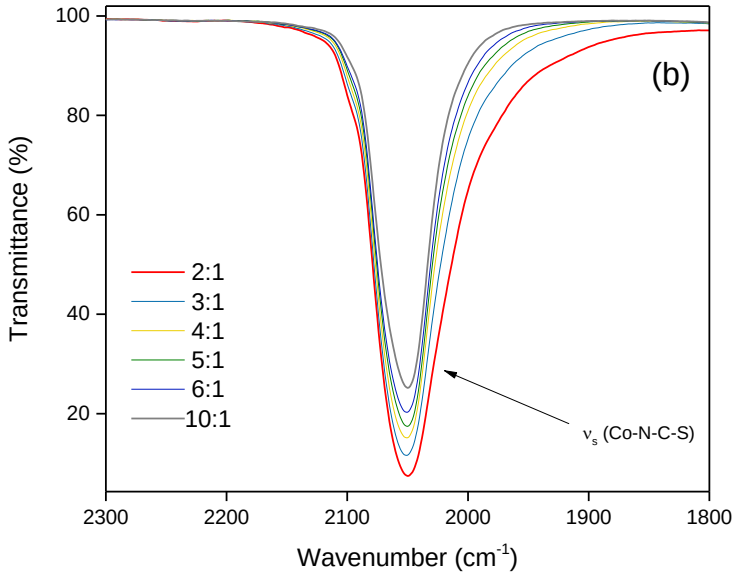

Figure 25. a) Infrared spectra of $[C_4Mim][SCN]$ + $Co(SCN)_2$ in various mole ratios, (b) shows the magnified region of the Co-NCS band showing a decrease in the stretching of the N-C-S band as the ionic liquid ratio is increased.

Table 1. Assigned bands in infrared spectrum

Wavenumber (cm^{-1})	Strength	Stretch
3426	Weak	N-H
2833 – 3180	Medium	C-H
2053	Strong	N=C=S
1596	Medium	C-C
1459	Medium	C-N
1168	medium	Ring stretch (sym.)

The infrared spectra of the trihexyl(tetradecyl)phosphonium thiocyanate systems are shown in Figure 26. The strong absorption band between 2794 and 2992 cm^{-1} is that of the C – H stretching mode of the cation $[P_{666\,14}]^+$. The Co-NCS stretch is at 2047 cm^{-1}. The P-C stretch is at 1460 cm^{-1} and the C-S stretch is seen at 717 cm^{-1}.

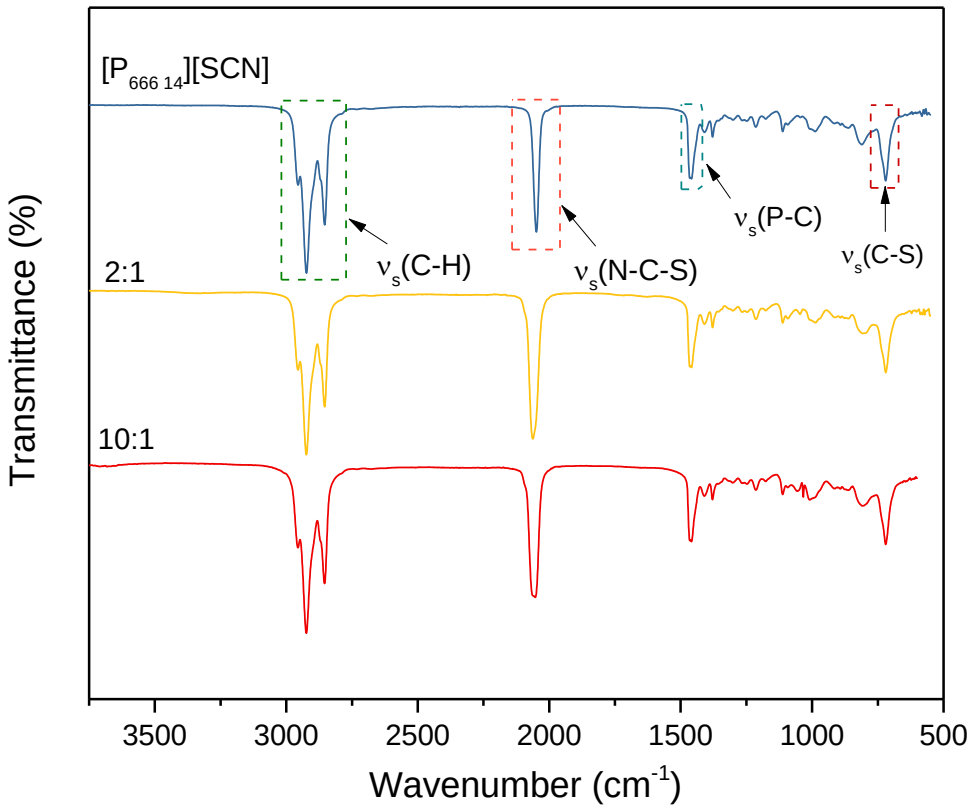

Figure 26. Infrared spectra of $[P_{666\ 14}][SCN]$ and $[P_{666\ 14}][SCN]$ in different mole ratios (2:1 and 10:1) of $Co(NCS)_2$ salt.

Table 2. Assigned bands in the infrared spectra of $[P_{666\ 14}][SCN]$ $Co(NCS)_2$ (2:1 and 10:1).

Wavenumber (cm^{-1})	Strength	Stretch
2954 -2841	strong	C-H
2056	strong	N=C=S
1460	medium	P-C
723	medium	C-S

2.3.3 Thermal properties

The thermal properties were investigated by means of thermogravimetric analysis (TGA) and differential scanning calorimetry (DSC). Results of TGA are presented in Table 3 showing a decrease in the decomposition temperatures as the ratio of ionic liquid to salt is increased for both the $[C_4Mim]^+$ and $[P_{666\,14}]^+$ systems. All ionic liquid systems investigated have high decomposition temperatures meaning that wide temperature ranges can be investigated without concern.

Table 3. Decomposition temperatures measured in the temperature range of 25 – 500 °C.

Ionic liquid	**T_{dec} (°C)**
$[C_4Mim][SCN]$	198
$[C_4Mim]_2[Co(NCS)_4]$	302
$[C_4Mim]_2[Co(NCS)_4]$ 2$[C_4Mim][SCN]$	222
$[C_4Mim]_2[Co(NCS)_4]$ 8$[C_4Mim][SCN]$	219
$[P_{666\,14}]_2[Co(NCS)_4]$ + 8$[P_{666\,14}][SCN]$	330
$[P_{666\,14}]_2[Co(NCS)_4]$ + 2$[P_{666\,14}][SCN]$	327

Upon cooling, the imidazolium based magnetic ionic liquids investigated can be vitrified as observed in the DSC profile (Figure 27). The measurements were performed between -100 and 150 °C with a cooling and heating rate of 10 °C/min.

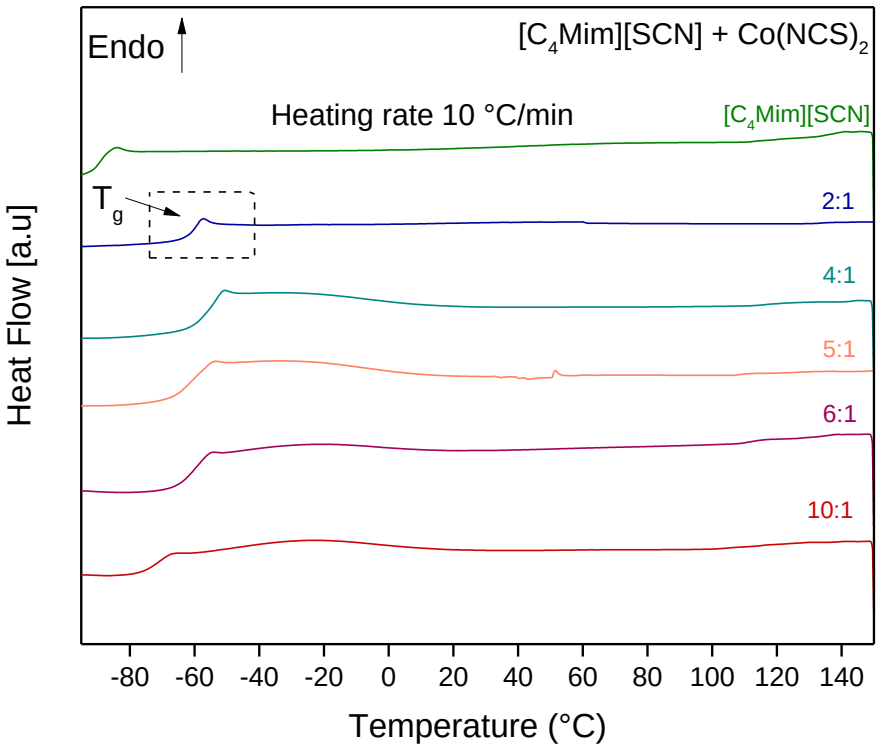

Figure 27. DSC profiles for the measured $[C_4Miim][SCN] + Co(NCS)_2$ series.

Table 4. Glass transition temperatures measured for the $[C_4Mim][SCN]$ $Co(NCS)_2$ salts.

Ionic Liquid	**T_g (°C)**
$[C_4Mim][SCN]$	-89
$[C_4Mim]_2[Co(NCS)_4]$	-61
$[C_4Mim]_2[Co(NCS)_4]$ 2$[C_4Mim][SCN]$	-55
$[C_4Mim]_2[Co(NCS)_4]$ 3$[C_4Mim][SCN]$	-61
$[C_4Mim]_2[Co(NCS)_4]$ 4$[C_4Mim][SCN]$	-61
$[C_4Mim]_2[Co(NCS)_4]$ 8$[C_4Mim][SCN]$	-72

In contrast, $[P_{666\ 14}][SCN] + Co(NCS)_2$ in mole ratio 10:1 (Figure 28), displays enthalpy changes upon heating/cooling. The exact nature of this enthalpy change will be discussed further in the section that follows.

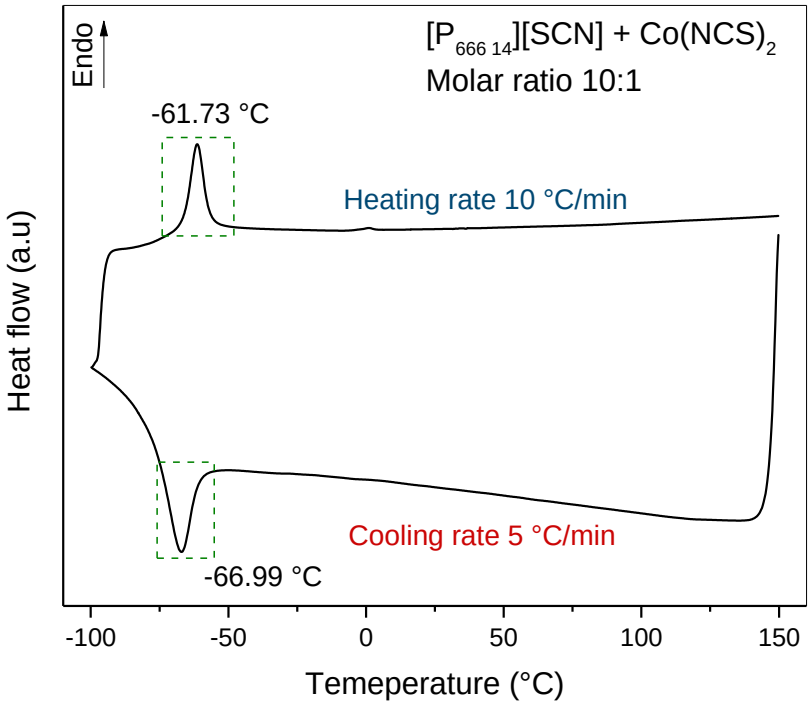

Figure 28. Calorimetric measurements of $[P_{666\ 14}][SCN] + Co(NCS)_2$ (10:1).

2.3.4 Broadband Dielectric Spectroscopic Investigations

To investigate the relaxation behaviour of the examined magnetic ionic liquids, we took advantage of broadband dielectric spectroscopy, a technique traditionally employed for studying the molecular dynamics of glass-forming systems. According to standard practice, the dielectric response of the studied IL is analysed in electric conductivity (σ') and electric modulus (M'') formalisms.[6] Each representation gives a different insight into aspects of the ion conductivity of the ionic liquid investigated meaning what is not apparent from one representation can be interpreted from the other. [21] Complex permittivity (ε^*), complex modulus (M^*) and complex conductivity (σ^*) formalisms can be readily obtained related by the following equation.

$$M^*(f) = \frac{1}{\varepsilon^*(f)} = \frac{i2\pi f\varepsilon_0}{\sigma^*}$$

Equation 2-1

M^* = Complex modulus

ε^* = Complex permittivity

σ^* = Complex conductivity

ε_0 = Dielectric permittivity of vacuum (ε_0 = 8.854 x 10^{-12} As V^{-1} m^{-1})

In the sections that follow the effects temperature and pressure will be discussed for the Co(II) thiocyanate complexes with different cations using electric conductivity and electric modulus formalisms.

2.3.5 $[C_4Mim]^+$ Cation

2.3.5.1 Effect of temperature

The dielectric response of different mole ratios, $[C_4Mim][SCN]$ + $Co(SCN)_2$, were measured over seven decades of frequency in a temperature range of 153 K – 393 K, in both modulus and conductivity formalisms . The data can be presented as seen in Figure 29 (mole ratio 5:1) and key features of these graphs will be discussed.

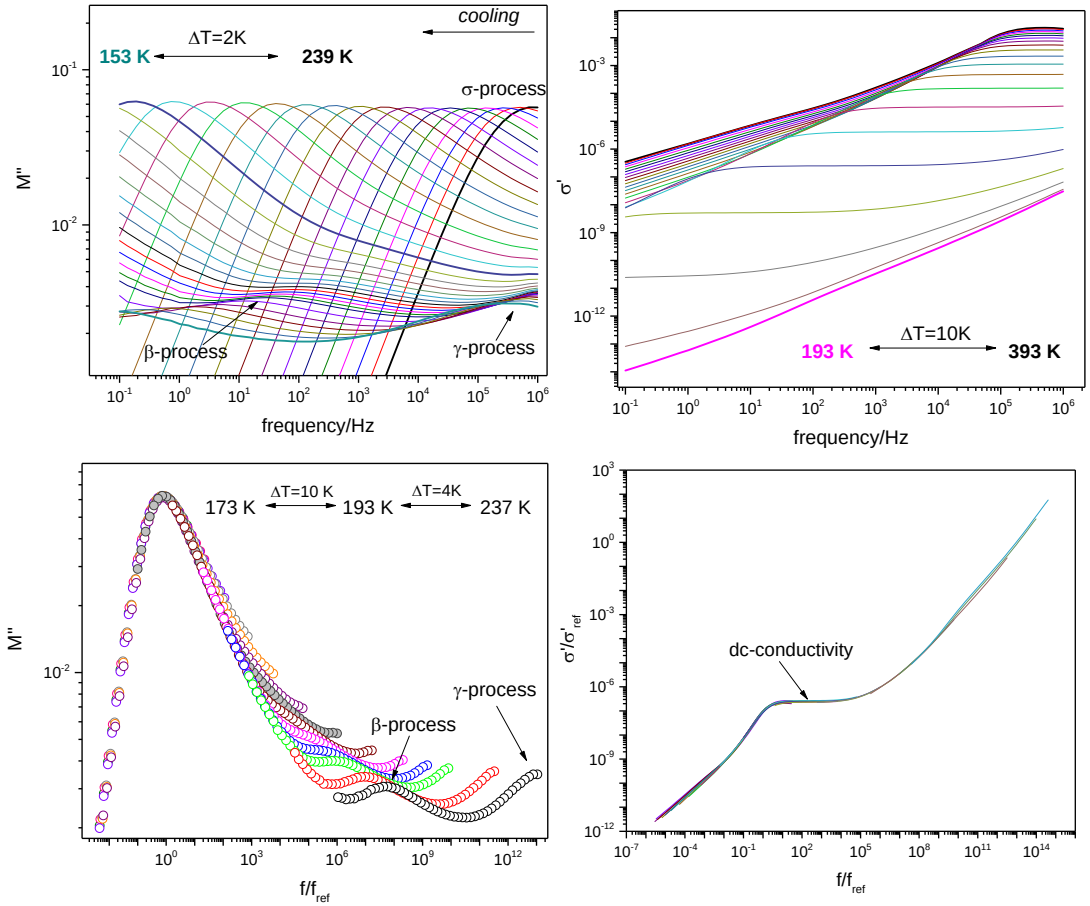

Figure 29. Molecular dynamics of $[C_4Mim][SCN]$ + $Co(NCS)_2$ mole ratio 5:1. Results are presented in modulus and conductivity representations in the form of frequency dependent data as well the master plots.

The imaginary part of complex modulus function M"*(f)* exhibits a well-resolved peak indicative of the main motion of ions and from which the maximum directly gives the conductivity relaxation time (τ_σ). Looking at the M''(*f)* plot we observe that as the temperature is decreased the maximum of the asymmetric loss peak moves towards lower frequencies. Modulus representation can be used to describe the electrical relaxation phenomena.[22] Notable, there are three different processes occurring within the sample over the temperature range, labelled above as α, β and γ processes. The main peak we observe is from that of primary relaxation process (α – process). This is characteristic of the main motion of ions *i.e.* the transition from liquid to the glass behaviour.[23] The β and γ processes which move towards higher frequencies as the temperature is increased can be related to secondary motions due to the localised motions of ions as described above. By shifting the data of each individual isotherm until they superimpose perfectly, a master curve for log M" could be constructed. Here, the secondary β and γ motions are clearly visible.

Electric conductivity can also be extracted from the measurement and was used to analyse the data in the temperature range 193 K to 393 K. One significant feature of this graph is the plateau which gives directly the dc-conductivity. As the temperature is decreased the plateau is seen to shift to lower frequencies. Again, a master plot was constructed by superimposing a number of curves measured at various temperatures to one plateau. This graph shows clearly three distinct regions. The main region of interest is the frequency independent part of σ', seen as a plateau in the above graph and corresponds to the dc-conductivity.

To gain further information it is important to look at the temperature dependencies of these systems. Using the above data, information about the temperature dependence on conductivity (σ_{dc}) and conductivity relaxation time (τ_σ) can be gained (Figure 30 and Figure 31, respectively). The dc-conductivity was determined from the plateau, whilst the conductivity relaxation process, τ_σ, observed in the M'' spectra were calculated from the peak maximum, f_{max} and extracted using Equation 2-2.

$$\tau_\sigma = \frac{1}{2\pi f_{max}}$$

Equation 2-2

2.3.5.1.1 Temperature dependence on conductivity ($\boldsymbol{\sigma_{dc}}$)

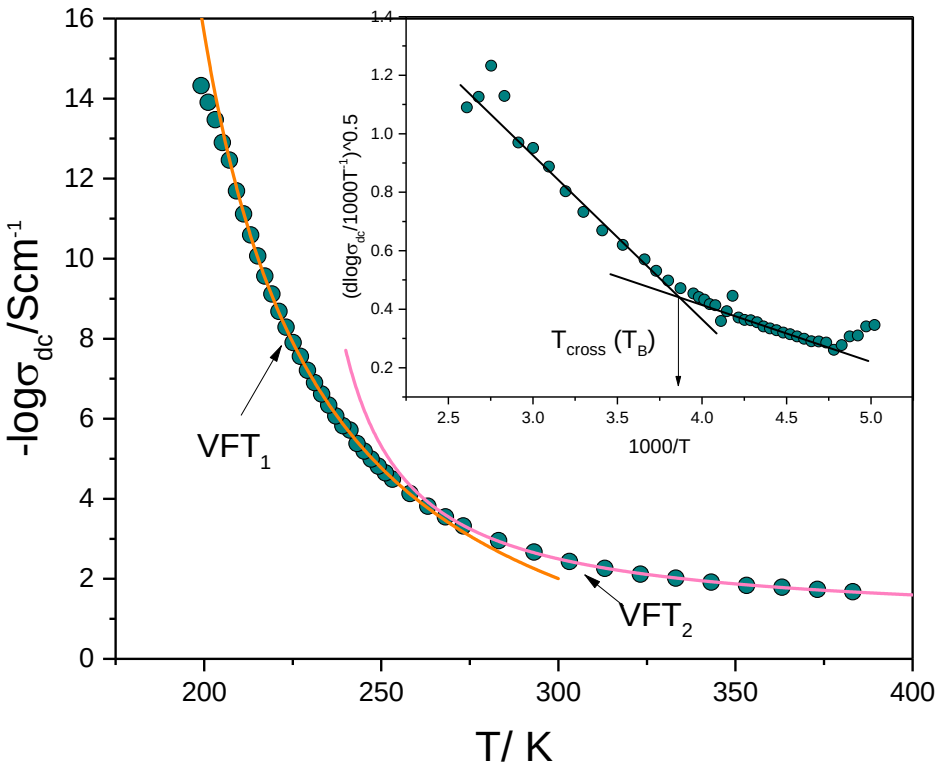

Figure 30. Temperature dependence on conductivity, inset of graph is Stickel analysis.

As the temperature is increased, σ_{dc} increases. Initially, it is apparent the data follows non-Arrhenius behaviour. This behaviour is often seen when analysing the molecular dynamics of ILs. The Vogel−Fulcher−Tammann (VFT) equation[24–26] is therefore commonly used to analyse the non-Arrhenius temperature dependence on dynamic properties of various supercooled liquids (Equation 2-3).

$$log\sigma_{dc} = \log \sigma_{\infty} + \frac{DT_0}{T - T_0} log_e$$

Equation 2-3

σ_{dc} = the dc-conductivity

D = the material constant

T_0 = the temperature usually regarded as the "ideal" glass temperature.

For data expected to show VFT behaviour one can calculate a derivative, known as the Stickel derivative operator[8] (Equation 2-4);

$$\left[dlog(x)/d\left(\frac{1}{T}\right)\right]^{-\frac{1}{2}} = (B)^{-\frac{1}{2}} \cdot \left(1 - \frac{T_0}{T}\right)$$

Equation 2-4

X = the studied property (in this case conductivity)

B = constant

A VFT dependence should be a straight line with non-zero intercept. Multiple VFT dependencies can be easily distinguished as an intersection of straight lines as observed in the inset of Figure 30.

In liquids with strong non-Arrhenius temperature variations of relaxation time, characteristic changes in the relaxation behaviour are usually observed;

(i) At high temperatures it generally follows Arrhenius law;

(ii) At a certain temperature, T_A, it follows VFT dependence,

(iii) At some point, T_B, between T_A and T_g it crosses to a second VFT dependence.[20] T_B is in the range ~ 1.2 – 1.5 T_g.[27]

(iv) At T_g the VFT temperature dependence crosses to Arrhenius behaviour.

The origin of T_B has been a point of much discussion, however, it is widely accepted that T_B is the temperature below which cooperativity becomes a crucial factor and where the behaviour of the glass-forming materials when undergoing a phase transition from liquid state to glassy sate starts to play a key role in the molecular dynamics.[20]

As seen in Figure 30, one VFT equation was able to satisfactorily fit the experimental data at high temperatures after which a second VFT is needed to accurately fit the super-cooled region. The exact temperature at which this crossover from one VFT to another occurs could be determined using Stickel analysis (inset of Figure 30, T_{cross}) and is 1.2 T_g. This is in contrast to the single VFT temperature dependence of $[C_4Mim]_2[Co(NCS)_4]$, reported by Hansel-Bielowka *et al.*[20]

Furthermore, as the glassy state is approached we see a clear deviation, decoupling from VFT to Arrhenius dependence. From this the glass transition temperature can be extracted.

Deviations from Arrhenius-type behaviour provide information on the fragility of the glass-formers.[28] The steepness index is generally used to determine the fragility (m) (Equation 2-5)[27] from which the VFT parameters and glass transition temperature must to be known.

$$m = \frac{B}{2.303}\frac{T_g}{\left(T_g - T_0\right)^2}$$

Equation 2-5

B = constant ($D*T_0$)

T_0 = the temperature usually regarded as the "ideal" glass temperature.

B and T_0 can be obtained from VFT fitting data.

Strong liquids exhibit near Arrhenius temperature dependence, whereas, fragile liquids generally display VFT behaviour.[29] In the studied case, $[C_4Mim][SCN]$ $Co(NCS)_2$ (5:1) can be described as a fragile liquid (Table 5).

Table 5. VFT parameters along with the calculated fragility.

$[C_4Mim]_2[Co(NCS)_4]$ + 3$[C_4Mim][SCN]$	**D**	**T_0**	**T_g (k)**	**m**
	8.69	165.83	205.41	82

2.3.5.1.2 Temperature dependence of conductivity relaxation times

Upon analysis of the $\log\tau_\sigma(T^{-1})$ we observe that as the temperature is increased τ_σ decreases in keeping with the lowering of viscosity and therefore enhanced mobility of ions. The temperature dependence of conductivity relaxation time follows VFT behaviour but a clear decoupling from VFT to Arrhenius type behaviour is observed in the low-temperature region. This decoupling is commonly associated with the glass transition (T_g).

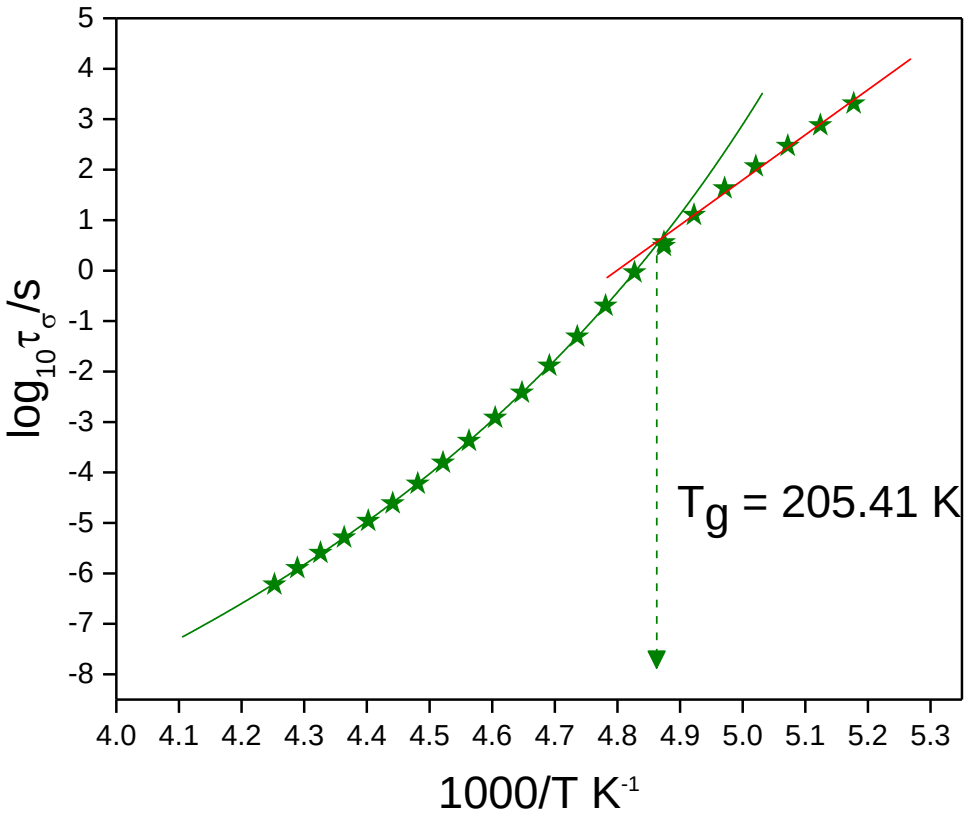

Figure 31. Temperature dependence on relaxation time.

Mapping both the conductivity and conductivity relaxation times to one graph we can obtain data over very wide temperature ranges *i.e.* the liquid, supercooled and glassy state (Figure 32). As clearly visible, there is a decoupling in both the conductivity and conductivity relaxation times in the low temperature region which is indicative of the glass transition.

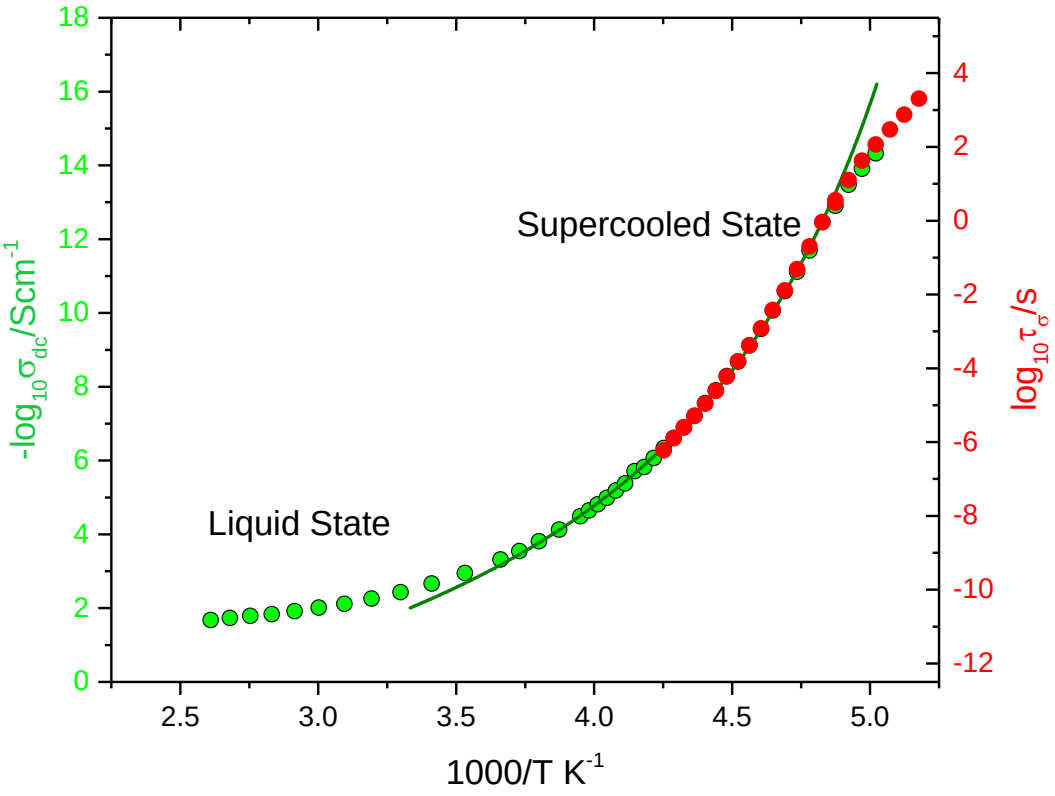

Figure 32. Combined plot of temperature dependence on conductivity and relaxation times.

The same method of analysis was applied to mole ratios; 2:1, 3:1, 4:1, 6:1 and 10:1. The temperature dependence of the conductivity relaxation times for all investigated systems could then be plotted onto one graph as shown in Figure 33.

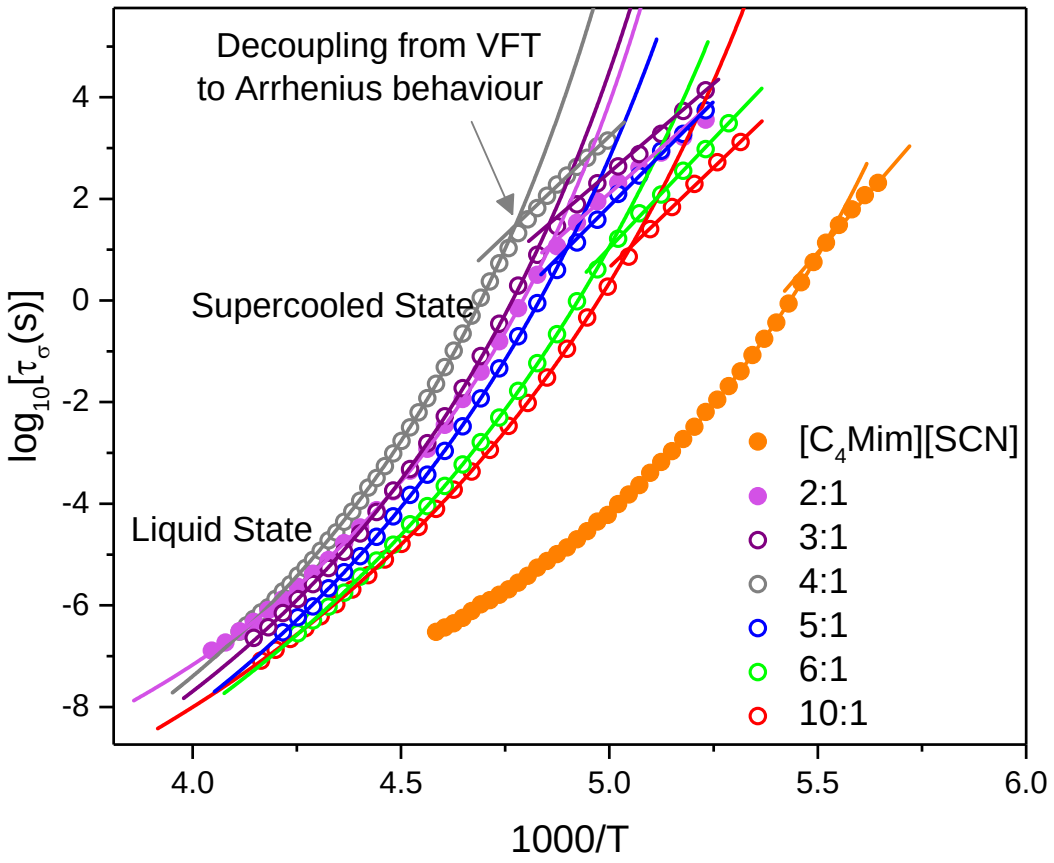

Figure 33. Conductivity relaxation times as a function of temperature for the $[C_4Mim][SCN] + Co(NCS)_2$ series.

The same pattern of behaviour discussed in detail for mole ratio 5:1 is observed in all systems. The difference in the spectra lies in the exact temperature of decoupling, which is different for each mole ratio and is a reflection of the differences in the glass transition temperatures.

With increasing concentration of ionic liquid from 2:1 we see a lowering of the glass transition temperature in all cases, with 4:1 being an exception. As the concentration of ionic liquid is increased the decoupling from VFT to Arrhenius dependence appears at lower temperatures. This may be explained by the fact that the excess ionic liquid

provides greater mobility (lower viscosity) and therefore takes longer to reach its new equilibrium state. The crossover linked to the glass transition could also be compared to the results obtained from calorimetric analysis using differential scanning calorimetry (Table 6). It must be noted that the crossover for VFT to Arrhenius is most pronounced in the cobalt based systems compared to the neat ionic liquid, [C_4Mim][SCN]. In addition, the conductivity is higher for the neat ionic liquid system as a result of a lower viscosity.

Table 6. Glass transitions obtained from BDS and DSC measurements.

Complex	T_g BDS (K)	T_g DSC (K)
2:1	205.65	212.1
3:1	205.99	209.71
4:1	209.45	216.6
5:1	208.85	212.45
6:1	200.07	212.69
10:1	197.87	201.2
[C_4Mim][SCN]	181.48	184.82

2.3.5.1.3 Viscosity

Approaching the glass transition the viscosity is seen to increase in a narrow temperature range. The viscosity (η) of sample $[C_4Mim][SCN] + Co(NCS)_2$ (10:1) was measured in the temperature range 200 - 400 K using rheology. The aim here was to relate the data obtained from the thermorheological transport properties of $[C_4Mim][SCN] + Co(NCS)_2$ (10:1) to the dielectric behaviour *i.e.* conductivity relaxation. In doing so, simultaneous information about the mechanical behaviour and structural changes can be obtained. The data of temperature dependence of η follows a similar trend to that gathered for the dielectric relaxation times (Figure 34).

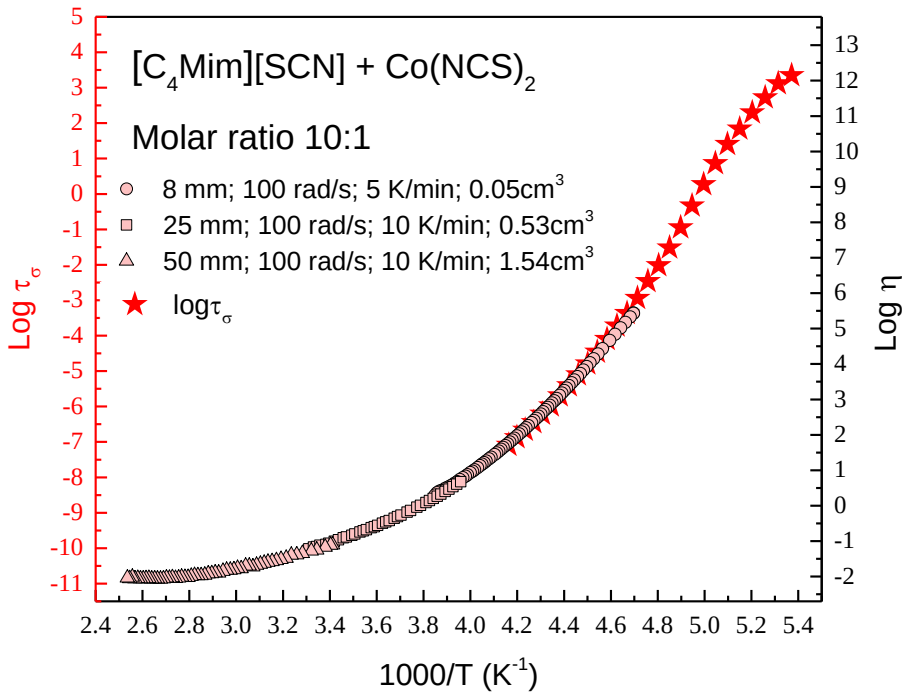

Figure 34. Relaxation map comparing the conductivity relaxation (red stars) to viscosity for $[C_4Mim][SCN] + Co(NCS)_2$ (10:1).

The dynamical shear modulus loss (G") was measured at several temperatures above T_g and compared to the dielectric modulus loss peak (M") (Figure 35). The shape of

both curves are similar although the peak in the dynamical shear modulus spectra is slightly broader. To parameterise the shape the spectra were fitted using the Kohlrausch and Williams and Watts equation.[30]

$$\phi(t) = \exp\left[-\left(\frac{t}{\tau_\sigma}\right)^{\beta_{KWW}}\right]$$

Equation 2-6

t = time

τ_σ = is the conductivity relaxation time

β_{KWW} ($0 < \beta_{KWW} < 1$) = stretch parameter, related to the width of the relaxation peak.

The broader more asymmetric the peak is, the lower the value of β_{KWW}. The value of β_{KWW} is equal to 0.5 and 0.37 for M" and G", respectively. This is an indication of slight differences in the conductivity relaxation and structural relaxation times.

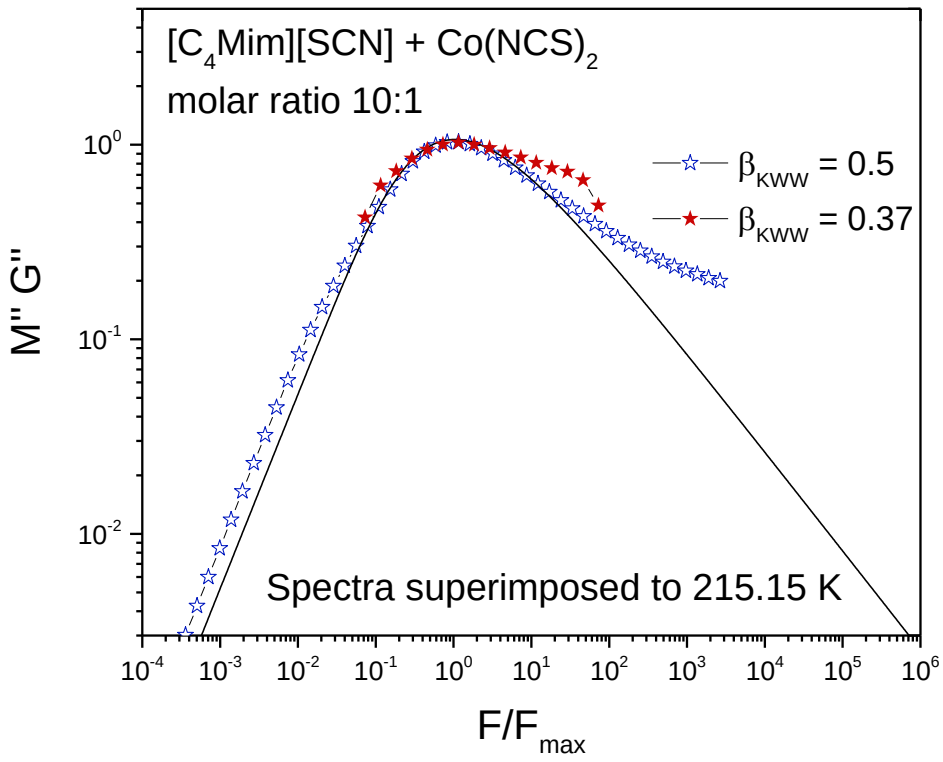

Figure 35. Comparing the mechanical loss modulus (G") to the imaginary part of dielectric modulus M".

2.3.5.2 Effect of pressure

Although rapid cooling is probably the simplest method for inducing changes in the magnetic properties of the ionic liquid, it does not mean that this is the only route. As previously discussed, Garciá -Saiz et al.[12] explored the properties of $[C_2Mim][FeCl_4]$ showing a transition from antiferromagnetic to ferromagnetic three dimensional ordering under hydrostatic pressure. In addition, the work by Abkemeier *et al.*[18] clearly demonstrates the potential for pressure induced coordination changes. Tidey *et al.*[31] have reviewed the effects of pressure on different coordination complexes. Pressure was seen to influence factors such as intermolecular distances which is accompanied by intramolecular changes to geometry and coordination number.

Moreover, in relation to the glass transition, a liquid can be vitrified by keeping temperature constant and increasing the pressure.[32] Like the effects of cooling, dramatic changes in the relaxation dynamics are observed in the vicinity of the glass transition. In the vicinity of the T_g, again the relaxation behaviour may be fitted using the VFT equation, and the non-Arrhenius behaviour of the isobaric dependence τ_α *(T)* is measured by determining the isobaric fragility. Furthermore, as the intermolecular distances are influenced by pressure, the α-relaxation can be considered as a volume-activated process.[32]

The activation volume ($\Delta V^{\#}$) can be obtained using Equation 2-7 and is a function of T and P.

$$\Delta V^{\#} = RT \ln(10) \left(\frac{\partial log \tau_{\alpha}}{\partial P}\right)_T$$

Equation 2-7

To analyse the effects of pressure, different isotherms (IT) were measured in a pressure range 0 – 600 mPa. The effects of pressure on the conductivity behaviour of $[C_4Mim][SCN] + Co(NCS)_2$ (10:1) was analysed at IT = -40 °C, shown in Figure 36.

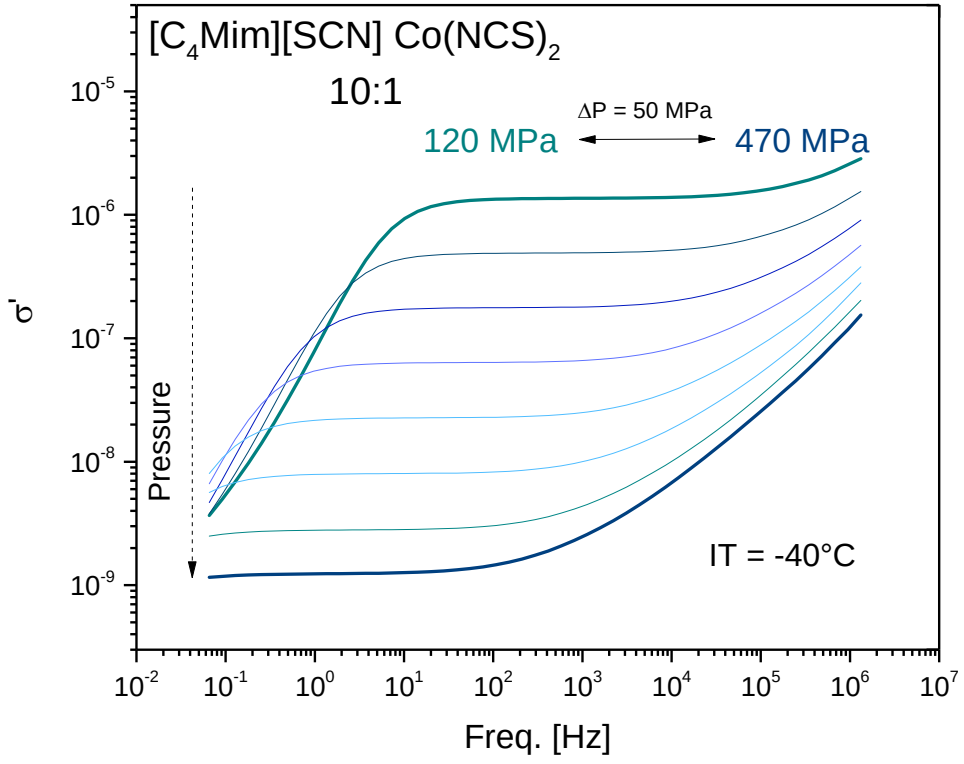

Figure 36. Conductivity behaviour as a function of frequency in the pressure range 120 – 470 MPa.

Upon elevating the pressure, we see that the conductivity moves towards lower frequencies. This is similar to the behaviour observed during isobaric cooling. To look at this effect in more detail the pressure dependence on the conductivity behaviour was analysed for isotherms -10, -30, -40 and -50 °C (Figure 37).

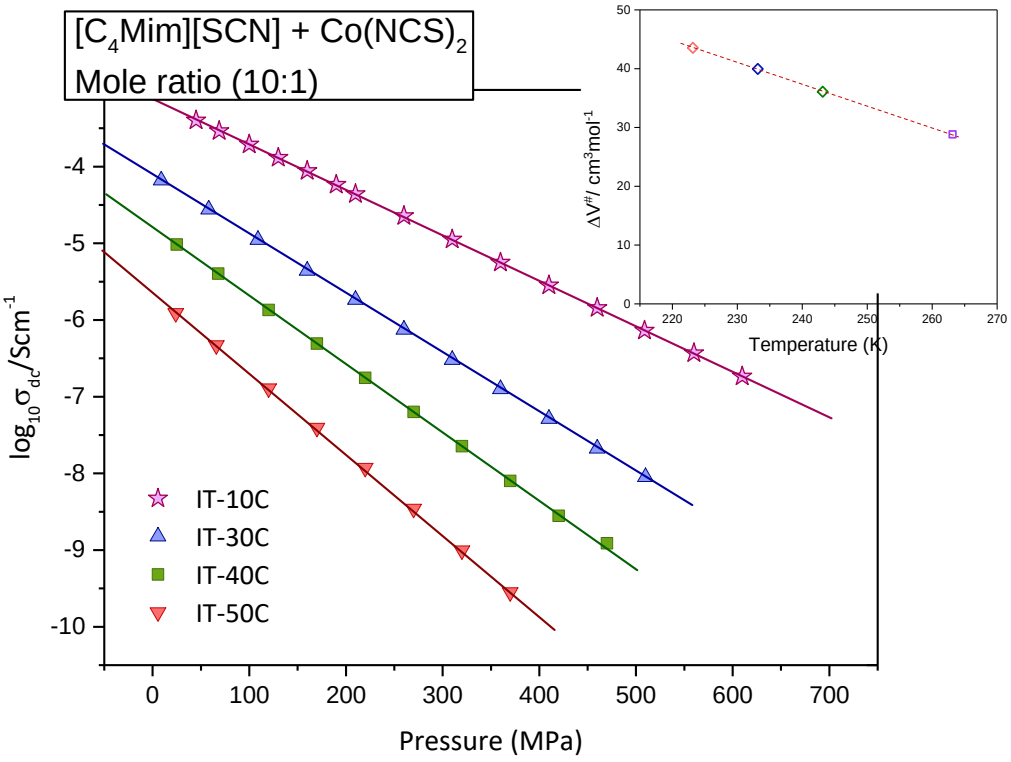

Figure 37. Pressure dependence on the conductivity behaviour was analysed for isotherms -10, -30, -40 and -50 °C.

In this graph it is clear that as the temperature is decreased from -10 to -50 °C, the conductivity decreases. In a similar way, as the pressure is increased the conductivity decreases in a linear fashion. From this the activation volume can be determined. The inset of Figure 37 shows the activation volume coefficients determined for $[C_4Mim][SCN] + Co(NCS)_2$ (10:1) which is seen to decrease with increasing temperature (from 43.5 cm^3/mol at 223 K to 28.8 cm^3/mol at 263 K) and is believed

to be specific feature of the dynamics of supercooled liquids and amorphous polymers (Table 7).

Table 7. Activation volume of $[C_4Mim][SCN] + Co(NCS)_2$ (10:1).

Temperature (K)	$\Delta V^{\#}$ (cm^3mol^{-1})
263	28.82
243	36.07
233	39.94
223	43.54

It must be noted, that in the data presented thus far, that there is no evidence of the changing coordination of cobalt visible in the conductivity behaviour under the various temperature and pressure conditions investigated. In the next section, we look at the effect of changing the cation. A bulky trihexyl(tetradecyl)phosphonium thiocyanate, $[P_{666\,14}][SCN]$, in different mole ratios of $Co(NCS)_2$ was used as a comparison.

2.3.6 $[P_{666\,14}]^+$ cation

2.3.6.1 Effect of temperature

In a similar manner, the results of $[P_{666\,14}][SCN]$ + $Co(NCS)_2$ series were analysed. The frequency-dependent conductivity plot of $[P_{666\,14}][SCN]$ + $Co(NCS)_2$ (molar ratio 10:1) is presented in Figure 38.

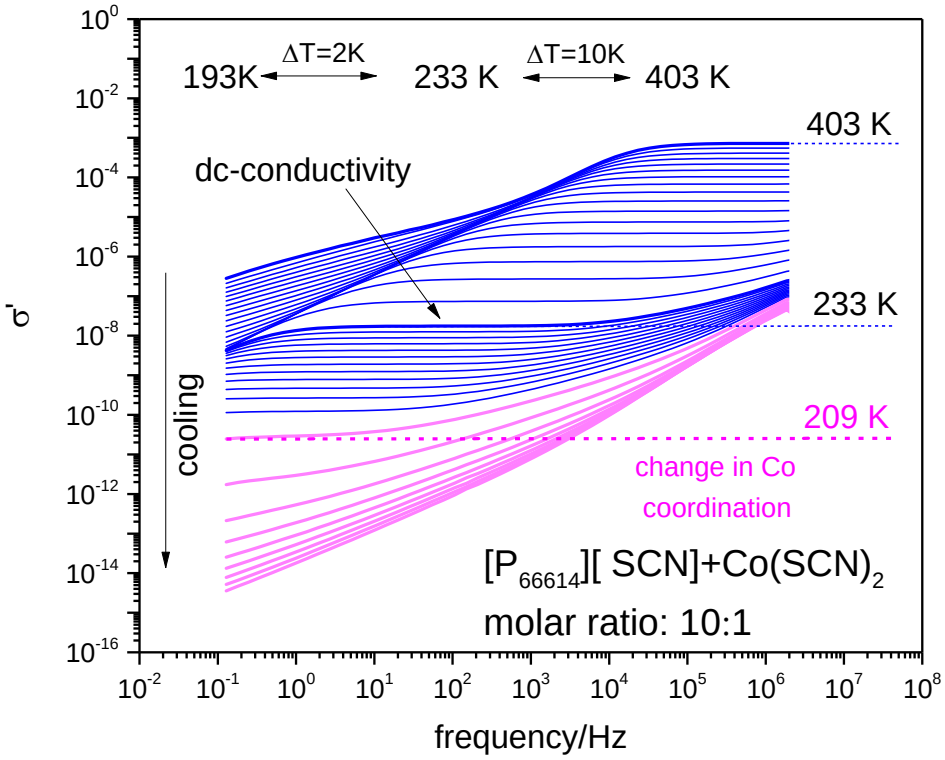

Figure 38. Conductivity behaviour of $Co(NCS)_2$ in excess ionic liquid $[P_{666\,14}][SCN]$ (1:10) presented over a frequency range from 10^{-1} to 10^{6} Hz.

As can be easily seen, the real part of the complex conductivity function (σ') is characterized by a frequency independent part which gives directly the dc-conductivity value of the studied system. From this graph, it is apparent that as the ionic liquid system is cooled, a shift in the dc-conductivity to lower values is observed.

This gradual change is in keeping with the effects of cooling seen in $[C_4Mim][SCN]$ + $Co(NCS)_2$ systems, and it is connected with suppressed mobility of ions. However, in contrast to other ionic conductors and $[C_4Mim][SCN]$ + $Co(NCS)_2$ systems at 209 K, a pronounced drop in dc-conductivity is observed.

Importantly, the shape of σ'(f) spectra as well as the value of dc-conductivity recorded during the subsequent heating from 193 K are exactly the same as that obtained during the first (cooling) step. Therefore, one can certainly say that the observed effect is reversible. To characterize this phenomenon in more detail, the values of σ_{dc} are plotted as a function of inverse temperature in Figure 39.

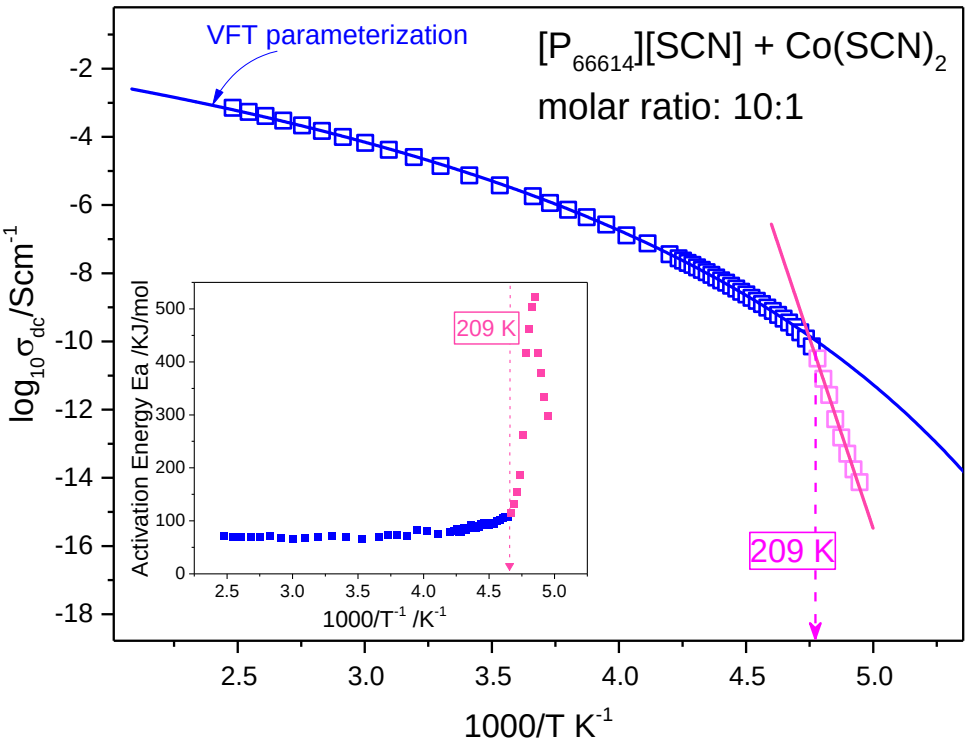

Figure 39. Temperature dependence of dc-conductivity presented in the temperature range 403−202 K. Solid line is the VFT with the following parameters: log σ_∞ = −0.44, D = 13.32, and T_0 = 130. Inset panel presents the activation energy as a function of inverse of temperature.

A number of points can be taken from this graph. The first is that upon cooling the conductivity data reveals non-Arrhenius behaviour that can be well-parametrized by means of the Vogel−Fulcher−Tammann (VFT) equation.[24–26]

The second, conditions where the σ'(f) spectra become much more sensitive on cooling, an evident deviation of σ_{dc}(T) points from the VFT law is observed. The fragility could be calculated and is equal to 26.78.

From first sight, such behaviour could be related to liquid−glass transition. However, according to the literature, generally Tg of ionic glass-formers is manifested by the characteristic crossover of temperature dependences of σ_{dc} from VFT-like to Arrhenius behaviour around 10^{-15} S/cm (σ_{dc} at T_g can be higher in the case of protic ionic liquids and solids[33,34]). Additionally, the activation energy (Ea) (as well as entropy) of ion dynamics in the glassy region is always much lower than Ea typical for the supercooled liquid state.[35]

$$E_a = -2.303R \left.\frac{\partial log\sigma_{dc}}{\partial(T^{-1})}\right|_P = 0.1\ MPa$$

Equation 2-8

As can be seen in the inset to Figure 39, the activation energy parameter of $[P_{666\,14}][SCN] + Co(NCS)_2$ calculated from the equation drastically increases above 209 K, and it reaches values even 5-times higher than those determined in the supercooled region. Therefore, one can surely say that the observed change in σ_{dc} behaviour is not a manifestation of the liquid−glass transition.

This is additionally confirmed by results obtained from differential scanning calorimetry studies. The DSC thermogram, reported in 2.3.3, recorded during cooling of examined IL, from 375 K down to 133 K with a rate of 10 K/min, reveals a small exothermic peak around 210 K. Note that at the same temperature the dramatic drop of σ_{dc} occurs.

The closer inspection of DSC data also exhibits the existence of a step-like change in the heat flow curve at 155 K. This effect can be associated with the liquid−glass transition of studied IL (see upper panel of Figure 40). On the other hand, during the subsequent heating of the studied IL, a small endothermic peak appears.

Because both cooling and heating scans of $[P_{666\,14}][SCN] + Co(NCS)_2$ (mole ratio 10:1) did not reveal any signs of cold crystallization, one can state that it remains disordered throughout the entire examined temperature range. This has been also confirmed by the results of the XRD method. As presented in the lower panel of Figure 40 the XRD data collected over a wide temperature range take the form of broad halo without any Bragg peaks that are characteristic for the crystalline state. Taking these facts together, one can state that the sharp change in conductivity of the $[P_{666\,14}][SCN] + Co(NCS)_2$ (mole ratio 10:1) sample observed at 209 K is a result of a reversible change in the coordination of the cobalt centre.

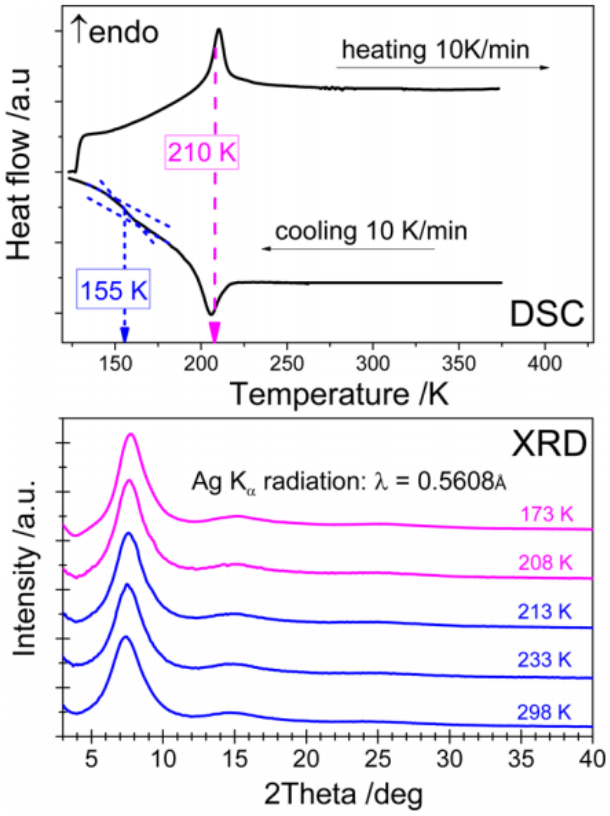

Figure 40. Results of DSC measurements (upper panel) and XRD measurements (lower panel).

As previously reported for other magnetic ionic systems, at room temperature the cobalt(II) centre preferably forms a tetrahedral complex.[16] However, if an excess of ionic liquid is added and the temperature is decreased, there is the possibility for the cobalt centre to change its equilibrium position and rearrange to form an octahedral complex. Because the size of the octahedral complex is increased and its charge changes from −2 (tetrahedral) to −4 (octahedral), its lower mobility compared with the tetrahedral form may be expected. Therefore, cobalt changing from tetrahedral to octahedral could result in a lowering of conductivity, as suggested by Figure 39. The same pattern of behaviour was observed in mole ratios 4:1 and 5:1 as observed in Figure 41.

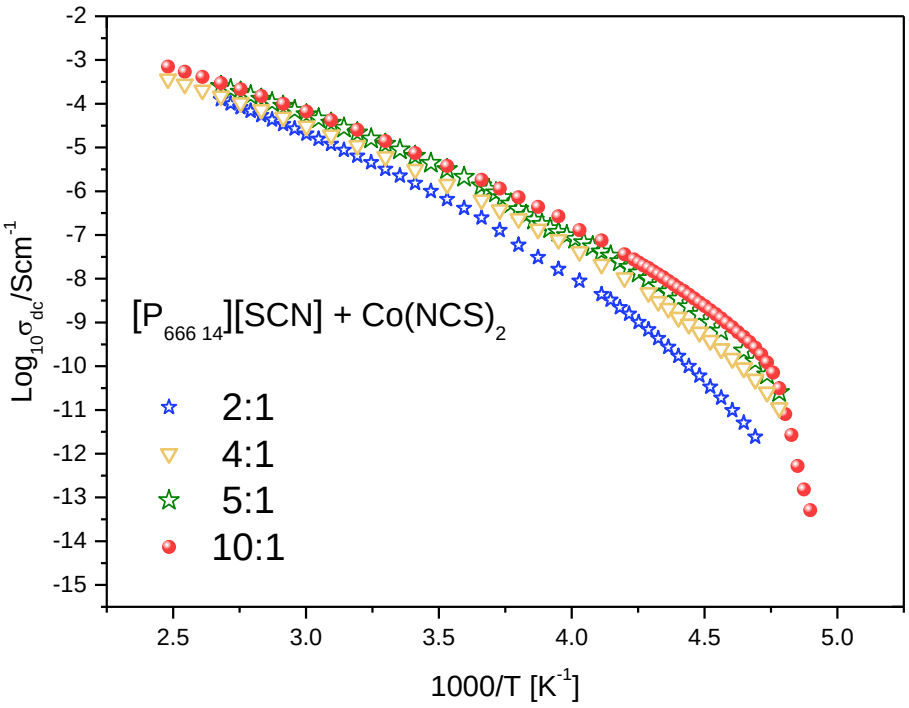

Figure 41. Spectra of temperature dependence on conductivity for $[P_{666\ 14}][SCN] + Co(NCS)_2$ mole ratios (2:1, 4:1, 5:1 and 10:1).

Mole ratio $[P_{666\ 14}][SCN] + Co(NCS)_2$ (2:1) was analysed further as a result of a secondary α- relaxation peak visible in the modulus spectrum (Figure 42). Furthermore, the sudden jump in conductivity in the low temperature region as seen for mole ratios 4:1, 5:1 and 10:1 is not evident in the conductivity representation. Bearing in mind that a mole ratio of 4:1 or higher is needed for low-temperature coordination changes in the cobalt system, this is not surprising.

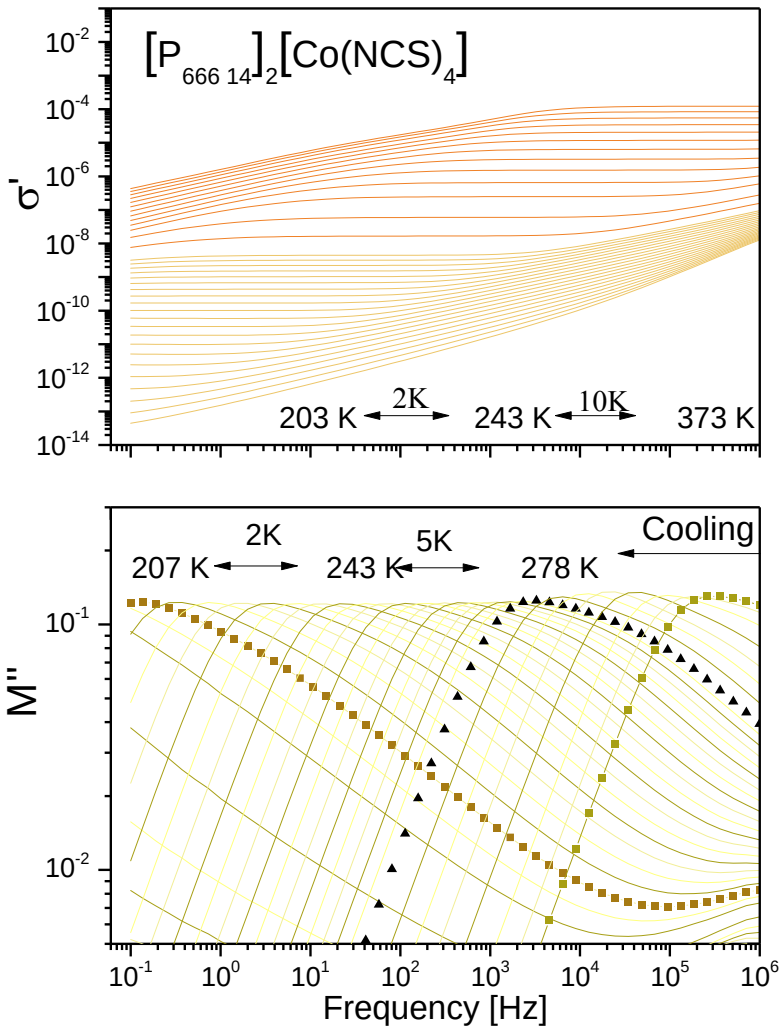

Figure 42. Sigma and modulus representation of $[P_{666\,14}][SCN]$ + $Co(NCS)_2$ (2:1).

The temperature dependence of conductivity relaxation time was analysed showing clearly the two relaxation modes observed in M'' representation.

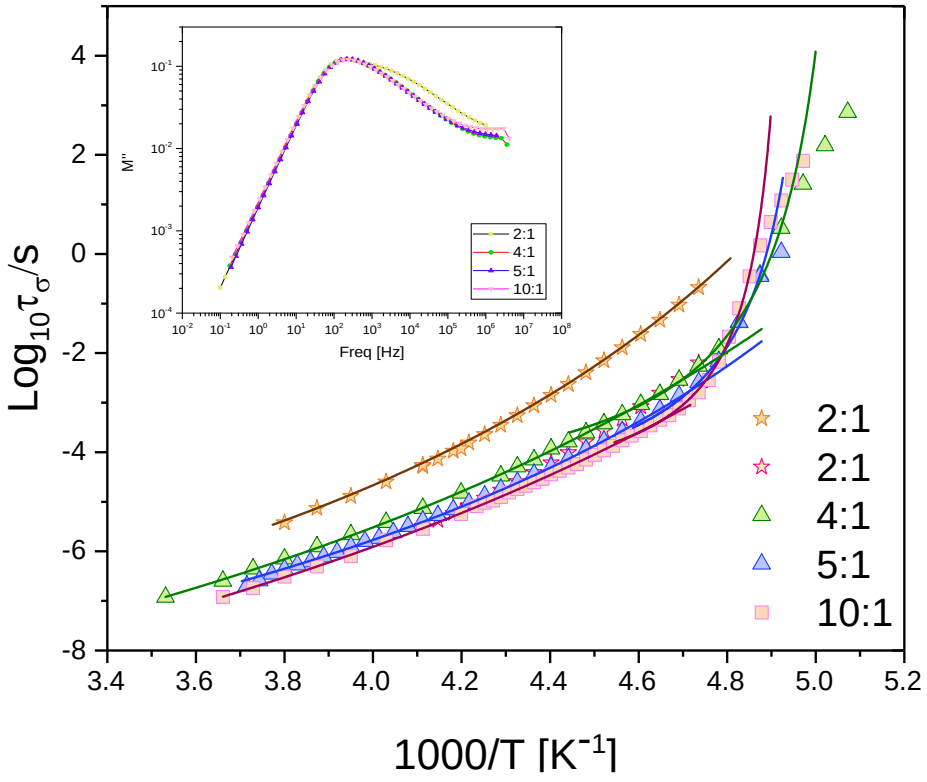

Figure 43. Conductivity relaxation times as a function of temperature for $[P_{666\,14}][SCN]$ + $Co(NCS)_2$ (2:1, 4:1, 5:1 and 10:1).

To see whether this is also evident in the structural behaviour, viscosity measurements were carried out using rheology (Figure 44). The rheological measurements are important in terms of developing a link between the molecular structure and physicochemical properties.

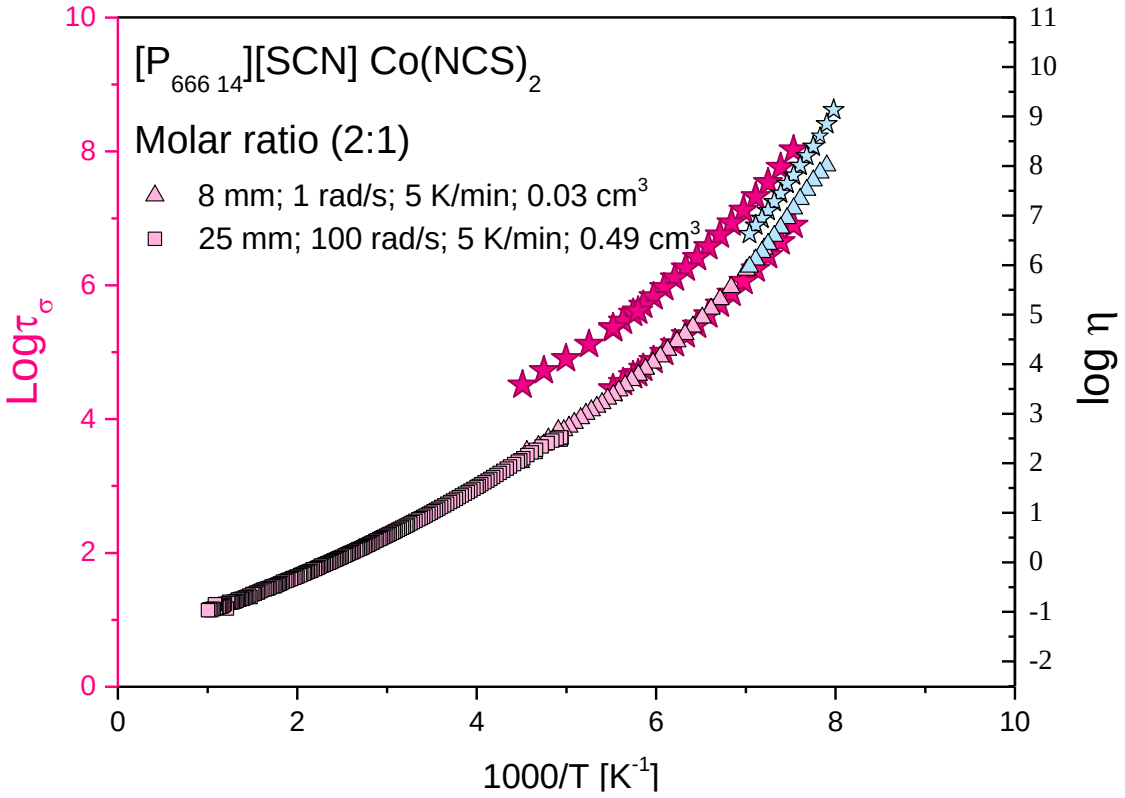

Figure 44. Relaxation map comparing the conductivity relaxation times to viscosity for $[P_{666\ 14}][SCN]:Co(NCS)_2$ (2:1).

As visible in Figure 44, the same pattern of behaviour is seen in the viscosity as was observed for the conductivity relaxation. The question remains *"What is the origin of this secondary process?".*

The most plausible explanation is if we take into account the types of anion and cation interactions in this system. In the phosphonium based systems the positive charge is mainly localised on the phosphorus atom and on the alpha carbon moieties, the overall cohesive energy of this solution is mainly driven by van der Waals interactions caused by the long alkyl chains as can be observed in Figure 45. Therefore, $[P_{666\ 14}]_2[Co(NCS)_4]$ is governed by two relaxation processes, namely, (i) van der Waals and (ii) Coulombic interactions. In molar ratio $[P_{666\ 14}][SCN] + Co(NCS)_2$ (2:1), a higher

concentration of cobalt leads to higher Coulombic interactions than would be in ratios (4:1 or higher). The cobalt movement is restricted between the bulky $[P_{666\ 14}]^+$ cations. In ratios 4:1, the higher concentration of $[P_{666\ 14}][SCN]$ leads to interactions which are now mainly governed by van der Waals interactions. As a result, the van der Waals interactions dominate, and one alpha process is visible.

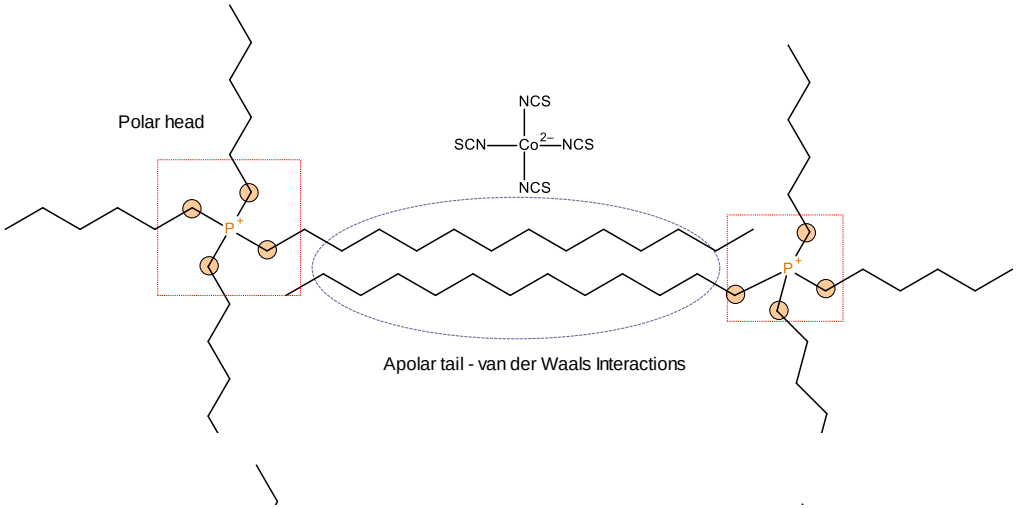

Figure 45. Cohesive energy is driven by both van der Waals and Coulombic interactions in $[P_{666\ 14}]_2[Co(NCS)_4]$.

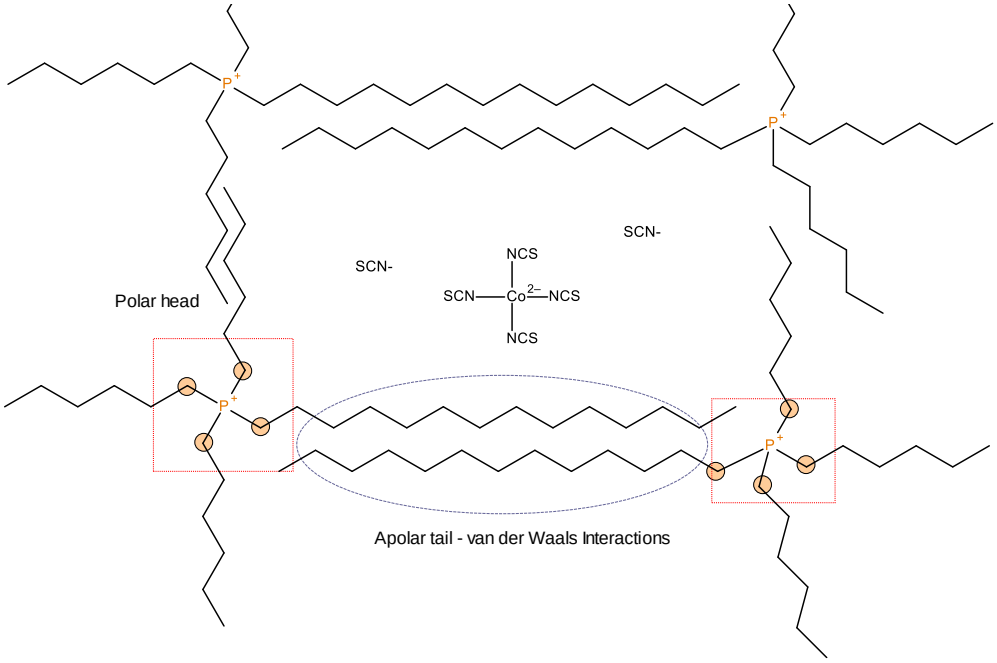

Figure 46. Cohesive energy is driven by van der Waals interactions in $[P_{666\ 14}]_2[Co(NCS)_4]$ + $2[P_{666\ 14}][SCN]$.

2.3.6.2 Effects of pressure

One may question the possibility of manipulating the cobalt coordination by means of isothermal compression. To shed more light on this issue, high-pressure BDS experiments of $[P_{666\,14}][SCN] + Co(NCS)_2$ (10:1) mixture were performed isothermally at 225, 235, and 245 K. Representative results are presented in Figure 47.

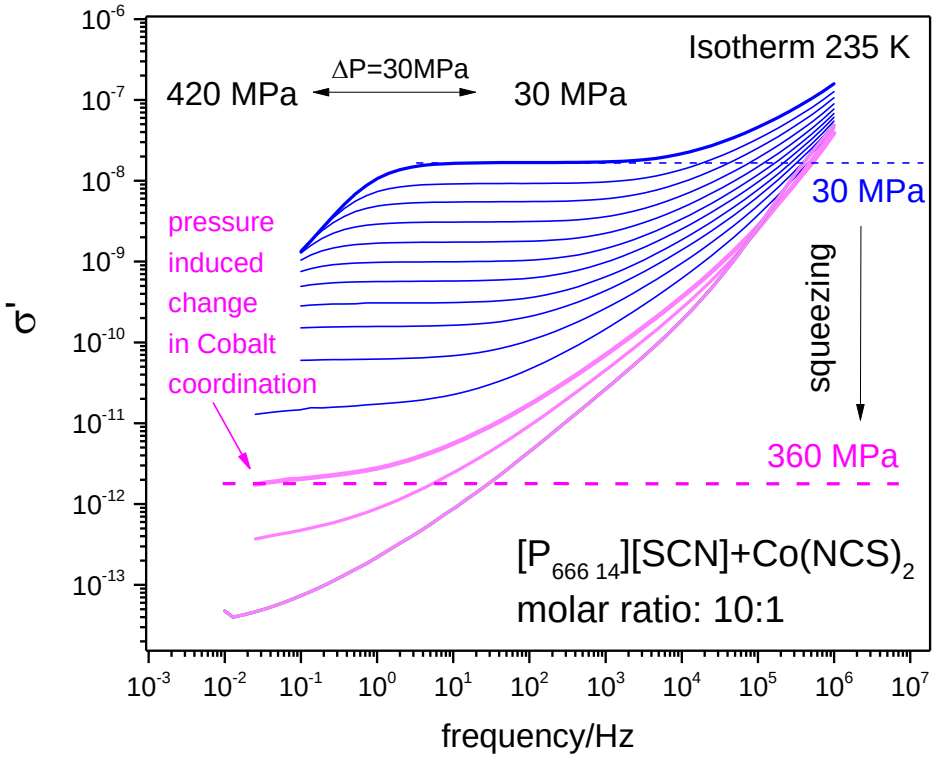

Figure 47. Dielectric spectrum presented in conductivity representation in the form of frequency-dependent data under pressure.

Interestingly, when $[P_{666\,14}][SCN] + Co(NCS)_2$ (mole ratio 10:1) is compressed, the same pattern of σ'(f) behaviour as during isobaric cooling is observed, i.e., despite the same pressure step, suddenly the σ_{dc} value gets markedly lower. This is clearly visible in Figure 48 as a characteristic crossover of $\sigma_{dc}(P)$ experimental points from one linear behaviour to another. Because in both these regions the dc-conductivity

varies with pressure in a linear fashion, it can be well-parametrized by means of a volume-activated law:

$$log\ \sigma_{dc}(P) = \log \sigma_0 + \frac{P\Delta V^{\#}}{RT}$$

Equation 2-9

log σ_0 being the value of dc-conductivity at atmospheric pressure,

R the universal gas constant,

$\Delta V^{\#}$ an apparent activation volume (commonly related to the local volume expansion required for ionic transport[34,36]).

As one can see in the inset to Figure 48, the activation volume coefficients determined for $[P_{666\ 14}][SCN] + Co(NCS)_2$ (mole ratio 10:1) system in the $P < P_{cross}$ range is relatively low, thereby reflecting the weak change in dc-conductivity of the studied IL with squeezing. Moreover, it was found to decrease with increasing temperature (from 48 cm^3/mol at 225 K to 30 cm^3/mol at 245 K), which is typical for many other ionic and non-ionized materials and is considered as a specific feature of the dynamics of supercooled liquids and amorphous polymers.

However, much more important information coming from the inset to Figure 48 is the markedly higher value of the apparent activation volume determined above the P_{cross}. Because $\Delta V^{\#}$ is defined as the local volume required for ionic transport, one can expect that the molecular dimension of conducting species in the region above P_{cross} should be larger than that below P_{cross}. Such a scenario comes true only if the switching of cobalt coordination from tetrahedral $[Co(NCS)_4]^{2-}$ to octahedral

$[Co(NCS)_6]^{4-}$ occurs. This is a clear proof that the kink of the σ_{dc}–P as well as σ_{dc}–T curves can be treated as a manifestation of changes in the coordination of a cobalt isothiocyanate complex.

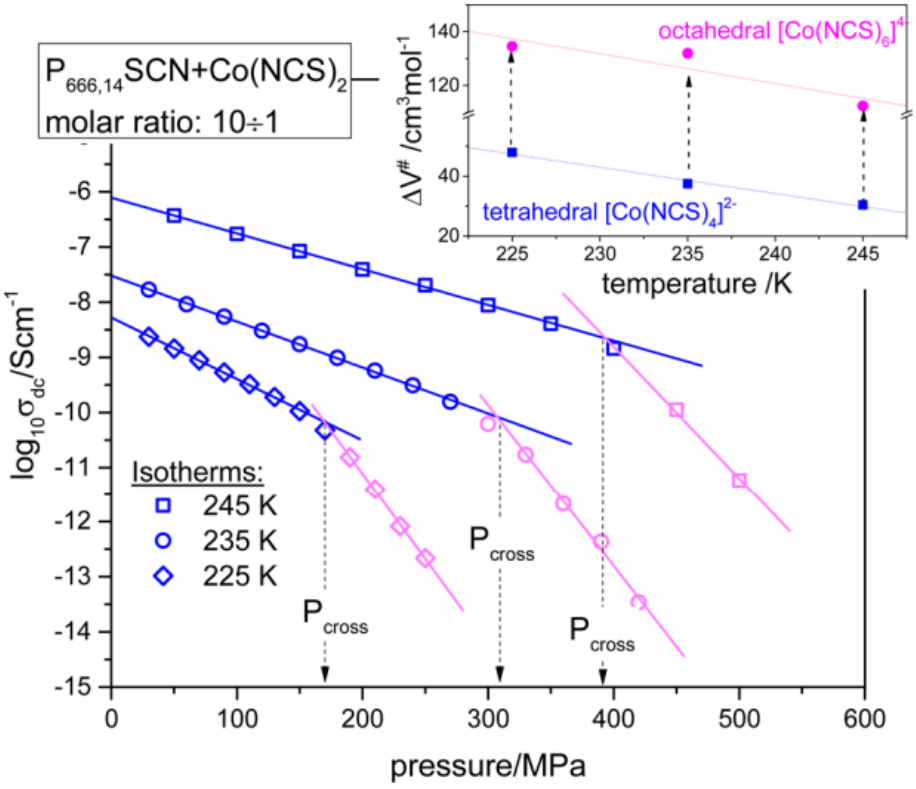

Figure 48. Effects of pressure on dc-conductivity behaviour of $[P_{666\,14}][SCN] + Co(NCS)_2$ (10:1). The inset presents the temperature dependence of activation volume parameter.

To determine the phase transition line between the tetrahedral and octahedral cobalt complex in the next step, the crossover temperature, T_{cross}, is plotted as a function of pressure.

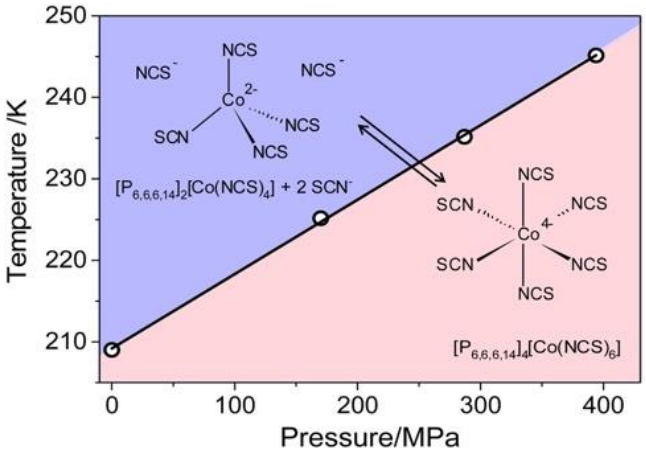

Figure 49. Phase diagram of $[P_{666\ 14}][SCN] + Co(NCS)_2$ (4:1)

As depicted in Figure 49, the T_{cross} rapidly increases with squeezing in linear fashion. Thus, the slope of $T_{cross}(P)$ curve, equal to 0.09 K/MPa, reflects the pressure sensitivity of Co^{2+} coordination changes. It means that an increase of pressure in the order of 100 MPa raises T_{cross} by 9 K. Consequently, to realize the coordination change of cobalt in the examined MIL under high-pressure conditions, temperatures as low as 209 K are no longer required.

2.4 Discussion

Variations in the conductivity behaviour in the two cationic, $[P_{666\,14}]^+$ and $[C_4Mim]^+$, systems are evident. First, we observe that the conductivity behaviour of the $[C_4Mim]^+$ system decreases, as expected, with a decrease in temperature and/or applied pressure . On the other hand, in the $[P_{666\,14}]^+$ system, a dramatic decrease in the conductivity behaviour is observed upon cooling and applied pressure. In this chapter, we first asked the question; *"Is it possible to observe transitions, in the form of metal complexation from tetrahedral to octahedral, by investigating the physical properties of the studied systems?".* In light of the measurements carried out and the data obtained, interesting conclusions can be drawn and to some extent we can say the answer to the question *vide supra* is affirmative.

To comprehend the differences in the data of these systems, we look further into the cation and anion interactions of the studied systems, presented in Figure 50.

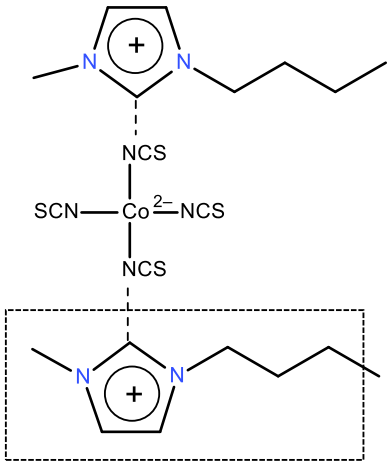

- Charge Delocalisation
- Cohesive energy is governed by the Coulombic interactions
- Globular solution

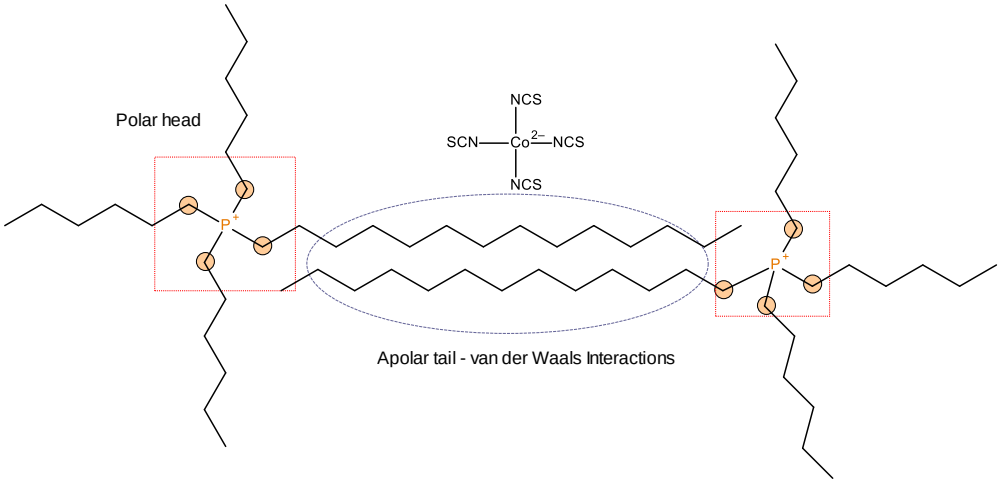

Figure 50. Structures and interactions governing the MILs; $[C_4Mim]_2[Co(NCS)_4]$ and $[P_{666\ 14}]_2[Co(NCS)_4]$.

The nature of the cation interactions differs markedly in both systems. The cohesive energy of the relatively small $[C_4Mim]^+$ cation, which has a well delocalised positive charge on each atom of this cation, is largely governed by Coulombic interactions. Based on the globular molecular shape and mobile nature of the anion and cation in solution, changes in the coordination of the cobalt centre from tetrahedral to octahedral upon cooling may not have a dramatic effect on the conductivity of the solution. In addition, any change in the pressure in the imidazolium system does not seem to dramatically change the variation of its transport properties (no crossover was observed). As observed in the data presented, the conductivity decreases monotonously with temperature and pressure. This result is to be expected and is characteristic of the slowing down of the motions of ions upon cooling or based on a decrease in the solution free volume with the applied pressure. According to the collected experimental data and based on the size of each ion and the nature of interactions (mainly Coulombic) in the imidazolium-based solution, one can

appreciate that there is space for the coordination reorganisation of the cobalt complex even by applying external stimuli, such as by decreasing the temperature and/or increasing the pressure. In other words, coordination changes from tetrahedral to octahedral may not be observed when using BDS as a technique.

On the other hand, in the phosphonium based systems where the positive charge is mainly localised on the phosphorus atom and on the alpha carbon moieties, the overall cohesive energy of this solution is mainly driven by van der Waals interactions caused by the long alkyl chains. Owing to the long alkyl chains, the charged parts of the system become further apart and segregated polar and non-polar domains are evident. This has been observed previously by Santos *et al.*[37] in varying the alkyl chain length in imidazolium ILs $[C_nMim][NTf_2]$ (n = 2 – 8), for example.

In the case of the system based on a mole ratio $[P_{666\,14}][SCN] + Co(NCS)_2$ (2:1), we have seen a combination of Coulombic and van der Waals interactions governing the dielectric behaviour, evident in the two visible alpha processes. The conductivity behaviour of $[P_{666\,14}][SCN] + Co(NCS)_2$ (2:1) is seen to decrease with temperature in a step like fashion, as expected.

Even more important is picturing the system, $[P_{666\,14}]_2[Co(NCS)_4]$ with excess ionic liquid $[P_{666\,14}][SCN]$ (Figure 51). Here, the increased concentration of $[P_{666\,14}][SCN]$ means that the Coulombic interactions are reduced and the van der Waals interactions dominate. Relating this to the data obtained we can surmise that the cobalt will be fixed somewhat between the bulky $[P_{666\,14}]^+$ cations with little room for its reorganisation (Figure 51). In this sense, the knowledge of the free volume is crucial, such that, changes in the coordination around the cobalt can result in drastic

changes in the free volume of the system. This is never more evident than in the cases where the temperature was decreased, or more importantly when the system was compressed (Figure 39 and Figure 48). As the temperature was decreased coordination changes in the cobalt structure from tetrahedral to octahedral can occur if there is an excess of ionic liquid. In the phosphonium-based systems the cobalt is more confined in the structure with little room for the reorganisation of the solution caused by the cobalt coordination change. As the temperature decreases, the structure becomes essentially frozen meaning any reorganisational changes in the cobalt structure will become pronounced and result in dramatic changes in the conductivity of the solution. In addition, a pressure increase causes a decrease in the free volume, meaning the reorganisational space is reduced; however, the octahedral species require more space than tetrahedral ones, leading in fact to a huge effect of the coordination change on the activation volume of the solution. Such effects must lead to dramatic changes in the transport properties. This is reflected in the both the calculated free volume and activation energy observed above.

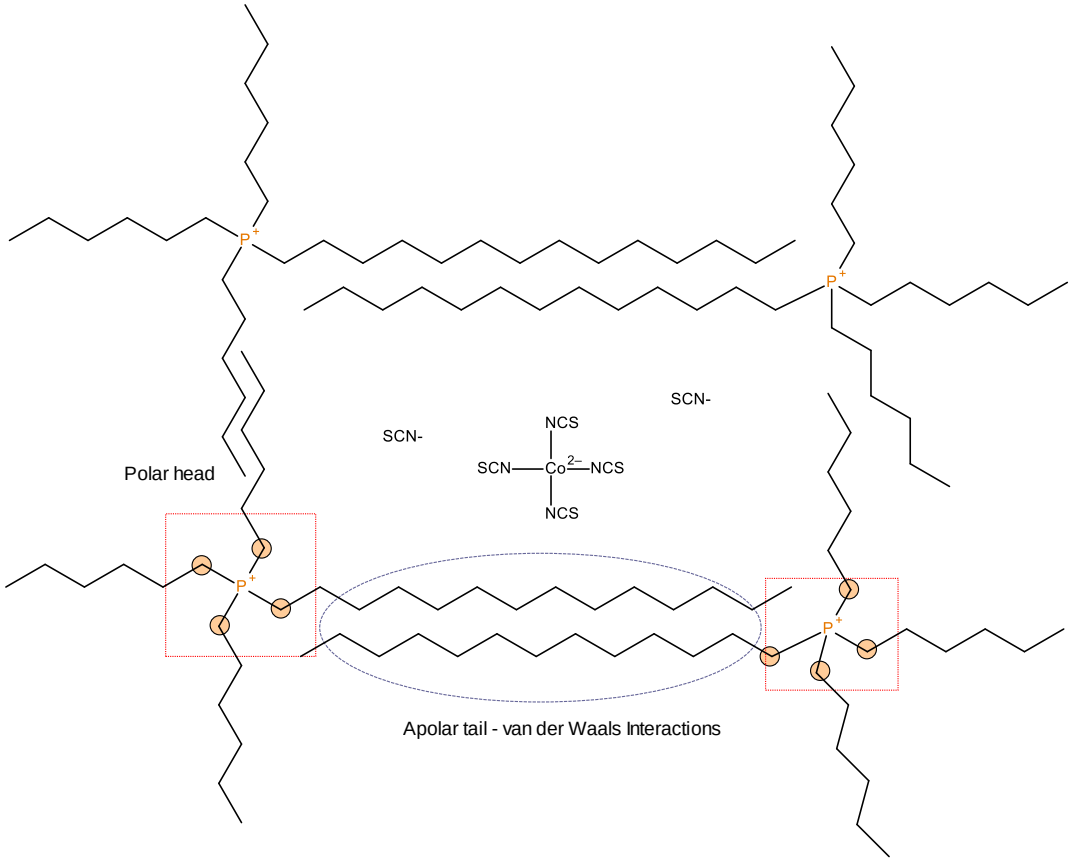

Figure 51. Structure of the $[P_{666\ 14}][SCN]$ + $Co(NCS)_2$ molar ratio (4:1), whereby, the cohesive energy is governed by the van der Waals interactions.

2.5 Conclusion

The molecular dynamics of $[C_4Mim][SCN] + Co(NCS)_2$ and $[P_{666\ 14}][SCN] + Co(NCS)_2$ in different mole ratios of ionic liquid to salt were investigated over very wide temperature and pressure ranges using broadband dielectric spectroscopy and rheology. The fragility of the ILs could be calculated and were seen to decrease with increasing cation size, from $[C_4Mim]^+$ to $[P_{666\ 14}]^+$. This could be rationalised according to Generalised Entropy Theory which suggest fragility is connected to the efficiency of molecular packing.[38,39] In combining rheological and dielectric measurements a link between the molecular reorientation and shear viscosity measurements could be made.

We asked the question; "*Is it possible to recognise changes in the structural properties of Co(II) from its conductivity behaviour?"*. As discussed, to some extent we can say the answer is affirmative.

The effects of temperature and pressure on inducing changes in the coordination of a cobalt isothiocyanate complex in a neat ionic liquid system was evident in the $[P_{666\ 14}][SCN] + Co(NCS)_2$ system (4:1 or higher). In this case we were also able to show the effects of hydrostatic pressure in the range of 0.1 − 600 MPa in inducing this change in coordination of Co(II). BDS was seen as a powerful and versatile tool to reveal stimuli responsive structural changes through the conductivity behaviour. However, it must be noted that this was very much cation dependent and this behaviour is governed by the cation and anion interactions in the systems.

2.6 Methods

2.6.1 Experimental

Potassium thiocyanate, KSCN; cobalt thiocyanate, $Co(NCS)_2$; absolute ethanol with purity > 99.5%; and acetone purists > 99% were purchased from Sigma-Aldrich and used without further purification. Trihexyl(tetradecyl)phosphonium chloride was donated to QUILL from Cytec.

2.6.2 Synthesis

2.6.2.1 Trihexyl(tetradecyl)phosphonium thiocyanate, $[P_{666\ 14}][SCN]$.

Trihexyltetra(decyl)phosphonium thiocyanate was prepared by reaction of equimolar amounts of trihexyltetra(decyl)phosphonium chloride, $[P_{666\ 14}]Cl$, and potassium thiocyanate, KSCN. In separate round-bottom flasks, $[P_{666\ 14}]Cl$ (6 g, 0.012 mol) was added to 10 mL of acetone and KSCN (1.123 g, 0.012 mol) in 10 mL of acetone. When fully dissolved, the reagents were added together, forming a milky white solution, and the solution was left to stir at room temperature overnight. KCl was filtered off, and acetone was removed by rotary evaporator. The resulting ionic liquid was washed twice with deionized water and dried under vacuum for 24 h at 70 °C. Karl Fischer analysis was used to analyse the water content in the prepared ionic liquid. The sample contained 660 ppm water.

2.6.2.2 Synthesis of $[P_{666\,14}]_2[Co(NCS)_4]$ with Excess Ionic Liquid.

Different mole ratios of ionic liquid, $[P_{666\,14}][SCN]$ to salt, $Co(NCS)_2$, were reacted together in a 50 cm^3 round-bottom flask with magnetic stirrer. Absolute ethanol was used as co-solvent. When the reaction was homogeneous, the ionic liquid was freed of solvent and dried under vacuum overnight at 85 °C. Karl Fischer analysis determined a water content of 710 ppm in $[P_{666\,14}][SCN]$ + $Co(NCS)_2$ (10:1).

Table 8. Elemental analysis of trihexyl(tetradecyl)phosphonium thiocyanate in combination with cobalt thiocyanate.

Complex	C	H	N	S
$[P_{666\,14}][SCN]$	73.14 (72.90)	12.65 (2.77)	2.58 (2.53)	5.92 (5.98)
X = 10	71.28 (71.00)	12.25 (12.59)	3.00 (2.95)	6.88 (6.51)

2.6.2.3 Synthesis of $[C_4Mim]_2[Co(NCS)_4]$ with excess ionic liquid

In a round-bottom flask with stirrer, 1-butyl-3-methylimidazolium thiocyanate, $[C_4Mim][SCN]$, and cobalt thiocyanate, $Co(SCN)_2$, were added in absolute ethanol. The mixture was left to stir overnight after which the ethanol was removed by rotary evaporation at 60 °C. Upon addition the mixture turns royal blue in colour. The product was further dried overnight under vacuum at 70 °C. Exact quantities of reagents are listed in Table 9. The purity of the product has been checked using elemental, CHNS analysis.

Table 9. Quantities of reagents used in the synthesis.

	$[C_4Mim][SCN]$			$Co(SCN)_2$	
X	**g**	**mL**	**mmol**	**g**	**mmol**
2	5	4.67	25.30	2.22	12.67
3	5	4.67	25.30	1.48	8.45
4	5	4.67	25.30	1.11	6.30
5	5	4.67	25.30	0.89	5.07
6	5	4.67	25.30	0.74	4.22
10	5	4.67	25.30	0.44	2.53

Table 10. Elemental analysis of 1-butyl-3-methylimidaolium thiocyanate and its mixture with cobalt thiocyanate. Theoretical % (Actual %)

Complex	**C**	**H**	**N**	**S**
$[C_4Mim]SCN$	52.49 (54.79)	7.66 (7.33)	21.3 (19.96)	16.25 (15.47)
X = 2	42.16 (42.53)	5.31 (5.23)	19.67 (19.44)	22.51 (20.79)
X = 3	45.41 (45.35)	5.91 (5.69)	20.09 (19.70)	20.90 (19.88)
X = 4	47.33 (46.49)	6.27 (6.22)	20.34 (19.67)	19.95 (19.24)
X = 5	47.73 (48.40)	6.45 (6.80)	20.40 (20.4)	18.61 (19.3)
X = 10	51.44 (49.50)	7.04 (7.19)	20.87 (20.07)	17.91 (17.23)

Metal analysis: $[C_4Mim]_2[Co(NCS)_4]$ = 5.6 %

Water content was obtained using Karl Fischer titration method and established to between 0.03 and 0.08 % after overnight drying at 70 °C.

2.6.3 Dielectric measurements

Broadband dielectric spectroscopic ambient pressure measurements were carried out on a Novo-Control GMBH alpha analyser in the frequency range of 10^{-1} – 10^{6} Hz. The sample was placed between two stainless steel electrodes, and the temperature was measured from 193 to 403 K in different heating steps controlled using a Novo-Control Quattro system with a liquid nitrogen cryostat. Temperature stability was greater than 0.1 K. High-pressure dielectric measurements were performed by placing the capacitor, containing the sample of interest, in a high-pressure chamber and compressing it using silicone oil. Low-temperature measurements were enabled using a Weiss fridge. During the high-pressure measurements, the sample was in contact only with stainless steel and Teflon. The sample was heated to 423 K prior to measurements to remove traces of water from the sample. The protocol of ambient and high-pressure measurements had two steps. First, the dielectric response of the sample was recorded during isobaric cooling [or isothermal compression in the case of high-pressure broadband dielectric spectroscopy (BDS) measurements. After that, the dielectric spectra of the studied IL were collected during heating (decompression) starting with low temperature and high pressure, respectively.

2.6.4 Calorimetric Measurements

The calorimetric measurements were carried out using a Mettler-Toledo DSC apparatus equipped with a liquid nitrogen cooling accessory and an HSS8 ceramic sensor (heat flux sensor with 120 thermocouples). The cooling system enabled the heat flow to be measured at temperatures as low as 133 K.

2.6.5 X-Ray Diffraction

Temperature-dependent XRD experiments were performed on a Rigaku-Denki D/MAX RAPID II-R diffractometer (Rigaku Corporation, Tokyo, Japan) equipped with a rotating anode Ag Kα tube (λ = 0.5608 Å), an incident beam (002) graphite monochromator, and an image plate in the Debye−Scherrer geometry. The pixel size was 100 µm × 100 µm. Studied samples were placed inside glass capillaries (1.5 mm in diameter). The temperature was controlled using the Oxford 700 Series Cryostream Cooler with the proven temperature stability of 0.1 K. The measurements were performed on sample-filled and empty capillaries, and the background intensity of the empty capillary was subtracted from the sample signal. The beam width at the sample was 0.3 mm. The two-dimensional diffraction patterns were converted into one-dimensional intensity data using suitable software.

2.6.6 Rheology

Small-amplitude oscillatory shear (SAOS) measurements were carried out on a stress-controlled rheometer AR2000ex (TA Instruments) with a parallel plates of 8, 25 and mm in diameter. The spectra were measured the spectra of angular frequency range from 100 to 0.1 rad/s at different temperatures from 243 to 423 K with an interval of 1 K close to the liquid glass transition and 5 K in the supercooled state.

2.7 References

1. Wasserscheid, P. & Welton, T. *Ionic Liquids in Synthesis*. *Wiley-VCH* **116,** (Wiley-VCH, 2008).
2. Zech, O., Stoppa, A., Buchner, R. & Kunz, W. The conductivity of imidazolium-based ionic liquids from (248 to 468) K. B. variation of the anion. *J. Chem. Eng. Data* **55,** 1774–1778 (2010).
3. Gaune-Escard, M. & Seddon, K. R. *Molten Salts and Ionic Liquids*. *Molten Salts and Ionic Liquids: Never the Twain?* (John Wiley & Sons, 2010). doi:10.1002/9780470947777.
4. Leys, J. *et al.* Temperature dependence of the electrical conductivity of imidazolium ionic liquids. *J. Chem. Phys.* **128,** 064509-1 - 064509-7 (2008).
5. Pogodina, N. V. *et al.* Molecular dynamics of ionic liquids as probed by rheology. *Journal of Rheology* **55,** 241–256 (2011).
6. Abbas, G., Lan, Y., Kostakis, G., Anson, C. E. & Powell, A. K. An investigation into lanthanide-lanthanide magnetic interactions in a series of $[Ln_2(mdeaH_2)_2(piv)_6]$ dimers. *Inorganica Chim. Acta* **361,** 3494–3499 (2008).
7. Walter Rhoades, D., Walter, D. & Dielectric Spectroscopy, B. *Broadband Dielectric Spectroscopy Studies of Nafion*. *Dissertation Archive,* **720** (2008).
8. Leys, J. *et al.* Influence of the anion on the electrical conductivity and glass formation of 1-butyl-3-methylimidazolium ionic liquids. *Mech. Heterog. Ion. Liq. J. Chem. Phys.* **133,** 034503-1 - 034503-10 (2010).
9. Nockemann, P. *et al.* Cobalt(II) complexes of nitrile-functionalized ionic liquids. *Chem. - A Eur. J.* **16,** 1849–1858 (2010).
10. Xie, Z.-L. & Taubert, A. Thermomorphic Behavior of the Ionic Liquids $[C_4mim][FeCl_4]$ and $[C_{12}mim][FeCl_4]$. *ChemPhysChem* **12,** 364–368 (2011).
11. Branco, A., Branco, L. C. & Pina, F. Electrochromic and magnetic ionic liquidsw. *Chem. Commun* **47,** 2300–2302 (2011).
12. García-Saiz, A., De Pedro, I., Blanco, J. A., González, J. & Fernández, J. R. Pressure effects on emim$[FeCl_4]$, a magnetic ionic liquid with three-dimensional magnetic ordering. *J. Phys. Chem. B* **117,** 3198–3206 (2013).
13. João Paulo Leal, S. *et al.* Showcasing research from the Photochemistry and As featured in: A thermochromic europium(III) room temperature ionic liquid with thermally activated anion–cation interactions. *Chem. Commun* **850,** 850–853 (2017).
14. Gandolfi, C., Morgan, G. G. & Albrecht, M. A magnetic iron(III) switch with controlled

and adjustable thermal response for solution processing. *Dalt. Trans.* **41,** 3726–3730 (2012).

15. Aoyagi, N. *et al.* Thermochromic properties of low-melting ionic uranyl isothiocyanate complexes. *This J. is Cite this Chem. Commun* **47,** 4490–4492 (2011).
16. Osborne, S. J. *et al.* Thermochromism and switchable paramagnetism of cobalt(ii) in thiocyanate ionic liquids. *Dalt. Trans.* **44,** 11286–11289 (2015).
17. García-Saiz, A. *et al.* A magnetic ionic liquid based on tetrachloroferrate exhibits three-dimensional magnetic ordering: A combined experimental and theoretical study of the magnetic interaction mechanism. *Chem. - A Eur. J.* **20,** 72–76 (2014).
18. Angell, C. A. & Abkemeier, M. L. Diamond Cell Study of Pressure-Induced Coordination Changes for Nickel(II) in Liquid Chloride Solvents. *Inorg. Chem.* **12,** 1463 (1973).
19. Martinez, L.-M. & Angell, C. A. *Chemical order lifetimes in liquids, and a second fictive temperature for glassformers*. *Physica A* **314,** 548 - 559 (2002).
20. Hansel-Bielowka, S. *et al.* Heterogeneous Nature of Relaxation Dynamics of Room-Temperature Ionic Liquids $(EMIm)_2[Co(NCS)_4]$ and $(BMIm)_2[Co(NCS)_4]$. *J. Phys. Chem. C* **119,** 20363–20368 (2015).
21. Wojnarowska, Z. *et al.* Conductivity Mechanism in Polymerized Imidazolium-Based Protic Ionic Liquid $[HSO_3$ −BVIm][OTf]: Dielectric Relaxation Studies. *Macromolecules* **47,** 4056–4065 (2014).
22. Kremer, F. & Schonhals, A. *Broadband Dielectric Spectroscopy*. *Springer - Verlag Berlin Heidelberg* (2003). doi:10.1007/978-3-642-56120-7.
23. Russina, O. *et al.* Temperature dependence of the primary relaxation in 1-hexyl-3-methylimidazolium bis{(trifluoromethyl)sulfonyl}imide. *J. Phys. Chem. B* **113,** 8469–8474 (2009).
24. Das, Vogel, H. Temperaturabhaṅ gigkeitsgesetz der Viskositat von Flüssigkeiten. *Phys. Z.* **22,** 645 (1921).
25. Fulcher, G. S. Analaysis of recent measurements of the viscosity of glasses. *J. Am. Ceram. Soc.* **8,** 339–355 (1925).
26. Tammann, G. & Hesse, W. Die Abhängigkeit der Viscosität von der Temperatur bie unterkühlten Flüssigkeiten. *Zeitschrift für Anorg. und Allg. Chemie* **156,** 245–257 (1926).
27. Novikov, V. N. & Sokolov, A. P. Universality of the dynamic crossover in glass-forming liquids: A “magic” relaxation time. *Phys. Rev. E - Stat. Physics, Plasmas, Fluids, Relat. Interdiscip. Top.* **67,** 031507-1 - 031507-6 (2003).
28. Böhmer, R., Ngai, K. L., Angell, C. A., Plazek, D. J. & Bohmer, R. Nonexponential

relaxations in strong and fragile glass formers. *J. Chem. Phys.* **99,** 4201 - 4209 (1993).

29. Qin, Q. & McKenna, G. B. Correlation between dynamic fragility and glass transition temperature for different classes of glass forming liquids. *J. Non. Cryst. Solids* **352,** 2977–2985 (2006).
30. Williams, G. & Watts, D. *Non-Symmetrical Dielectric Relaxation Behaviour Arising From a Simple Empirical Decay Function*. *Transactions of The Faraday Society* **66,** 80 - 85 (1970).
31. Tidey, J. P., Wong, H. L. S., Schröder, M. & Blake, A. J. Structural chemistry of metal coordination complexes at high pressure. *Coord. Chem. Rev.* **277–278,** 187–207 (2014).
32. Paluch, M., Grzybowska, K. & Grzybowski, A. Effect of high pressure on the relaxation dynamics of glass-forming liquids. *J. Phys. Condens. Matter* **19,** 205117–12 (2007).
33. Wojnarowska, Z. *et al.* Molecular origin of enhanced proton conductivity in anhydrous ionic systems. *J. Am. Chem. Soc.* **137,** 1157–1164 (2015).
34. Paluch, M., Grzybowska, K. & Grzybowski, A. Effect of high pressure on the relaxation dynamics of glass-forming liquids. *J. Phys. Condens. Matter* **19,** 205117–12pp (2007).
35. Debenedetti, P. G. & Stillinger, F. H. Supercooled liquids and the glass transition. *Insight Rev. Artic.* **410,** 259–267 (2001).
36. Floudas, G. *Molecular dynamics of glass-forming systems: the effect of pressure*. (Springer, 2011).
37. Santos, L. M. N. B. F. L. M. N. B. F. *et al.* Ionic liquids: First direct determination of their cohesive energy. *J. Am. Chem. Soc.* **129,** 284–285 (2007).
38. Adam, G. & Gibbs, J. H. On the Temperature Dependence of Cooperative Relaxation Properties in Glass-Forming Liquids. *J. Chem. Phys.* **43,** 139 - 145 (1965).
39. Freed, K. F. The simplified generalized entropy theory of glass-formation in polymer melts. *Cit. J. Chem. Phys.* **141,** 051102-1 - 051102-5 (2015).

Chapter 3. Designing Dimeric Lanthanide(III)-Containing Ionic Liquids.

3.1 Chapter Aims

This chapter explores the tunability and magnetic properties of a series of lanthanide-containing soft materials. We report on the preparation of liquid dimeric lanthanide(III)-containing compounds. Starting from the design of dimeric solids, we demonstrate that by tuning of the anion and cation structures we can lower the melting points below room temperature, whilst maintaining the dimeric structure. Magnetic measurements were able to establish the spin-spin interactions of the neighbouring lanthanide(III) ions in the liquid state at low temperatures, which matched the interactions of the analogous crystalline solid compounds.

It is important to note that the work described was done in collaboration with Dr Solveig Felton and Dr Kane Esien in the School of Maths and Physics, Queen's University of Belfast. Their input and constructive discussions regarding the magnetic properties of the synthesised compounds has been invaluable in allowing us to gain a better understanding of the synthesised series of dimeric lanthanide complexes.

The work presented herein has been submitted to a journal and our findings are discussed.

3.2 Introduction

Lanthanide-containing soft materials are a fascinating class of materials with intrinsic luminescent[1] and magnetic properties.[2] The lanthanide or rare-earth series is made up of atoms ranging from lanthanum (atomic number 57) to lutetium (atomic number 71), and also include scandium and yttrium (atomic number 21 and 39, respectively). Along with the actinides, the lanthanides are commonly referred to as the f-block elements due to the gradual filling of the 5f and 4f shells, respectively. Trivalent lanthanide ions have distinct spectroscopic properties which results from the shielding of the spectroscopically active 4f-electrons by filled 5s and 5p orbitals. In addition, as a result of this shielding, the ionic radii are seen to decrease as the series is traversed, a trend known as the lanthanide contraction. Such effects result in unique optical properties of the lanthanide ions. In addition, owing to the large ionic radii, coordination numbers as high as 12 have been reported for lanthanide complexes.[3]

The potential of lanthanides to generate significant magnetic anisotropy, has led to di- or polynuclear lanthanide(III) complexes receiving great attention.[4–8] Polymetallic assemblies can exhibit cooperative metal-metal interactions affecting their magnetic, electronic and photophysical properties.[9] The quindecim (15^+) charged pentanuclear rare-earth containing IL, $[Ho_5(C_2H_5\text{-}C_3H_3N_2\text{-}CH_2COO)_{16}(H_2O)_8][TfN_2]_{15}$, reported by Prodius *et al.*[10] has the highest charge ever observed for an ionic liquid with an effective magnetic moment equal to 23.3 μ_β.

The incorporation of lanthanide ions into ionic liquids (ILs) has extended their properties. As previously discussed, this incorporation leads to intrinsic magnetic and

spectroscopic properties. Furthermore, the ability to modify the anion and cation structures of ionic liquids means the physical and chemical properties of lanthanide-containing ionic liquids can be fine-tuned. For example, the cation and anion size, hydrogen bonding ability and alkyl chain lengths are all known to affect the melting points of ionic liquids. Nockemann *et al.* have previously reported the first liquid complexes containing lanthanide anions with thiocyanate ligands.[11] The magnetic and luminescent properties of $[C_6Mim]_{5-X}[Dy(SCN)_{8-X}(H_2O)_X]$ where subsequently explored by Mallick *et al.*[2] Single-ion magnetic behaviour at low temperature has been reported for the dysprosium-containing ionic liquid $[Dy(R\text{-}Im\text{-}CH_2COO)_3(H_2O))_2][(PF_6)_3{\cdot}2H_2O]$.[12] In this case the intrinsic magnetic functionality was incorporated into the cation structure. Recently, Alvarez-Vicente *et al.*[13] investigated the physical and magnetic properties of the series $[P_{666\ 14}][RECl_6]$ (RE = Rare Earth).[13] Further low-temperature magnetic measurements on $[P_{666\ 14}][RECl_6]$ ILs were subsequently carried out by Monson *et al.,*[14] reporting unusual behaviour at temperatures below 50 K, attributed to the trapping of intermediate structures during glass formation.

In this work, the magnetic and structural properties of novel crystalline, glassy and liquid lanthanide(III) containing ionic compounds, $[C_4Mim]_2[Ln_2(CH_3COO)_8]$, $[P_{666\ 14}]_2[Ln_2(CH_3COO)_8]$ and $[P_{666\ 14}]_2[Ln_2(C_7H_{15}COO)_8]$ are reported (Ln = lanthanide series). We demonstrate the ability to fine-tune both the anion and cation structures to realise room-temperature lanthanide-containing ionic liquids shown in Figure 52.

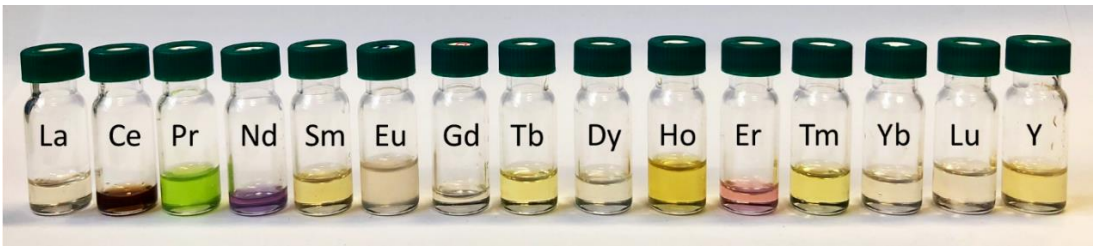

Figure 52. Room-temperature lanthanide-containing ionic liquids, $[P_{666\,14}]_2[Ln_2(C_7H_{15}COO)_8]$ (Ln = lanthanide).

Single-crystal X-ray diffraction provided direct evidence of the formation of dimeric complexes in the solid state. The crystal structure of dimeric $[C_4Mim]_2[Dy_2(CH_3COO)_8]$ is shown as an example in Figure 53.

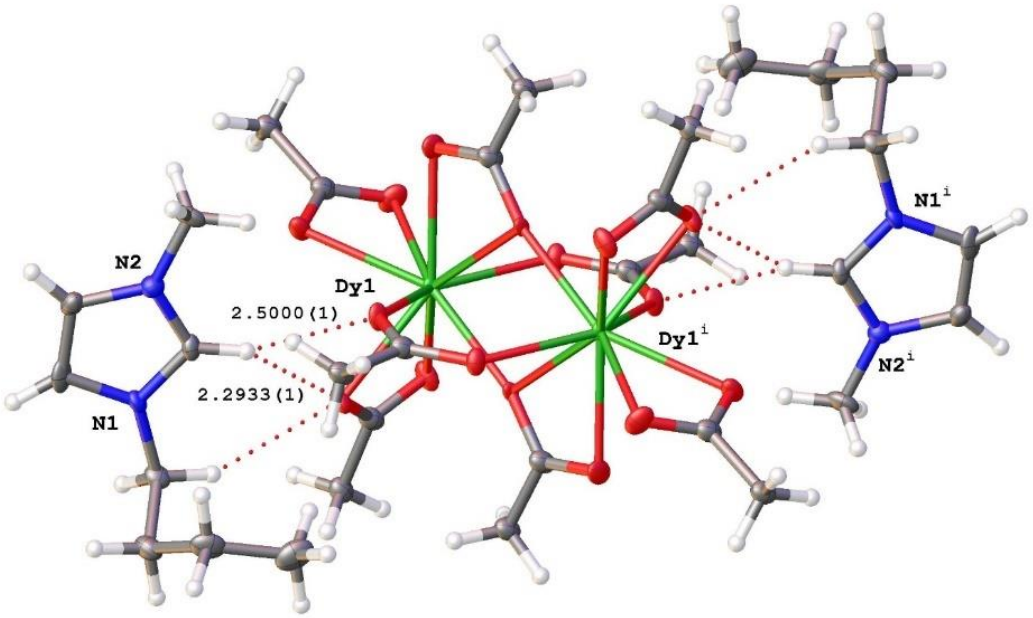

Figure 53. Crystal structure of $[C_4Mim]_2[Dy_2(CH_3COO)_8]$.

This ultimately led to the questions (i) *"Can a dimeric structure be obtained in the liquid state?"* and, in case the answer is affirmative, (ii) *"How can the presence of a dimer be proven in a liquid?"*.

These questions are the underlying foundation of this chapter and we endeavour to answer them through a combination of techniques discussed herein. In particular, SQUID (Superconducting Quantum Interference Device) magnetometry enabled us to explore the magnetic properties of these three systems bestowing insights into the magnetic behaviour over a wide temperature range. The speciation of metal complexes in ionic liquids has been the subject of different review articles.[15,16] Although multiple-technique approaches, including HEXS (High Energy X-ray Scattering) and EXAFS (Extended X-ray Absorption Fine Structure) to probe the speciation of metals in the liquid state have been previously reported, the methods may provide limited information and are not easily accessible.[17] Therefore, we looked for the presence of a magnetic interaction between the neighbouring lanthanide ions. Comparison between the magnetic properties of the samples in crystalline, glass and liquid phases, if such an interaction is present, would allow us to infer structure in the liquid and glassy states.

3.3 Results and discussion

3.3.1 Synthesis

The novel lanthanide(III)-containing ionic compounds, $[C_4Mim]_2[Ln_2(CH_3COO)_8]$, $[P_{666\ 14}]_2[Ln_2(CH_3COO)_8]$ and $[P_{666\ 14}]_2[Ln_2(C_7H_{15}COO)_8]$ were synthesised *via* addition reactions, whereby, equimolar ratios of lanthanide(III) salt (acetate or octanoate) were reacted with the ionic liquids 1-butyl-3-methylimidazolium acetate, trihexyltetra(decyl)phosphonium acetate and trihexytetra(decyl)phosphonium octanoate. By careful selection of the cation and anion components the melting points could be tuned forming the crystalline, glass and liquid lanthanide(III)-containing ionic compounds shown in Figure 54.

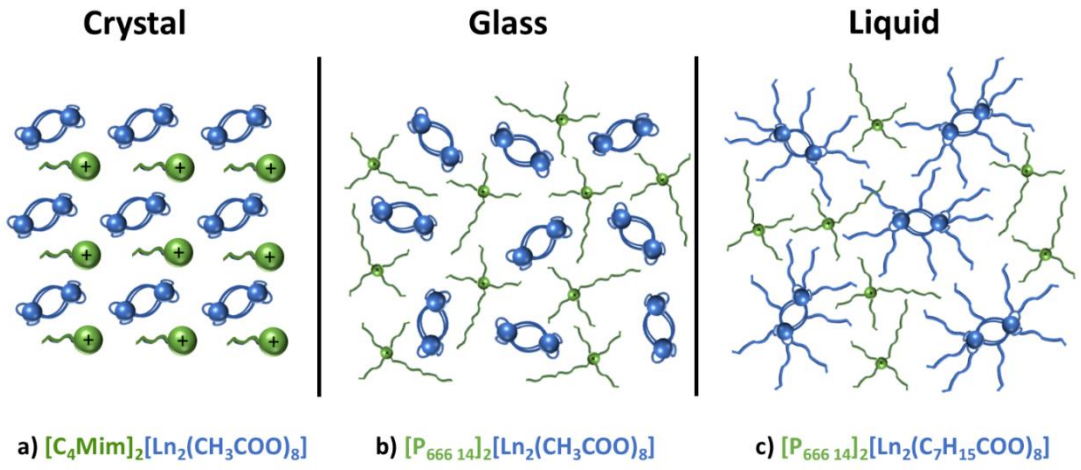

Figure 54. Variations in anion and cation structure upon changing from crystalline solid to glass to liquid, with a → b changing cation from $[C_4Mim]^+$ to $[P_{666\ 14}]^+$ and b → c changing coordinating anion from $[OAc]^-$ to $[C_7H_{15}COO]^-$ (Ln = lanthanide).

3.3.2 Crystallography

By either a method of slow crystallisation in a Reacti-Therm, starting from the molten state with a cooling rate of -5 °C to 50 °C or by solvent recrystallization from ethanol, single crystals of $[C_4Mim]_2[Ln_2(CH_3COO)_8]$ (Ln = Dy, Nd, Gd, Er and Y) were obtained. In addition to obtaining single crystals of the aforementioned dimeric lanthanide(III)-containing compounds, interesting tetrameric and polymeric structures of Gd and Nd also formed. The crystal structure of $[C_4Mim]_2[Dy_2(CH_3COO)_8]$ is presented in Figure 55.

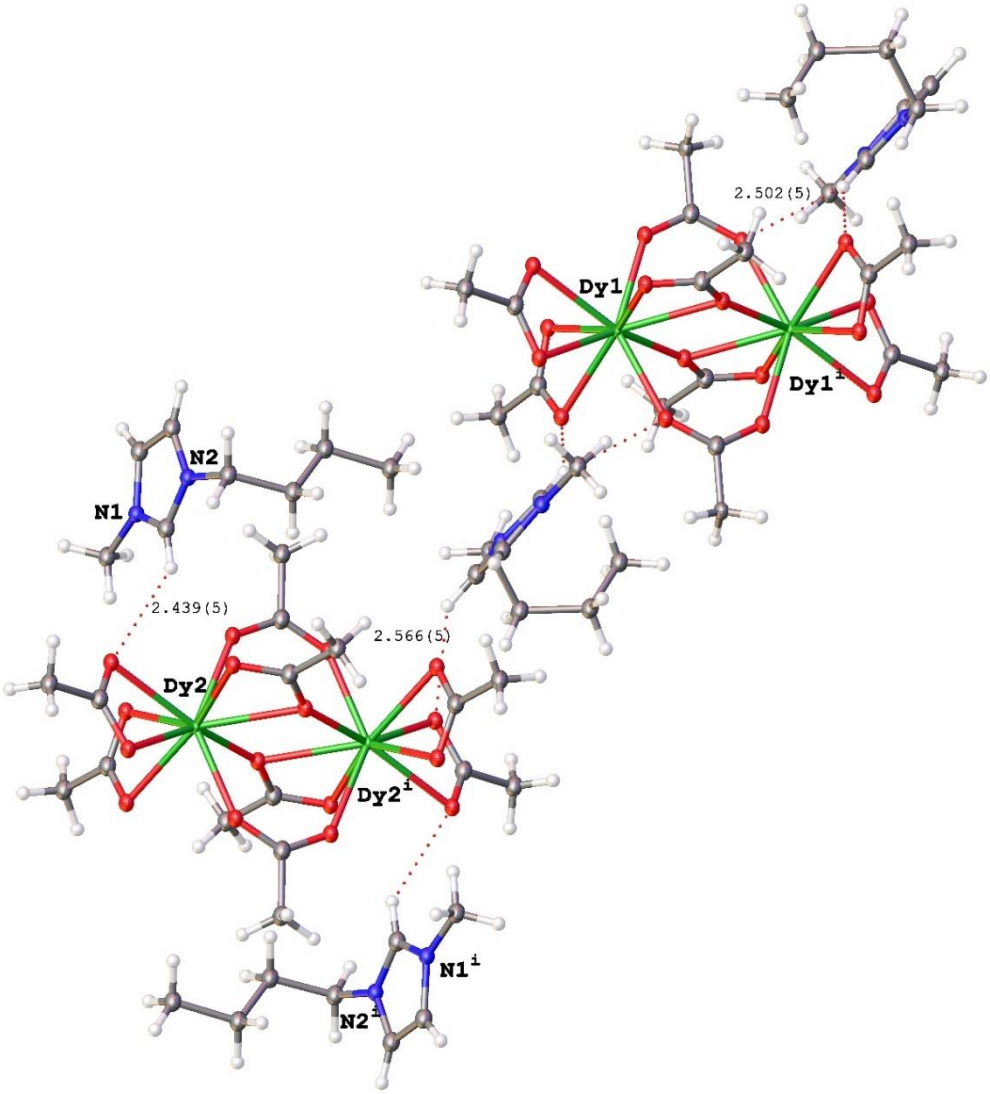

Figure 55. Crystal structure of $[C_4Mim]_2[Dy_2(CH_3COO)_8]$ showing two crystallographically independent dysprosium atoms present.

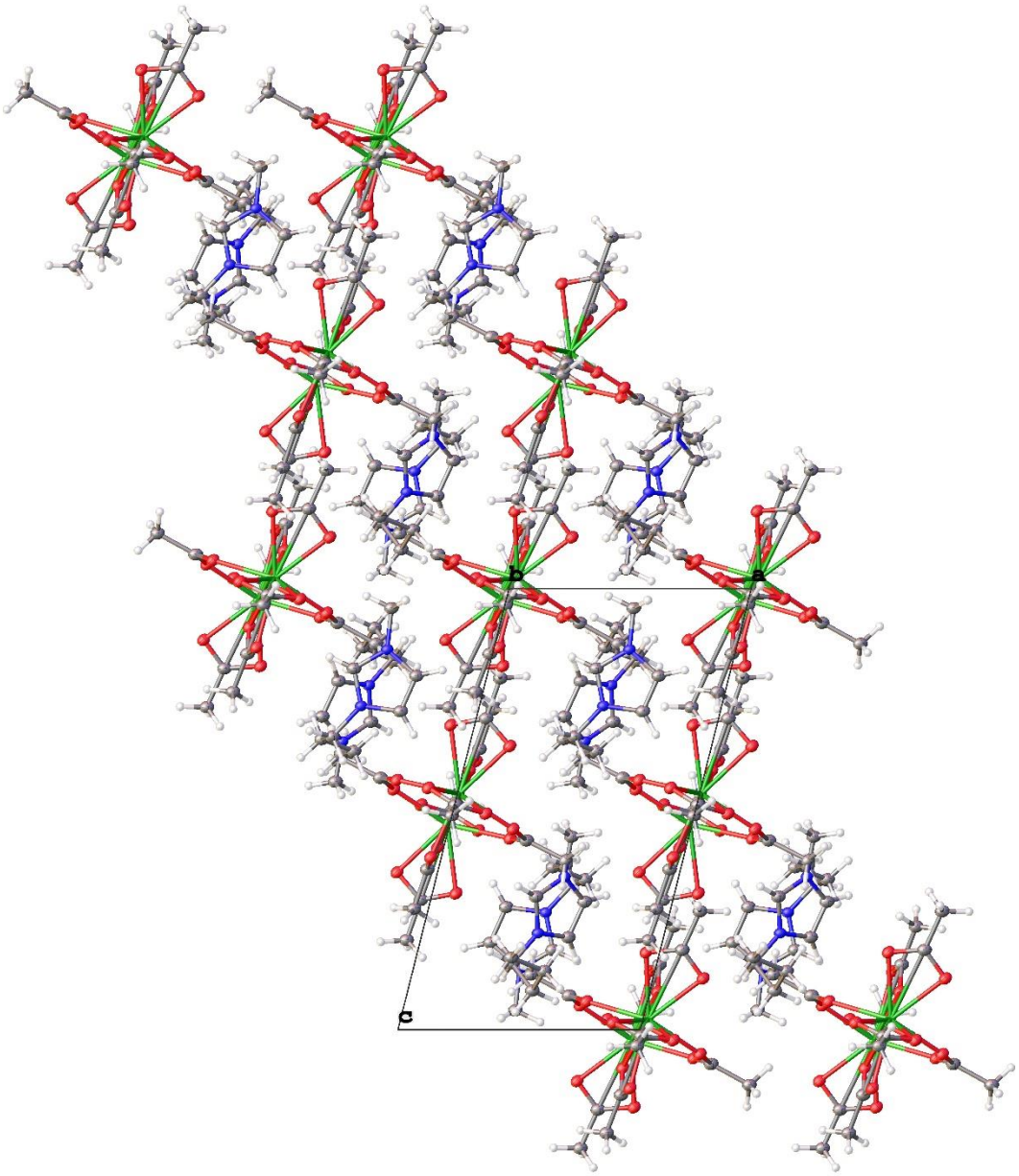

Figure 56. Crystal packing of $[C_4Mim]_2[Dy_2(CH_3COO)_8]$. View along [010].

$[C_4Mim]_2[Ln_2(CH_3COO)_8]$ (Ln = Dy, Gd and Nd) crystallized in a triclinic space group $P\bar{1}$. The structure presented in Figure 55 and crystal packing presented in Figure 56 is for that of the dysprosium compound which will be used as an example for analysis.

As seen, $[C_4Mim]_2[Dy_2(CH_3COO)_8]$ consists of a $[Dy_2(CH_3COO)_8]^{2+}$ anion and two 1-butyl-3-methylimidazolium, $[C_4Mim]^+$ counterions. The symmetry centre is located in the centre of the dimers, and there are two crystallographically independent dysprosium atoms present in the structure.

Powder XRD was used to confirm that what was obtained in the single crystal was indicative of the bulk sample. A simulated powder-XRD pattern was generated from the single crystal structure and matched to the powder-XRD obtained for the bulk powder showing good agreement between the two (Figure 57).

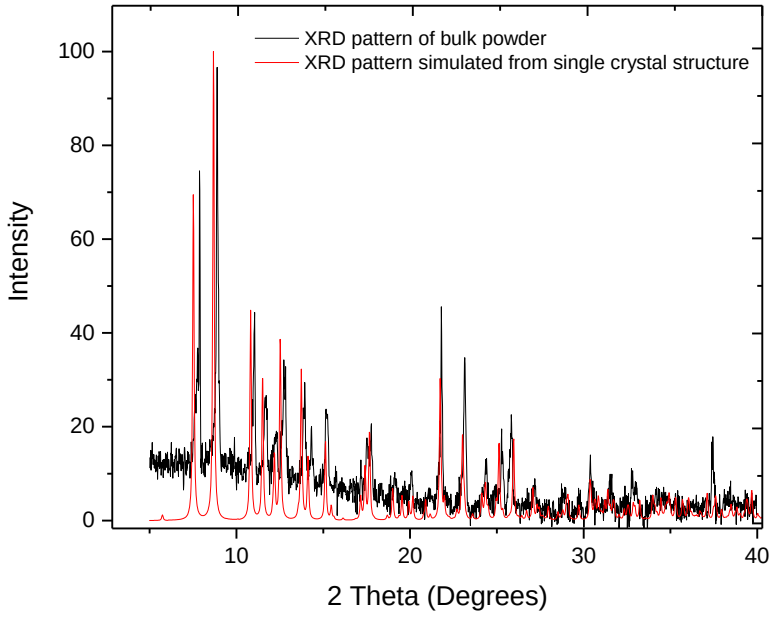

Figure 57. Powder XRD pattern of the bulk $[C_4Mim]_2[Dy_2(CH_3COO)_8]$ sample (black) and pattern simulated from single crystal structure (red).

The dysprosium (III) ions are linked by two carboxylate ligands in a bridging bidentate ($\eta^1:\eta^1:\mu_2$) fashion and two in a bridging chelating ($\eta^1:\eta^2:\mu_2$) mode. Each dysprosium(III) ion is further surrounded by two chelating carboxylates giving a total coordination number of nine. As previously discussed by Ouchi *et al.,*[7] in the bridging

chelating carboxylate groups, one of the oxygen atoms is bound in a μ_2-bridging manner to both dysprosium atoms and the second is bound directly to one dysprosium atom as also observed in Figure 53. The coordination polyhedron can be described as a distorted tricapped trigonal prism with Dy – O (carboxylate) bond lengths ranging from 2.329 – 2.509 Å and the Dy⋯Dy distance within the dimer is 3.8587(6) Å (for Dy1) and 3.8872(6) Å (for Dy2), respectively.

Neodymium, gadolinium and lanthanum crystallised in a similar manner. The bond lengths and Ln⋯Ln distance within each dimer are presented in Table 11 and crystal refinement data presented in Tables 12 and 13.

Table 11. Ln – O bond lengths and Ln⋯Ln distances within the dimers of Dy, Nd, Gd, Er and La crystal structures.

Compound	Ln – O bond lengths (Å)	Ln ⋯ Ln distance (Å)
$[C_4Mim]_2[La_2(CH_3COO)_8]$	2.454(8) – 2.61(1)	4.0962(6)
$[C_4Mim]_2[Nd_2(CH_3COO)_8]$	2.394(9) – 2.64(1)	3.9965(9)
$[C_4Mim]_2[Gd_2(CH_3COO)_8]$	2.341(5) – 2.565(4)	3.8143(8) Gd1, 3.9236(8) Gd2
$[C_4Mim]_2[Dy_2(CH_3COO)_8]$	2.317(5) – 2.534(5)	3.8587(6) Dy1, 3.8872(6) Dy2
$[C_4Mim]_2[Er_2(CH_3COO)_8]$	2.30253(8) – 2.4526(1)	3.85856(1)

$[C_4Mim]_2[Y_2(CH_3COO)_8{\cdot}2H_2O]$ is an example showing the hygroscopic nature of the lanthanide(III) complexes. The crystal structure of the yttrium is presented in Figure 58 and is seen to crystallize in a triclinic $P\bar{1}$ space group. There is an inversion centre located within the centre of the dimer. There is just one crystallographically independent yttrium site present in the structure. The yttrium (III) ions are linked by two carboxylate ligands in a bridging chelating (η^1:η^2:μ_2) mode and further

surrounded by two carboxylates in a chelating mode, one in a monodentate and one water molecule, giving a total coordination number of nine. The coordination polyhedron can be described as a distorted tricapped trigonal prism with Y···Y distance within the dimer equal to 4.1916(2) Å and Y – O (carboxylate) bond lengths ranging from 2.3075(1) Å to 2.5451(1) Å. The Y – O (H_2O) bond length is equal to 2.3562(1) Å. There is hydrogen bonding evident between the acidic proton of the $[C_4Mim]^+$ and the carboxylate oxygen with a distance of 2.1736(1) Å and hydrogen bonding between the water and carboxylate equal to 1.84208(9) Å (chelating) and 1.76552(9) Å (monodentate).

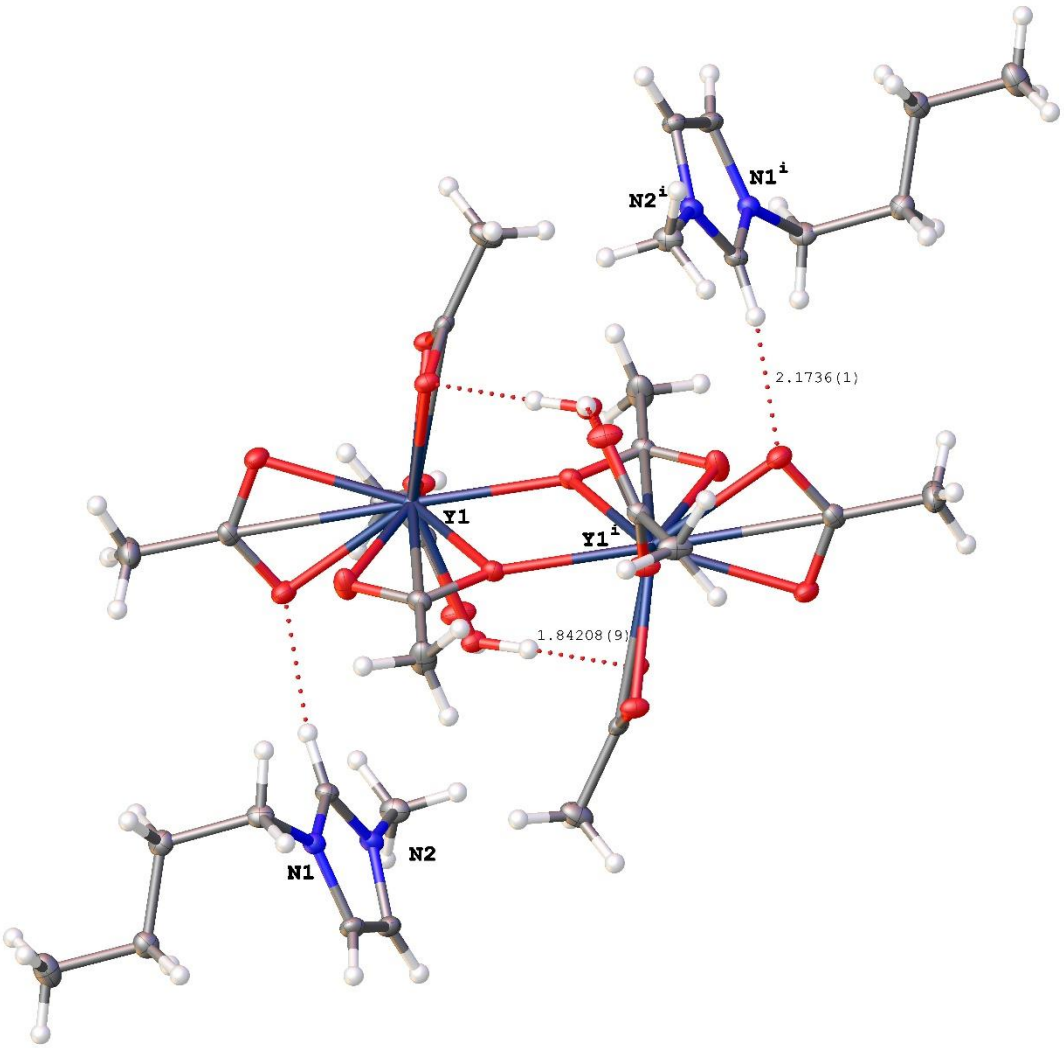

Figure 58. Crystal structure of $[C_4Mim]_2[Y_2(CH_3COO)_8{\cdot}2H_2O]$.

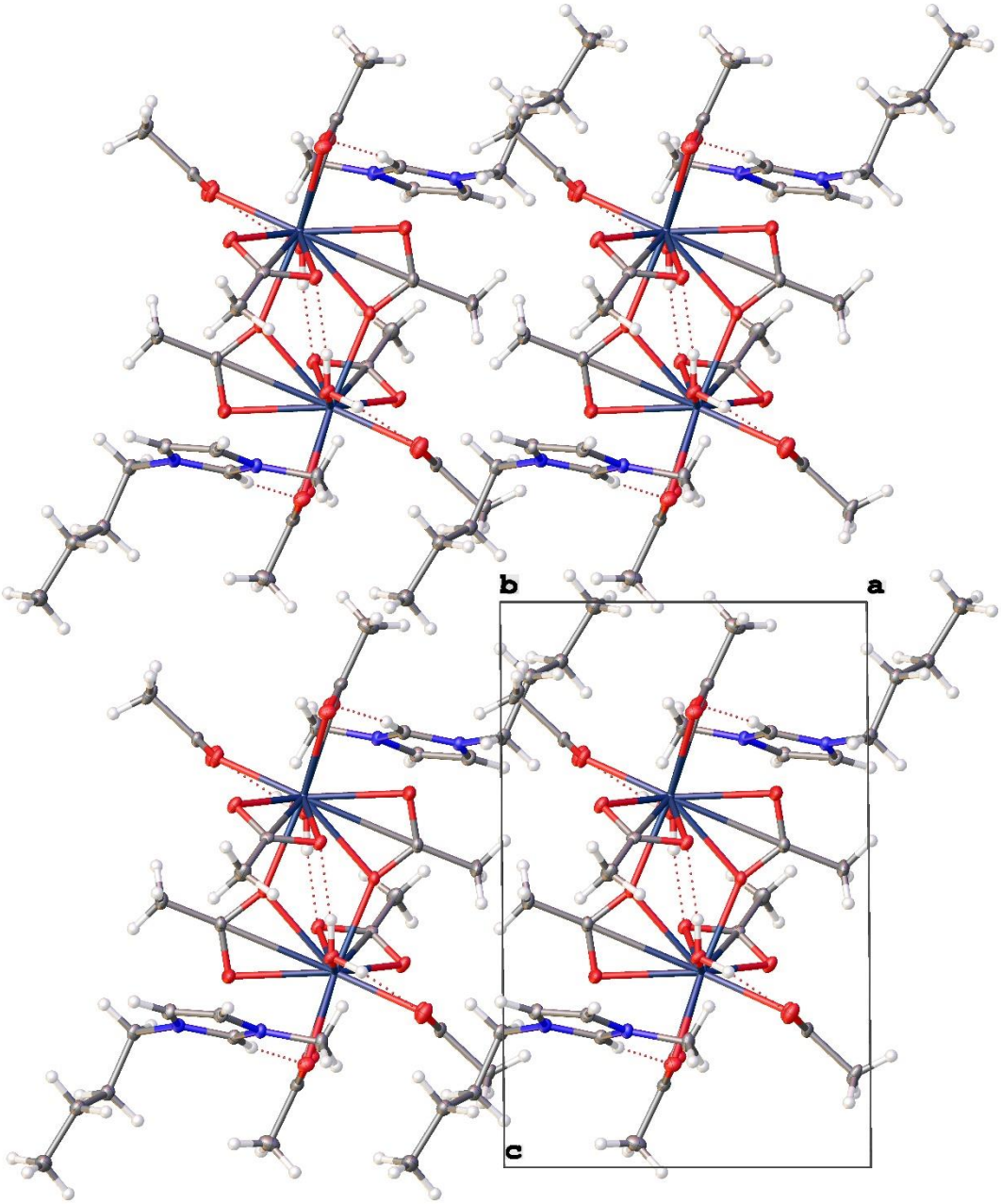

Figure 59. Crystal packing of $[C_4Mim]_2[Y_2(CH_3COO)_8{\cdot}2H_2O]$. View along [010].

3.3.2.1 Observations

In general, the Ln-O distances decrease slightly upon going from La(III) to Er(III) as expected due to the lanthanide contraction. The increasing charge density leads to a stronger attraction between the lanthanide ion and the ligand. The lanthanide

contraction is also evident in the Ln···Ln distances within the dimers. As observed the Ln···Ln distance decreases across the series.

Table 12. Crystal data refinement table of $[C_4Mim]_2[Ln_2(CH_3COO)_8]$ series(Ln = Dy, Gd and Nd).

Identification code	**Dy**	**Gd**	**Nd**
Empirical formula	$C_{32}H_{54}N_4O_{16}Dy_2$	$C_{32}H_{54}N_4O_{16}Gd_2$	$C_{32}H_{54}N_4O_{16}Nd_2$
Formula weight	1075.79 g/mol	1065.29 g/mol	1039.27 g/mol
Temperature/K	293(2)	100.00(10)	293.30(10)
Crystal system	triclinic	triclinic	triclinic
Space group	P-1	P-1	P-1
a/Å	8.4373(3)	8.4341(2)	12.3083(5)
b/Å	15.5572(4)	15.6337(3)	13.6875(6)
c/Å	15.9881(5)	16.0215(3)	14.6145(6)
α/°	97.705(2)	97.818(2)	110.047(4)
β/°	103.952(3)	103.920(2)	102.369(4)
γ/°	90.338(2)	90.267(2)	104.515(4)
Volume/Å^3	2016.71(11)	2029.90(8)	2113.66(17)
Z	29	29	30
ρ_{calc}g/cm^3	4.908	4.751	4.414
μ/mm^{-1}	141.307	150.818	138.198
F(000)	2552.0	2494.0	2460.0
Radiation	CuKα (λ = 1.54184)	CuKα (λ = 1.54184)	CuKα (λ = 1.54184)
2Θ range for data collection/°	10.814 to 177.41	7.506 to 148.374	6.82 to 145.564
Index ranges	-10 ≤ h ≤ 10, -19 ≤ k ≤ 19, -18 ≤ l ≤ 20	-10 ≤ h ≤ 8, -19 ≤ k ≤ 19, -19 ≤ l ≤ 19	-15 ≤ h ≤ 15, -16 ≤ k ≤ 15, -14 ≤ l ≤ 18
Reflections collected	31451	31672	14191
Independent reflections	7713 [R_{int} = 0.0688, R_{sigma} = 0.0581]	8139 [R_{int} = 0.1433, R_{sigma} = 0.0856]	8197 [R_{int} = 0.0392, R_{sigma} = 0.0669]
Data/restraints/parameters	7713/0/499	8139/0/392	8197/0/366
Goodness-of-fit on F^2	1.089	1.032	1.075
Final R indexes [I>=2σ (I)]	R_1 = 0.0476, wR_2 = 0.1365	R_1 = 0.0657, wR_2 = 0.1750	R_1 = 0.0920, wR_2 = 0.2628
Final R indexes [all data]	R_1 = 0.0557, wR_2 = 0.1503	R_1 = 0.0721, wR_2 = 0.1843	R_1 = 0.1153, wR_2 = 0.2914
Largest diff. peak/hole / e Å^{-3}	1.21/-2.25	3.63/-3.21	6.29/-0.99

Table 13. Crystal data refinement table of $[C_4Mim]_2[Ln_2(CH_3COO)_8]$ (Ln = erbium, yttrium and lanthanum.

Identification code	**Er**	**Y**	**La**
Empirical formula	$C_{32}H_{54}N_4O_{16}Er_2$	$C_{32}H_{58}O_{18}N_4Y_2$	$C_{32}H_{54}N_4O_{16}La_2$
Formula weight	1085.30 g/mol	964.63 g/mol	1028.60 g/mol
Temperature/K	293(2)	293(2)	293.30(10)
Crystal system	monoclinic	triclinic	monoclinic
Space group	$P2_1/n$	P-1	Pn
a/Å	9.2232(4)	9.0307(4)	9.59400(10)
b/Å	13.2769(6)	9.3071(5)	12.63000(10)
c/Å	17.3203(8)	13.2604(6)	16.7754(2)
α/°	90	82.718(4)	90
β/°	97.641(4)	87.226(4)	93.3240(10)
γ/°	90	70.946(4)	90
Volume/$Å^3$	2102.14(17)	1044.94(9)	2029.29(4)
Z	30	15	9
$\rho_{calc}g/cm^3$	4.983	3.145	1.382
μ/mm^{-1}	29.633	27.084	4.610
F(000)	2700.0	915.0	876.0
Radiation	MoKα (λ = 0.71073)	CuKα (λ = 1.54184)	CuKα (λ = 1.54184)
2Θ range for data collection/°	7.58 to 58.516	10.126 to 148.484	6.998 to 145.534
Index ranges	$-4 \le h \le 11$, $-17 \le k \le 16$, $-23 \le l \le 22$	$-11 \le h \le 11$, $-11 \le k \le 11$, $-16 \le l \le 16$	$-11 \le h \le 11$, $-15 \le k \le 15$, $-20 \le l \le 19$
Reflections collected	9043	12776	19942
Independent reflections	4805 [R_{int} = 0.0380, R_{sigma} = 0.0676]	4149 [R_{int} = 0.0535, R_{sigma} = 0.0405]	6473 [Rint = 0.0458, Rsigma = 0.0446]
Data/restraints/parameters	4805/0/173	4149/0/261	6473/2/462
Goodness-of-fit on F^2	1.072	1.044	0.998
Final R indexes [I>=2σ (I)]	R_1 = 0.0509, wR_2 = 0.1003	R_1 = 0.0311, wR_2 = 0.0802	R1 = 0.0314, wR2 = 0.0753
Final R indexes [all data]	R_1 = 0.0607, wR_2 = 0.1063	R_1 = 0.0323, wR_2 = 0.0812	R1 = 0.0373, wR2 = 0.0802
Largest diff. peak/hole / e $Å^{-3}$	2.58/-2.65	1.15/-1.00	0.78/-0.76

Furthermore, in addition to the dimeric structures obtained across the lanthanide series, a tetrameric gadolinium and polymeric neodymium compound was also observed.

3.3.2.2 Tetrameric gadolinium compound

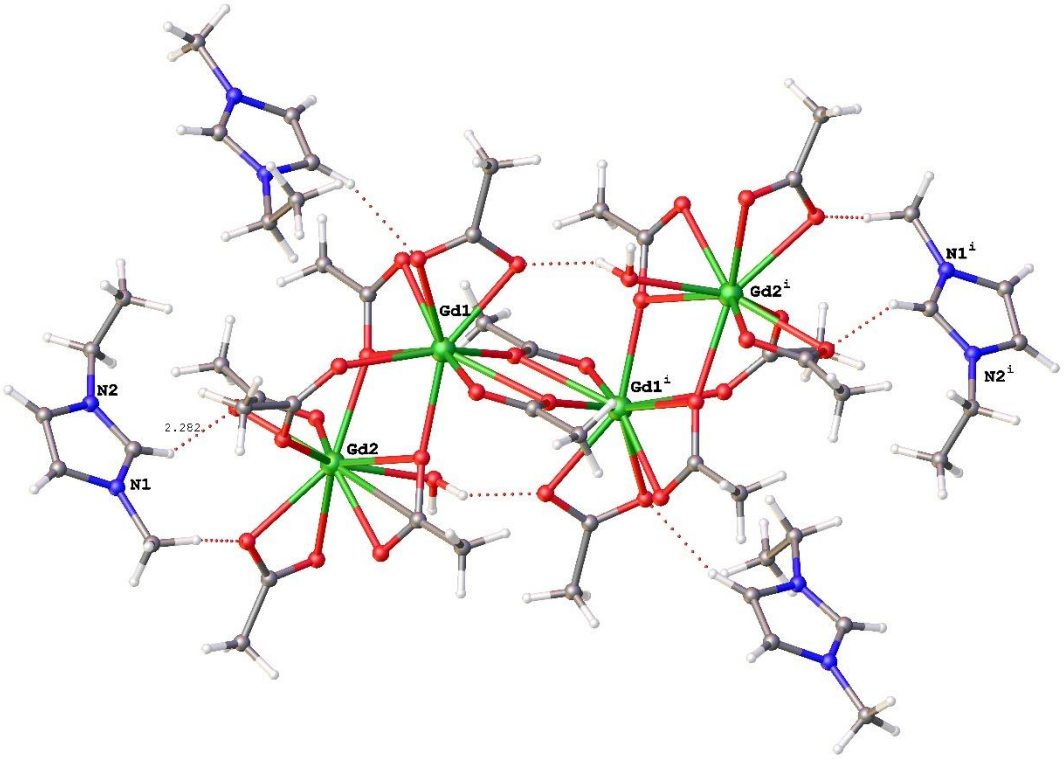

Figure 60. Tetrameric gadolinium compound.

From crystal structure analysis, there are two sets of equivalent gadolinium ions, labelled as Gd1, Gd1^{i} and Gd2, Gd2^{i}. Each have a coordination number of nine. The gadolinium ions are linked *via* two carboxylates in a bridging chelating mode, Gd1 and Gd2 are linked *via* carboxylates in a bidentate bridging mode, and the gadolinium centres are further surrounded by two carboxylates in a chelating mode. Gd2 has an additional water molecule present. The Gd1···Gd2 distance within the tetramer is

4.07(2) Å and Gd1···Gd1^{i} distance within the tetramer is 4.117(1) Å. The Gd-O bond lengths range from 2.38(1) – 2.55(1) Å.

Table 14. Crystal data refinement table of the tetrameric gadolinium compound.

Identification code	$[C_4Mim]_4[Gd_4(CH_3COO)_{15}\cdot 2H_2O]$
Empirical formula	$(C_8H_{15}N_2)_4[Gd_4(CH_3COO)_{15}\cdot 2H_2O]$
Formula weight	2045.32 g/mol
Temperature/K	293(2)
Crystal system	monoclinic
Space group	C2/c
a/Å	22.2133(12)
b/Å	12.3305(7)
c/Å	25.2927(14)
α/°	90
β/°	103.124(5)
γ/°	90
Volume/Å^3	6746.8(7)
Z	94
ρ_{calc}g/cm^3	4.634
μ/mm^{-1}	147.083
F(000)	8084.0
Radiation	CuKα (λ = 1.54184)
2Θ range for data collection/°	8.254 to 151.338
Index ranges	-26 ≤ h ≤ 27, -14 ≤ k ≤ 15, -30 ≤ l ≤ 31
Reflections collected	20915
Independent reflections	6796 [R_{int} = 0.2344, R_{sigma} = 0.1685]
Data/restraints/parameters	6796/108/142
Goodness-of-fit on F^2	1.519
Final R indexes [I>=2σ (I)]	R_1 = 0.2062, wR_2 = 0.4495
Final R indexes [all data]	R_1 = 0.2362, wR_2 = 0.4764
Largest diff. peak/hole / e Å^{-3}	5.98/-10.47

3.3.2.3 Polymeric neodymium compound

The polymeric neodymium structure is presented in Figure 61. Each neodymium centre is linked *via* carboxylate ligands in a bridging bidentate mode and for Nd1, two in a tridentate chelating-bridging mode. Nd2 has four carboxylate in a bridging-chelating mode. Nd1 has a carboxylate in a bidentate mode. The coordination number of Nd1 and Nd2 is nine. The Nd···Nd distance within the polymer ranges from 4.0737(3) to 4.1907(3) Å and the Nd – O bond lengths range from 2.359(4) to 2.650(5) Å.

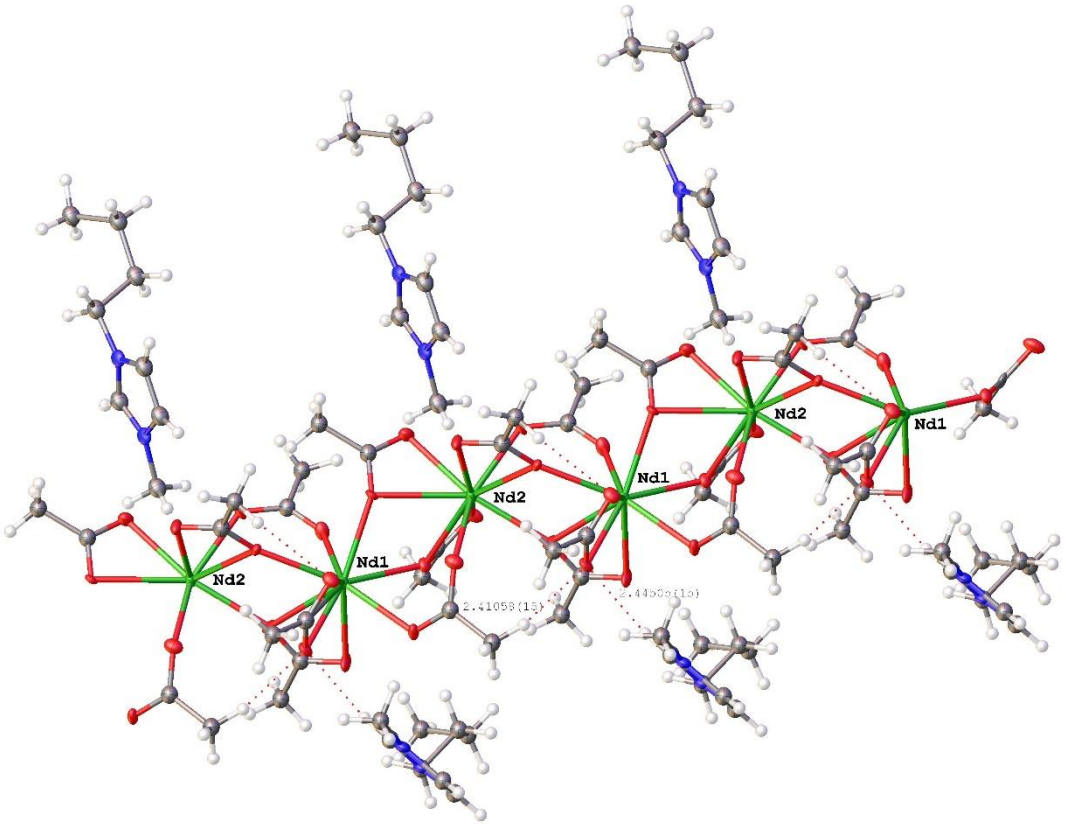

Figure 61. Polymeric neodymium compound.

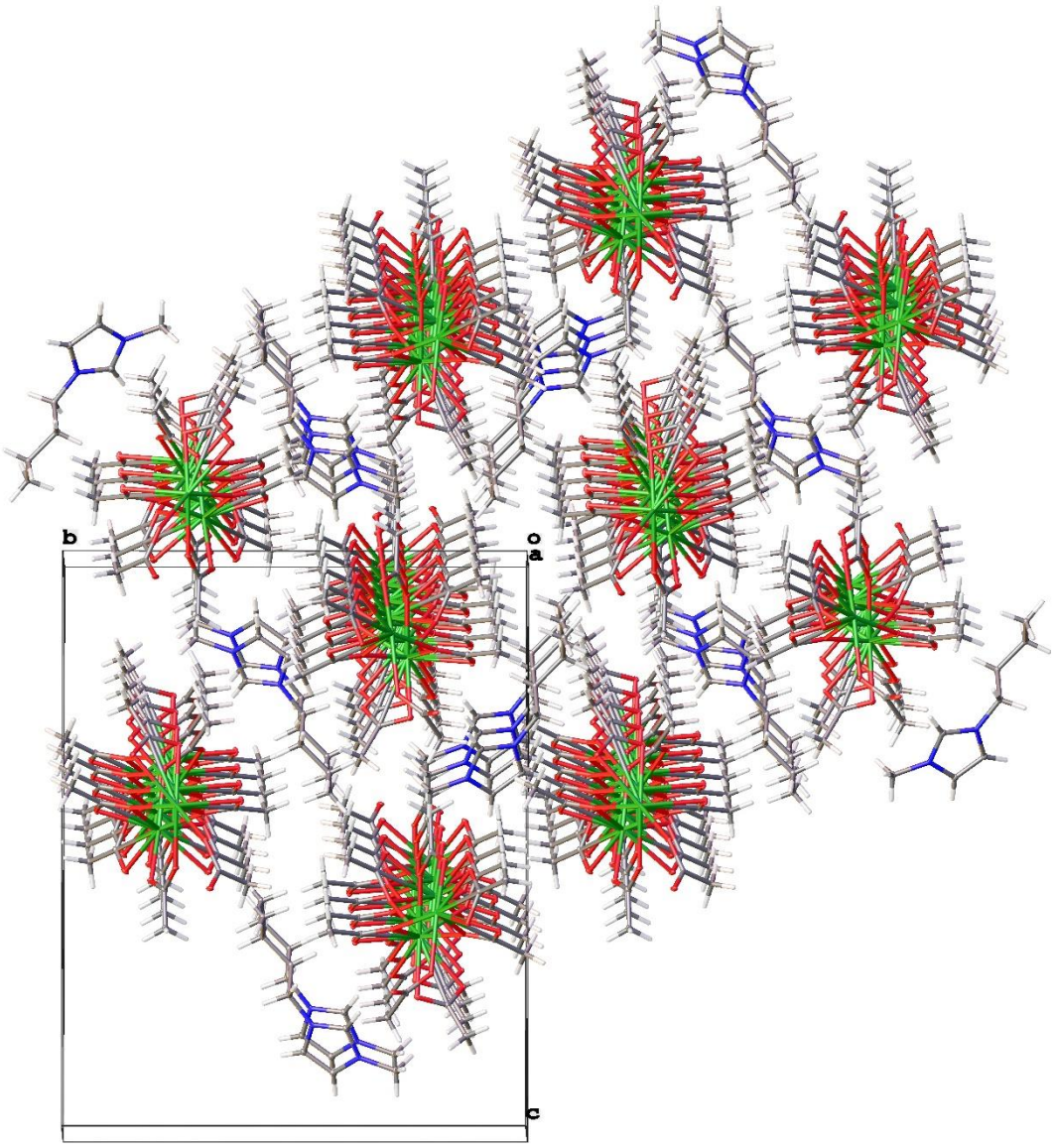

Figure 62. Crystal packing of polymeric neodymium complex. View along [100].

Table 15. Crystal data table of polymeric neodymium compound.

Identification code	**Nd**
Empirical formula	$([C_4Mim][Nd(CH_3COO)_6)_n$
Formula weight	
Temperature/K	293(2)
Crystal system	monoclinic
Space group	$P2_1/n$
a/Å	7.8078(6)
b/Å	17.4129(13)
c/Å	22.0493(16)
α/°	90
β/°	97.552(7)
γ/°	90
Volume/Å^3	2971.7(4)
Z	42
ρ_{calc}g/cm^3	4.395
μ/mm^{-1}	18.040
F(000)	3444.0
Radiation	MoKα (λ = 0.71073)
2Θ range for data collection/°	7.16 to 58.218
Index ranges	$-10 \le h \le 10$, $-23 \le k \le 18$, $-19 \le l \le 28$
Reflections collected	13013
Independent reflections	6774 [R_{int} = 0.0436, R_{sigma} = 0.0943]
Data/restraints/parameters	6774/0/173
Goodness-of-fit on F^2	1.108
Final R indexes [I>=2σ (I)]	R_1 = 0.0533, wR_2 = 0.0865
Final R indexes [all data]	R_1 = 0.0725, wR_2 = 0.0941
Largest diff. peak/hole / e Å^{-3}	1.44/-1.68

3.3.3 Spectroscopic methods

As diffraction experiments are limited to the crystalline sample, other spectroscopic techniques such as IR and UV-Vis were investigated, however, it must be noted, whilst affording some insight into the structure, the standard spectroscopic techniques did not provide hard evidence for question *(ii)* (*vide supra*) regarding the dimeric structure in the glass and liquid state**.**

The carboxylate ion, RCO_2^-, has several possible coordination modes to a metal e.g. monodentate, bidentate, bridging bidentate and tridentate chelating bridging as presented in Figure 63 (left to right).

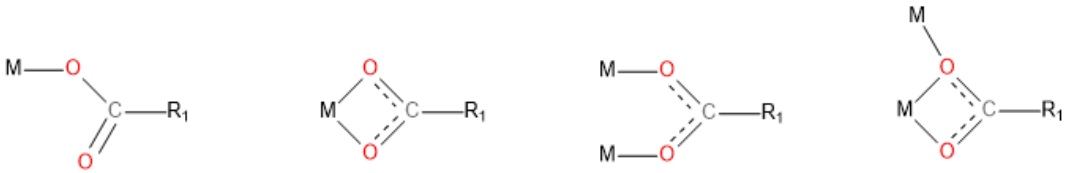

Figure 63. Various coordination modes of carboxylates to metal centre.

Analysis of the differences (Δv) in the asymmetric $v_a(COO^-)$ and symmetric $v_s(COO^-)$ wavenumbers, can be used to gain insight into the coordination modes, [$\Delta v = v_a(COO^-) - v_s(COO^-)$].[18] It is generally believed, that if the carboxylate is bonding in a monodentate fashion, the Δv of the complex is higher than the value of Δv of the complex; if bonding is *via* bidentate chelate mode, the Δv of the complex is smaller than the value for the complex and for bidentate bridge mode the value of Δv of the complex is similar to the value of Δv of the complex.

Infrared spectra were recorded on a PerkinElmer Spectrum 100 spectrometer in the spectral region 550 – 3500 cm^{-1}. Figure 64 and Figure 65 are the spectra of the $[C_4Mim]_2[Ln_2(CH_3COO)_8]$ and $[P_{666\ 14}]_2[Ln_2(C_7H_{15}COO)_8]$, respectively, with Ln = Y, Ce, Nd, Sm, Gd, Er, Dy, Yb, Eu, Lu and Figure 66 is the spectra of the glassy compounds, $[P_{666\ 14}]_2[Ln_2(CH_3COO)_8]$ with Ln = Dy, La and Nd.

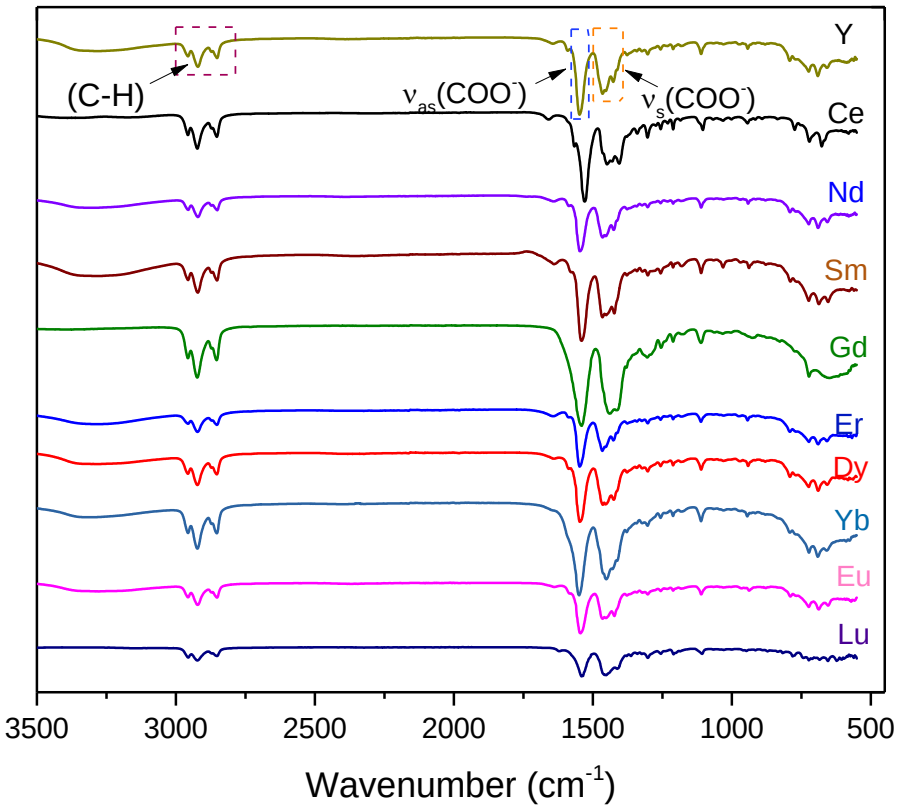

Figure 64. Infrared spectra of $[C_4Mim]_2[Ln_2(CH_3COO)_8]$,

The broad peak observed at 3302 cm^{-1} in a number of the spectra above corresponds to the O-H stretching of either water molecules or ethanol. Highlighted in the spectra are the stretching bands of C-H which include, ν_{as} (CH_2) = 2959, ν_{as} (CH_3) = 2926, ν_s (CH_3) = 2858, ν_s (CH_2) = 2852, δ_{as} (CH_2) = 1456 and δ_{as} (CH_3) = 1435 cm^{-1} (where, δ =

bending) and the symmetric (ν_s) and asymmetric stretching bands (ν_a) of the carboxylate (COO^-) ligand.

Table 16. Symmetric and asymmetric stretching bands of the carboxylate (COO^-) in $[C_4Mim]_2[Ln_2(CH_3COO)_8]$.

Compound	$\nu_a(COO^-)$	$\nu_s(COO^-)$	Δ
Y	1589.1, 1546.4	1453	136.1, 93.4
Ce	1565.5, 1530.1	1449.1	116.4, 81
Nd	1584.4, 1545.3	1450.8	133.6, 94.5
Sm	1579.5, 1538.3	1448.0	131.5, 90.3
Gd	1542.2	1442.1	100.1
Er	1546.1	1424.5	121.6
Dy	1586.1, 1546.0	1451.1	135, 94.9
Yb	1590.2, 1550.1	1444	146.2, 106.1
Eu	1543.2	1444.2	99
Lu	1541.8, 1535.1	1438.8	103, 96.3

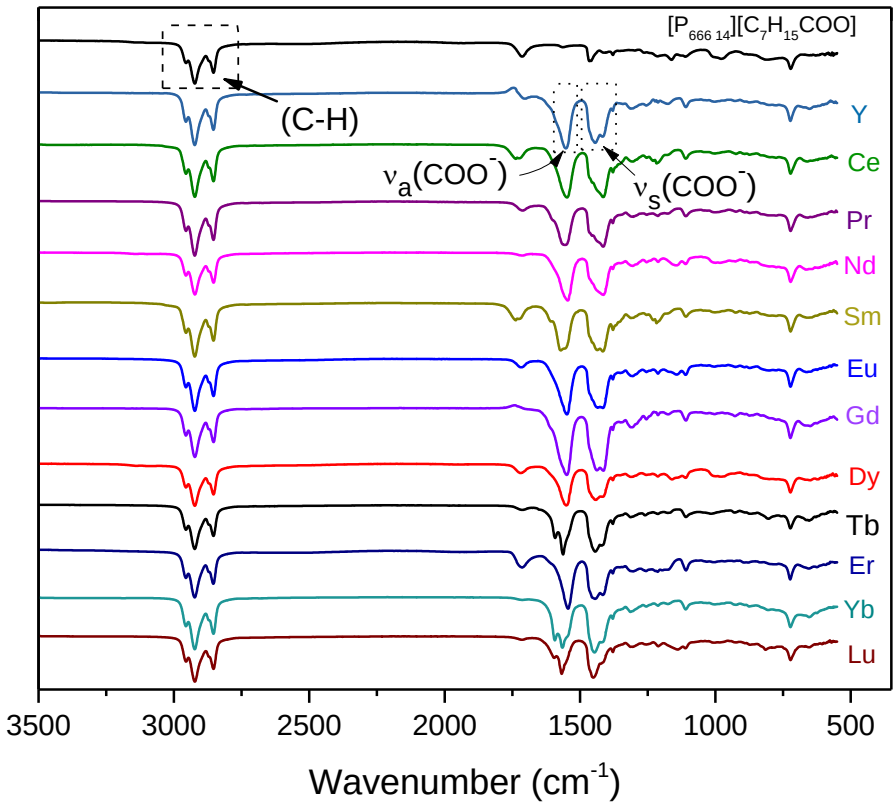

Figure 65. Infrared spectra of $[P_{666\,14}]_2[Ln_2(C_7H_{15}COO)_8]$.

The O-H stretching band is not evident in the liquid samples indicating that water is not present in these samples. Like in the solid samples we have C-H stretching in the region 2994 – 2806 cm^{-1}, the long chain rocking at 718 cm^{-1} and the symmetric (COO^-) stretch ranging from 1461 – 1429 cm^{-1} and asymmetric carboxylate (COO^-) stretch ranging from 1609 – 1544 cm^{-1} for the different lanthanides.

Table 17. Symmetric and asymmetric stretching bands of the carboxylate (COO^-) in $[P_{666\,14}]_2[Ln_2(C_7H_{15}COO)_8]$.

Compound	$\nu_a(COO^-)$	$\nu_s(COO^-)$	Δ
$[P_{666\,14}][C_7H_{15}COO]$	1562.12	1461.7	100.42
Y	1550.84	1442.6	108.24
Ce	1552.28	1417.3	143.98
Pr	1599.0, 1560.8	1423.2	175.8, 137.6
Nd	1552.3	1429.2	123.1
Sm	1566.5, 1550.9	1438.2	128.3, 112.7
Gd	1557	1430.0	127
Er	1609.7, 1544.9	1436.3	173.4, 108.6
Dy	1547.7	1433.0	114.7
Yb	1591.5, 1563.4	1433.2	158.3, 130.2
Eu	1547.7	1426.0	121.7
Lu	1597.5, 1569.7	1445.7	151.8, 124.0

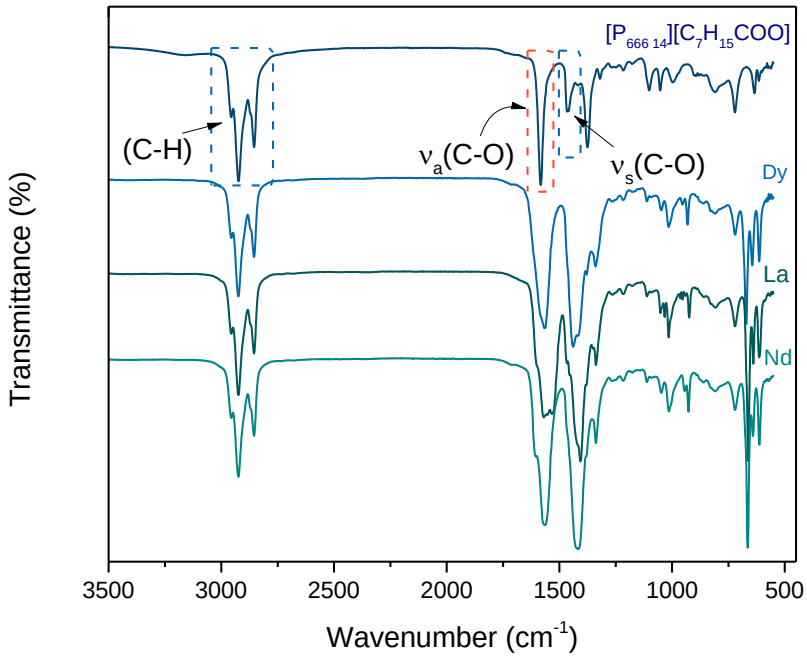

Figure 66. Infrared spectra of $[P_{666\,14}]_2[Ln_2(CH_3COO)_8]$, Ln = Dy, La and Nd.

Table 18. Symmetric and asymmetric stretching bands of the carboxylate (COO^-) in $[P_{666\ 14}]_2[Ln_2(CH_3COO)_8]$.

Compound	$\nu_a(COO^-)$	$\nu_s(COO^-)$	Δ
$[P_{666\ 14}][CH_3COO]$	1584	1461	123
Dy	1587, 1569	1438	149, 131
La	1560, 1533	1415	145, 118
Nd	1605, 1560	1415	190, 145

From the spectra and values presented in Tables 16 – 18, splitting of $\nu_a(COO^-)$ is observed in the crystalline, glassy and liquid samples. This splitting leads to two separation values indicative of different bonding modes present within the sample.

A mix of bidentate bridging and chelating may therefore be deduced for all states. It is clear from this data that although Δ_ν is documented for establishing the coordination mode of carboxylates to a metal[18], in this case it is unsatisfactory given that a combination of bonding modes are present as seen in the splitting of the $\nu_{as}(COO^-)$ band and further confirmed in the crystal structures.

3.3.4 UV/Vis Spectroscopy

The shielding of the 4f-electrons by the $5p^6 6s^2$ sub-shells results in interesting spectroscopic properties with the parity-forbidden 4f-4f absorptions having very low molar absorption coefficients and characteristic narrow-line emission in the visible and near infrared ranges.[19] The energies of these levels are well-defined, and, in addition, do not vary much with the chemical environments in which the lanthanide ions are placed.[20]

Figures 67 – 70 show the UV/Vis spectra of some of the liquid dimeric lanthanide(III) series. It must be noted, in the spectra obtained a tailing upwards of absorption at wavelengths lower than 300 nm can be attributed to the interaction of the ionic liquid with the radiation at these energies, thus making detection and identification of peaks below this point unfeasible. The peaks which can be observed however, can be matched with the energy transition causing the occurrence of the peak (as presented in the tables that follow). There may also be some broadening of the peaks due to the highly polar nature of the ionic liquid, but this should have minimal effect on the energy states of the lanthanides involved and is likely due to the resolution used of the spectrometer.

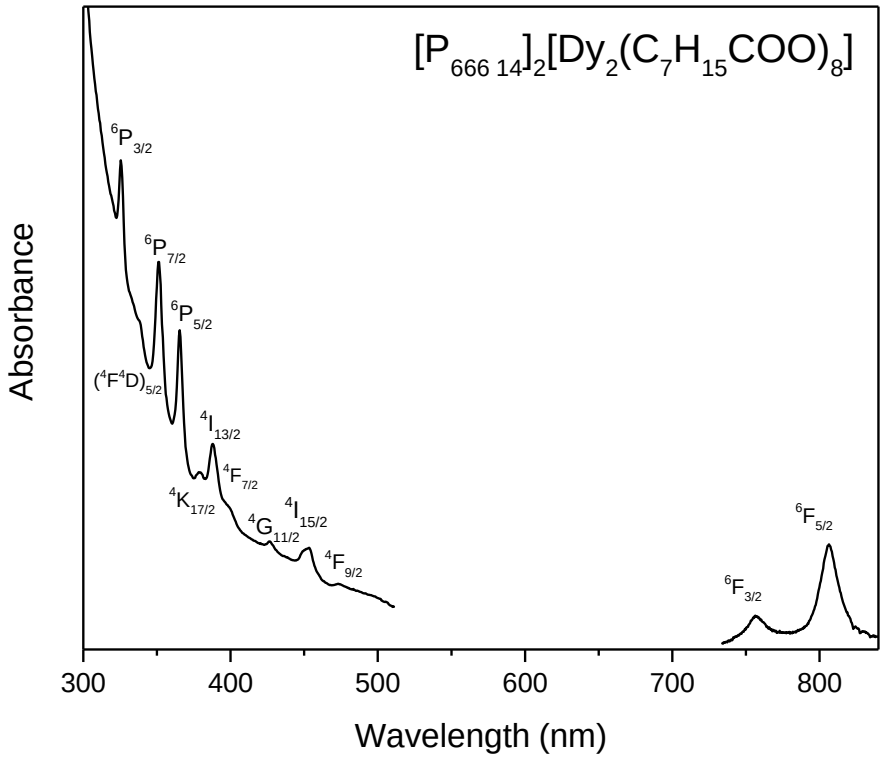

Figure 67. UV/Vis of $[P_{666\ 14}]_2[Dy_2(C_7H_{15}COO)_8]$.

Table 19. Assignment of the f – f transitions in $[P_{666\ 14}]_2[Dy_2(C_7H_{15}COO)_8]$.

Wavelength (nm)	Transition
325.73	$^6H_{15/2} \rightarrow {}^6P_{3/2}$
338.53	$^6H_{15/2} \rightarrow ({}^4F^4D)_{5/2}$
351.34	$^6H_{15/2} \rightarrow {}^6P_{7/2}$
365.75	$^6H_{15/2} \rightarrow {}^6P_{5/2}$
380.15	$^6H_{15/2} \rightarrow {}^4K_{17/2}$
388.15	$^6H_{15/2} \rightarrow {}^4I_{13/2}$
399.36	$^6H_{15/2} \rightarrow {}^4F_{7/2}$
426.56	$^6H_{15/2} \rightarrow {}^4G_{11/2}$
452.17	$^6H_{15/2} \rightarrow {}^4I_{15/2}$
474.58	$^6H_{15/2} \rightarrow {}^4F_{9/2}$
756.49	$^6H_{15/2} \rightarrow {}^6F_{3/2}$
807.49	$^6H_{15/2} \rightarrow {}^6F_{5/2}$

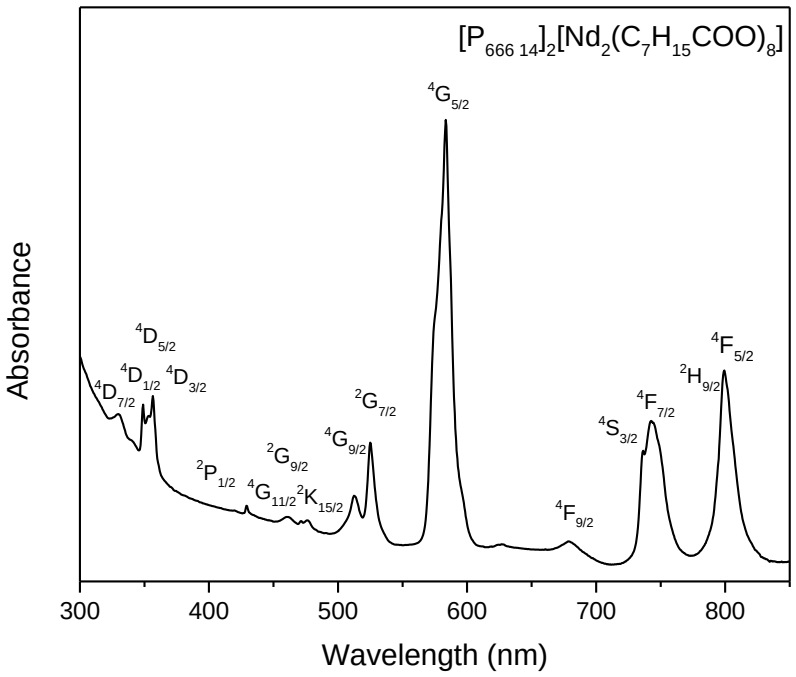

Figure 68. UV/Vis of $[P_{666\ 14}]_2[Nd_2(C_7H_{15}COO)_8]$.

Table 20. Assignment of the f – f transitions in $[P_{666\ 14}]_2[Nd_2(C_7H_{15}COO)_8]$.

Wavelength (nm)	Transition
329.34	$^4I_{9/2} \rightarrow {}^4D_{7/2}$
348.90	$^4I_{9/2} \rightarrow {}^4D_{1/2}$
352.16	$^4I_{9/2} \rightarrow {}^4D_{5/2}$
357.05	$^4I_{9/2} \rightarrow {}^4D_{3/2}$
428.78	$^4I_{9/2} \rightarrow {}^2P_{1/2}$
461.38	$^4I_{9/2} \rightarrow {}^4G_{11/2}$
471.16	$^4I_{9/2} \rightarrow {}^2G_{9/2}$
513.55	$^4I_{9/2} \rightarrow {}^2K_{15/2}$
524.96	$^4I_{9/2} \rightarrow {}^4G_{9/2}$
583.65	$^4I_{9/2} \rightarrow {}^4G_{5/2}$
679.83	$^4I_{9/2} \rightarrow {}^4F_{9/2}$
736.89	$^4I_{9/2} \rightarrow {}^4S_{3/2}$
743.41	$^4I_{9/2} \rightarrow {}^4F_{7/2}$
800.46	$^4I_{9/2} \rightarrow {}^2H_{9/2}$
800.46	$^4I_{9/2} \rightarrow {}^4F_{5/2}$

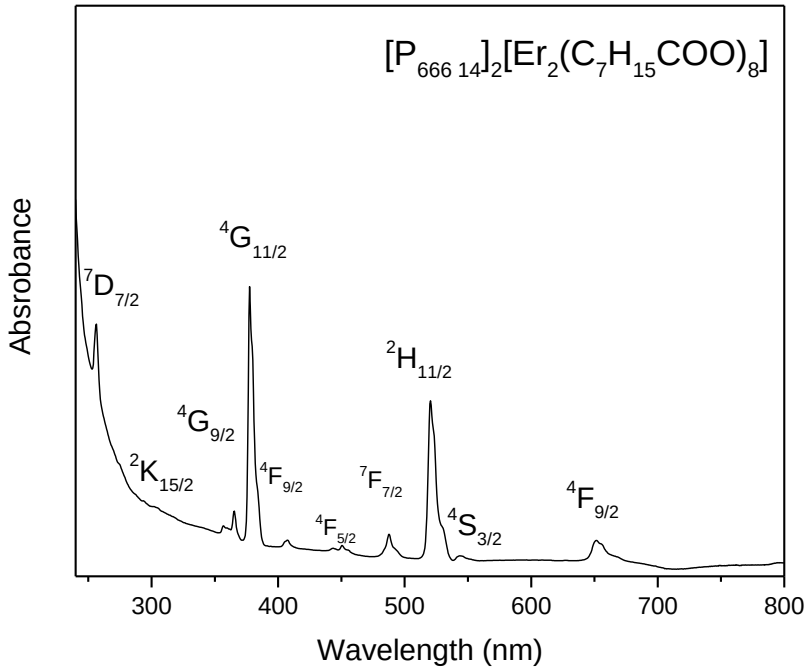

Figure 69. UV/Vis of $[P_{666\ 14}]_2[Er_2(C_7H_{15}COO)_8]$.

Table 21. Assignment of the f – f transitions in $[P_{666\ 14}]_2[Er_2(C_7H_{15}COO)_8]$.

Wavelength (nm)	Transition
653	$^4I_{15/2} \rightarrow {}^4F_{9/2}$
547	$^4I_{15/2} \rightarrow {}^4S_{3/2}$
520	$^4I_{15/2} \rightarrow {}^2H_{11/2}$
488	$^4I_{15/2} \rightarrow {}^4F_{7/2}$
452	$^4I_{15/2} \rightarrow {}^4F_{5/2}$
409	$^4I_{15/2} \rightarrow {}^4F_{9/2}$
377	$^4I_{15/2} \rightarrow {}^4G_{11/2}$
366	$^4I_{15/2} \rightarrow {}^4G_{9/2}$
356	$^4I_{15/2} \rightarrow {}^2K_{15/2}$
256	$^4I_{15/2} \rightarrow {}^7D_{7/2}$

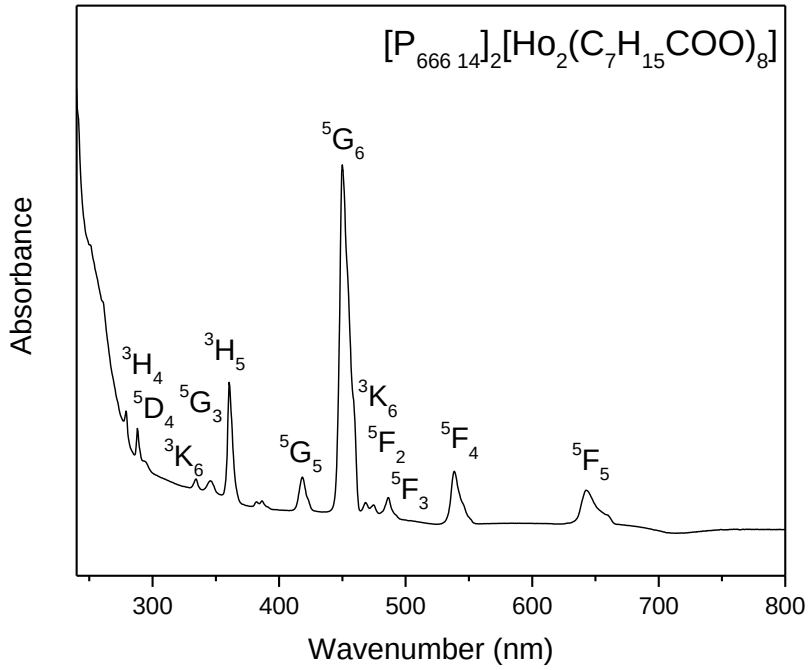

Figure 70. UV/Vis of $[P_{666\ 14}]_2[Ho_2(C_7H_{15}COO)_8]$.

Table 22. Assignment of the f – f transitions in $[P_{666\ 14}]_2[Ho_2(C_7H_{15}COO)_8]$.

Wavelength (nm)	Transition
645	$^5I_8 \rightarrow {}^5F_5$
540	$^5I_8 \rightarrow {}^5F_4$
487	$^5I_8 \rightarrow {}^5F_3$
476	$^5I_8 \rightarrow {}^4F_2$
469	$^5I_8 \rightarrow {}^3K_8$
450	$^5I_8 \rightarrow {}^5G_6$
419	$^5I_8 \rightarrow {}^5G_5$
388	$^5I_8 \rightarrow {}^5fG_4$
361	$^5I_8 \rightarrow {}^3H_5$
349	$^5I_8 \rightarrow {}^5G_3$
335	$^5I_8 \rightarrow {}^3K_6$
289	$^5I_8 \rightarrow {}^5D_4$
279	$^5I_8 \rightarrow {}^3H_4$

Overall, the spectra show the characteristic absorption spectra of the lanthanide(III) ions. However, in terms of providing structural information regarding the presence of dimeric complexes the information we obtain from UV/Vis and Infrared alike, is limited.

3.3.5 Physical properties

The thermal properties of the synthesised complexes were established my means of thermal gravimetrical analysis (TGA) and differential scanning calorimetry (DSC). TGA confirmed decomposition temperatures above 250 °C for the crystalline, glassy and liquid complexes. Increasing thermal stability is observed upon going from $[C_4Mim]_2[Ln_2(CH_3COO)_8]$ to $[P_{666\,14}]_2[Ln_2(C_7H_{15}COO)_8]$ (Table 23) as expected.[21] The TGA spectra of the dysprosium crystalline solid, glass and liquid compounds are shown as an example in Figure 71.

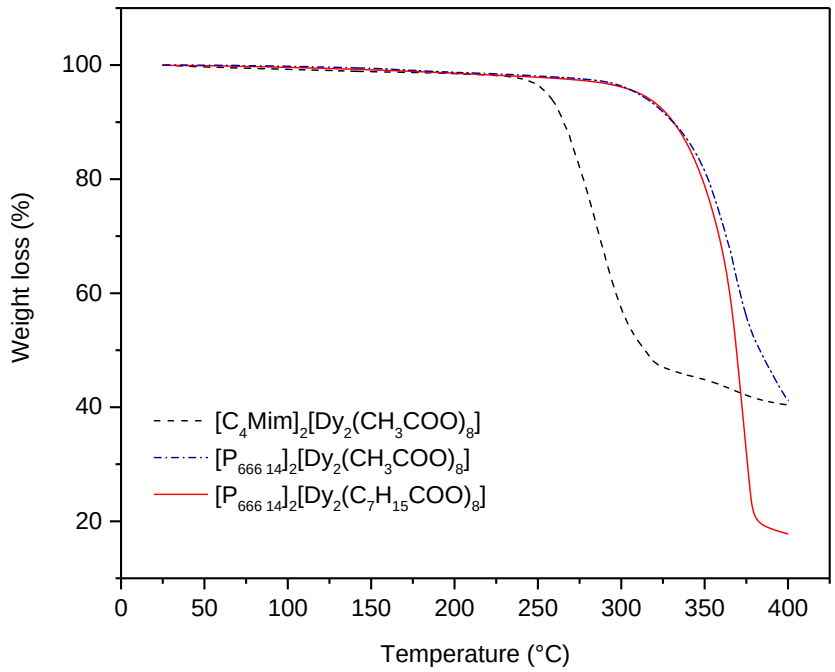

Figure 71. TGA of $[C_4Mim]_2[Dy_2(CH_3COO)_8]$ (black dash), $[P_{666\,14}]_2[Dy_2(CH_3COO)_8]$ (blue) and $[P_{666\,14}]_2[Dy_2(C_7H_{15}COO)_8]$ (red).

DSC provided information about the phase transitions present within the samples. The crystalline solids have melting points ranging from 118 °C to 134 °C. The $[P_{666\,14}]_2[Ln_2(CH_3COO)_8]$ series showed only glass transitions within the studied temperature ranges. The liquid lanthanide(III)-containing complexes (Ln = Dy and Lu), have glass transitions equal to -80.4 °C and -53.8 °C, respectively. The remaining lanthanides did not show any obvious transitions within the temperature range studied. It is possible however, the remaining liquid lanthanide(III)-containing complexes have glass transitions beyond the machine cooling limit which is -90 °C. Again, as an example the DSC profiles of dysprosium solid, glass and liquid compounds are presented in Figures 72 – 74 with data obtained, where possible, of the remaining lanthanides presented in Table 23.

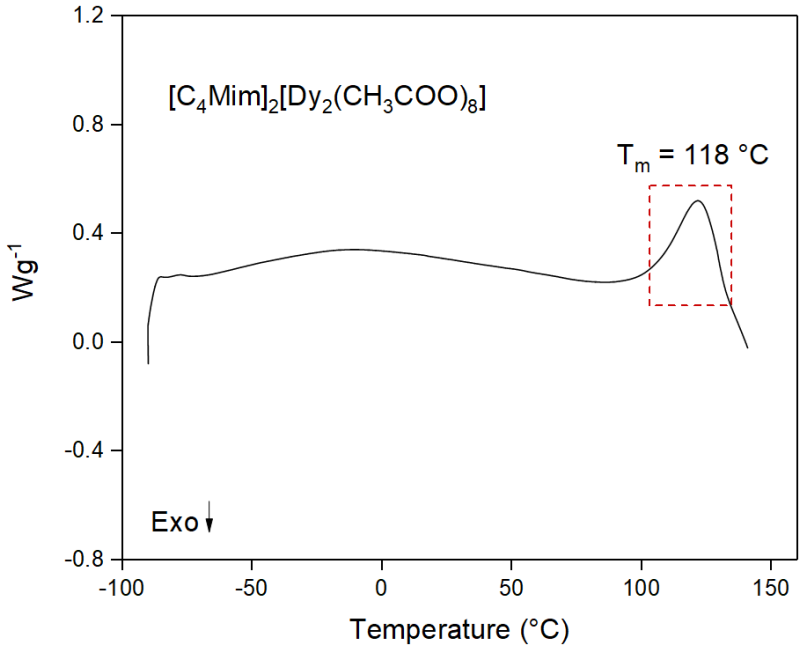

Figure 72. DSC of $[C_4Mim]_2[Dy_2(CH_3COO)_8]$.

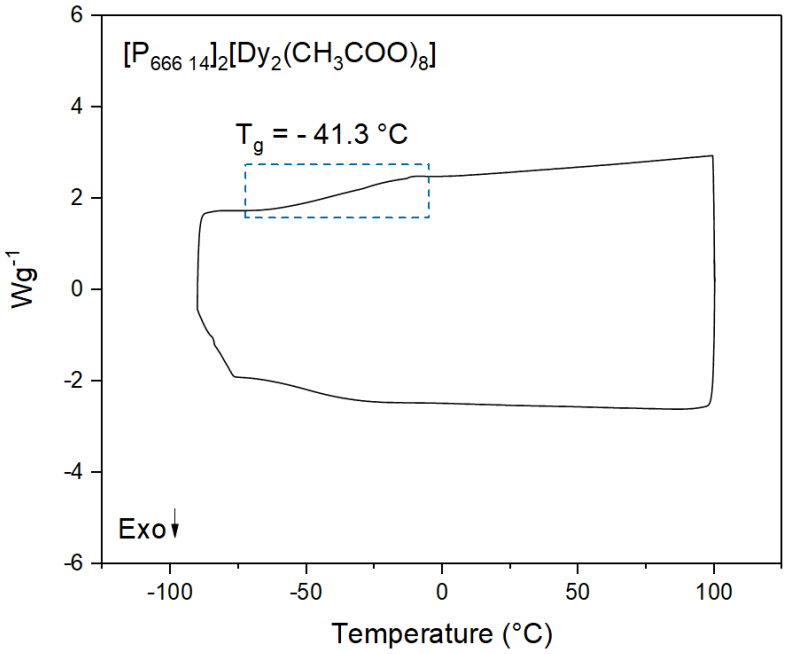

Figure 73. DSC of $[P_{666\ 14}]_2[Dy_2(CH_3COO)_8]$

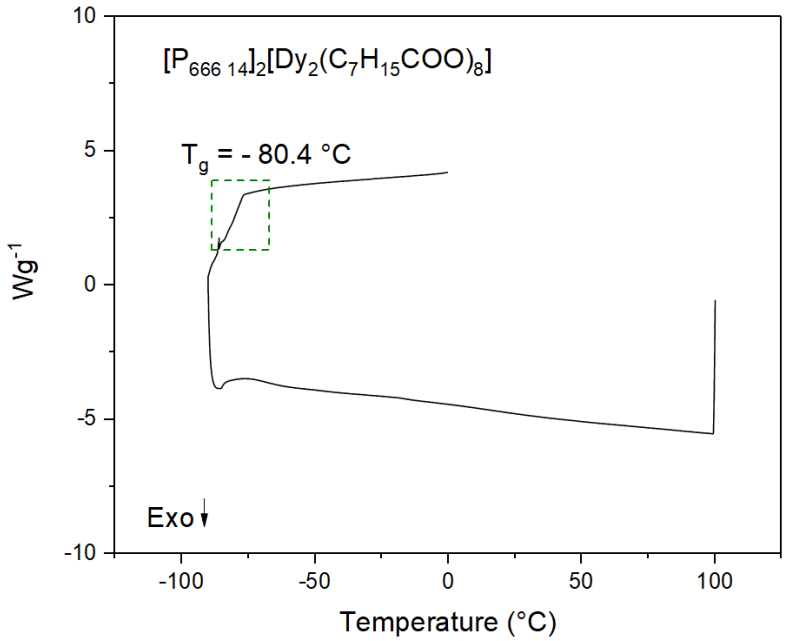

Figure 74. DSC of $[P_{666\ 14}]_2[Dy_2(C_7H_{15}COO)_8]$.

Table 23. Melting points, crystallisation temperatures, glass transitions and decomposition temperatures of the crystalline, glassy and liquid series.

Ln	Solid (°C)	Glass (°C)	Liquids (°C)
La	267 (T_{dec})	-60 (T_g), 250 (T_{dec})	
Ce			328 (T_{dec})
Nd	73 (T_m) 262 (T_{dec})	-78 (T_g),267 (T_{dec})	333 (T_{dec})
Sm	259 (T_{dec})	-75 (T_g), 244 (T_{dec})	341 (T_{dec})
Gd	260 (T_{dec})		317 (T_{dec})
Dy	118 (T_m), 292 (T_{dec})	-41.3 (T_g), 335 (T_{dec})	-80.40 (T_g), 348 (T_{dec})
Er	261 (T_{dec})		317 (T_{dec})
Y	261 (T_{dec})		322 (T_{dec})
Lu			-59.38 (T_g)

T_m = melting point, T_g = glass transition temperature, T_{dec} = decomposition temperature.

These techniques combined give an overall insight into the physical properties of the studied systems. On their own, however, they are inadequate in confirming the hypothesis that the dimeric Ln···Ln sub-units established in the solid state are evident in the glass and liquid state. To gain a more in-depth understanding of the glass and liquid properties, it was postulated that the magnetic properties of the synthesised samples would shed light on the types of interactions present within the samples and therefore may infer similarities in the structure of the lanthanide compounds.

As magnetic measurements and data analysis can be time-consuming and carried out as part of a collaboration, the magnetic properties of the crystalline solid, glass and liquid dysprosium compounds were chosen as the focus for this work.

3.3.6 DC SQUID Magnetometry

The magnetic properties of lanthanides are strongly governed by the large unquenched orbital angular momentum associated with the internal nature of the valence f orbitals.[22] Gadolinium(III) being an exception due to the half full f^7 shell and orbitally nondegenerate ground state. All remaining lanthanide(III) ions have orbitally degenerate ground states and these states are split by crystal field effects and spin-orbit coupling. Compared to transition metals the spin-orbit coupling is much larger for f-electrons whilst the crystal field effects are smaller. As a consequence, the orbital component is much more important for the lanthanides compared to the transition metals and greatly influences the magnetic anisotropy.[22]

A superconducting quantum interference device (SQUID) magnetometer was employed to monitor the magnetic moment of each dysprosium compound over a wide temperature range; it was hoped that an antiferromagnetic or ferromagnetic signature would be observed in the magnetic susceptibility of each respective compound, indicative of magnetic dimers beginning to order.

The susceptibility and inverse susceptibility as a function of temperature for the crystalline solid, liquid and glassy dysprosium compounds are presented in Figure 75.

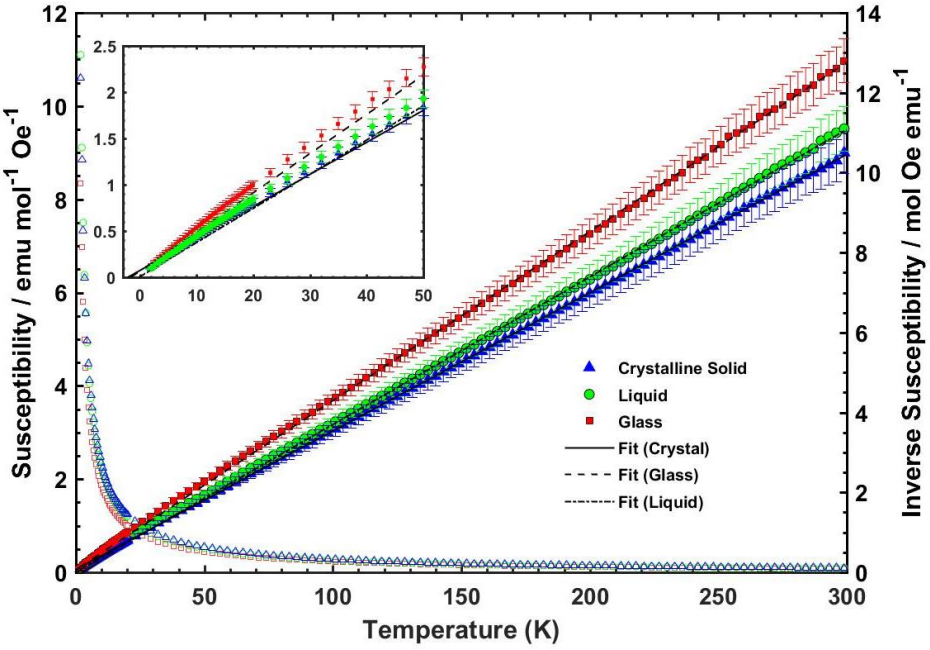

Figure 75. Susceptibility and inverse susceptibility as a function of temperature (K). Inset shows low temperature region of the inverse susceptibility in more detail.

The results obtained from fitting the inverse susceptibilities using the Curie-Weiss law (Equation 3-1) are summarized in Table 24. The Curie-Weiss law was used to fit to the inverse susceptibilities in the temperature range 50 to 300 K for all compounds, and the fitting was carried out using a linear least squares method with fits weighted to account for the variation in error as a function of temperature.

$$\chi = \frac{C}{T - \theta}$$

Equation 3-1

χ = magnetic susceptibility

C = material specific Curie constant

T = the absolute temperature (K)

θ = Weiss constant

Table 24. Curie-Weiss fit results.

Phase	Fitting Range (K)	θ (K) – Ordering Temperature	Effective Moment Per Dy Ion (Bohr Magnetons)
Solid Crystal	50 - 300	-2.1	10.7
Liquid	50 - 300	-0.2	10.4
Glass	50 - 300	-1.6	9.7

The Curie-Weiss law does not take any interactions or zero field splitting into account and therefore must be viewed cautiously. To avoid perturbing the obtained results, the fitting range was limited to 50 – 300 K, fitting to the low T region using the Curie-Weiss law is nonsensical as the compounds are not behaving as simple paramagnets below this temperature. Even at temperatures higher than 50 K one would expect the Stark levels to begin depopulating. However, all the extracted ordering temperatures (θ) are small and negative, implying deviation from paramagnetism at low temperature, this can be attributed to a range of effects, one of which may be antiferromagnetism. To examine this in more detail the susceptibility multiplied by temperature, as a function of temperature was plotted (Figure 76).

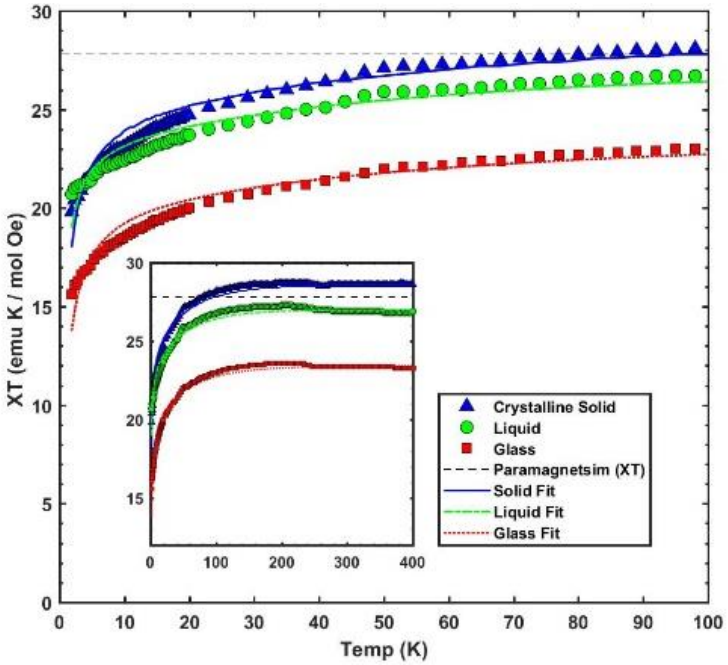

Figure 76 Susceptibility multiplied by the temperature as a function of temperature. Fit including interactions and zero-field splitting.

Figure 76 presents the susceptibility multiplied by the temperature as a function of temperature (χT), for the crystalline solid, liquid and glass compounds, along with an inset of a larger temperature window. Figure 76 shows clear deviation from non-interacting behaviour at around 100 K for each compound. The χT value that is predicted for two non-interacting Dy ions ($^6H_{15/2}$ with g = 4/3[23]) per formula unit is shown in Figure 76 by the dashed line. Considering the constant high temperature regions of Figure 76, it was found that the solid crystalline sample and the liquid sample yielded effective magnetic moments per Dy ion of 10.7 μ_B and 10.4 μ_B respectively. These values agree very well with the predicted value of 10.6 μ_B, corresponding to two Dy ions per formula unit in the ground state $^6H_{15/2}$ with g = 4/3.[23] The glass sample returned an effective magnetic moment of 9.7 μ_B per Dy ion. This is 5% lower than the expected value; however, given that the measurement

uncertainty is 5%, these values agree within uncertainty. Regarding experimentally measured magnetic moments of Dy ions, a range or 10.2 – 10.6 μ_B per Dy ion is observed in the literature[24–26], with our previous work investigating monomeric lanthanide-based ionic liquids yielding a value of 10.2 μ_B per Dy ion.[13]

We can conclude from Figure 76 that above 100 K, we see no evidence of any interactions between Dy ions. Below 100 K the measured χT values begin to deviate from that predicted for non-interacting magnetic moments. For Dy ions, one cannot simply assume that a decrease in χT values directly corresponds to an antiferromagnetic coupling; the possibility that this decrease is due to a combination of dysprosium's magnetic anisotropy, progressive depopulation of the Stark levels – arising from crystal field splitting – and the exchange interaction[27] must be entertained.

A full numerical treatment isn't viable due to the large anisotropy of the Dy ion. However, it is possible to make a rough quantitative model of the system. This method was first introduced by McPherson *et al.*[28] and has been widely used to describe the magnetic behaviour of lanthanide containing chemical compounds.[6,29–32] The crux of the model is that the magnetic energy levels (m_J) are considered to be LS coupled energy levels which are zero-field-split in an axial field geometry ($\widehat{H} = \Delta \hat{J}_Z^2$). The magnetic susceptibility of each Dy ion is then given by Equation 3-2.

$$\chi_{Dy} = \frac{Ng^2\beta^2}{4kT}\frac{A}{B}$$

Equation 3-2

N = Avogadro constant

g = g factor (scaling parameter)

β = Bohr magnetron

K = Boltzmann constant

Δ = Zero-field splitting parameter (shape of fitting)

$$A = 225e^{\frac{-225\Delta}{4kT}} + 169e^{\frac{-169\Delta}{4kT}} + 121e^{\frac{-121\Delta}{4kT}} + 81e^{\frac{-81\Delta}{4kT}} + 49e^{\frac{-49\Delta}{4kT}} + 25e^{\frac{-25\Delta}{4kT}} + 9e^{\frac{-9\Delta}{4kT}} + e^{\frac{-\Delta}{4kT}}$$

$$B = e^{\frac{-225\Delta}{4kT}} + e^{\frac{-169\Delta}{4kT}} + e^{\frac{-121\Delta}{4kT}} + e^{\frac{-81\Delta}{4kT}} + e^{\frac{-49\Delta}{4kT}} + e^{\frac{-25\Delta}{4kT}} + e^{\frac{-9\Delta}{4kT}} + e^{\frac{-\Delta}{4kT}}$$

The interactions **between** magnetic moments are simulated by incorporating the Weiss parameter according to Equation 4.2.

$$\chi_m = \frac{T}{T-\theta}2\chi_{Dy}$$

Equation 3-3

Through fitting the data it is then possible to extract numerical values for the zero-field-splitting parameter (Δ), the temperature at which magnetic ordering occurs (θ) along with the g-factor (g) for each system. Applying the model to each dataset by

means of a non-linear least squares fitting routine resulted in the values displayed in Table 25. The resulting fits are plotted on top of the experimental data points in Figure 76, showing good agreement.

Table 25. Results of the non-linear least squares fitting applied to the model developed by McPherson *et al.*

Phase / Ref	Fitting Range (K)	g - factor	Δ [a]	θ [b]
Crystalline solid	1.8 - 400	1.25	1.3	-0.69
Liquid	1.8 - 400	1.22	1.45	-0.42
Glass	1.8 - 400	1.14	1.26	-0.88
Binuclear Mo(V)–Dy(III) [6]	1.8 - 400	1.34	92.8	+ 0.9
Mn(III) - Dy(III) complexes[5]	1.8 - 400	1.37	1.4	- 0.02K[c]

[a] Δ = zero-field splitting parameter (cm^{-1}) x 10^{-3}; [b]θ = Magnetic Ordering Temperature (K); [C] converted the wavenumber to Temperature for comparison.

The fit parameters from equations [3.2] and [3.3] are presented in Table 25 for all three samples, alongside parameters for two compounds from literature. The numerical value of the zero-field splitting parameter obtained for all three compounds are very similar, implying they experience very similar zero field splitting, as expected since the Dy ions in each respective compound are in very similar coordination environments. It is the ligands that differ and give rise to the observed phase changes between compounds. The zero-field splitting parameters found for the samples here are of the same order of magnitude as those reported in literature.[5,6] The magnetic ordering temperatures obtained for all compounds are under 1 K; this is as expected due to the localised nature of the 4f magnetism exhibited by rare-earth ions. The Weiss parameters for all three compounds are

identical within uncertainty. This implies that the distance between the ions are the same, since the magnetic interaction decreases with distance between moments.

Simply fitting using equation (3.1), ignoring the Weiss parameter for antiferromagnetic interaction, **does not** accurately reproduce the data as seen in Figure 77.

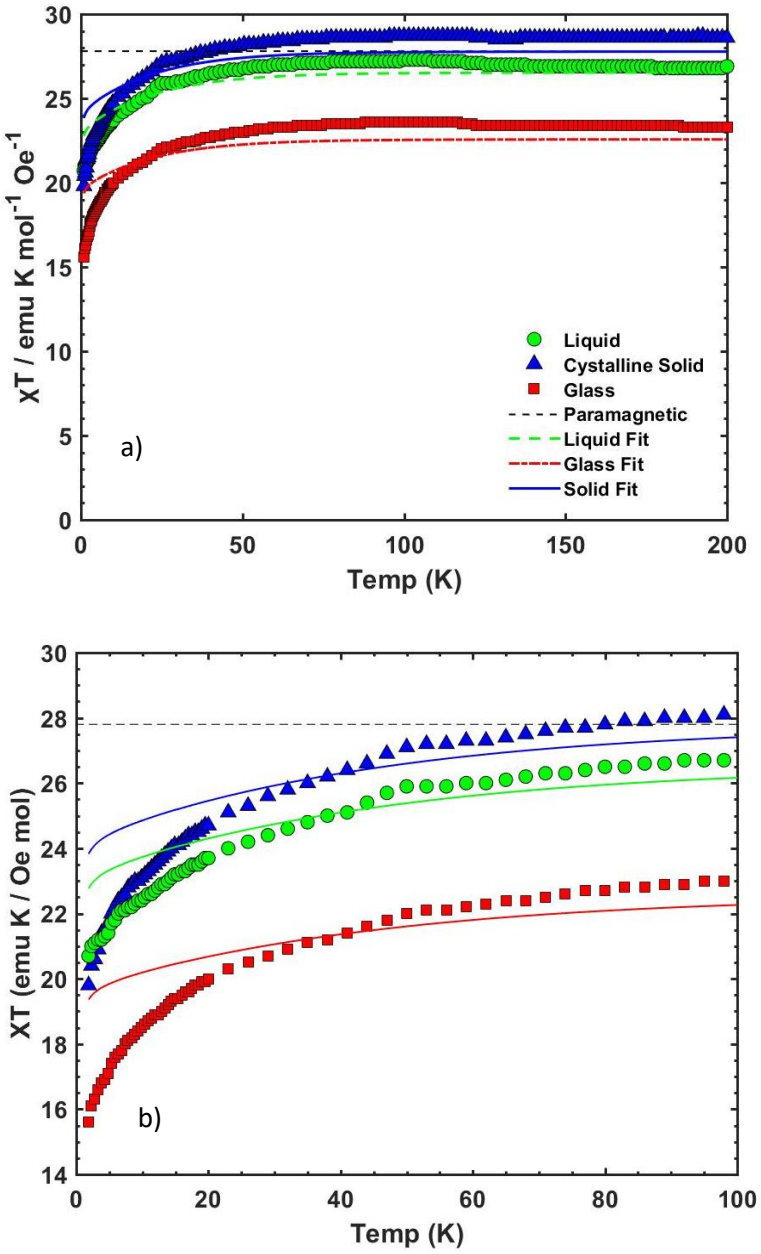

Figure 77. Susceptibility multiplied by temperature, as a function of temperature (a). Fit only including zero field interactions. Image b) shows the low temperature region of image a) in greater detail.

Hence, the decrease in χT at low temperatures must be a combination of both depopulation (zero field splitting) effects and antiferromagnetism. This holds for all the datasets and is consistent with magnetic dimers being present in all the measured compounds, with magnetic ordering temperatures under 1 K. It must be noted this is the first demonstration of a dimeric lanthanide based magnetic ionic liquid, exhibiting a weak antiferromagnetic interaction within the magnetic dimers at low temperatures.

3.4 Conclusion

Taking advantage of the ability to fine-tune the anion and cation structures of ionic liquids has led to the ability to synthesise interesting solid, glass and most importantly, liquid di-nuclear lanthanide(III)- containing ionic compounds. In addition, depending on the method of crystallisation tetrameric and polymeric structures were also obtained. Single crystal X-ray diffraction confirmed the presence of the dimeric Ln (III) complexes in the solid state. Various techniques were employed to ascertain whether the dimeric Ln (III) complexes we obtain in the crystalline solid are in fact maintained in the glass and liquid states. Of all the techniques at our disposal it was SQUID magnetometry which enabled us to infer structure in the liquid and glassy states. Taking the crystalline solid, glassy and liquid dysprosium compounds as an example, magnetic measurements enabled comparison of the susceptibilities at low temperatures ultimately giving insight into whether dimers had formed in all complexes. The same antiferromagnetic signature was observed in all dysprosium compounds, a strong indicator that the magnetic dimers formed in the crystalline solid were in fact formed in the glass and liquid state as well.

Given the crystalline solid, glass and liquid dysprosium compounds displayed this behaviour, analysis of the magnetic properties of the remaining lanthanides in the series will be the focus going forward. The crystalline solid, glass and liquid gadolinium compounds are considered a sensible place to start magnetic measurements, appealing, due to the large local spin and the lack of orbital contribution to the magnetic moment.[33]

3.5 Methods

3.5.1 Materials and instrumentation

$Ln(CH_3COO)_3.4H_2O$ (Ln = La, Nd, Eu, Gd, Dy, Ho, Er, Lu and Y), chemical grade, 99.9% and sodium acetate anhydrous, 99% were purchased from Alfa Aesar. $[C_4Mim][CH_3COO]$, ≥ 95% was purchased from Sigma Aldrich. $[P_{666\ 14}][Cl]$ was donated from Cytec and used without further purification. Nuclear magnetic resonance (NMR) spectra were recorded on a Bruker 400 MHz ultrashield spectrometer. TGA and DSC were conducted on a TA Q5000 and Q2000 equipped with a refrigerated cooling system 90 (temperature range -90 – 150 °C) and auto-sampler, respectively. In addition, elemental analysis was determined using a PerkinElmer 2400 series 2 CHNS/O analyser. FTIR was carried out on a PerkinElmer Spectrum 100 spectrometer and UV/Vis spectra were recorded on an Agilent, Cary 60 spectrophotometer.

3.5.2 X-ray crystallographical analysis

Crystal data collection was performed on a Rigaku Single Crystal X-ray diffractometer, equipped with cryostat. Measurements were carried out at 100 K using a Cu Kα, monochromator, λ = 1.54184 Å. Using Olex2, the structure was solved with the ShelXT structure solution program using Intrinsic Phasing and further refined with the ShelXL refinement package using least squares minimisation.

3.5.3 D.C. superconducting quantum interference device magnetometry

The DC magnetic susceptibility of samples presented in this paper were measured using a Quantum Design MPMS XL SQUID, utilizing the reciprocal sample option (RSO). The magnetization was measured over a temperature range of 1.8 to 400 K. All samples were zero-field cooled from 400 K down to 1.8 K, and upon reaching the lowest temperature a field of 500 Oe was applied. The sample was then heated from 1.8 to 400 K in the applied field. Measurements of the magnetization were taken in 0.5 K intervals (when $T < 20$ K) and 3 K intervals (when $T > 20$ K) and the temperature was allowed to stabilize prior to any measurements being made. For verification of the paramagnetic behaviour (non-hysteretic behaviour) of the samples, data were collected upon cooling and warming and no differences were observed between the two protocols. Diamagnetic corrections were calculated for the relevant chemical structures using Pascal's constants and applied to all data. The measurement of the magnetic moment in our MPMS SQUID has an uncertainty of 5 % which arises mainly from differences in sample mounting and cannot be eliminated.

3.5.4 Synthesis of $[C_4Mim]_2[Ln_2(CH_3COO)_8]$

To a GC sample vial $[C_4Mim][CH_3COO]$ (59 mg, 0.297 mmol) and $Ln(CH_3COO)_3 \cdot xH_2O$ (0.297 mmol) were added. The vial was sealed and wrapped in aluminium foil and placed in a Reacti-Therm to be slowly heated to the molten state. The vial was subsequently cooled over a period of 48 h to allow $[C_4Mim]_2[Ln_2(CH_3COO)_8]$ crystals to form.

Table 26. Elemental analysis of $[C_4Mim]_2[Ln_2(CH_3COO)_8]$ compounds.

$[C_4Mim]_2[Ln_2(CH_3COO)_8]$	C	H	N
Nd	36.98 (35.48)	5.24 (4.44)	5.39 (5.24)
Dy	35.73 (33.98)	5.06 (4.84)	5.21 (5.69)
Dy	35.73 (35.37)	5.06 (4.99)	5.21 (5.81)
La	37.37 (36.94)	5.29 (5.27)	5.45 (5.61)
Sm	36.55 (32.94)	5.18 (5.03)	5.33 (4.40)
Gd	36.08 (33.47)	5.11(4.47)	5.26 (4.48)
Er	35.41 (35.37)	5.02 (4.93)	5.16 (5.12)
Y	41.39 (41.29)	5.86 (5.69)	6.03 (6.01)

3.5.5 Synthesis of $[P_{666\ 14}]_2[Ln_2(CH_3COO)_8]$

$[P_{666\ 14}][CH_3COO]$ was prepared as follows; To a solution of $[P_{666\ 14}][Cl]$ (5.1 g, 9.82 mmol) in ethanol, $Na(CH_3COO)$ (0.81 g, 9.82 mmol) dissolved in ethanol was added. The reaction was left to stir for 48 hours at room temperature. Büchner filtration was used to remove the by-product NaCl. The ethanol was removed by rotary evaporation at 60 °C. Centrifugation was necessary to further remove NaCl. The final product was dried under vacuum at 70 °C. A pale yellow viscous liquid was obtained. ^1H NMR (400 MHz, $CDCl_3$): δ = 2.43 (m, 8 H), 1.94 (s, 3 H), 1.47 – 1.24 (m, 48 H), 0.90 – 0.85 (m, 12

H) ppm. ^{13}C NMR (100 MHz, $CDCl_3$): δ = 176.86 (COO), 31.91 (CH_2COO), 30.90 – 21.88 (CH_2), 19.17 (CH_3), 14.10 (PCH_2) ppm. ^{31}P NMR (162 MHz, $CDCl_3$): δ = 33.02 ppm.

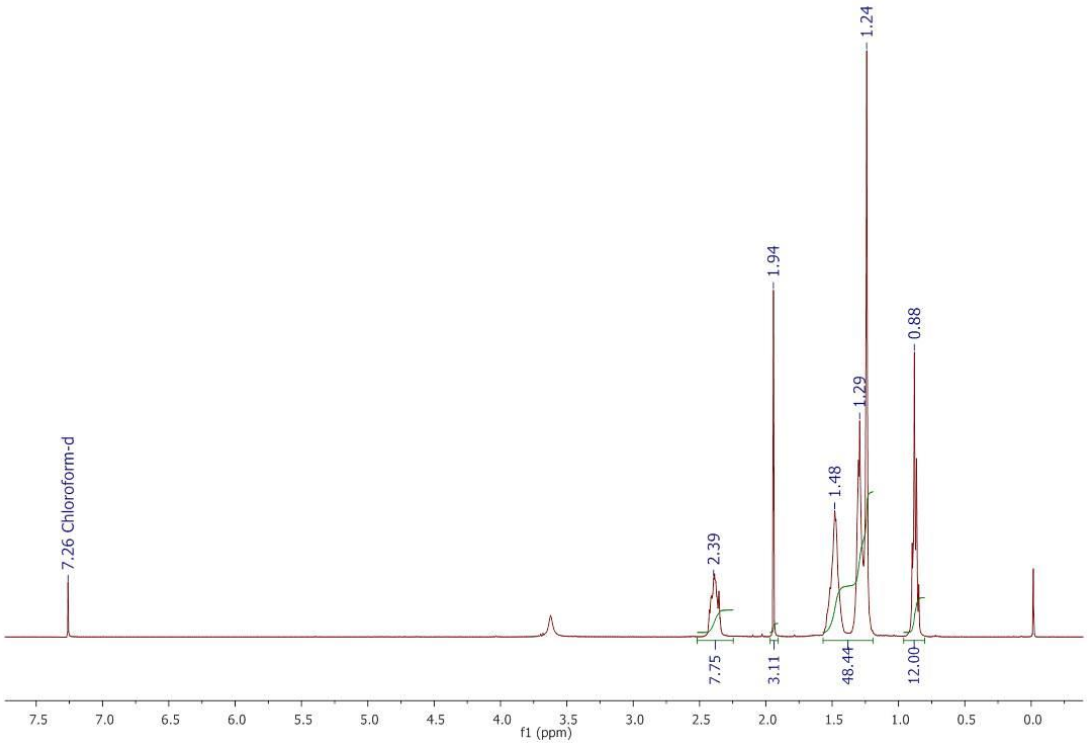

Figure 78. ^{1}H-NMR of [$P_{666\ 14}$][CH_3COO]

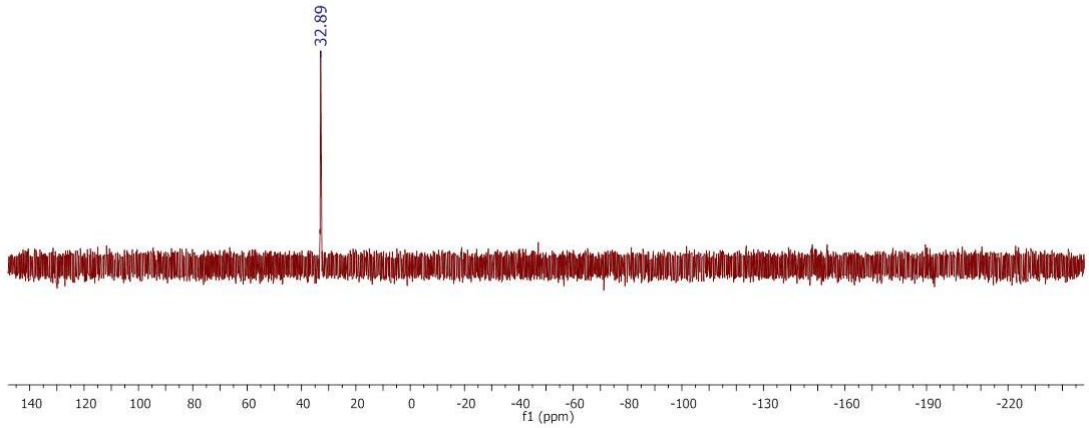

Figure 79. ^{31}P-NMR of $[P_{666\ 14}][CH_3COO]$**.**

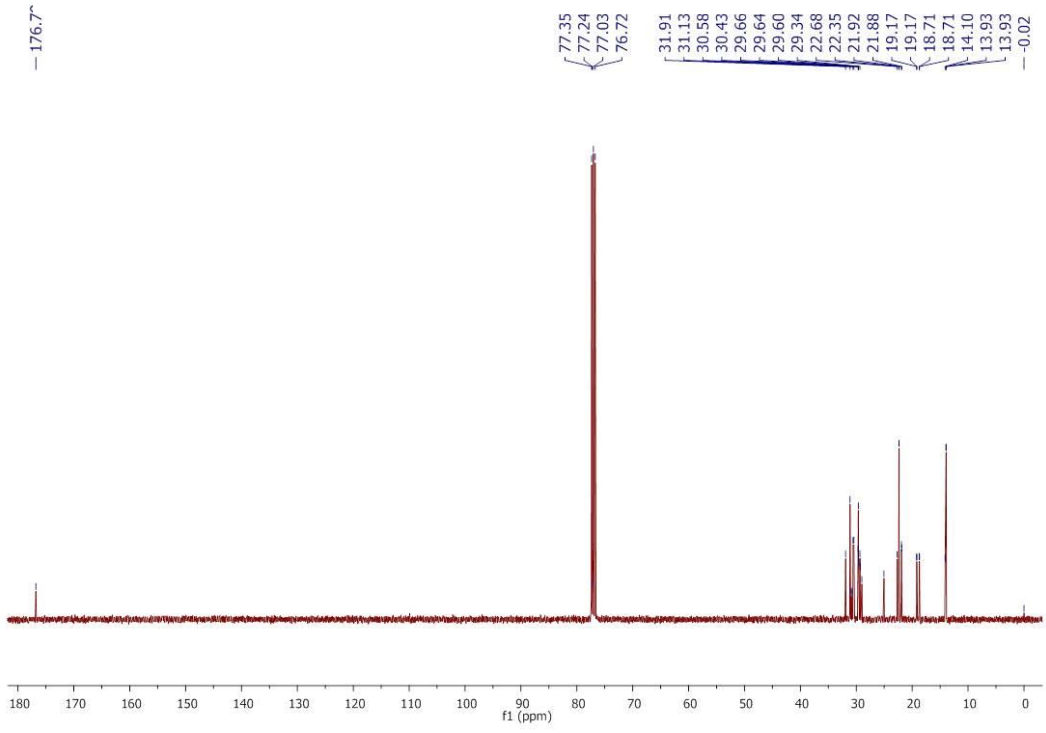

Figure 80. ^{13}C- NMR of $[P_{666\ 14}][CH_3COO]$**.**

In a sealed vial $[P_{666\,14}][CH_3COO]$ (166 mg, 0.31 mmol) was then added to $Ln(CH_3COO)_3{\cdot}4H_2O$ (0.31 mmol) and the reaction mixture was stirred for 24 hours at 80 °C.

Table 27. Elemental analysis of the synthesized $[P_{666\,14}]_2[Ln_2(CH_3COO)_8]$ compounds. Actual (theoretical) %.

$[P_{666\,14}]_2[Ln_2(CH_3COO)_8]$	C (%)	H (%)
Dy	53.89 (54.43)	9.66 (9.14)
La	55.00 (55.93)	9.30 (9.39)
Sm	55.15 (55.20)	9.50 (9.26)
Gd	52.87 (54.76)	9.02 (9.19)
Er	53.87 (54.15)	9.19 (9.09)
Y	59.56 (59.39)	10.09 (9.97)

3.5.6 Powder XRD of the $[C_4Mim]_2[Ln_2(CH_3COO)_8]$

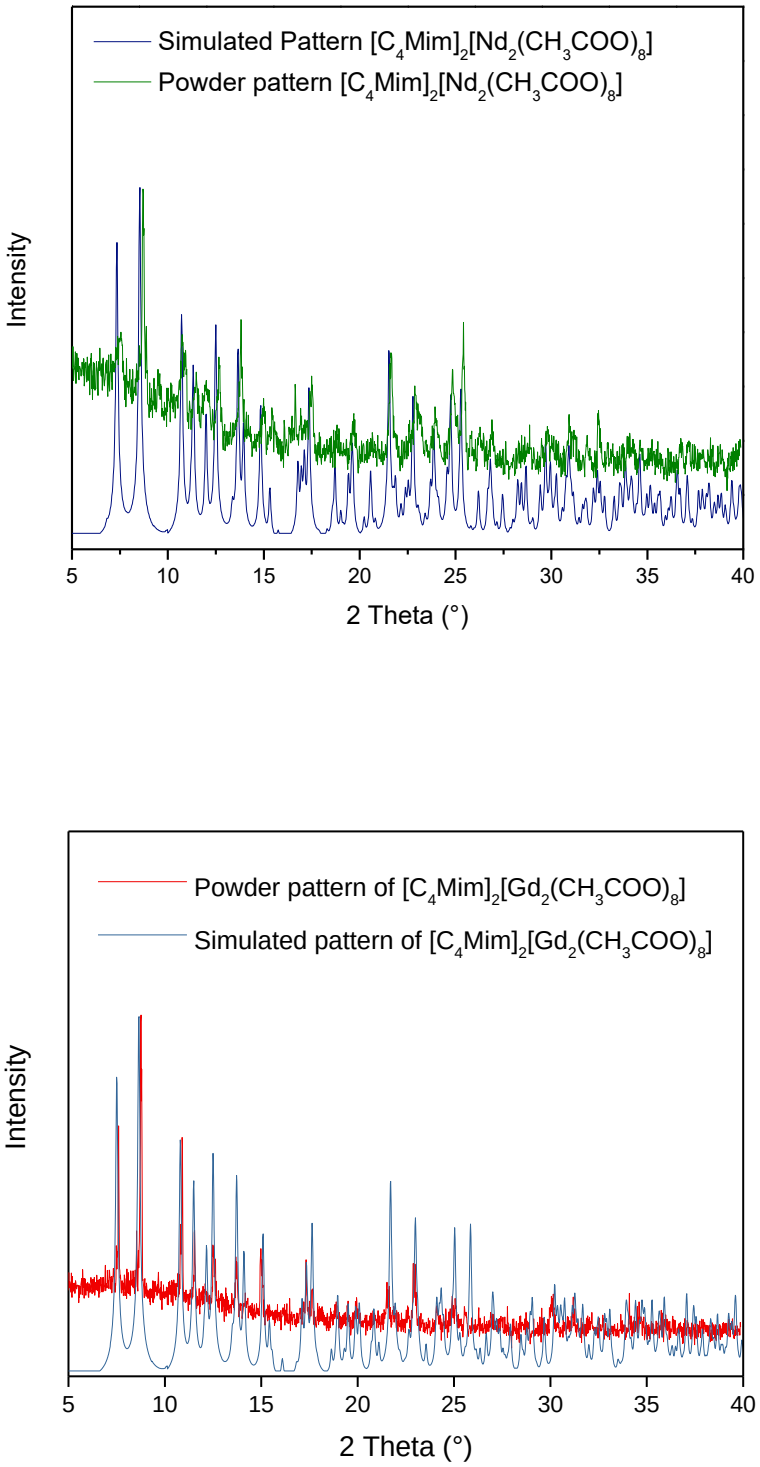

Figure 81. Powder XRD of $[C_4Mim]_2[Nd_2(CH_3COO)_8]$ (top) and $[C_4Mim]_2[Gd_2(CH_3COO)_8]$ (bottom).

3.5.7 Synthesis of $[P_{666\,14}]_2[Ln_2(C_7H_{15}COO)_8]$

$[P_{666\,14}][C_7H_{15}COO]$ and $Ln(C_7H_{15}COO)_3{\cdot}xH_2O$ were prepared according to previously reported literature[34,35] described as follows; octanoic acid (5.53 g, 38.4 mmol) and $[P_{666\,14}]Cl$ (19.94 g, 38.4 mmol) were dissolved in 75 mL of hexane. A solution of NaOH (1.54 g, 38.4 mmol, in 75 mL of H_2O) was added dropwise at room temperature (RT). The mixture was stirred at RT overnight. The upper organic phase was separated and washed four times with H_2O. Solvent was removed by rotary evaporator and the product was dried at 70°C under vacuum for 24 hours to yield $[P_{666\,14}][C_7H_{15}COO]$ as a viscous liquid. $[P_{666\,14}][C_7H_{15}COO]$: ^{1}H NMR (400 MHz, $CDCl_3$) δ 2.44 (m, *J* = 14.3 Hz, 8 H), 2.15 (t, *J* = 15.6 Hz, 2 H), 1.58 – 1.45 (m, 18 H), 1.32 – 1.21 (m, 40 H), 0.86 – 0.80 (m, 15 H) ppm. ^{13}C NMR (100 MHz, $CDCl_3$): δ = 180.40 (COO), 39.30 (CH_2COO), 31.94 – 21.91 (CH_2), 19.15 (CH_3), 14.07 (P-CH_2) ppm. ^{31}P NMR (162 MHz, $CDCl_3$): δ = 32.98 ppm. Anal. Calcd for $C_{80}H_{160}O_{16}P_2Dy_2$: C, 63.05; H, 10.58. Found: C, 65.39; H, 11.46.

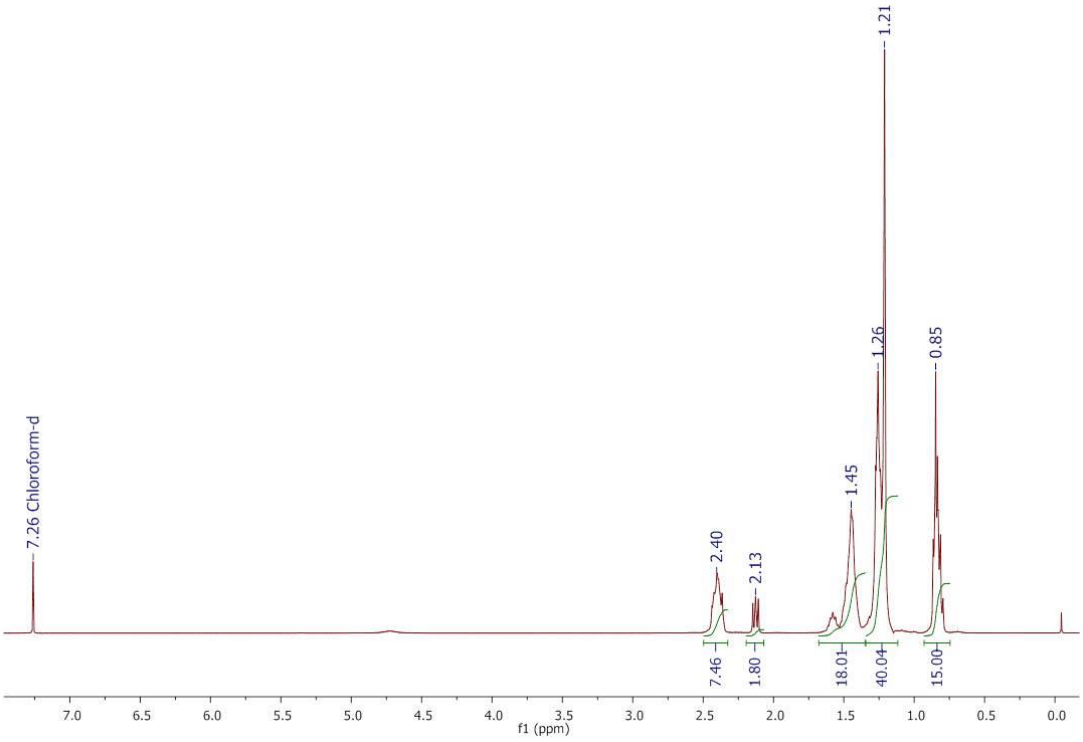

Figure 82. ^{1}H-NMR of $[P_{666\ 14}][C_7H_{15}COO]$.

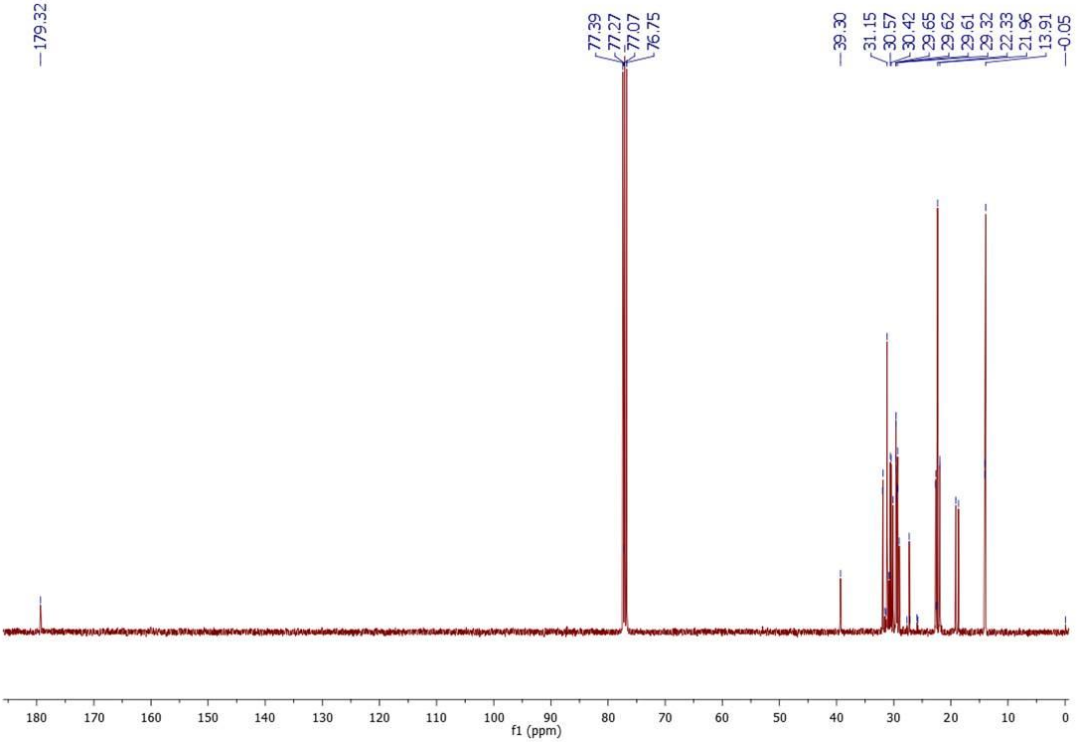

Figure 83. ^{13}C-NMR of $[P_{666\ 14}][C_7H_{15}COO]$.

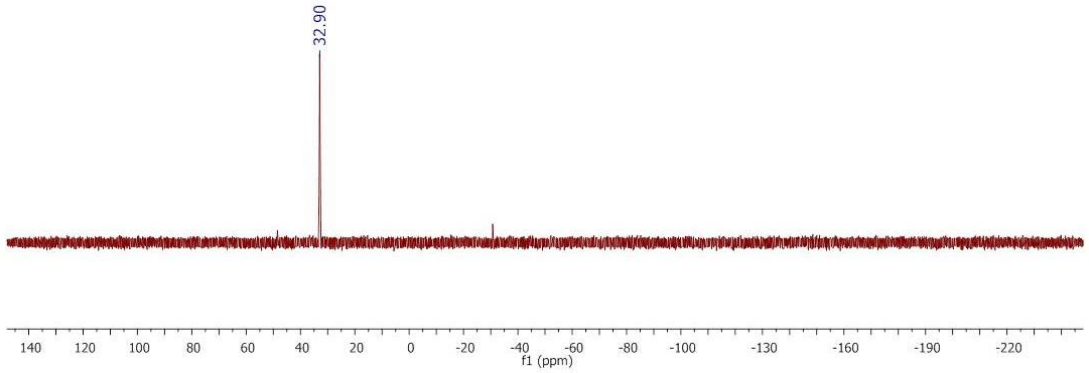

Figure 84. ^{31}P-NMR of $[P_{666\ 14}][C_7H_{15}COO]$.

$Ln(C_7H_{15}COO)_3$ was synthesised according to previously reported syntheses by Binnemans *et al.*[35] Octanoic acid was dissolved in an ethanol/water mixture and transformed to sodium octanoate by adding an equivalent amount of 1 M/L NaOH standard aqueous solution (addition dropwise *via* a burette). Ln (III) nitrate hydrate was dissolved in 100 mL ethanol/water mixture and added dropwise to the sodium octanoate solution. Upon addition a white precipitate formed immediately. The reaction was left to stir for a further 1 hour after which the white precipitate was filtered and washed with ethanol/water mixture and the product was dried overnight at 30°C. Ln octanoate was obtained as a fine powder.

Table 28. Elemental analysis of lanthanide octanoate salts. Actual (theoretical) %.

Ln octanoate	C	H
Nd	49.72 (50.23)	7.26 (7.90)
Dy	47.61 (48.68)	7.91 (7.66)
La	51.47 (50.70)	8.96 (7.98)
Sm	49.47 (49.70)	8.02 (7.73)
Er	47.23 (49.30)	8.00 (7.60)
Y	54.14 (55.59)	8.63 (8.75)
Pr	48.28 (50.53)	8.02 (7.95)
Ce	48.70 (50.60)	8.02 (7.96)

$[P_{666\ 14}]_2[Ln_2(C_7H_{15}COO)_8]$: In a sealed vial $[P_{666\ 14}][C_7H_{15}COO]$ (166 mg, 0.26 mmol) was added to $Ln(C_7H_{15}COO)_3 \cdot xH_2O$ (0.26 mmol) and the reaction mixture was stirred in ethanol for 24 hours at 70 °C. $[P_{666\ 14}]_2[Ln_2(C_7H_{15}COO)_8]$ was obtained as viscous liquids as seen in Figure 52.

Table 29. Elemental analysis of $[P_{666\ 14}]_2[Ln_2(C_7H_{15}COO)_8]$ compounds. Actual (theoretical) %.

$[P_{666\ 14}]_2[Ln_2(C_7H_{15}COO)_8]$	C (%)	H (%)
Nd	64.18 (63.90)	11.42 (11.10)
Dy	65.39 (63.05)	11.46 (10.58)
La	64.25 (64.29)	10.98 (10.77)
Sm	63.38 (63.50)	11.07 (11.10)
Gd	64.23 (63.32)	10.90 (10.63)
Er	61.81 (62.80)	10.01 (10.54)
Y	66.23 (67.47)	10.88 (10.43)
Ho	63.14 (62.92)	10.51 (10.56)
Pr	62.78 (64.19)	10.74 (10.77)
Ce	62.98 (64.23)	10.24 (10.78)

3.5.8 Pascal Correction

3.5.8.1 $[C_4Mim]_2[Dy_2(CH_3COO)_8]$

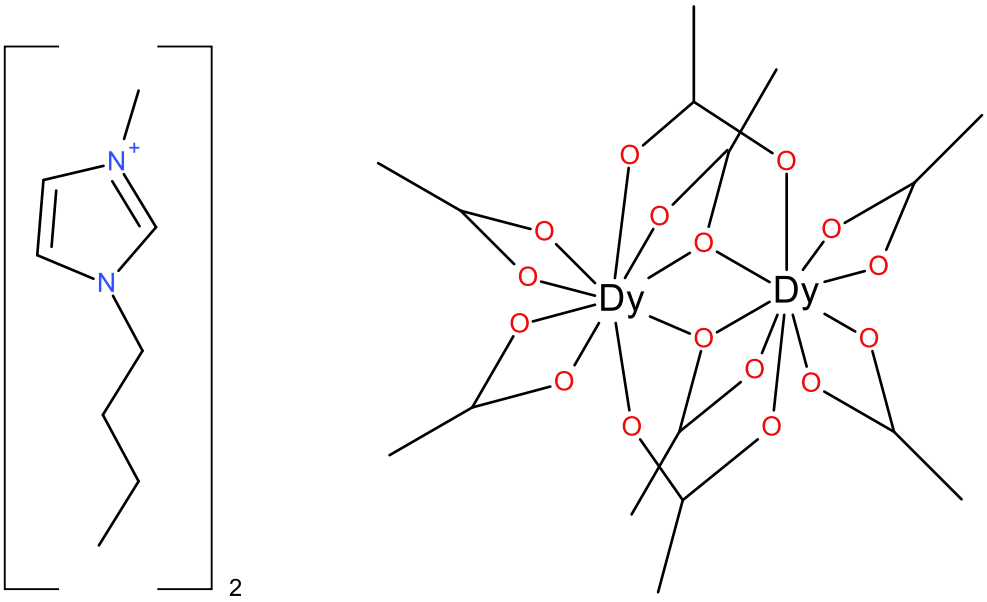

Molecular formula: $C_{32}H_{54}N_4O_{16}Dy_2$

Molecular weight: 1075.79 g/mol

Pascal Correction

$$\chi_D = \Sigma \chi_{Di} + \Sigma \lambda_i$$

1-butyl-3-methylimidazolium

C_4Mim		***10^{-6} emu mol^{-1}**	***10^{-6} emu mol^{-1}**
χ_{Di}	5 C	5 * (-6)	-30
	3 C_{ring}	3 * (-6.24)	-18.72
	15 H	15 * (-2.93)	-43.95
	2 N_{ring}	2 * (-4.61)	-9.22
λ	imidazole	(+ 8)	+8
χ_D			-93.89

2 χ_D[C_4Mim] + 2 χ_D (Dy) + 8 χ_D (OAc^-)

2(-93.89) + 2 (-19) + 8 (-31.5)

= 477.78 * 10^{-6} emu mol^{-1}

= 0.00047778 emu mol^{-1}

3.5.8.2 $[P_{666\,14}]_2[Dy_2(CH_3COO)_8]$

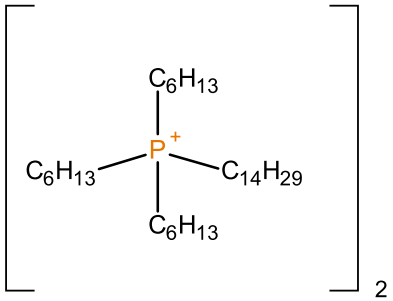

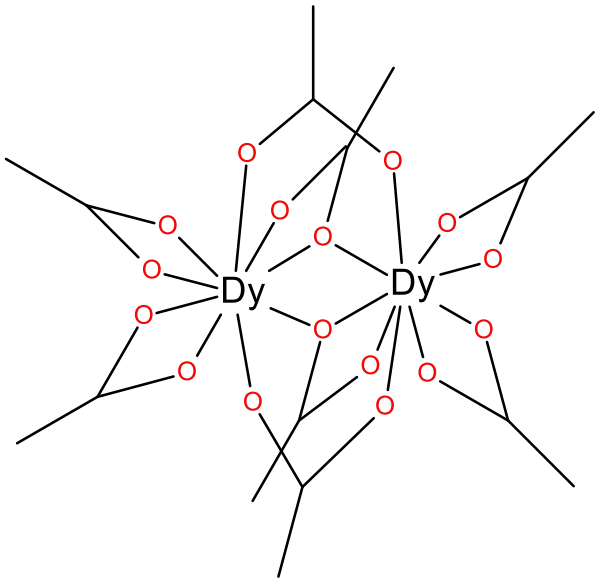

Molecular formula: $C_{80}H_{160}O_{16}P_2Dy_2$

Molecular weight: 1765.06 g/mol

2 χ_D[P] + 64 χ_D (C) + 136 χ_D (H) + 2 χ_D (Dy) + 8 χ_D (OAc^-)

2 (-26.3) + 64 (-6) + 136 (-2.93) + 2 (-19) + 8 (-31.5)

= -1125.08 * 10^{-6} emu mol^{-1}

= 0.00112508 emu mol^{-1}

3.5.8.3 $[P_{666\,14}]_2[Dy_2(C_7H_{15}COO)_8]$

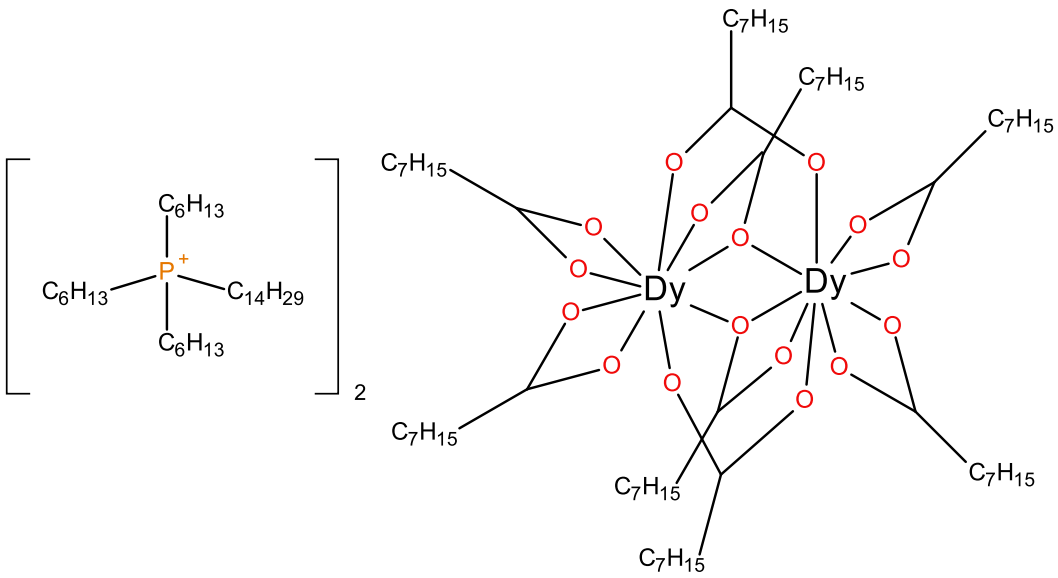

Molecular formula: $C_{128}H_{256}O_{16}Dy_2$

Molecular Weight: 2438.3 g/mol

Octanoate : $C_7H_{15}CO_2^-$

$C_7H_{15}CO_2^-$		$*10^{-6}$ emu mol^{-1}	$*10^{-6}$ emu mol^{-1}
χ_{Di}	8 C	8 * (-6)	-30
	15 H	15 * (-2.93)	-43.95
	Carboxylate O_2	(-7.95)	-7.95
χ_D			-99.9

2 χ_D[P] + 64 χ_D (C) + 136 χ_D (H) + 2 χ_D (Dy) + 8 χ_D ($C_7H_{15}COO$)

2 (-26.3) + 64 (-6) + 136 (-2.93) + 2 (-19) + 8 (-99.9)

= -1672.28 * 10^{-6} emu mol^{-1}

= 0.00167228 emu mol^{-1}

3.6 References

1. Bünzli, J.-C. G. & Piguet, C. Taking advantage of luminescent lanthanide ions. *Chem. Soc. Rev.* **34,** 1048 - 1077 (2005).

2. Mallick, B., Balke, B., Felser, C. & Mudring, A.-V. Dysprosium Room-Temperature Ionic Liquids with Strong Luminescence and Response to Magnetic Fields. *Angew. Chemie Int. Ed.* **47,** 7635–7638 (2008).

3. Prodius, D. & Mudring, A.-V. Coordination Chemistry in Rare Earth Containing Ionic Liquids. *Handb. Phys. Chem. Rare Earths* **50,** 395 - 420 (2016).

4. Costes, J.-P., Dahan, F., Dupuis, A., Lagrave, S. & Laurent, J.-P. Homo- (4f, 4f) and Heterodimetallic (4f, 4f') Complexes. The First Structurally Characterized Example of a Heterodimetallic (Yb, La) Complex (1'). Magnetic Properties of 1' and of a Homodinuclear (Gd, Gd) Analogue. *Inorg. Chem.* **37,** 153–155 (1998).

5. Liao, Yu-Zhang Tong, Qing-Lun Wang, Ai-Ping Zhang, Yue Ma, Shi-Ping Yan, Guang-Ming Yang, Peng Cheng, D.-Z. Crystal structure and magnetism of two new 3d–4f complexes contain Dy 3 atoms.pdf. *Inorg. Chem. Commun.* **32,** 32–36 (2013).

6. Ren, S. *et al.* A new binuclear MoV-DyIIIassembly and its magnetism. *Inorg. Chem. Commun.* **14,** 1124–1127 (2011).

7. Ouchi, A., Suzuki, Y., Ohki, Y. & Koizumi, Y. Structure of rare earth carboxylates in dimeric and polymeric forms. *Coord. Chem. Rev.* **92,** 29–43 (1988).

8. Mironov, V. S., Galyametdinov, Y. G., Ceulemans, A., Görller-Walrand, C. & Binnemans, K. Room-temperature magnetic anisotropy of lanthanide complexes: A model study for various coordination polyhedra. *J. Chem. Phys.* **116,** 4673 - 4685 (2002).

9. Woodruff, D. N., Winpenny, R. E. P. & Layfield, R. A. Lanthanide single-molecule magnets. *Chem. Rev.* **113,** 5110–5148 (2013).

10. Prodius, D. *et al.* Breaking the paradigm: record quindecim charged magnetic ionic liquids. *Mater. Horiz.* **4**, 217 - 221 (2017). doi:10.1039/C6MH00468G.

11. Nockemann, P. *et al.* Anionic rare-earth thiocyanate complexes as building blocks for low-melting metal-containing ionic liquids. *J. Am. Chem. Soc.* **128,** 13658–13659 (2006).

12. Prodius, D. *et al.* Evidence of slow relaxation of magnetization in dysprosium-based ionic liquids. *Chem. Commun. Chem. Commun* **49,** 9215–9217 (2013).

13. Alvarez-Vicente, J. *et al.* Easily Accessible Rare-Earth-Containing Phosphonium Room-Temperature Ionic Liquids: EXAFS, Luminescence, and Magnetic Properties. *J. Phys. Chem. B* **120,** 5301–5311 (2016).

14. Monson, T. C. *et al.* Unprecedented magnetic behaviour in lanthanide-based ionic liquids. *Chem. Commun.* **53,** 11682–11685 (2017).

15. Estager, J., Holbrey, J. D. & Swad Ba-Kwa Ny, M. Chem Soc Rev Halometallate ionic liquids – revisited. *Chem. Soc. Rev. Chem. Soc. Rev* **43,** 737–962 (2014).

16. Hardacre, C. Application of EXAFS to Molten Salts and Ionic Liquid Technology. *Annu. Rev. Mater. Res.* **35,** 29–49 (2005).

17. Nockemann, P. *et al.* Speciation of rare-earth metal complexes in ionic liquids: A multiple-technique approach. *Chem. Eur. J.* **15,** 1449–1461 (2009).

18. Deacon, G. B. & Phillips, R. J. Relationship Between The Carbon-Oxygen Stretching Frequencies of Carboxylato Complexes and the Type of Carboxylate Coordination. *Coord. Chem. Rev.* **33,** (1980).

19. Bünzli, J.-C. G. & Piguet, C. Taking advantage of luminescent lanthanide ions. *Chem. Soc. Rev.* **34,** 1048 - 1077 (2005).

20. Eliseeva, S. V. & Bünzli, J. C. G. Lanthanide luminescence for functional materials and bio-sciences. *Chem. Soc. Rev.* **39,** 189–227 (2010).

21. Bradaric, C. J., Downard, A., Kennedy, C., Robertson, A. J. & Zhou, Y. Industrial preparation of phosphonium ionic liquids. *Green Chem.* **5,** 143–152 (2003).

22. Benelli, C. & Gatteschi, D. Magnetism of lanthanides in molecular materials with transition-metal ions and organic radicals. *Chem. Rev.* **102,** 2369–2387 (2002).

23. Coey, J. M. D. *Magnetism and Magnetic Materials*. (Cambridge University Press, 2010). doi:10.1017/CBO9780511845000

24. Peng, Y., Mereacre, V., Anson, C. & Powell, A. Tuning of Hula-Hoop Coordination Geometry in a Dy Dimer. *Inorganics* **4,** 2 (2016).

25. Liu, L., Li, Y., Deng, S. X. & Zhang, Y. P. A dysprosium(III) complex based on Schiff-base ligand exhibiting two magnetic relaxation processes. *Inorganica Chim. Acta* **457,** 1–6 (2017).

26. Comba, P. *et al.* Magnetic Interactions in a Series of Homodinuclear Lanthanide Complexes. *Inorg. Chem.* **54,** 11247–11258 (2015).

27. O'Connor, C. J. Magnetochemistry—Advances in Theory and Experimentation. in *Progress in Inorganic Chemistry* (ed. Lippard, S. J.) 203–282 (Wiley, 2007).

28. Kahwa, I. A., Selbin, J., O'Connor, C. J., Foise, J. W. & McPherson, G. L. Magnetic and luminescence characteristics of dinuclear complexes of lanthanides and a phenolic schiff base macrocyclic ligand. *Inorganica Chimica Acta* **148,** 265–272 (1988).

29. Li, B. *et al.* $[Ln_2(C_2O_4)_2(pyzc)_2(H_2O)_2]n$[Ln = Pr (1), Er (2)]: novel two-dimensional lanthanide coordination polymers with 2-pyrazinecarboxylate and oxalate. *Inorg. Chem.* **45,** 10425–10427 (2006).

30. Xu, N., Shi, W., Liao, D. Z., Yan, S. P. & Cheng, P. Template synthesis of lanthanide (Pr, Nd, Gd) coordination polymers with 2-hydroxynicotinic acid exhibiting ferro-/antiferromagnetic interaction. *Inorg. Chem.* **47,** 8748–8756 (2008).

31. Xu, N. *et al.* Magnetic and luminescent properties of Sm, Eu, Tb, and Dy coordination polymers with 2-hydroxynicotinic acid. *Eur. J. Inorg. Chem.* 2387–2393 (2011). doi:10.1002/ejic.201100022

32. Tang, J.-K. *et al.* A novel tetranuclear lanthanide(III)–copper(II) complex of the macrocyclic oxamide [PrCu3] (macrocyclic oxamide = 1,4,8,11-tetraazacyclotradecanne-2,3-dione): synthesis, structure and magnetism. *Inorganica Chim. Acta* **358**, 325–330 (2004).

33. Canadillas-Delgado, L. *et al.* Dinuclear and two- and three-dimensional gadolinium(III) complexes with mono- and dicarboxylate ligands: synthesis, structure and magnetic

properties. *CrystEngComm* 10–11 (2009). doi:10.1039/b905912a

34. Zhou, Y. *et al.* Ionic Liquids Composed of Phosphonium Cations and Organophosphate, Carboxylate, and Sulfonate Anions as Lubricant Antiwear Additives. *Langmuir* **30,** 13301–13311 (2014).

35. Binnemans, K. *et al.* Lanthanide(III) Dodecanoates: Structure, Thermal Behaviour, and Ion-Size Effects on the Mesomorphism. *Eur. J. Inorg. Chem.***,** 1429–1436 (2000).

Chapter 4. Application of Magnetic Ionic Liquids

4.1 Chapter Aims

In this chapter, we combine the ability of a functionalised ionic liquid to selectively coordinate to a metal cation in solution and the magnetic properties of an ionic liquid, which is expected to lead to easier separation of the organic phase from an aqueous phase. Therefore, we tune the anion and cation properties of ionic liquids in the development of a task-specific magnetic ionic liquid for application in the extraction of uranyl nitrate from aqueous feed solutions. The novel task-specific magnetic ionic liquid, named as amide-functionalised paramagnetic ionic liquid, and abbreviated to AFPMIL, has been synthesized and its capability investigated for the extraction of U(VI) from a nitric acid medium. Variations in the pH of the feed solution greatly influenced the extraction efficiency. Slope analysis was used to determine the stoichiometry of U (VI) to the AFPMIL. The nature of uranyl nitrate coordination to AFPMIL was further explored via speciation techniques such as Fourier transform infrared, UV-Vis spectroscopy and theoretical calculations. Finally, it is shown how employing a task-specific magnetic ionic liquid in this context can offer superior control during the separation and recovery of the ionic liquid through application of an externally applied magnetic field.

4.2 Introduction

The recovery and extraction of actinides, uranium and plutonium, is a key step in reprocessing of spent nuclear fuel. Liquid-liquid extraction processes, the PUREX[1,2] (*plutonium and uranium recovery by extraction*) or TRUEX[3] (*TRansUranium Extraction*) process, for example, employ tri-*n*-butylphosphate (TBP) or octyl(phenyl)-*N,N*-diisobutylcarbamoyl methyl phosphine oxide (CMPO) as extractants dissolved in organic solvents such as kerosene or dodecane. Although TBP is effectively used at industrial scale it has shown various limitations; e.g. the inability to incinerate leads to large volumes of secondary radioactive waste, the generation of radiolytic degradation products decreases the stripping efficacy.[4] Alternative extractants that may overcome these limitations therefore become attractive. Siddall[5] was the first to explore N,N-dialkyl aliphatic amide based extractants, beneficial given the incinerable nature of N,N-dialkyl amides, which decreases secondary waste.[5]

Over the years, ionic liquids (ILs) have been omnipresent in this field in two main roles; (i) as diluents (ii) as the extractant itself. ILs are well-documented as having unique physical and chemical properties such as non-volatility, high thermal and chemical stability, wide liquid range and tunability which make them appealing in this context.[6] Moreover, IL's can offer a unique solvent environment for extraction processes as reported by Gutowski *et al*.[7] Understanding the solvation of metal ions in ILs is however key for furthering our development of the extraction process in ILs. Speciation of the uranyl in ILs gives valuable insights into the molecular symmetry of the uranyl complex and can give an insight into the coordination behaviour.[8–10]

The ability to fine-tune both the cation and anion structure enables numerous possibilities and exciting potential to incorporate specific features into the ionic liquid structure which further broadens their scope. In this respect, various groups have been able to develop liquid-liquid extraction processes using functionalised ionic liquids (FILs) or task-specific ionic liquids (TSILs). There are many examples where this has been effective. Visser *et al*. investigated the coordination and extraction of Hg^{2+} and Cd^{2+} by incorporating urea, thiourea and thioether into an imidazolium cation.[11] Ouadi *et al*. synthesised hydrophobic ionic liquids based on quaternary ammonium cations bearing phosphoryl moieties and their application in the extraction of U (VI) was investigated.[12] Odinets *et al*. effectively incorporated the CMPO moiety into the alkyl chain of an imidazolium cation and report promising properties for actinide and rare-earth element recovery from acidic solutions.[13] Rout *et al.* investigated the extraction of Pu (IV), U (VI) and Am (III) from nitric acid medium using an amide functionalised ionic liquid.[14] Pu (IV) was selectively extracted and understood to follow an anion exchange mechanism at concentrations above 4 M. The distribution ratios for U (VI) or Am (III) were however insignificant over the entire acidity range investigated. Incorporating amides can be advantageous as in addition to their ability to be readily incinerated, they exhibit high stability towards hydrolysis and radiolysis.[4]

Paramagnetic ionic liquids have been seen as effective catalysts, extractants and due to their intrinsic magnetic properties, manipulation of the ionic liquid by means of an externally applied magnetic field allows for ease of separation.[15] The incorporation of paramagnetic components into either the anion or cation structure further broadens the scope of ionic liquids with most applications exploiting their inherent magnetic responsivity. In liquid-liquid extraction studies, this property has

been found to be most beneficial in phase separation. Deng *et al.* explored the use of $[P_{666\,14}][FeCl_4]$ as an extraction solvent for the separation of phenolic compounds from aqueous solutions in the presence of a neodymium magnet.[16] Paramagnetic ionic liquids have also been shown to be efficient solvents for the rapid and efficient extraction of DNA from aqueous solutions.[17,18] The ability to incorporate this control was considered a significant benefit in addressing time constraints encountered by traditional extraction procedures where centrifuging techniques are required. Given the above considerations, it is therefore not unreasonable to suggest that paramagnetic ionic liquids could prove beneficial in the separation and recovery of metal ions e.g. actinides from acid media.

4.3 Results and Discussion

4.3.1 Design and Synthesis

In the work described herein, a novel amide-functionalised paramagnetic ionic liquid (AFPMIL) was specifically developed, seizing the opportunity to incorporate and tune the anion and cation properties for the extraction of U(VI) from nitric acid medium. AFPMIL, presented in Figure 85, comprises of following components, each playing a specific role as described;

(i) A mono-amide moiety tethered to the cationic part of ionic liquid for U(VI) extraction.

(ii) A phosphonium moiety with three bulky alkyl chains (octyl) to provide hydrophobicity to the ionic liquid to avoid leaching into the aqueous phase.

(iii) At least three carbon atoms in the linker chain to minimise charge repulsion between the cationic core (ionic liquid) and uranyl ion complexed with amidic linkage.

(iv) Incorporation of paramagnetic properties through $[FeCl_4]^-$ anion of the ionic liquid.

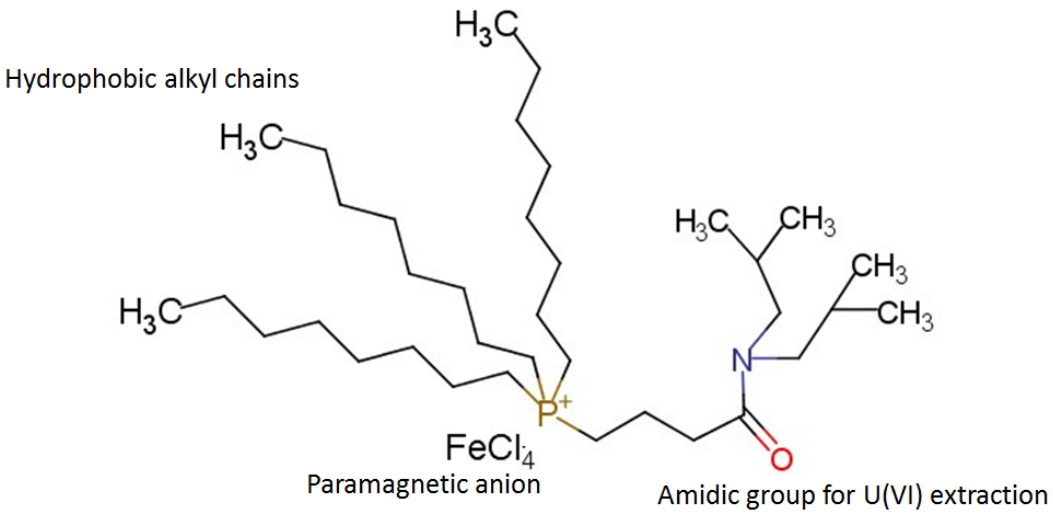

Figure 85. Amide functionalised paramagnetic ionic liquid, AFPMIL.

4.3.2 Extraction

It is well known, that extraction and recovery of U(VI) is most efficient in nitric acid media.[19] To investigate the effect of nitric acid concentration on the extraction efficiency of AFPMIL, various concentrations of aqueous feed solutions from 0.01 M – 1 M HNO_3, containing 250 ppm U (VI) were contacted with 0.05 M AFPMIL in a $[P_{666\ 14}][FeCl_4]$ diluent.

As presented in Figure 86, an increase in the distribution ratio and the extraction efficiency as the nitric acid concentration increases from 0.01 M – 1 M was observed. An increase in HNO_3 concentration was therefore seen to assist the extraction process. This increase in extraction efficiency when using ionic liquids was also previously observed by Giridhar *et al*.[20] and was attributed to the solubility of the uranyl nitrate species in RTILs.

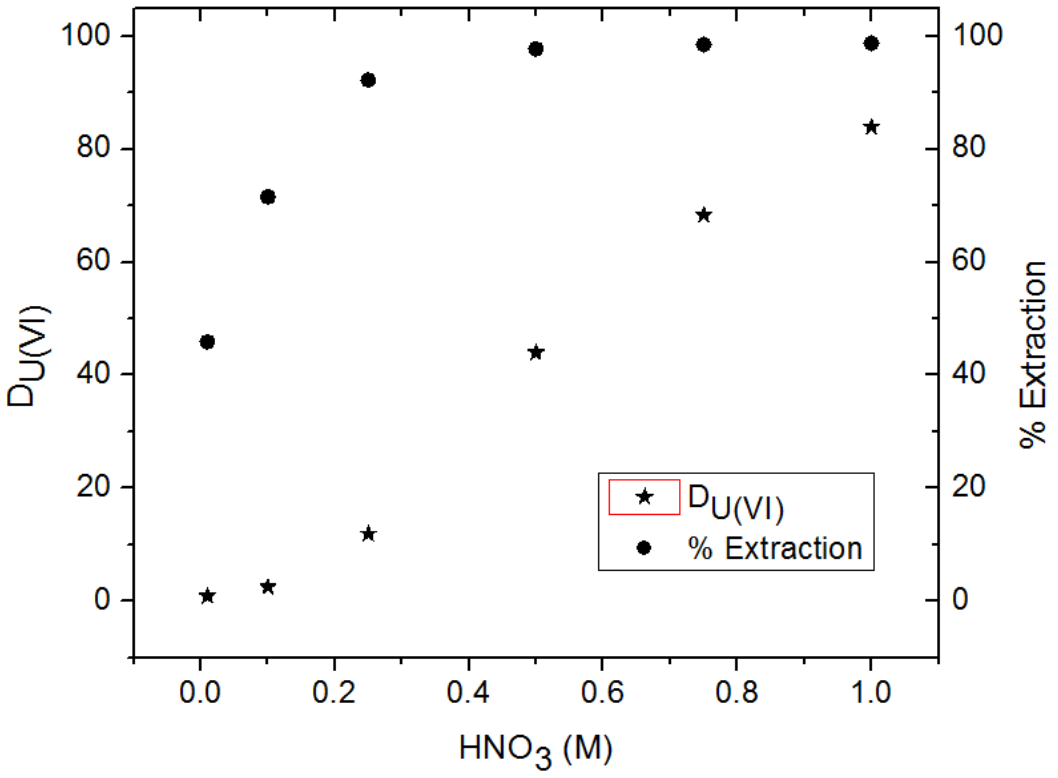

Figure 86. Variation of distribution ratio (D) and the extraction efficiency (E), 0.05 M AFPMIL/$[P_{666\ 14}][FeCl_4]$.

To study the effect of AFPMIL concentration on the extraction efficiency, the extraction of uranium as a function of concentration of AFPMIL (varied from 0.03 M – 0.13 M) at fixed feed acidity of 0.25 M HNO_3 was investigated. As demonstrated in Figure 87 as the concentration of AFPMIL is increased, a significant increase in the distribution ratio from 3.9 to 72.1 is observed.

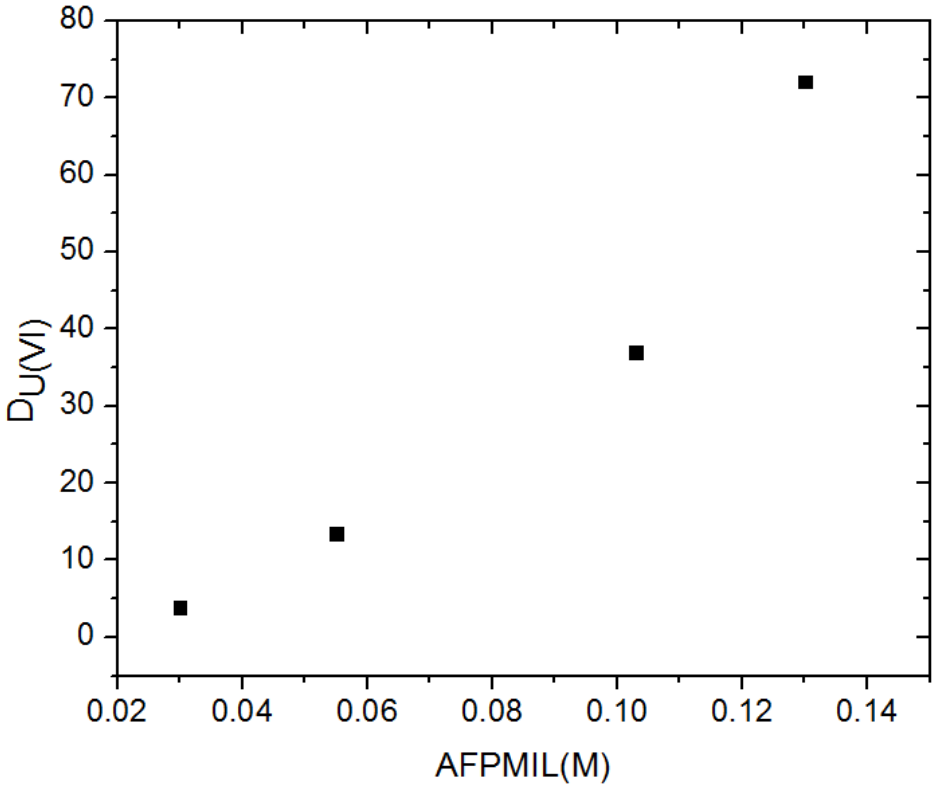

Figure 87. Variation of the distribution ratio (D) as a function of AFPMIL concentration.

Furthermore, mechanistic insight into the extraction process could be achieved *via* slope analysis of the extraction data. The ratio of metal ion to AFPMIL was determined by plotting log D_U vs. log [AFPMIL] at a fixed feed acidity. A slope of 1.91 was obtained, an indication of a 2:1 (AFPMIL: U (VI)) stoichiometry (Figure 88).

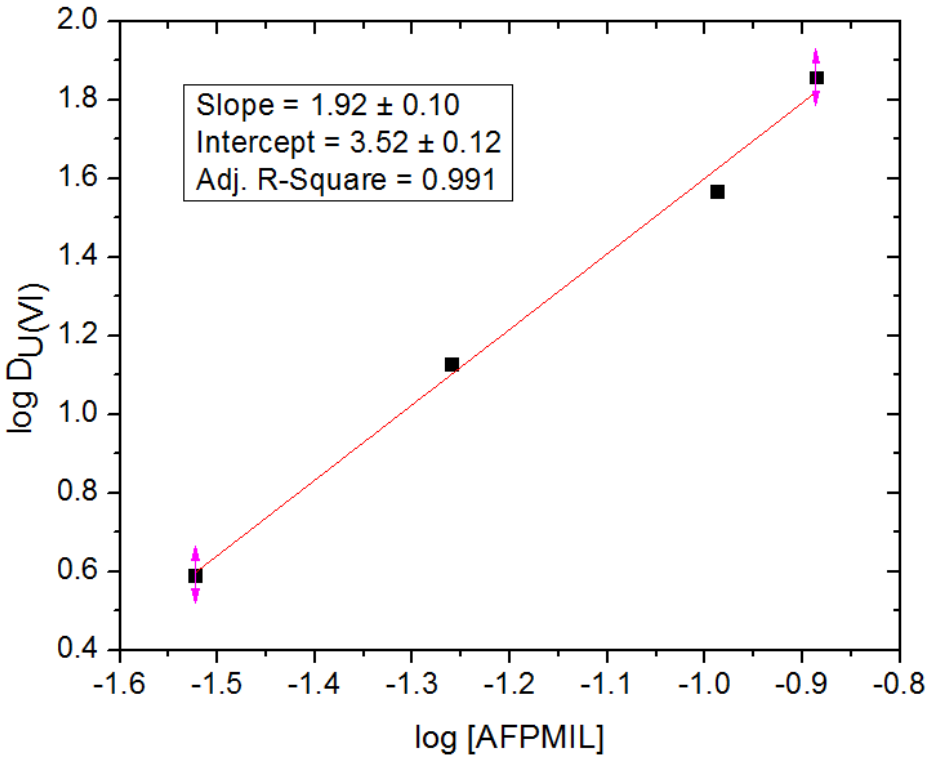

Figure 88. Plot of log [AFPMIL] vs. log $D_{U(VI)}$ (slope analysis).

So far, the capability of AFPMIL to extract UO_2^{2+} has been demonstrated. In addition, the intrinsic paramagnetic properties enable ease of separation. The effect of applying an external magnetic field on the paramagnetic IL is demonstrated in Figure 89 (on the right shows AFPMIL in contact with uranium feed solution and figure on the left is AFPMIL in contact with uranium feed solution under external magnetic field (neodymium magnet). It can be easily seen that on applying an external magnetic field, the AFPMIL phase could be effectively separated from the aqueous phase, thereby providing a promising option of magnetic field-assisted phase separation.

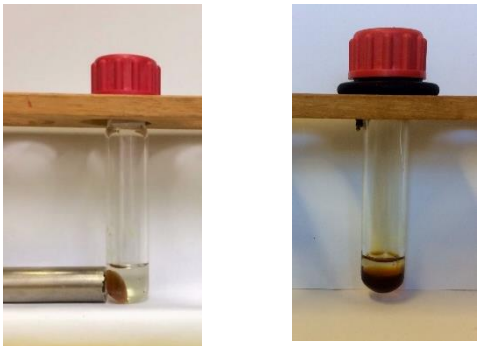

Figure 89. AFPMIL contacted with feed solution (0.1 M HNO_3 containing 250 ppm U (VI), with (left) and without (right) the application of an external magnetic field.

4.3.3 Spectroscopic techniques

To establish a clear mode and pathway of extraction in ionic liquids, FT-IR and UV/vis spectroscopic techniques were employed to aid in the understanding of the speciation of uranyl in AFPMIL. FT-IR analysis of neat AFPMIL and AFPMIL loaded with uranyl nitrate is presented in Figure 90. Significant shifts in the carbonyl stretching frequency (C=O) from 1621 cm^{-1} to 1571 cm^{-1},[21] observed in the spectra below gave clear indication of the coordination of uranium to the carbonyl moiety of the AFPMIL. Furthermore, additional peaks are observed at 1270 cm^{-1} (N–O stretching frequency of nitrate ions) and 921 cm^{-1} (O=U=O stretching frequency of UO_2^{2+} ions), further confirming the uptake of uranium by AFPMIL as uranyl nitrate.

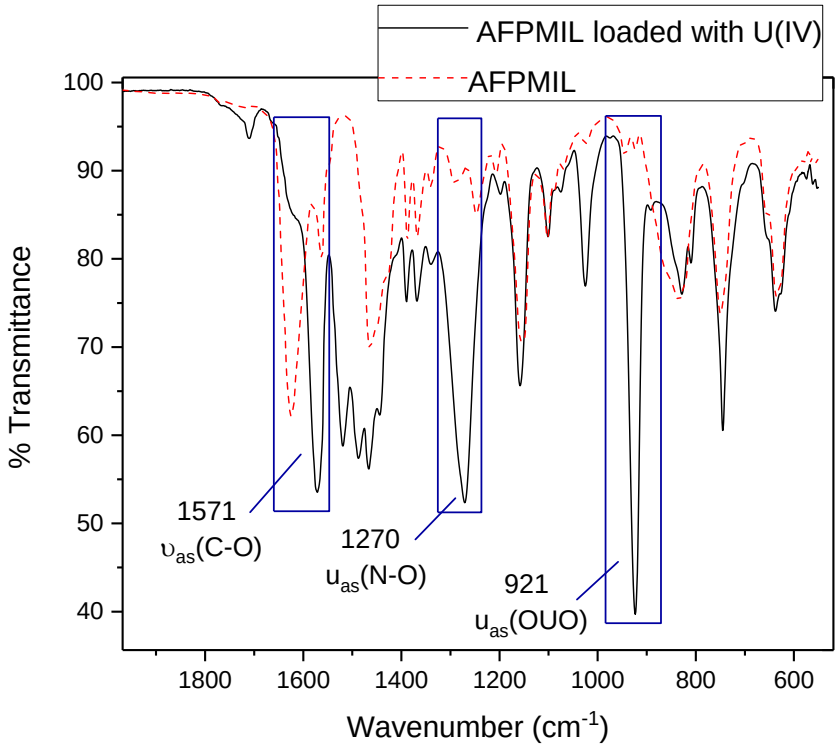

Figure 90. FTIR spectra of the neat AFPMIL (red) and U (VI) loaded AFPMIL (black).

UV-visible spectroscopic studies were carried out to give further understanding of the speciation of uranyl nitrate to AFPMIL. All spectra were recorded at room temperature using a 1 cm^3 quartz cell. The absorption spectra were recorded with varying AFPMIL/uranyl ratios, ranging from 0 to 5 equivalents of the amide-functionalised paramagnetic ionic liquid. The uranyl ion has a characteristic vibronic fine structure with a geometry and coordination symmetry that enables UV/vis to elucidate and structure and speciation of the complex in solution. The coordination of the UO_2^{2+} ion is normally occurring in the equatorial plane. Figure 91 shows the effect of addition of various equivalents of AFPMIL to the uranyl in acetonitrile as a solvent. Initial $UO_2(NO_3)_2{\cdot}6H_2O$ solution show characteristic absorption bands similar to those reported in the literature for aqueous solutions.[22] On addition of 1

equivalent AFPMIL, the absorption spectra become more intense and continues changing with up to two equivalents where an obvious flattening of the UO_2 absorbance spectrum is observed. This is an indication of a change in symmetry around the uranyl ion, and a further indication of a changing coordination.

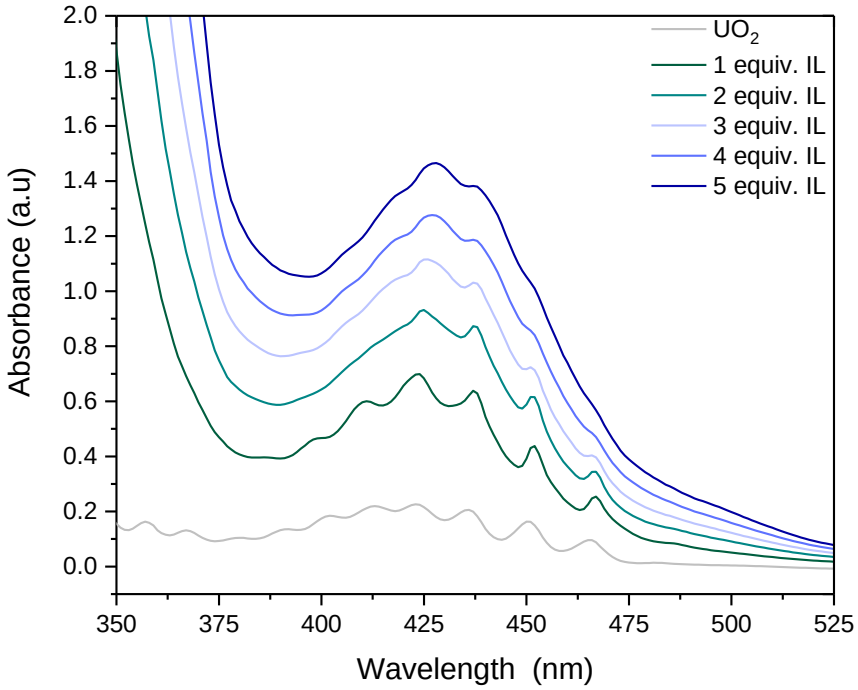

Figure 91. UV/vis spectra of uranyl nitrate in various mole ratios of AFPMIL.

4.3.4 Geometry optimisation *via* simulation

Due to the bulky nature of the amide-functionalised magnetic ionic liquid, crystallisation is unlikely. To explore the coordination of uranyl to the AFPIL, geometry optimisation was done *via* simulation, employing a BP86 functional with def-SV(P) basis set for each element except uranium which used an ECP-def-SV(P) basis set. Figure 92 shows the optimized geometry of the $UO_2(NO_3)_2$-AFPMIL complex. It can be seen that the cationic (phosphonium) and anionic part ($[FeCl_4]^-$) of

the ionic liquid moiety are at a distance of 4.72 Å, which is very typical of most of the ionic liquids.[23] The optimized geometry of the complex conforms to a bipyramid centred on the uranium (of uranyl ion) surrounded by eight oxygen atoms.[24] The ligation came from two oxygen atoms of the uranyl ion, two oxygen atoms of each of the nitrate group and oxygen atom of each of the amidic moiety of AFPMIL. It is also observed that oxygen (amidic moiety) is at shorter distance to uranium {U–O (2.4 Å)} as compared to oxygen atoms of the nitrate ion {U–O (2.52 Å)}, thus showing the greater interactions of the amidic moiety with uranium.

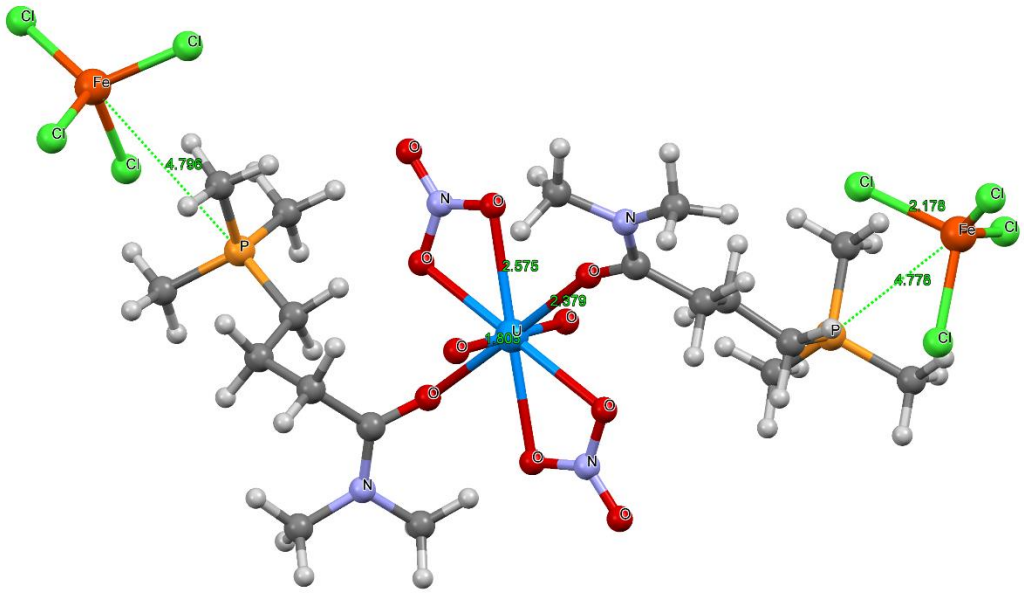

Figure 92. Optimised geometry of $UO_2(NO_3)_2$-AFPMIL complex. Optimization of geometry (for all species) was done using BP86 functional with def-SV(P) basis set for each element except uranium (ECP-def-SV(P)).

4.3.5 Considerations

4.3.5.1 Long term stability of AFPMIL

Short term stability of the magnetic ionic liquid for extraction of uranyl nitrate has not been a concern. However, after one month, the amide-functionalised paramagnetic ionic liquid was observed to crystallise.

Single crystals were analysed showing the formation of diisobutyl(tetrahydro-2,2-furylidene)aminium tetrachloroferrate. The crystal structure is presented is Figure 93 and illustrated in Figure 94. Similar structures have been reported previously by Zlokazov *et al*.[25] and is believed to be a ring-chain tautomeric conversion.

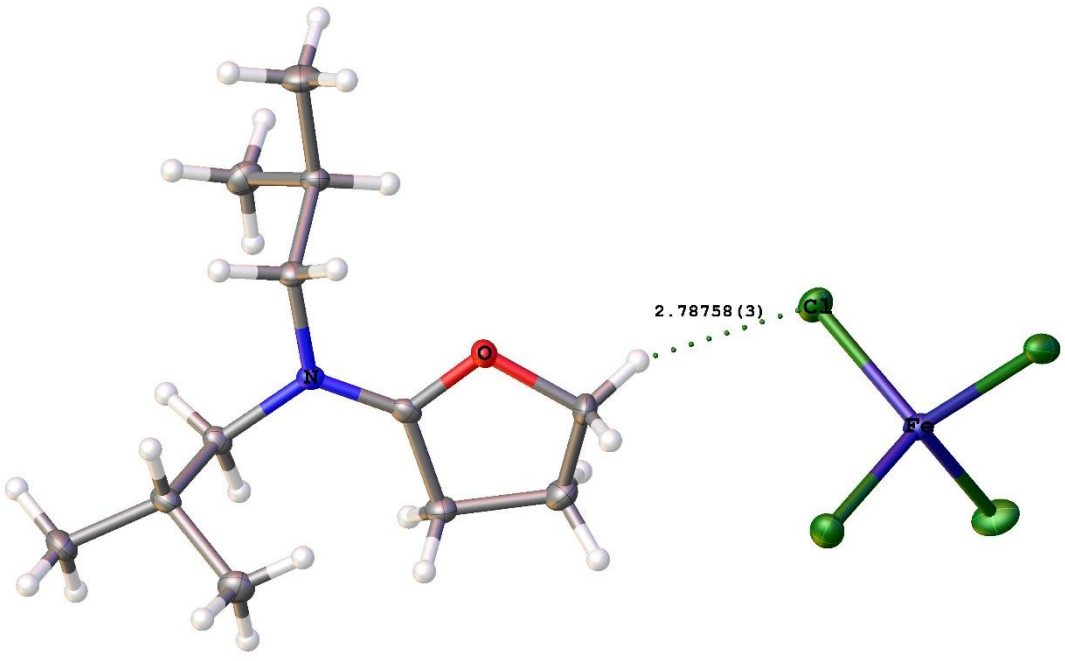

Figure 93. Crystal structure showing the formation of a diisobutyl(tetrahydro-2,2-furylidene)aminium tetrachloroferrate.

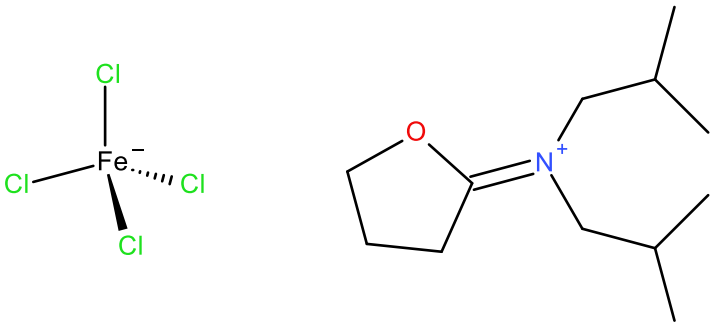

Figure 94. Formation of diisobutyl(tetrahydro-2,2-furylidene)aminium tetrachloroferrate.

Table 30. Crystal refinement data for crystal structure presented in Figure 94.

Identification code	diisobutyl(tetrahydro-2,2-furylidene)aminium tetrachloroferrate
Empirical formula	$C_{12}H_{24}NO.Cl_4Fe$
Formula weight	396.99
Temperature/K	100.01(11)
Crystal system	monoclinic
Space group	$P2_1/c$
a/Å	8.74250(10)
b/Å	9.6392(2)
c/Å	22.1625(3)
α/°	90
β/°	93.4030(10)
γ/°	90
Volume/Å^3	1864.36(5)
Z	18
ρ_{calc}g/cm^3	2.650
μ/mm^{-1}	37.352
F(000)	1440.0
Crystal size/mm^3	0.755 × 0.534 × 0.211
Radiation	CuKα (λ = 1.54184)
2Θ range for data collection/°	7.992 to 148.46
Index ranges	-9 ≤ h ≤ 10, -10 ≤ k ≤ 11, -27 ≤ l ≤ 27
Reflections collected	16821
Independent reflections	3752 [R_{int} = 0.0825, R_{sigma} = 0.0481]
Data/restraints/parameters	3752/0/176
Goodness-of-fit on F^2	1.067
Final R indexes [I>=2σ (I)]	R_1 = 0.0437, wR_2 = 0.1141
Final R indexes [all data]	R_1 = 0.0469, wR_2 = 0.1167
Largest diff. peak/hole / e Å^{-3}	0.85/-0.82

4.3.5.2 Hydrophobicity

In terms of the application of magnetic ionic liquids, the $[FeCl_4]^-$ anion has been most widely investigated. The long-term stability of this anion towards hydrolysis, however, must also be considered.[26] The work presented herein, has focused on securing hydrophobic character in the cation by the inclusion of a bulky trioctylphosphonium group. However, Pierson *et al.*[27] have looked at alternatives to the $[FeCl_4]^-$ anion by incorporating chelating ligands in the form of hexafluoroacetylacetonate ($[hfacac]^-$). This was first explored by Medhi *et al.*[28], where, the hexafluoroacetylacetonate anion was highlighted as exhibiting strong metal-complexing ability and hydrophobicity. In the work of Pierson *et al.*,[29] both transition and rare-earth containing ionic liquids were formed, $[P_{666\,14}][M(II)(hfacac)_3]$ (M = Co, Mn and Ni) and $[P_{666\,14}][M(III)(hfacac)_4]$ (M = Dy, Gd and Nd). Going forward this is an important consideration and something that still needs to be investigated.

4.4 Conclusion

The synthesis of a novel task-specific paramagnetic ionic liquid for the extraction of U(VI) from nitric acid medium is reported. Not only is this ionic liquid intrinsically paramagnetic the ability to fine tune the ionic liquid structure has enabled the incorporation of an extracting moiety, in the form of a monoamide functional group to the cation structure. Preliminary results show high extraction efficiency and distribution ratios at 1 M HNO_3. Mechanistic insights into the extraction process were gained through DFT, FTIR and slope analysis. Combining these methods we can conclude that U(VI) is extracted in a 2:1 AFPMIL:UO_2^{2+} ratio through the carbonyl moiety of the amide. The effect of the magnetic on separating the AFPMIL has been visually demonstrated. Inducing this control, we believe, serves as a benefit during the separation process.

4.5 Experimental methods

4.5.1 Chemicals

N,N-diisobutylamine (99 %), trimethylamine (99 %), 4-chlorobutyryl chloride (98 %) and iron chloride hexahydrate (97 %) were purchased from Alfa Aesar. Trihexyl(tetradecyl)phosphonium chloride (95 %) was donated by Cytec (now Solvay).

4.5.2 Synthesis of AFPMIL

To a two-neck flask equipped with reflux condenser was added; *N,N*-diisobutylamine (10 g, 70 mmol), triethylamine (9.39 g, 93 mmol) and chloroform (50 mL). The flask was immersed in an ice bath and 4-chlorobutyryl chloride (10.89 g, 77 mmol) was added dropwise. The reaction mixture was stirred at 0 °C for 1 hour after which the temperature was allowed to increase to room temperature and further stirred for 8 hours. The product was successively washed with 0.1 M HCl, 0.1 M Na_2CO_3, deionised water and finally separated. Chloroform was removed from organic phase by rotary evaporation at 60 °C and the product was dried under high *vac.* overnight at 65 °C. ^{1}H (300 MHz, $CDCl_3$) δ 0.88 (dd, 12 H, 4 X CH_3), 1.96 (ddd, 2 H,) 2.12 (dt, 2 H, CH_2), 2.50 (q, 2, CH_2), 3.14 (dd, 4 H), 3.63 (t, 2 H). Theoretical %: C, 61.65, H, 10.35, N, 5.99. Actual %: C, 62.2, H, 10.62, N, 6.09.

MS: *m/z* (+) 234.16

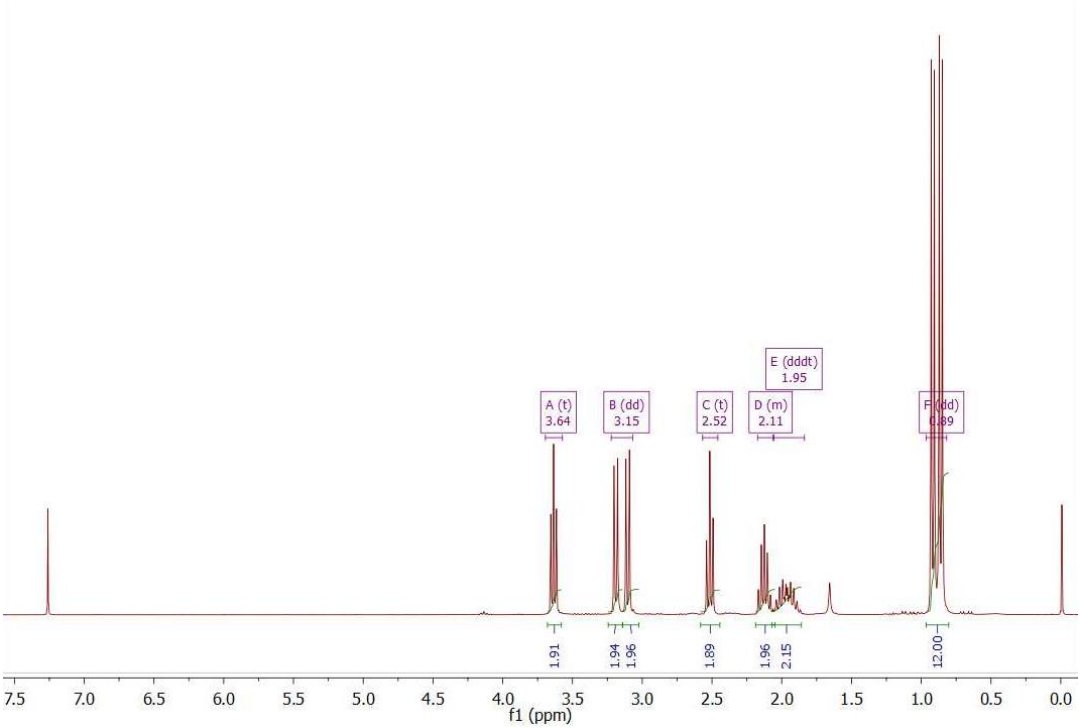

Figure 95. ^{1}H-NMR spectrum of 4-chloro-(N,N-diisobutyl) butyramide.

Under an argon atmosphere trioctylphosphine was added to the synthesised 4-chloro-(*N,N*-diisobutyl) butyramide in acetonitrile (Scheme 3). The reaction was heated to 65 °C and stirred for one week after which the acetonitrile was removed by rotary evaporation and the product dried under high *vac* at 65 °C. ^{1}H (300 MHz, $CDCl_3$) δ 0.88 (m, 21 H, 7 X CH_3), 1.34 (d, 25 H,) 1.60 (m, 10 H, CH_2), 1.93 (m, 3 H), 2.10 (dt, 2 H), 2.51 (dd, 2 H), 3.12 (dd, 4 H), 3.61 (m, 2 H).

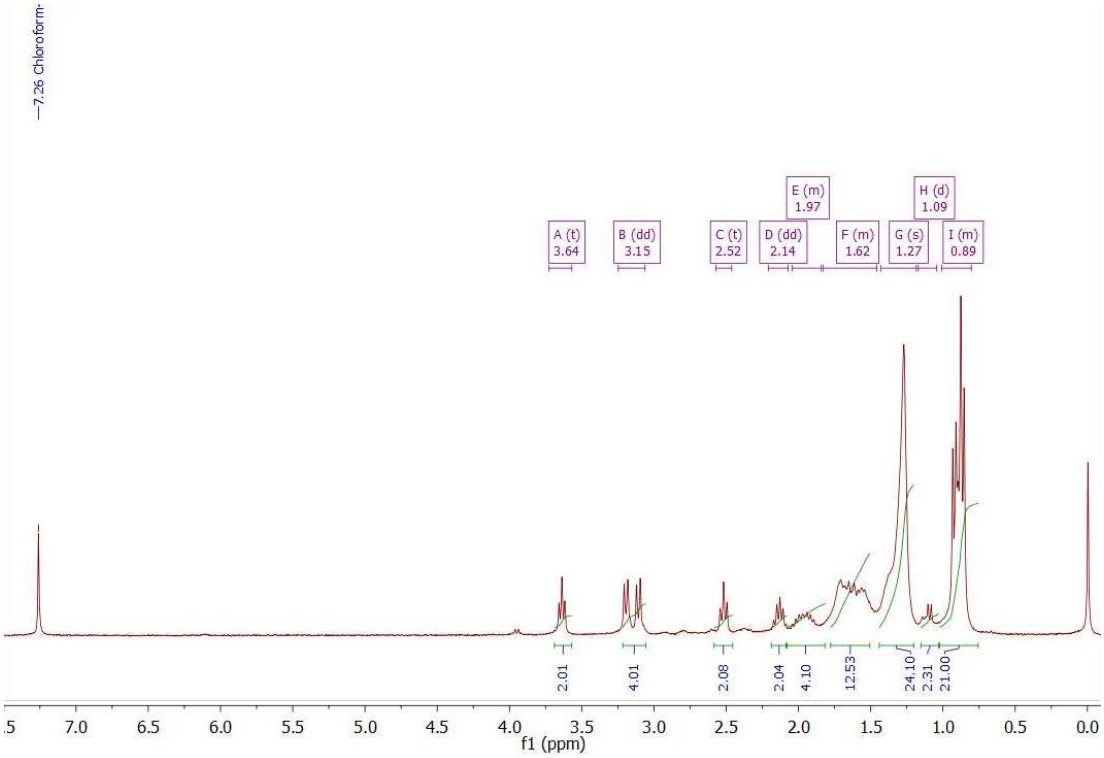

Figure 96. ^{1}H-NMR of trioctyl(diisobutylbutyramide)phosphonium chloride.

The paramagnetic moiety was incorporated by reaction of trioctyl(diisobutylbutyramide)phosphonium chloride with iron chloride hexahydrate in chloroform. The reaction was stirred overnight after which the water layer was separated from the organic layer and the chloroform removed by rotary evaporation to yield the paramagnetic trioctyl(diisobuytlbutyramide)phosphonium tetrachloroferrate.

Scheme 3. Reaction mechanism for the synthesis of the amide functionalised paramagnetic ionic liquid, AFPMIL, which follows an SN2 reaction.

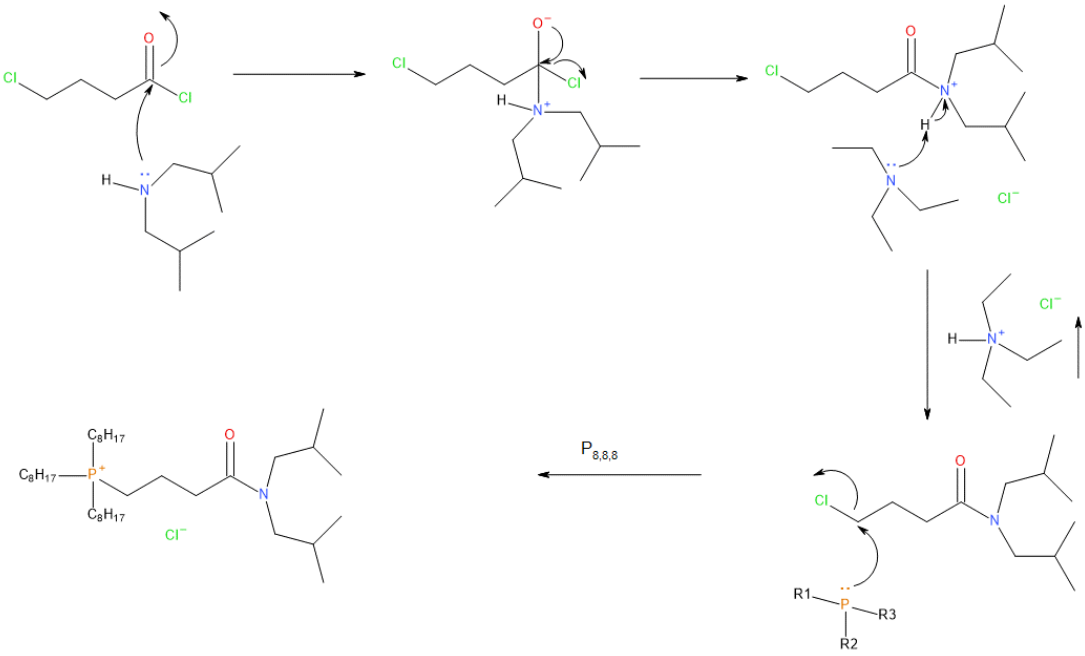

4.5.3 Synthesis of $[P_{666\ 14}][FeCl_4]$

$[P_{666\ 14}][FeCl_4]$ was used as a diluent for the extraction studies. This paramagnetic ionic liquid was prepared according to standard literature procedure[30] where trihexyl(tetradecyl)phosphonium chloride, $[P_{666\ 14}][Cl]$, (20 g, 38.5 mmol) was added in equimolar amounts to iron chloride hexahydrate (10.40 g, 38.5 mmol) in chloroform. The reaction was stirred at room temperature overnight and the water was separated from the organic layer. The organic phase was dried over $MgSO_4$ and filtered. Chloroform was removed by rotary evaporation and ionic liquid was dried overnight under high *vac* at 65 °C.

4.5.4 Liquid-liquid extraction experiments

Nitric acid solutions of various acidities, ranging from 0.01 M – 1 M, were prepared and to these, 250 ppm of U(VI) from uranyl nitrate hexahydrate was added, herein called feed solutions. AFPMIL was dissolved in diluent, namely, $[P_{666\,14}][FeCl_4]$ to make the ionic liquid extractant (organic phase) of various concentrations, and was used for liquid-liquid extraction with feed solutions. Typically 1 mL of 0.05 M AFPMIL/$[P_{666\,14}][FeCl_4]$ was taken in a 10 mL screw top glass vial. Prior to all uranium extraction experiments this was pre-equilibrated with 1 mL of the nitric acid concentration (representing feed solution acidity) using a wrist-action shaker (Burrell, model 75). The organic phase was then separated from the acid solution and subsequently contacted for 10 minutes on the wrist-action shaker with 1 mL of feed solution. The raffinate was separated from the organic phase and analysed by UV/Vis spectroscopy as discussed below. Extraction studies were performed in duplicate for the reproducibility purposes.

The distribution ratio (*D*) and extraction efficiency (*E*) were determined using the following equations:

$$\mathrm{D} = \frac{\mathrm{C_I} - \mathrm{C_F}}{\mathrm{C_F}}$$

Equation 4-1

$$\mathrm{E} = \frac{\mathrm{C_I} - \mathrm{C_F}}{\mathrm{C_I}} \times 100\ \%$$

Equation 4-2

C_I = initial concentration of feed solution

C_F = final concentrations of the feed solution

4.5.5 UV-visible Analysis

Uranium in the aqueous phase was analysed using a procedure reported earlier by Das *et al*.[31] Typically suitable aliquots from feed and raffinate solution were taken in a flask, a complexing solution (to avoid complexing with other metal ions if any) and a buffer solution (to maintain pH) were added to it and finally chromogenic reagent Br-PADAP was added. And after about 30 minutes, this solution containing [uranyl-(2-(5-bromo-2-pyridylazo)-5-diethylaminophenol)] was measured at 578 nm in a 1 cm^3 quartz cuvette on a spectrophotometer (Agilent, Cary 60 model).

As can be observed in Figure 97, at high concentrations of uranyl the solution is bright pink in colour with high absorbance as seen in Figure 98.

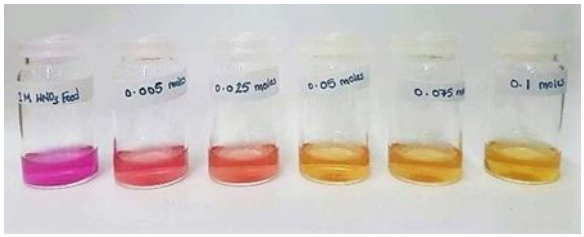

Figure 97. Colour changes observed with decreasing uranyl concentration left to right and using Br-PADAP as a complexing agent.

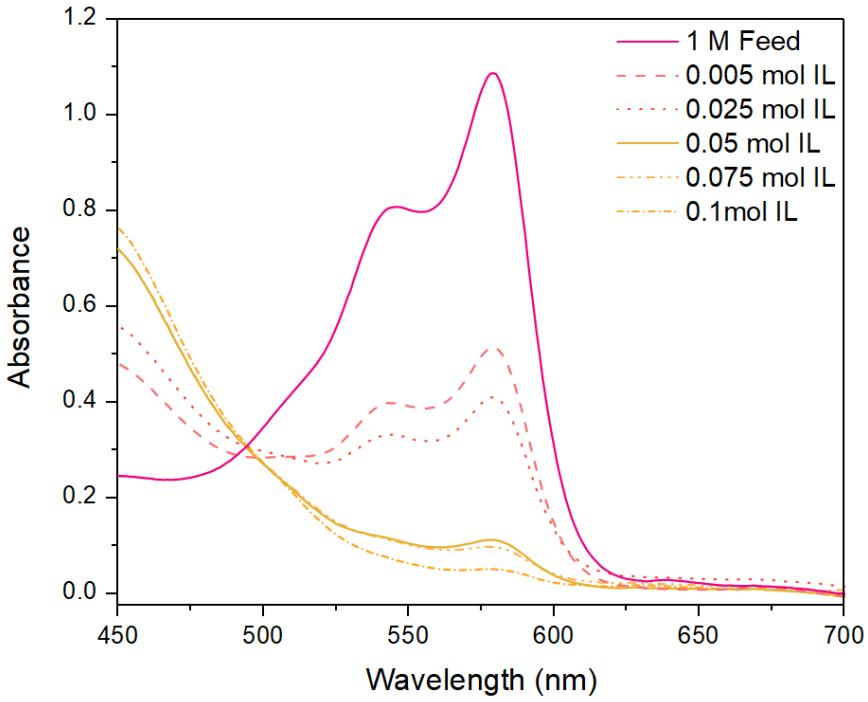

Figure 98. UV/Vis absorption spectra recorded at 578 nm for uranyl nitrate showing the decrease in uranyl concentration in the raffinate at higher acidities.

4.5.6 Calculation details

Optimization of geometry (for all species) was done using BP86 functional with def-SV(P) basis set for each element except uranium (ECP-def-SV(P)). The optimized geometries were subjected to vibrational calculations wherein the absence of imaginary harmonic vibrational frequencies suggested the attainment of energetic minima. Further to ease the calculations, the bulkier alkyl groups (e.g. isobutyl and octyl) were replaced by methyl groups.[32]

4.6 References

1. Choppin, G. R. Solvent Extraction Processes in the Nuclear Fuel Cycle. *Solvent Extr. Res. Dev. Japan* **12,** 1–10 (2005).
2. Myasoedov, B. F. THE SCIENCE AND TECHNOLOGY OF TRIBUTYL PHOSPHATE". *Solvent Extr. Ion Exch.* **4,** 1077–1078 (1986).
3. Schulz, W. W. & Horwitz, E. P. The Truex Process and the Management of Liquid Tru Uwaste. *Sep. Sci. Technol.* **23,** 1191–1210 (1988).
4. Mccann, K., Drader, J. A. & Braley, J. C. Comparing Branched versus Straight-chained Monoamide Extractants for Actinide Recovery Comparing Branched versus Straight-chained Monoamide Extractants for Actinide Recovery. *Sep. Purif. Rev.* **47,** 49–65 (2017).
5. Siddall, T. H. Effect of Structure of N,N-Disubstituted Amides on Extraction. *J. Phys. chem.* **64,** 1863–1866 (1960).
6. Freemantle, M. *An Introduction to Ionic Liquids*. *The Royal Society of Chemistry* (RSC Pub, 2010). doi:10.1016/S1351-4180(10)70136-7.
7. Gutowski, K. E. *et al.* in *Ionic Liquids Iiib: Fundamentals, Progress, Challenges and Opportunities: Transformations and Processes* **902,** 33–48 (2005).
8. Servaes, K. *et al.* Speciation of uranyl nitrato complexes in acetonitrile and in the ionic liquid 1-butyl-3-methylimidazolium bis(trifluoromethylsulfonyl)imide. *Eur. J. Inorg. Chem.* 5120–5126 (2007). doi:10.1002/ejic.200700475
9. Hennig, C. *et al.* Species Distribution and Coordination of Uranyl Chloro Complexes in Acetonitrile. *Inorg. Chem.* **47,** 2987–2993 (2008).
10. Nockemann, P. *et al.* Speciation of Uranyl Complexes in Ionic Liquids by Optical Spectroscopy. *Inorg. Chem* **46,** 11335–11344 (2007).
11. Visser, A. E. *et al.* Task-specific ionic liquids for the extraction of metal ions from aqueous solutions. *Chem. Commun* 135–136 (2001). doi:10.1039/b008041l.
12. Ouadi, A., Klimchuk, O., Gaillard, C. & Billard, I. Solvent extraction of U(vi) by task specific ionic liquids bearing phosphoryl groups. *Green Chem.* **9,** 1160 - 1162 (2007).
13. Odinets, I. L. *et al.* Novel class of functionalized ionic liquids with grafted CMPO-moieties for actinides and rare-earth elements recovery. *Dalt. Trans* **39,** 4170–4178 (2010).
14. Rout, A., Venkatesan, K. A., Srinivasan, T. G. & Vasudeva Rao, P. R. Extraction behavior of actinides and fission products in amide functionalized ionic liquid. *Sep. Purif. Technol.* **97,** 164–171 (2012).
15. Yoshida, Y. & Saito, G. Progress in Paramagnetic Ionic Liquids. *InTech* **3,** (2011).
16. Deng, N. *et al.* Highly efficient extraction of phenolic compounds by use of magnetic room temperature ionic liquids for environmental remediation. *J. Hazard. Mater.* **192,** 1350–1357 (2011).
17. Clark, K. D. *et al.* Extraction of DNA by magnetic ionic liquids: Tunable solvents for rapid and selective DNA analysis. *Anal. Chem.* **87,** 1552–1559 (2015).

18. Clark, K. D., Yamsek, M. M., Nacham, O. & Anderson, J. L. Magnetic ionic liquids as PCR-compatible solvents for DNA extraction from biological samples. *Chem. Commun. Chem. Commun* **51,** 16771–16773 (2015).

19. Liyong, Y. *et al.* Solvent extraction of U(VI) by trioctylphosphine oxide using a room-temperature ionic liquid. *Sci. China Chem.* **57,** 1432–1438 (2014).

20. Giridhar, P., Venkatesan, K. A. & Srinivasan P R Vasudeva Rao, T. G. Extraction of uranium(VI) from nitric acid medium by 1.1M tri-n-butylphosphate in ionic liquid diluent. *J. Radioanal. Nucl. Chem.* **265,** 31–38 (2005).

21. Prestianni, A. *et al.* IR Fingerprints of U(VI) Nitrate Monoamides Complexes: A Joint Experimental and Theoretical Study. *J. Phys. Chem. A* **114,** 10878–10884 (2010).

22. McGlynn, S. P. Spectroscopy and Photochemistry of Uranyl Compounds. *J. Am. Chem. Soc.* **87,** 2527 - 2527 (1965).

23. Yan, T., Wang, Y. & Knox, C. On the Structure of Ionic Liquids: Comparisons between Electronically Polarizable and Nonpolarizable Models I. *J. Phys. Chem. B* **114,** 6905–6921 (2010).

24. Ruhela, R. *et al.* N,N,N-Trimethyl benzyl ammonium bis-(2-ethylhexyl)-phosphonate grafted polymer – a solid supported ionic liquid for the separation of uranium from aqueous processing streams. *Green Chem* **17,** 827 - 830 (2015).

25. Zlokazov, M. V, Lozanova, A. V & Veselovsky, V. V. New examples of ring-chain tautomeric conversions. *Mendeleev Commun.* 242–243 (2003). doi:10.1070/MC2003v013n06ABEH001835

26. Xie, Z.-L. & Taubert, A. Thermomorphic Behavior of the Ionic Liquids $[C_4mim][FeCl_4]$ and $[C_{12}mim][FeCl_4]$. *ChemPhysChem* **12,** 364–368 (2011).

27. Pierson, S. A. *et al.* Synthesis and characterization of low viscosity hexafluoroacetylacetonate-based hydrophobic magnetic ionic liquids. *New J. Chem. New J. Chem* **5498,** 5498–5505 (2017).

28. Mehdi, H., Binnemans, K., Van Hecke, K., Van Meervelt, L. & Nockemann, P. Hydrophobic ionic liquids with strongly coordinating anions. *Chem. Commun.* **46,** 234–236 (2010).

29. Nacham, O., Clark, K. D., Yu, H. & Anderson, J. L. Synthetic Strategies for Tailoring the Physicochemical and Magnetic Properties of Hydrophobic Magnetic Ionic Liquids. *Chem. Mater* **9,** 923 - 931 (2015).

30. Sesto, R. E. Del *et al.* Structure and magnetic behavior of transition metal based ionic liquids. *Chem. Commun* **4,** 447–449 (2008).

31. K Das S G Regc, A. S., Mukherjee Ramanujam, A. A. & Dhumwad, R. K. Direct Spectrophoto Method for the Determination of Microgram Quantities of Uranium with BROMO PADAP in Aqueous and Organic Waste Streams of PUREX AND THOREX Processes. *B.A.R.C - 1539* (1991).

32. Ruhela, R., Tomar, B. S., Singh, A. K., Hubli, R. C. & Suri, A. K. Investigation of the extraction complexes of palladium(II) with novel thiodiglycolamide and dithiodiglycolamide ligands by EXAFS and computational methods. *Dalt. Trans.* **42,** 7085–7091 (2013).

Chapter 5. General Conclusions

In this thesis, various aspects of the design, characterisation, and application of magnetic ionic liquids have been investigated. In doing so, the course of this work has diverged into three main sections exploring metals ranging from d-block transition metals to 4f lanthanides and 5f actinides. Throughout this research, specific questions were asked in each chapter.

In chapter two, we questioned; (i) *Is it possible to recognise changes in the structural properties of Co(II) from its conductivity behaviour?* and secondly (ii) *Is it possible to induce changes in the coordination geometry of a cobalt complex through the use of high pressure?*

Chapter two explored the stimuli-responsive nature of cobalt-based magnetic ionic liquids. Cobalt thiocyanate salt in a reservoir of mobile thiocyanate ionic liquid $[C_4Mim][SCN]$ was observed to change coordination from tetrahedral to octahedral upon cooling which was reflected in a colour change and importantly the magnetic properties. To further explore the effects of stimulants we employed broadband dielectric spectroscopy which enabled the exploration of temperature and most importantly, pressure effects in inducing such a transition. Analysing the conductivity behaviour of cobalt thiocyanate, $Co(NCS)_2$, in ionic liquids $[P_{666\,14}][SCN]$ and $[C_4Mim][SCN]$ over very wide temperature, pressure and frequency ranges we questioned whether such transitions would be visible in the conductivity behaviour of the system. In changing the cation from $[C_4Mim]^+$ to $[P_{666\,14}]^+$ interesting conclusions could be drawn. Firstly, it was observed that changes in the coordination environment as a result of temperature were reflected in a sudden drop in the

conductivity behaviour. What is more, the same pattern of behaviour was also observed under the influence of hydrostatic pressure, albeit, at much higher temperatures. This meant that to realise a coordination change in the $[P_{666\,14}]^+$ cation system using pressure, such low temperatures were no longer required. Interestingly, the same pattern of behaviour was not observed in the $[C_4Mim][SCN]$ ionic liquid system. As a result, this made us look further into the types of cation and anion interactions present in the different types of ionic liquids. The cohesive energy of the relatively small $[C_4Mim]^+$ cation, which has a well delocalised positive charge on each atom of this cation, is largely governed by Coulombic interactions. Based on the globular molecular shape and mobile nature of the anion and cation in solution, changes in the coordination of the cobalt centre from tetrahedral to octahedral upon cooling may not have a dramatic effect on the conductivity of the solution. In addition, any change in the pressure in the imidazolium system does not seem to dramatically change the variation of its transport properties (no crossover was observed). On the other hand, in the phosphonium based systems where the positive charge is mainly localised on the phosphorus atom and on the alpha carbon moieties, the overall cohesive energy of this solution is mainly driven by van der Waals interactions caused by the long alkyl chains. As the temperature decreases, the structure becomes essentially frozen meaning any reorganisational changes in the cobalt structure become pronounced and result in dramatic changes in the conductivity of the solution. In addition, a pressure increase causes a decrease in the free volume, meaning the reorganisational space is reduced; however, the octahedral species require more space than tetrahedral ones, leading in fact to a huge effect of the coordination change on the activation volume of the solution. Therefore, we may

conclude that changes in the structural properties can be reflected in the conductivity behaviour, however, it is cation dependent, depending on the interactions governing the movement.

In chapter three, the design of dimeric lanthanide(III)-containing ionic compounds was investigated. We questioned: *"Can a dimeric structure be obtained in the liquid state?"* and, in case the answer is affirmative, (ii) *"How can the presence of a dimer be proven in a liquid?"*. By tuning the cation combination from 1-butyl-3-methylimidazolium, $[C_4Mim]^+$, to the bulky trihexyltetra(decyl)phosphonium, $[P_{666\ 14}]^+$, and further elongating the alkyl chain length of the ligands from acetate, $[CH_3COO]$, to octanoate, $[C_7H_{15}COO]$, the melting points could be tuned to create room temperature liquid lanthanide(III)-containing ionic compounds. Having confirmation of the formation of a dimeric structure in the solid state, we looked at whether the dimeric structure was maintained in the liquid state and, if so, how we might prove this theory. By investigation of the magnetic properties using SQUID magnetometry, we looked at the types of lanthanide(III) ion interactions present within each state. The same antiferromagnetic signature was observed in the crystalline, glass and liquid compounds a strong indicator that the magnetic dimers formed in the crystalline solid were in fact formed in the glass and liquid state as well.

In the final chapter, we questioned: "*How might magnetic ionic liquids be applied?*". The ability to tune the anion and cation structures of magnetic ionic liquids led to the successful development of a task-specific magnetic ionic liquid for extraction of uranyl from nitric acid medium. There were three specific design criteria. The first was that it contained extraction functionality. This was achieved by tethering a mono-

amide functional group to the cation. To achieve efficient extraction with minimal loss to the aqueous layer, a bulky trioctylphosphine was used to create hydrophobicity. Finally, to enable ease of separation, a magnetic component was incorporated in the form of a $[FeCl_4]^-$ anion. It was shown that as the nitric acid feed solutions increased in acidity the extraction efficiency increased. However, the long-term stability of the amide-functionalised cation and the hydrophobicity of the anion is something that needs to be further investigated.

5.1 Future Work

Broadband dielectric measurements investigating the effects of temperature and pressure provided interesting data when different cations were investigated. Going forward, it would be interesting to further explore the effect of cation, paying particular attention to the cation and anion interactions.

Continuing with the dimeric lanthanide(III)-containing ionic liquids, it would be beneficial to explore the magnetic properties of the remaining lanthanides. In doing so, a comparison between the light and heavy lanthanide elements may be deduced. In addition, there is further scope to investigate the physical properties of the lanthanide(III) complexes. In particular, the lanthanides can have interesting luminescent properties. Owing to the forbidden f-f transitions, however, the absorption of lanthanide(III) ions can be weak. Organic ligands may be used to incorporate organic chromophores which absorb light and further transfer the energy to the lanthanide ion in an effect known as the “Antenna Effect”. This ultimately enhances the luminescent properties. A future project could look at the effect of organic ligands in enhancing the luminescent properties of these lanthanide(III)-containing ionic liquids. To this end, β-diketones have been widely investigated for lanthanide coordination complexes.

Looking at the design of magnetic ionic liquids for application in metal extraction, it would be beneficial to look at anions other than the commonly used $[FeCl_4]^-$. In light of the thermomorphic behaviour of the $[FeCl_4]^-$ further work to prepare and ensure hydrophobicity in the anion will be important going forward. The extraction investigated herein has been limited to uranyl (VI) from nitric acid feed solutions as a

result of limited analysis techniques. Mixed metal systems that mimic industrial processes would be beneficial to further explore. Total reflectance X-ray fluorescence (TXRF) was recently purchased which would enable mixed metal systems to be investigated in the future. In addition, the efficient stripping and reusability of the magnetic ionic liquids need to be further explored.